
Interferometry in Astronomy

The GRAVITY Metrology System and Galaxy Evolution with the IRAM Interferometer

Magdalena Anna Lippa



München 2018

Interferometry in Astronomy

The GRAVITY Metrology System and Galaxy Evolution with the IRAM Interferometer

Magdalena Anna Lippa

Dissertation der Fakultät für Physik
der Ludwig–Maximilians–Universität München

vorgelegt von
Magdalena Anna Lippa
aus Pyskowice

München, 27. April 2018

Erstgutachter: Prof. Dr. Reinhard Genzel

Zweitgutachterin: Prof. Dr. Paola Caselli

Datum der mündlichen Prüfung: 7. Juni 2018

Table of Contents

Zusammenfassung	xiii
Abstract	xv
1 Introduction	1
2 The Principles of Interferometry	5
2.1 Spatial Resolution in Astronomy	5
2.1.1 Single Aperture	6
2.1.2 Multiple Apertures	9
2.1.3 Interferometric Observables	12
2.2 Radio Interferometry	15
2.2.1 Observations	15
2.2.2 Calibrations	18
2.2.3 Imaging	21
2.2.4 The IRAM Interferometer	27
2.3 Optical Interferometry	31
2.3.1 Adaptive Optics	32
2.3.2 Fringe Tracking	36
2.3.3 Phase Referencing	38
2.3.4 The Very Large Telescope Interferometer	40
3 The GRAVITY Metrology System	45
3.1 The VLTI Instrument GRAVITY	46
3.1.1 The Beam Combiner Instrument	46
3.1.2 Science Cases	53
3.2 Dual-Beam Scheme	57
3.2.1 Phase-Shifting Interferometry	59
3.2.2 Phase-Step Insensitive Calibration of the Phase Shifter	69
3.3 Three-Beam Scheme	84
3.3.1 Raman Scattering and Fluorescence in Optical Fibers	84
3.3.2 Mitigation Strategies	98

4	Galaxy Evolution with the IRAM Interferometer	115
4.1	Molecular Gas as the Fuel of Star Formation	116
4.1.1	Probing the Molecular Gas	118
4.1.2	The PHIBSS and PHIBSS2 Surveys	124
4.2	Spatially-Resolved Molecular Gas and Star Formation at $z \sim 1$	131
4.2.1	Analysis of Properties from Stellar Continuum and Molecular Emission	133
4.2.2	Results on the Morphologies and Dynamics	147
4.3	Molecular Outflows in EGS13004291	168
4.3.1	Resolved Mapping of Stellar Continuum and Molecular Emission . .	170
4.3.2	Spectral Analysis of Molecular Emission	175
5	Conclusions	193
5.1	Galaxy Evolution with the IRAM Interferometer	193
5.1.1	Spatially-Resolved Molecular Gas and Star Formation at $z \sim 1$. . .	194
5.1.2	Molecular Outflows in EGS13004291	196
5.2	The GRAVITY Metrology System	197
5.2.1	Phase-Step Insensitive Calibration of the Phase Shifter	198
5.2.2	Raman Scattering and Fluorescence in Optical Fibers	198
	Bibliography	203
	List of Acronyms and Abbreviations	215
	Acknowledgments	219

List of Figures

2.1	Geometry of observations with a single aperture	7
2.2	Young's two-slit experiment	9
2.3	Basic interferometric setup	11
2.4	Polychromatic fringe pattern	13
2.5	Comparison between a typical optical and radio interferometer	15
2.6	Down-conversion of the radio frequency	17
2.7	Atmospheric profiles	19
2.8	Atmospheric opacity	20
2.9	Observation sequence	20
2.10	Calibrated data	21
2.11	Dirty components	23
2.12	Clean components	24
2.13	Definition of intensity	27
2.14	The IRAM interferometer	28
2.15	Visibility models	30
2.16	Comparison of the Fizeau and Michelson configuration	32
2.17	The working principle of adaptive optics	33
2.18	Closure-phase technique	37
2.19	Differential optical path difference	39
2.20	VLTI infrastructure	41
3.1	Working principle of GRAVITY at the VLTI	47
3.2	Beam combiner instrument of GRAVITY	48
3.3	Integrated-optics chip	51
3.4	The Galactic Center	54
3.5	Dual-beam astrometry of the binary GJ 65 AB	58
3.6	Working principle of the dual-beam metrology	60
3.7	Design of the dual-beam metrology	63
3.8	Polarization-maintaining fiber and connector	65
3.9	Metrology receivers	68
3.10	Phase shifter	70
3.11	Fusion splicer from the company Fujikura	72
3.12	Calibration of the phase shifter by a linear scan	73

3.13	Transmission modulation of the phase shifter	75
3.14	Schematic setup for the phase-step insensitive calibration	76
3.15	Laboratory setup for the phase-step insensitive calibration	79
3.16	Measurements by the phase-step insensitive algorithm	80
3.17	Backscattering of the metrology light on the science detectors	85
3.18	Energy transitions of Raman scattering	87
3.19	Backscattering spectrum measured in the GRAVITY cryostat	89
3.20	Raman spectra in fluoride-glass fibers from literature	90
3.21	Laboratory setup for the analysis of the main backscattering component . .	91
3.22	Wavelength calibration for measuring the backscattering spectrum in the laboratory	93
3.23	Main results from the laboratory measurements of the backscattering . . .	94
3.24	Backscattering strength for different fiber lengths	95
3.25	Absorption and emission spectra of Thulium and Holmium	97
3.26	Backscattering spectrum from a 1550 nm laser compared to Thulium fluo- rescence	102
3.27	Backscattering spectrum measured in GRAVITY for different excitation wa- velengths	103
3.28	Tests to evaluate the metrology accuracy at a laser wavelength of 1700 nm	104
3.29	Scheme of the three-beam metrology	108
3.30	Detection by phase modulation at characteristic frequencies	110
3.31	Hardware of the three-beam metrology	112
4.1	Star-formation history	117
4.2	Main sequence of star-forming galaxies	118
4.3	CO rotational lines	120
4.4	Rayleigh-Jeans and Planck's law for the lowest rotational lines of CO . . .	121
4.5	High-resolution maps of the presented sample	128
4.6	Location of the selected sample in the $M_* - SFR$ plane	129
4.7	Imaging from the Hubble Space Telescope	132
4.8	Comparison of different redshift measurements	134
4.9	Stellar-population properties of EGS13004291	137
4.10	Position angles in EGS13004291 derived from different tracers	140
4.11	GALFIT models and residuals on the basis of the stellar-mass distributions	142
4.12	Comparison of position angles from different tracers	144
4.13	DYSMAL flux model of a rotating exponential disk with the resulting velo- city and velocity dispersion map.	146
4.14	Dynamical modeling of the CO kinematics for the sample	148
4.15	CO maps from extended array configurations together with rest-frame UV/optical stellar continuum	148
4.16	Stellar-mass and star-formation rate maps derived from SED fitting	149
4.17	Comparison of sizes from different tracers	151
4.18	Rotation curves as derived from the interferometric CO data of the sample	157

4.19	Sample dynamics in the context of galaxy evolution	165
4.20	Integrated CO line maps and imagery from the Hubble Space Telescope . .	169
4.21	Comparison of effective radii as traced in the different CO data	172
4.22	Dynamical modeling of the CO kinematics for EGS13004291	176
4.23	Comparison of the CO kinematics to potential tidal streams	177
4.24	Rotation curves as derived from the interferometric CO data of EGS13004291	178
4.25	Spectral fitting of the CO (3-2) line	183
4.26	Spectral fitting of the CO (4-3) line prior to continuum subtraction	185
4.27	Map of the continuum emission from dust detected in the CO (4-3) data .	186
4.28	Spectral fitting of the continuum-subtracted CO (4-3) line	187
4.29	Model spectrum of the dust continuum around the five lowest CO rotational transitions	188
4.30	Spectral fitting of the merged CO (3-2 + 4-3) lines	189
4.31	Mapped outflow of the CO (3-2 + 4-3) data	190
4.32	Model of the outflow orientation	191

List of Tables

2.1	Differences between a typical optical and radio interferometer	16
3.1	Role of the phase-shift calibration within the astrometric error budget . . .	62
3.2	Specifications of the phase shifter	70
3.3	Calibration results of the phase-step insensitive algorithm compared to the linear scan	81
3.4	Comparison of the fluorescence backscattered from the fluoride-glass fibers between the instrument and laboratory	98
3.5	Reduction factors for backscattering levels not restricting the GRAVITY operation	99
3.6	Backscattering level of the three-beam metrology	113
4.1	CO observations	125
4.2	Sample properties	130
4.3	GALFIT results on the stellar-mass surface density	141
4.4	Average structural parameters of the sample	150
4.5	DYSMAL results for the sample	162
4.6	Integrated flux densities with errors	169
4.7	DYSMAL results for EGS13004291	179

Zusammenfassung

Interferometrie wird in der Astronomie als eindrucksvolle Technik für hochaufgelöste und empfindliche Himmelsbeobachtungen eingesetzt. Ich stelle hier diese Anwendung von Interferometrie an Hand zweier weltführender Repräsentanten vor. Das IRAM Interferometer besteht aus Radioteleskopen, während das GRAVITY Instrument am optischen Observatorium des Very Large Telescope Interferometer in Betrieb ist.

GRAVITY beobachtet simultan zwei Himmelsobjekte bei Wellenlängen von $\sim 2 \mu\text{m}$. Die Messung des differentiellen Wegunterschieds zwischen beiden Signalen an Teleskoppaaren entschlüsselt die intrinsische Phaseninformation des Forschungsobjekts sowie seinen Winkelabstand zur Referenzquelle, mit noch nie da gewesener Genauigkeit. Hierzu müssen die Weglängenunterschiede im Instrument und Observatorium mit Hilfe einer interferometrischen Laser-Metrologie auf Nanometer genau gemessen werden. Im Rahmen der Entwicklung dieses Systems erarbeitete ich eine Methode zur Kalibrierung eines Phasenschiebers sowie die Verringerung unerwarteter Rückstreuung des Metrologie-Lasers auf die GRAVITY Detektoren.

Die hier neu eingeführte Methode misst die zu kalibrierenden Phasenverschiebungen direkt und aufeinanderfolgend, so dass Umgebungsschwankungen vernachlässigbar sind. Die Kalibration basiert auf robustem Fitting von Ellipsen durch eine χ^2 -Minimierung. Die im Labor erreichte Genauigkeit von 1 nm entspricht dem angestrebten Fehlerbudget für eine astrometrische Präzision von 10 μas .

Das Metrologie-System misst den Lichtweg ausgehend von den GRAVITY Spektrometern zurück zu den Teleskopen. In der ersten Inbetriebnahme stellte sich leider heraus, dass unerwartete Rückstreuung des Metrologie-Lichts die Instrumentdetektoren um mehrere Größenordnungen überstrahlte. Die Behebung dieses Effekts erforderte eine wesentliche Erweiterung der Zwei-Strahl Metrologie. In Labormessungen konnte ich den Ursprung des zurückgestreuten Lichts als Ramanstreuung sowie Fluoreszenz in Fluoridglas-Fasern identifizieren. Anschließend wurden mehrere Lösungsstrategien untersucht mit dem Ergebnis einer Drei-Strahl Metrologie mit homodyner Detektion. Die verbleibende Rückstreuung auf den astronomischen Detektoren entspricht dem thermischen Hintergrund beziehungsweise ist nur um wenige Faktoren höher.

Das IRAM Interferometer untersucht Millimeter-Wellenlängen und konnte dadurch die erste große statistische Erfassung von molekularem Gas in weit entfernten Galaxien erstellen. Auf dieser Basis untersuchte ich das räumlich aufgelöste molekulare Gas in einer kleinen Stichprobe von Galaxien während des Höhepunkts der kosmischen Sternentste-

hung. Ich verglich die Morphologie des molekularen Gases mit den Strukturen des stellaren Kontinuums, stellarer Masse und der Sternentstehungsrate. Außerdem extrahierte ich die Kinematik des molekularen Gases. Während ähnliche Studien bereits zahlreich in großen statistischen Stichproben für ionisiertes Gas durchgeführt wurden, ist die entsprechende Analyse von molekularem Gas neuartig.

Im Vergleich zu den ausgedehnten Scheiben des stellaren Kontinuums zeigen stellare Masse, molekulares Gas und Sternentstehung kompakte Verteilungen mit zentralen Maxima. Hohe zentrale Konzentrationen der stellaren Masse deuten auf Bulge-Wachstum hin. Das molekulare Gas und die Sternentstehungsrate haben Profile von exponentiellen Scheiben. Das molekulare Gas zeigt außerdem eine Tendenz von zentralem Schwund, wahrscheinlich bedingt durch den Bulge-Aufbau. Diese Ergebnisse stehen im Einklang mit der Annahme, dass Galaxien von innen nach außen wachsen. In diesem Szenario verlagert sich die Sternentstehung in den Galaxien nach außen, die durch Gasakkretion sowie Interaktion oder Verschmelzung mit anderen Galaxien wachsen. Eine der untersuchten Galaxien mit vorangegangener Verschmelzung zeigt einen kompakten Ausbruch von Sternentstehung mit molekularen Ausflüssen. Letztere sind in regulären Galaxien mit Sternentstehung selten sichtbar auf Grund begrenzter Signalerfassung. Die Dynamik des molekularen Gases in den untersuchten Galaxien zeigt rotationsdominierte, turbulente Scheiben, wie im Fall von ionisiertem Gas, sowie Hinweise auf zentrales Bulge-Wachstum. Die abgeleiteten dynamischen Massen bestehen hauptsächlich aus Baryonen.

Auf diese Weise kann die Anwendung von Interferometrie vorherige Beobachtungsgrenzen überwinden. Zum Zeitpunkt des Zusammenfassens beobachtet GRAVITY das Galaktische Zentrum in der Nähe des Ereignishorizonts eines supermassiven schwarzen Lochs, um zum ersten Mal in einer solchen Umgebung die Effekte der allgemeinen Relativitätstheorie zu messen. Das IRAM Interferometer wurde für eine höhere Empfindlichkeit durch zusätzliche Teleskope ergänzt, so dass in Zukunft noch detailliertere Beobachtungen von molekularem Gas in weit entfernten Galaxien möglich sein werden.

Abstract

Interferometry is a powerful tool in astronomy used for sky observations with increased spatial resolution and sensitivity. Here, I demonstrate these capabilities using two leading world-class representatives of both radio and optical interferometry, namely the IRAM interferometer and the GRAVITY instrument at the Very Large Telescope Interferometer.

GRAVITY observes two sky objects simultaneously at wavelengths of $\sim 2 \mu\text{m}$. Measuring the differential optical path difference (dOPD) between both signals for pairs of telescopes provides the intrinsic phase of the science object as well as its angular separation to the reference target, known as phase-referenced imaging and narrow-angle astrometry. For this purpose, the internal dOPDs in the instrument and observatory need to be measured with nanometer accuracy. This is realized by a laser metrology based on phase-shifting interferometry. During the development of this system, I elaborated a new calibration method for the phase shifter as well as the mitigation of unexpected backscattering of the metrology laser on the GRAVITY detectors.

The newly introduced phase-step insensitive algorithm measures the phase shifts directly and subsequently, such that environmental fluctuations can be neglected. This calibration is based on robust ellipse fitting by a χ^2 -minimization. The achieved accuracy of 1 nm in the laboratory is compliant with the error budget and the astrometric precision of 10 μas .

The laser metrology traces the light paths from the GRAVITY spectrometers back to the telescopes. The first integration of the instrument unfortunately showed that unexpected backscattering of the metrology light onto the instrument detectors exceeds the noise level by several orders of magnitude. The mitigation of this effect required a substantial extension of the dual-beam metrology. In laboratory tests I could identify the origin of the backscattered light as Raman scattering and fluorescence in fluoride-glass fibers. Several mitigation strategies were investigated. The final metrology scheme is based on three-beam interference with a homodyne detection. The remaining backscattering level on the science detectors is at the level of the thermal background or slightly above, by a factor of few.

The IRAM interferometer provided a first large statistical census of the molecular gas in distant galaxies at the peak of cosmic star formation. On this basis, I studied spatially-resolved molecular gas in a small sample of galaxies. I compared the morphology of the molecular gas with the structures of stellar continuum, stellar mass and star-formation rate. Furthermore, I extracted the kinematics of the molecular gas. While similar studies are frequently done for the ionized-gas component on large statistical samples, the corresponding analysis of molecular gas is still rather rare.

In comparison to the extended disks of the stellar continuum, stellar mass, molecular gas and star-formation rate show compact, centrally peaked distributions. High central concentrations of the stellar mass are consistent with the build-up of bulges. The molecular gas and star-formation rate have exponential-disk profiles. The molecular gas shows a trend of central depletion, probably by the bulge assembly in agreement with the paradigm of inside-out growth of galaxies. In this scenario, star formation moves outwards in the galaxies, which grow through gas accretion, galaxy-galaxy interactions and mergers. Induced by a merger, one sample galaxy shows a compact starburst with molecular outflows, which are rarely observed in normal star-forming galaxies due to detection limits. The molecular-gas dynamics of the galaxy sample show rotation-dominated, turbulent disks, as known from ionized gas, and indications on central bulge growth. The dynamical masses are dominated by baryons.

In this way, the application of interferometry pushes observation limits to the next level. At the time of writing GRAVITY probes the Galactic Center close to the event horizon of a super-massive black hole, measuring effects of general relativity for the first time in this unique environment. The IRAM interferometer has been constantly upgraded by the installation of additional apertures increasing its sensitivity, such that even deeper observations of the molecular gas in distant galaxies will become available.

Chapter 1

Introduction

The work performed in the framework of this thesis is based on the application of interferometric principles in the field of astronomy. Moreover, the two main realization techniques of interferometry in astronomy are covered, arising from the individual developments in optical and radio observations. Historically these two approaches emerged from the different facilities used to capture, detect and process the underlying wavelengths. But both optical and radio interferometry are based on the same fundamental principles. Combining several apertures helps to increase the spatial resolution and the sensitivity of astronomical observations.

I outline the common principles of interferometry as well as the different practical realizations in Chapter 2. First, I describe the gain in spatial resolution by moving from the use of a single telescope to the combination of several apertures from first principles. This description leads to the introduction of the basic interferometric observables, namely visibilities carrying amplitude and phase information in a Fourier space of the observed intensity distribution. I present the techniques used specifically in radio interferometry, going into detail on the concrete realization in the millimeter-interferometer by the Institut de Radioastronomie Millimétrique (IRAM). A particularly important development in radio interferometry is the conversion of the measured visibilities into images by Fourier transforms known as aperture synthesis. Optical interferometry is more affected by atmospheric distortions than the radio regime due to the operation at shorter wavelengths. I summarize the most common techniques to control the influence of the atmosphere. For GRAVITY the phase information in the measured interference is of special importance for so called phase-referenced imaging as well as narrow-angle astrometry. I explain these concepts and present the Very Large Telescope Interferometer (VLTI), for which GRAVITY was built.

Chapter 3 first presents GRAVITY in more detail in order to put the developments of the metrology system into context. Consisting of several subsystems including new research and development highlights, GRAVITY is a very complex beam-combiner instrument beginning a new era of interferometry, in particular at the VLTI. As this instrument was specifically designed for the observations of the Galactic Center with the super-massive black hole and the well-known stellar orbits around this central mass, I discuss this goal as well as other applications for this instrument.

In the following, I outline the dual-beam scheme of the original metrology design. The concept is based on phase-shifting interferometry with the main goal of narrow-angle astrometry of science targets with respect to a reference object. The metrology tracks internal differential Optical Path Differences (OPDs) between those targets in order to extract the real differential Optical Path Difference (dOPD) on sky, which determines their angular separation on sky. Optical path differences emerge when the incoming light of a source is captured by multiple telescopes. For measuring the interference of the observed light beams the OPDs need to be compensated for coherent combination of the beams. For the simultaneous observation of two targets the individual OPDs for the sources are different due to their angular separation on sky.

The corresponding measurement of the dOPD is performed by a dedicated metrology system. Phase measurements are performed by phase-shifting of laser beams with respect to each other. The calibration of the involved phase shifter is one main focus of the work presented here. I elaborated a calibration routine in the laboratory which is phase-step insensitive and improves a previous method by a factor of two meeting the requirements for narrow-angle astrometry. The other focus in the development of the metrology was set on the analysis of unexpected backscattering of the metrology light onto the science detectors caused by Raman scattering and fluorescence in optical fibers of the GRAVITY instrument. The work led to several mitigation strategies to suppress this backscattering by several orders of magnitude for nominal science operations. The successful realization of the developed design change resulted in a three-beam metrology and a homodyne detection scheme coupling lock-in amplifiers to the phase-shifted signals. By this implementation the backscattering could be reduced almost to the optimum level.

Chapter 4 describes the other regime of interferometry, but not in its technical realization but on astronomical data. By the use of the IRAM interferometer new and unique insights into galaxy evolution are established. The special capabilities in sensitivity and resolution of such a facility allow for detecting the cool and faint molecular gas in distant galaxies around the peak of cosmic star formation close to the redshift $z \sim 1$ probed here. As the fuel of star formation this gas component is of special importance for the analysis of galaxy evolution through cosmic time. The cosmological redshift z is linked to the distance of the object observed from Earth as described by Hubble's law. The emitted wavelength λ_e of light propagating towards the observer through the expanding space is redshifted to $\lambda_o = \lambda_e(1 + z)$.

For the first time the molecular gas of high-redshift systems can be studied in spatially-resolved observations together with complementary galaxy properties such as star formation and stellar mass from single-aperture photometry by the Hubble Space Telescope (HST). The results on a small sample including a particularly rich data set for starburst object are presented here based on the Plateau de Bure HIgh-z Blue Sequence Survey (PHIBSS), which is a first large statistical census of molecular gas at high redshifts. The interferometric quantities allow to map the galaxies spatially and to provide additional spectral information such that the molecular-gas kinematics can be analyzed for the first time in objects of this epoch. In addition, molecular outflows are detected in a starburst galaxy, which is still rare for normal star-forming galaxies due to detection limits.

In Chapter 5 I conclude on the results from the Chapters 3 and 4. The overall goal of the presented work is to demonstrate the benefits of interferometry to both instrumental and scientific aspects of astronomy in two distinct regimes of infrared and millimeter interferometry.

Chapter 2

The Principles of Interferometry

Interferometry is a powerful tool for astronomical research. The idea behind this approach is to use more than one telescope to simultaneously observe a celestial target in order to overcome the resolution limit of an individual aperture. As a consequence ground-based observations performed via interferometry can even excel space missions although the latter have the advantage not to be affected by atmospheric distortion. In this respect, optical interferometry nowadays is able to exceed the angular resolution by more than one order of magnitude compared to the Hubble Space Telescope (Monnier & Allen, 2013).

The increased resolution probably is the most prominent advantage of interferometric compared to single-dish measurements but by far not the only one. Interferometry also comes with additional pieces of information that cannot be retrieved from single-telescope observations in such a direct way. The beam combiner instrument GRAVITY at the VLTI interferometer for instance will be able to perform narrow-angle astrometry because the interferometric observables also trace the object positions or movements on sky. On the other hand observations of high-redshift galaxies with the IRAM interferometer reveal spectral information in addition to the spatial brightness distribution without the use of a dedicated spectroscopic instrument. The drawback of interferometric observations especially in the optical case is the incomplete reconstruction of source structure. By the unfilled synthetic aperture imaging relies on modeling.

Being based on the same interferometric principles, the VLTI and the IRAM interferometer reflect the two different realizations of astronomical interferometry namely in the optical and radio regime. In the following chapter I introduce their common basis as well as their individual characteristics.

2.1 Spatial Resolution in Astronomy

Astronomical observations are fundamentally limited by their spatial resolution, by the diffraction limit of the telescope and instrument as well as by the atmospheric conditions in case of ground-based studies. For the classical single-telescope observations this resolution limit is inversely proportional to the diameter of the aperture. While atmospheric

conditions can partly be corrected by means of dedicated adaptive optics systems, resolving smaller scales on sky requires increasing the aperture sizes of observing facilities. The latter approach however is very cost-intensive and technically challenging.

In the optical regime telescopes then need to be manufactured from segments instead of single mirrors. The increased size and weight of larger mirrors put strong requirements on the design and supporting structure of the telescope. Corresponding facilities are already planned for the near future, but overcoming the resolution limit of single-aperture observations has already been possible for decades now without these future developments. The technique of interferometry allows to combine currently available telescopes creating super-telescopes with improved resolution limits.

Pioneering work in this field was done in radio astronomy developing the imaging techniques of “aperture synthesis” since the 1940s. Although the first interferometric measurements were performed in the optical, the radio regime provided ideal conditions for further intense developments. One reason are the long radio wavelengths put less demanding restrictions on the technical realization of aperture synthesis than in the optical case (Monnier & Allen, 2013). But both regimes profit from the same underlying principle, in which the use of multiple apertures overcomes the classical resolution limit as described in the following.

2.1.1 Single Aperture

Every astronomical observation is influenced by the diffraction of the light coming into the observing facility, as the physical boundaries of the aperture alter the light wave. A mathematical description can be given by a monochromatic complex harmonic wave corresponding to one of the two orthogonal components of the electric field vector for large apertures compared to the wavelength λ and a distant observation plane:

$$v(\mathbf{r}, t) = V(\mathbf{r}) e^{-i2\pi\nu t} \quad (2.1)$$

including the time t , the frequency $\nu = c/\lambda$ with the speed of light c and the amplitude $V(\mathbf{r})$ as function of the position vector \mathbf{r} with the length $r = |\mathbf{r}|$. The argument of the exponential encodes the phase of the cyclic function.

Rayleigh-Sommerfeld Diffraction

The behavior of the wave needs to fulfill Maxwell’s equations, which describe the propagation of the electromagnetic field. The wave equation can be formulated as time-independent Helmholtz equation that only acts on the amplitude $V(\mathbf{r})$ of the harmonic wave.

Solving this problem for light propagation through an aperture leads to a description of the diffraction pattern as detected in a observation plane. With a geometry as shown in Figure 2.1 and for small diffraction angles described by the coordinate $\boldsymbol{\alpha}$, the amplitude in each point \mathbf{x} of the observed image plane is then given by the Rayleigh-Sommerfeld diffraction formula:

$$V(\mathbf{x}) = \frac{1}{i\lambda} \iint_{\mathbf{A}} V(\boldsymbol{\xi}) \frac{e^{ikr}}{r} d\boldsymbol{\xi} \quad , \quad (2.2)$$

with the aperture coordinate vector $\boldsymbol{\xi}$, the closed surface in the aperture plane \mathbf{A} and the wavenumber by $k = 2\pi/\lambda$.

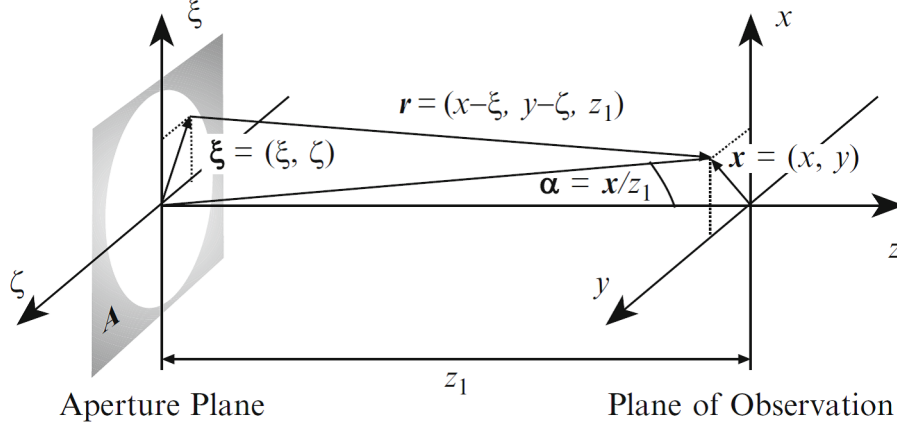


Figure 2.1: Geometry of observations with a single aperture A from Glindemann (2011). The aperture and observation planes are oriented perpendicular and centered with respect to the optical axis z at a distance z_1 .

Huygens-Fresnel Principle

Astronomical sources can be approximated by point sources due to their large distance such that their light approaching the observer arrives in the form of plane wavefronts corresponding to surfaces of equal phase. For a plane wave the amplitude is

$$V(\boldsymbol{\xi}) = V_0 e^{ikz} \quad , \quad (2.3)$$

which simplifies to $V(\boldsymbol{\xi}) = V_0$ in the aperture plane at $z = 0$.

Inserting this description of a plane wave in the diffraction formula (2.2) from above shows that when the plane wave enters the aperture its further propagation can be described by the Huygens-Fresnel principle, after which each aperture point passed by light can be seen as the origin of a spherical wave, which has the form:

$$V(r) = \frac{V_0}{r} e^{ikr} \quad . \quad (2.4)$$

In approximation, the impact of the spatial limitation as given by a telescope can therefore be understood as the superposition, also known as interference, of all spherical waves in the aperture plane. Depending on the position of measurement the light can interfere constructively producing intensity peaks or destructively such that intensity nulls are formed (Born & Wolf, 1999; Lawson, 2000; Jackson, 2008; Glindemann, 2011).

Diffraction-Limited Intensity Distribution

From the Rayleigh-Sommerfeld diffraction formula and the Huygens-Fresnel principle further approximations can be introduced such as by Fresnel for the near-field diffraction and by Fraunhofer for small diffraction angles. These steps lead to the description where the observed amplitude distribution in the focal plane is proportional to the spatial Fourier transformation of the wave amplitude in the aperture $FT(V_{ap}(\boldsymbol{\xi}))$:

$$V(\boldsymbol{\alpha}) \propto \iint V_{ap}(\boldsymbol{\xi}) e^{ik\boldsymbol{\alpha} \cdot \boldsymbol{\xi}} d\boldsymbol{\xi} \quad . \quad (2.5)$$

The aperture amplitude is given by the product of the incident amplitude and the aperture function $V_{ap}(\boldsymbol{\xi}) = V(\boldsymbol{\xi})A(\boldsymbol{\xi})$. The aperture function includes the modulus of the aperture shape as well as optical aberrations in the form of phase information. The detected diffraction-limited intensity distribution $I(\boldsymbol{\alpha})$ of a point source for a single aperture is proportional to the squared modulus of the amplitude in the observation plane:

$$I(\boldsymbol{\alpha}) = |V(\boldsymbol{\alpha})|^2 \quad (2.6)$$

$$= V_0^2 PSF(\boldsymbol{\alpha}) \quad . \quad (2.7)$$

Since the plane wave coming from a distant point-like object has a constant amplitude V_0 , the Fourier transform only applies to the aperture function and results in the dimensionless Point Spread Function (PSF) $PSF(\boldsymbol{\alpha}) \propto |FT(A(\boldsymbol{\xi}))|^2$. For a circular aperture like telescopes, the produced intensity pattern is the so called Airy disk described by a Bessel function with a central peak and decreasing side lobes.

Telescope Resolution

This response of the optical system directly relates to the resolution capability of the facility. The spatial resolution corresponds to the smallest angular separation at which two objects can still be distinguished from each other. This condition is classically defined as the diffraction pattern of one source falling onto the first null of the other. This diffraction limit is also known as ‘‘Rayleigh Criterion’’. The Rayleigh Criterion for a circular aperture with diameter D defines its resolution $\Delta\Theta$ for the wavelength λ as

$$\Delta\Theta_{telescope} = 1.22 \frac{\lambda}{D} \quad . \quad (2.8)$$

Therefore, a point-source cannot be imaged as such but is blurred by the diffraction at the aperture, which poses a fundamental resolution limit on any astronomical observation with a single telescope. This mathematical relation also shows that longer wavelengths such as radio are more limited by the fundamental diffraction barrier than optical observations in the visible or infrared - one of the main drivers for the development of radio interferometry.

2.1.2 Multiple Apertures

For interferometric observations the resolution is no longer determined by the aperture size but by the so called baseline as motivated by the famous Young's experiment from 1803 (Monnier, 2003; Labeyrie et al., 2006; Monnier & Allen, 2013). A corresponding setup consists of a monochromatic light source and a screen with two pinholes as illustrated in Figure 2.2.

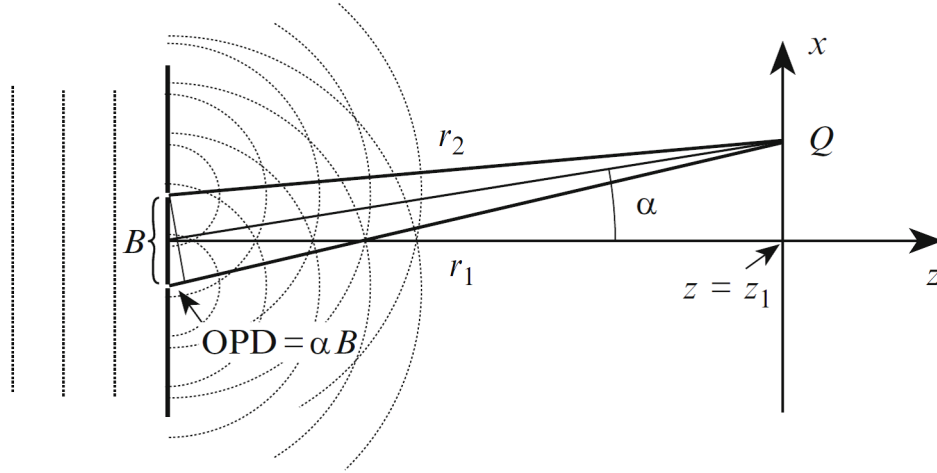


Figure 2.2: Illustration of Young's two-slit experiment from Glindemann (2011): monochromatic, plane waves perpendicular to the z -axis reach a plane with two pinholes at separation B . The light as propagated from the pinholes can be treated as two spherical waves according to the Huygens-Fresnel principle. Their interference pattern is detected on a screen behind, here denoted as x -axis. The illumination at the point $Q(x)$ relates to the OPD $OPD = r_1 - r_2 = \alpha B$, between the light waves for small angles which fulfill $\alpha = x/z_1$.

Young's Experiment

The light of the distant point source travels in the form of plane waves towards the screen. At each pinhole a spherical wave is created according to the Huygens principle. Each such wave can be described as displacement $v(r, t)$ at a distance r from its origin at the time t :

$$v(r, t) = \frac{V}{r} e^{i(kr - 2\pi\nu t)} \quad , \quad (2.9)$$

where V denotes the peak amplitude.

Those waves interfere constructively and destructively such that the intensity distribution on the detection screen behind the slits shows an interference pattern. These so called fringes which appear due to the interference show a certain spacing in which constructive

or destructive wave combination is found respectively. The mathematical description of the superposition at the point $Q(x)$ can be written as

$$v(r_1, r_2, t) = v_1(r_1, t) + v_2(r_2, t) \quad (2.10)$$

$$= \frac{V_1}{r_1} e^{i(kr_1 - 2\pi\nu t)} + \frac{V_2}{r_2} e^{i(kr_2 - 2\pi\nu t)} \quad . \quad (2.11)$$

The intensity distribution as resulting from the interference is then given by the squared modulus of the wave superposition:

$$I(r_1, r_2) = |v(r_1, r_2, t)|^2 \quad (2.12)$$

$$= \frac{V_1^2}{r_1^2} + \frac{V_2^2}{r_2^2} + \frac{V_1 V_2}{r_1 r_2} e^{-ik(r_1 - r_2)} + \frac{V_1 V_2}{r_1 r_2} e^{ik(r_1 - r_2)} \quad (2.13)$$

$$= \frac{V_1^2}{r_1^2} + \frac{V_2^2}{r_2^2} + 2 \frac{V_1 V_2}{r_1 r_2} \cos(k(r_1 - r_2)) \quad (2.14)$$

$$= I_1 + I_2 + 2\sqrt{I_1 I_2} \cos(k(r_1 - r_2)) \quad , \quad (2.15)$$

where the intensities of the individual waves are defined as $I_i := |v_i(r_i, t)|^2 = V_i^2/r_i^2$ and $i \in \{1, 2\}$ (Glindemann, 2011).

The two light waves reach the point Q with an OPD of $r_1 - r_2$, which for small angles can be approximated with $\alpha = \tan(x/z_1) \approx x/z_1$ and the pinhole distance B to

$$r_1 - r_2 = B \sin \alpha \approx \alpha B \quad . \quad (2.16)$$

Intensity Distribution for Two-Beam Interference

The interference pattern can then be expressed by the diffraction angle and pinhole distance:

$$I(\alpha) = I_1 + I_2 + 2\sqrt{I_1 I_2} \cos(k\alpha B) \quad . \quad (2.17)$$

The fringe spacing can be deduced from the position of the first maximum next to the central maximum at $\alpha = 0$. The first maximum is found at $k\alpha B = 2\pi$ such that the fringe spacing is at

$$\alpha_{max} = \frac{2\pi}{B} \frac{1}{k} = \frac{2\pi}{B} \frac{\lambda}{2\pi} = \frac{\lambda}{B} \quad . \quad (2.18)$$

Thus, the fringe spacing $\Delta\Theta$ in unit angle depends on the slit separation or baseline B and the wavelength of the light λ :

$$\Delta\Theta = \frac{\lambda}{B} \quad (2.19)$$

as demonstrated in Figure 2.3.

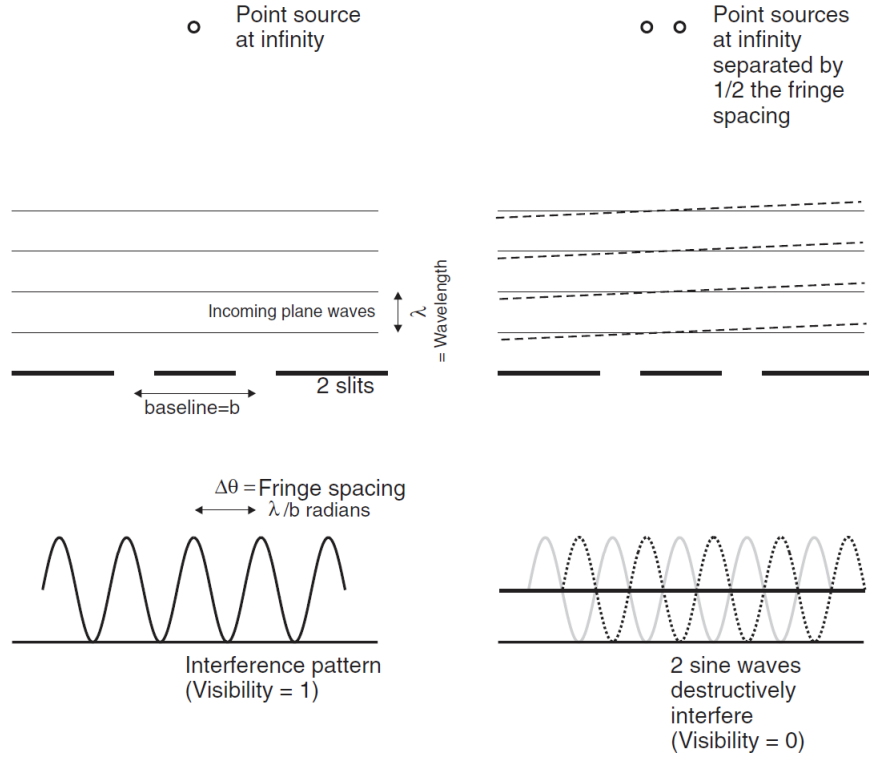


Figure 2.3: Basic interferometric setup as demonstrated in Monnier (2003) and Monnier & Allen (2013), not on scale: on the left, a distant light source acting as point source sends monochromatic, plane waves onto a screen with two slits with separation b . The light of wavelength λ travels as spherical waves from each point of the slits according to the Huygens-Fresnel principle. On a screen behind, interference fringes are detected with a spacing of $\frac{\lambda}{b}$. On the right, a double source separated exactly by half of this spacing creates fully destructive interference resulting in a uniformly illuminated screen with visibility amplitude of zero.

Interferometer Resolution

In order to retrieve the resolution capability of a double aperture, the Rayleigh criterion can be applied to the intensity distribution of equation (2.17). This requires the central intensity peak of a second light source to fall onto the first fringe minimum of the other, which is located at half the fringe spacing. According to these relations, the resolution of an interferometer as defined by the discriminability of two objects is

$$\Delta\theta_{interferometer} = \frac{\lambda}{2B} \quad , \quad (2.20)$$

where B denotes the maximum baseline between the combined apertures. The applied formalism for the fundamental resolution limits for single and multiple aperture observations assumes $D \gg \lambda$ or $B \gg \lambda$, a detection plane at large distance z and small diffraction angles α .

The interferometric diffraction limit explains how the resolution limit of a single dish can be overcome by using multiple apertures. The downside of this technique however is that it does not directly produce an image of the observed target but an interference pattern that has some link to the original brightness distribution of the source. The according interferometric quantities and relations are the topic of the next section.

2.1.3 Interferometric Observables

Interference patterns as measured by interferometric facilities can be described by a few quantities. Figure 2.3 demonstrates that for two illuminating sources the individual fringe patterns have a phase difference of π on the detection screen canceling each other out to a fringe contrast, or so called visibility amplitude, of zero when their separation is half the fringe spacing. This setup not only illustrates the definition of an interferometric resolution limit, but also that the size of extended sources can be identified by adjusting the fringe spacing through the baseline such that a visibility amplitude of zero is seen. The application of this theory was first formulated by Fizeau in 1868 and demonstrated by Michelson in 1891 who measured the angular diameters of the moons orbiting Jupiter and later of stars as well (Glindemann, 2011; Monnier & Allen, 2013; Thompson et al., 2017).

Visibility Amplitude

The visibility amplitude or fringe contrast $|\mathcal{V}|$ can also be expressed as mathematical term using the minimum and maximum fringe intensity, I_{min} and I_{max} :

$$|\mathcal{V}| = \frac{I_{max} - I_{min}}{I_{max} + I_{min}} \quad . \quad (2.21)$$

This definition of fringe contrast corresponds to the ratio of amplitude to the average intensity of the fringe. The maximum contrast amounts to 1 and is only achieved for perfectly coherent light as given by ideally monochromatic waves, which show a constant phase relation. In reality, polychromatic light is detected with a finite spectral bandwidth $\Delta\nu$.

The diffraction pattern for two-beam interference looks different in the polychromatic case than for monochromatic light. For interference fringes this means the superposition of multiple diffraction patterns of the different spectral components. While the central maximum called Wight-Light Fringe (WLF) overlaps for all of them at $\alpha = 0$ or zero OPD, the side lobes have different positions depending on the wavelength. The difference in position increases with larger diffraction angles α such that the fringe contrast decreases by the individual maxima and minima smearing out each other as demonstrated in Figure 2.4.

This effect on fringe contrast when operating with polychromatic light poses a second limit to interferometric observations next to the resolution limit, namely coherence. For incoherent interference no fringes can be detected, which is the case when the time delay τ between the beams is larger than their coherence time as given by the spectral bandwidth

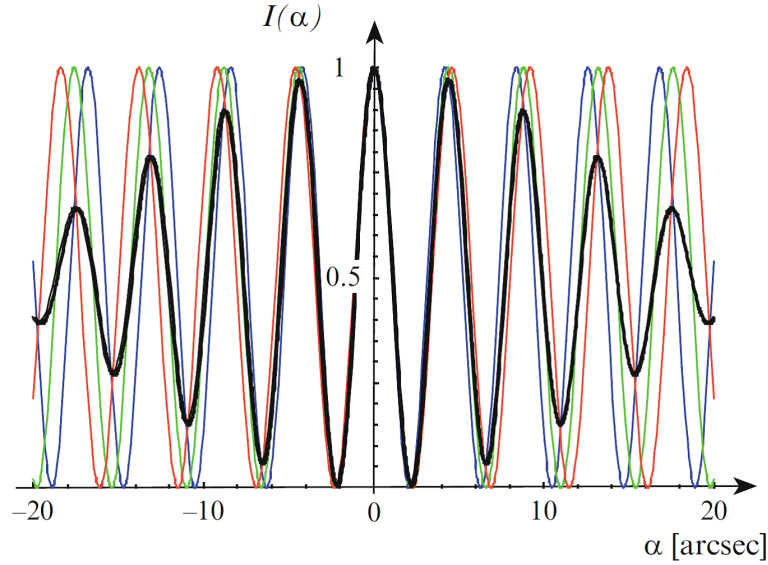


Figure 2.4: A polychromatic fringe pattern is shown for the spectral range of the full K-band and for a pinhole separation of 10 cm, from Glindemann (2011). Furthermore, three individual wavelengths are visualized namely 2.0, 2.2 and 2.4 μm in blue, green and red. With increasing diffraction angles α the fringe contrast decreases producing a so called fringe packet because the minima of the individual wavelengths wash out the maxima. Only the central white-light fringe is preserved.

$\tau_c \sim 1/\Delta\nu$. Practically, this means that the OPD in the interferometric facility needs to be smaller than the coherence length $l_c = c\tau_c$ such that the relative phase between the interfering waves remains constant (Quirrenbach, 2001; Glindemann, 2011; Monnier & Allen, 2013).

But there is more information in an interference pattern than the visibility amplitude as measure of fringe contrast.

Complex Visibility

The complete description of the fringes is given by the complex visibility following the van Cittert-Zernike Theorem. This quantity is given by the previously defined visibility modulus $|\mathcal{V}|$ and in addition the fringe phase ϕ as argument of an exponential function.

As a full measure of an interference pattern, the complex visibility $\mathcal{V}(u, v)$ can be linked to the intrinsic brightness distribution of the light emitter $I(l, m)$ by a simple Fourier transformation following the mentioned van Cittert-Zernike Theorem. The two corresponding distributions are given in the coordinates (u, v) and (l, m) in the observation and source plane respectively. The mathematical description therefore can be written as:

$$\mathcal{V}(u, v) = |\mathcal{V}| e^{i\phi} = \iint \frac{A_N(l, m) I(l, m)}{\sqrt{1 - l^2 - m^2}} e^{-i2\pi(ul+vm)} dl dm \quad . \quad (2.22)$$

$A_N(l, m)$ is the aperture function normalized by the collecting area and the denominator comes from the coordinate transform in the integral from solid angle to the sky coordinates (l, m) . This theorem is based on a large distance to the source, small angular size of the latter and a spatially incoherent emission. The latter criterion is fulfilled by astronomical objects because their radiation at each point of the source is statistically independent from the one of all other points. The monochromatic case shown here can be extended to a polychromatic form by including the wavelength dependence in the deduction.

(u,v)-Coverage The coordinates of the complex visibility (u, v) span the baseline vector in the Fourier plane, which is parallel to the sky plane. This means that per baseline one point is measured in this Fourier space and hence one corresponding “spatial” frequency of the underlying intensity distribution. The sky coordinates (l, m) describe the sky plane tangential to the celestial sphere and perpendicular to the line of sight in direction of the source.

The process of imaging therefore is a measurement series with multiple baselines, where N telescopes deliver $\binom{N}{2} = N(N-1)/2$ baselines. The number of baselines can be increased by connecting more apertures or wavelengths as well as using the baseline drift due to the rotation of the Earth with time. The better this so called (u,v)-coverage is done, a more accurate image reconstruction, also known as image synthesis, can be achieved by an inverse Fourier transform. Thus, interferometric imaging is more time consuming and complicated than for single-telescope observations, but comes with better spatial resolution.

Phase Information Another big advantage of interferometry is the phase information that cannot be retrieved by single-dish measurements. The fringe phase not only carries information about the spatial structure of the light source needed for the imaging, but it is also influenced by the source location on sky. This relation allows for the measurement of the position in the sky commonly known as astrometry.

In reality, the phase is also influenced by atmospheric distortions or internal variations in the interferometer. These effects need to be stabilized in order to make reliable phase measurements. In this respect, GRAVITY uses the technique of phase-referencing for narrow-angle astrometry. Internal stabilization is provided by a dedicated metrology system as one focus of this thesis. On the other hand internal phase or time delays respectively can be introduced in a controlled fashion in order to retrieve spectral information as demonstrated in the analysis of astronomical data for this thesis.

Different approaches of exploitation of phases or delays are also linked to the individual developments of radio and optical techniques for interferometry. Although there is no fundamental difference between the main principles of the two, their realizations typically differ from each other. For this reason the next sections illuminate the individual implementations of radio and optical interferometry with a focus on the two flagships for this thesis: the GRAVITY and IRAM interferometer concept. As a general overview, Figure 2.5 compares the basic concepts of such an optical and radio interferometer while Table 2.1 picks up the main differences between both.

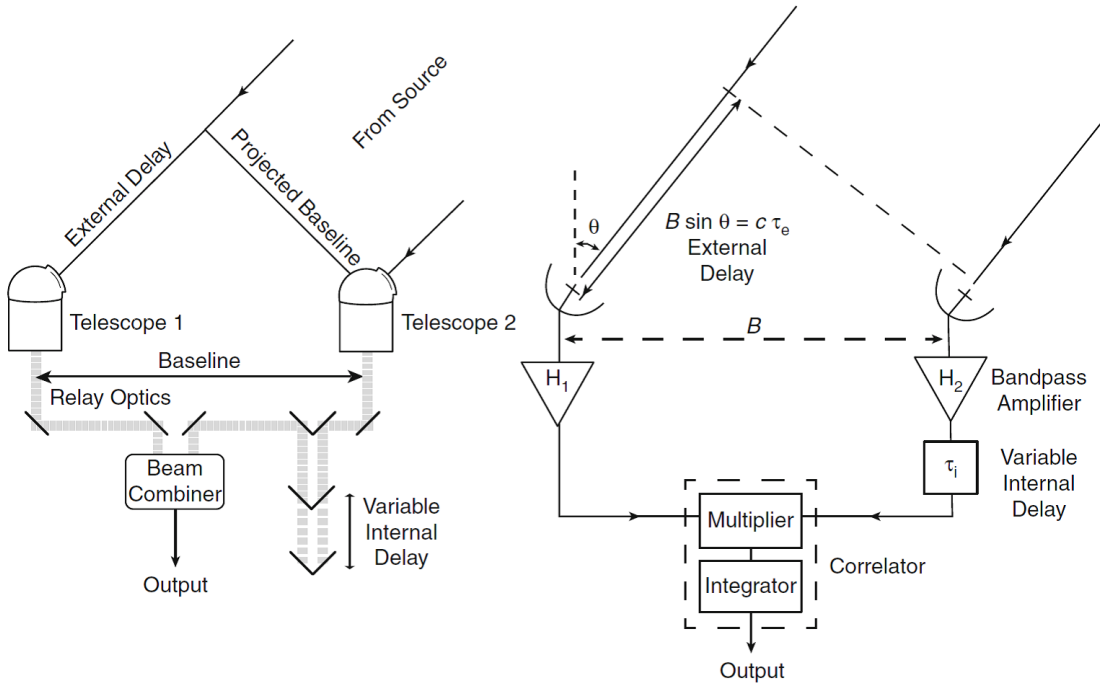


Figure 2.5: Comparison between a typical optical (left) and radio (right) interferometer illustrated for two apertures in Monnier & Allen (2013). Two telescopes at a separation of the so called baseline B receive the light from an astronomical source. The external delay τ_e between the incoming light waves due to the different location of the telescopes relates to their projected baseline times the angle θ , which denotes the angular position of the source via the speed of light c . In the optical design, the light is guided further via relay optics and a variable internal delay to compensate for the external delay, which allows for combining the light beams coherently in the beam combiner. For the radio regime the electric fields of the light captured at the apertures are amplified for a selected band and also internally delayed in one arm before they are correlated by the use of a multiplier and integrator.

2.2 Radio Interferometry

After the first interferometric measurements in the optical regime started by Michelson, radio interferometry revolutionized astronomy in the middle of the 20th century. Only then, many bright radio sources could be resolved and linked to optical counterparts using aperture synthesis (Monnier & Allen, 2013; Burke & Graham-Smith, 2014).

2.2.1 Observations

The fundamental difference between radio and optical interferometry is how the observed light is processed and detected. For the longer radio wavelengths the electrical field of the wave is gathered by an antenna and transformed to a voltage waveform. Before the

Property	Optical interferometry	Radio interferometry
Wavelength	nm to μm	sub-mm to m
Atmosphere	mostly online correction necessary	some offline correction possible
Aperture	telescope with mirror	dish with antenna
Amplification	uncommon	common
Internal delay	delay optics	cables with switchable lengths
Frequency	unchanged (homodyne)	shifted (heterodyne)
Interference	beam combination	signal correlation

Table 2.1: Differences between a typical optical and radio interferometer

relatively weak electrical signals from every telescope can be further processed, they have to be amplified and for that converted to lower frequencies.

Mixing

A mixer performs the frequency-conversion by introducing a Local Oscillator (LO) signal at similar frequency ν_{LO} to the one of the detected electric field ν_s . The input of the mixer typically accepts signals in two bands close to the oscillator frequency centered at $\nu_{LO} - \nu_0$ and $\nu_{LO} + \nu_0$, the lower and upper sideband as demonstrated in Figure 2.6. This oscillator signal is mixed with the signal by a nonlinear voltage-current response for instance using a diode. The second-order terms of the product show frequencies defined by the sum $\nu_s + \nu_{LO}$ and the difference $\nu_s - \nu_{LO}$ of the original ones.

For the down-conversion of the signal the difference becomes important and is selected by a filter. Since the received signal frequency is located in one of the sidebands for instance at $\nu_s = \nu_{LO} + \nu_0$ this filtering leads to a shift to the low frequency ν_0 by $\nu_s - \nu_{LO} = (\nu_{LO} + \nu_0) - \nu_{LO} = \nu_0$. This resulting intermediate frequency ν_0 is low enough for the amplification of the signal. This process is denoted as heterodyne frequency conversion (Guilloteau, 1997; Thompson et al., 2017).

After the mixing, the compensation of delay or phase change is realized either in a separate building block, as coaxial cables with switchable lengths for instance, or within the correlator. This step requires a continuous measurement of the cable lengths between the antennas and the correlation to a millimeter-accuracy.

Correlation

Afterwards, the signals from the antennas are finally brought together and the correlator performs a cross-correlation $r(\tau)$ for every pair of telescopes, which consists of a multiplication of two measured voltages V_1 and V_2 and an integration step over a time period of

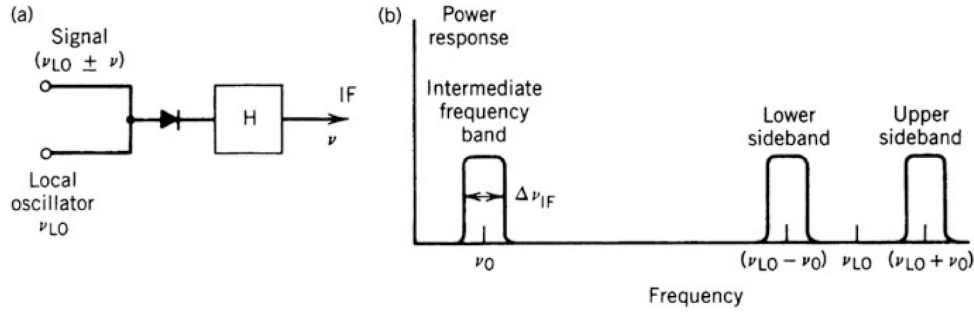


Figure 2.6: Down-conversion of the radio frequency from Thompson et al. (2017): illustrated as diagram in panel (a) (with intermediate frequency written as ν) and power response versus frequency (with intermediate frequency ν_0) in panel (b). The signal is mixed with a local oscillator signal by a nonlinear element such as a diode. Afterwards, it is filtered by the filter H, which selects the frequency term of the output corresponding to the signal minus the oscillator frequency such that the resulting power output lies within the intermediate frequency band. The mixer input accepts signals within a lower or upper sideband.

$2T$ according to this formula:

$$r(\tau) = \lim_{T \rightarrow \infty} \frac{1}{2T} \int_{-T}^T V_1(t) V_2^*(t - \tau) dt \quad . \quad (2.23)$$

The time τ is a measure of the delay between the waveforms and the superscript asterisk denotes the complex conjugate of the corresponding function. The integrator performs a time-averaging task, which suppresses the noise component appearing in signal variations at high frequencies and by that can filter out even small signals, which do not vary over time. At the same time the delay from the antenna positions, cable lengths and earth rotation is compensated. The cable lengths are continuously measured to a millimeter accuracy for this reason. The delay corrected by this interferometer term provides the position of the observed source on sky.

Controlled time lags can be added between the pairs of used telescopes to cross-correlate the signals temporally. This measurement provides spectral information in a wavelength-dependent visibility next to the included spatial information given by the points in the (u,v) -plane resolved by different baselines. Therefore, for each reconstructed point of the source plane a spectrum becomes available or put differently multiple images are taken for various frequencies. As such, observations of spectral lines become possible without a dedicated spectroscopic instrument covering entire galaxies, which is not the case for classical slit observations.

This abundance of measured quantities in radio interferometry allows for various techniques of data analysis ranging from studying the source intensity distribution in the form of mapping, also known as imaging, to spectroscopic approaches or even modeling the data right away in the (u,v) -plane. Before such steps can be undertaken calibrations of the raw visibilities are performed, which are topic of the next section.

2.2.2 Calibrations

Before one can interpret the signals regarding their astronomical meaning, instrumental and atmospheric effects need to be removed by an according calibration of the data.

Atmospheric Effects

The neutral gas in the atmosphere influences light properties mainly in three ways. Next to scattering and absorption effects, large-scale structures show variations in the refractivity. Absorption and scattering can lead to variations in the received signal amplitude. Refraction changes and scattering alter the optical path length and by this the phase of the arriving wave, which works against the coherent beam combination in spatial and temporal terms.

Water vapor in the troposphere imposes the main limits in radio interferometry as illustrated in Figure 2.7. The refractivity in this wavelength regime amounts to a level twenty times higher than for optical observations. Water vapor not only causes line absorption as demonstrated in Figure 2.8, but additionally causes phase variations. The advantage with respect to optical interferometry however is that the so called isoplanatic patch is generally larger than the beam of the reflector antennas for millimeter-wavelengths. The isoplanatic patch corresponds to the scale in the sky in which the observed light has experienced roughly the same atmospheric perturbations (Monnier & Allen, 2013; Thompson et al., 2017).

Offline Calibrations

On the telescope side, antenna relocations come with changes in the baselines, antenna pointings and delay settings. However, once the relocation is fixed they do not vary and therefore can be calibrated by point-source observations with known object coordinates.

On the other hand there are effects present during the data acquisition that vary, of which some can be predicted and others have to be determined by the observation of a reference object. In the first case, calculations can deal with the constant term of the atmospheric absorption versus the zenith angle and the variation of the antenna gain with elevation due to deformation by gravity. In the other category, measurements need to be executed in order to account for the variation of the system noise and gain as well as phase variations in the LO and induced by the atmosphere due to fluctuations of water vapor content.

Online Calibrations

While the previously described effects can be corrected by measuring the system and environment behavior, others need calibrations on sky as they fluctuate within typical observation times of minutes or hours as in Figure 2.9. An unresolved calibrator can be positioned in the phase center of the field of view, which immediately reveals the instrumental phase.

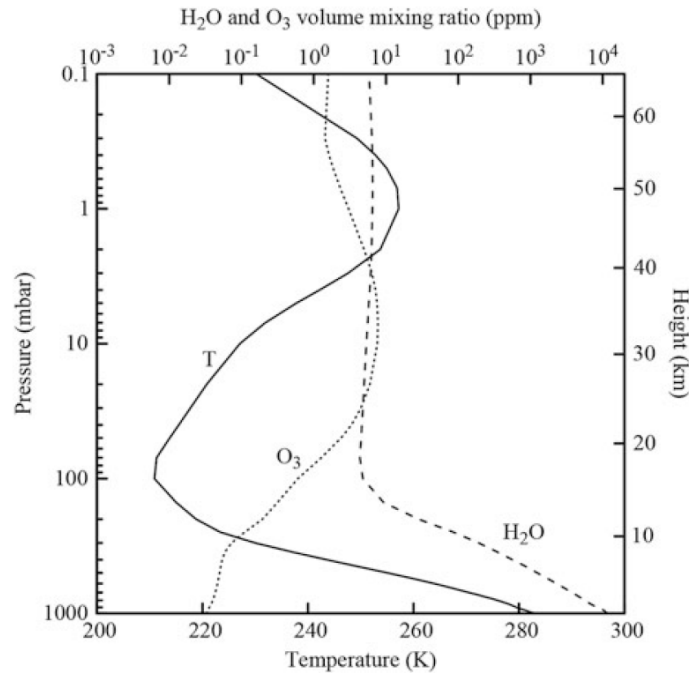


Figure 2.7: Atmospheric profiles of temperature (solid line) and the volume-mixing ratios of water vapor and ozone (dashed and dotted line) from a NASA program as printed in Thompson et al. (2017). The dominant influence on radio waves comes from water vapor in the troposphere, which covers 12 km above the ground.

Subtracting this quantity from the observed phase delivers the needed phase calibration as captured by Figure 2.10.

The amplitude can also be calibrated in this manner knowing the flux density of the reference source and measuring the response of the system to it. This calibration formally determines a gain term on the right side of the van Cittert-Zernike Theorem (Equation (2.22)) as a function of antenna. Usually, the observations are interrupted regularly for calibrator observations. At millimeter wavelengths the time interval between those typically amounts to an order of one minute. Interpolations are used to calculate the corrections during the target observations for phase and amplitude separately.

The calibrator has to fulfill the following requirements. A high Signal-to-Noise Ratio (SNR) should be achieved in short time intervals, which requires a high known and stable flux density. Furthermore, the calibrator should be unresolved such that it works for all baselines. The position of the calibrator should be close to the target such that similar gains apply, which typically is the case for distances less than a few degrees on sky. The latter criterion sometimes cannot be easily fulfilled, the previous ones however are found in quasars.

After online and offline calibrations have been applied and sometimes re-checked manually, the analysis of the data can be done in the (u,v) -plane or through imaging by the

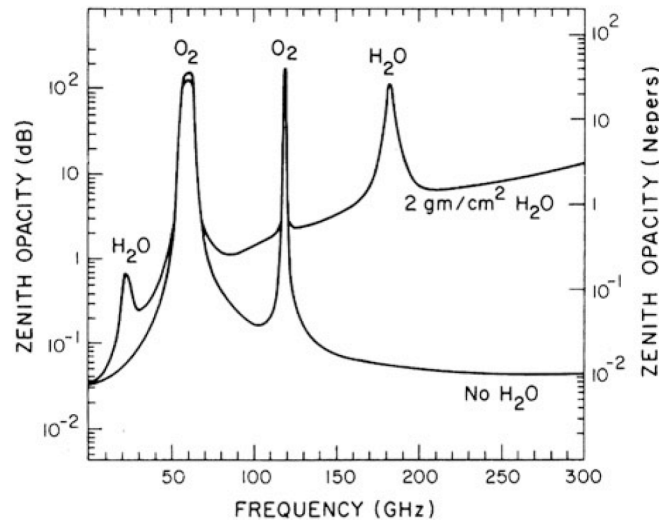


Figure 2.8: Atmospheric opacity in zenith as shown in Thompson et al. (2017), which is dominated by water vapor absorption for frequencies above 150 GHz as treated in this work.

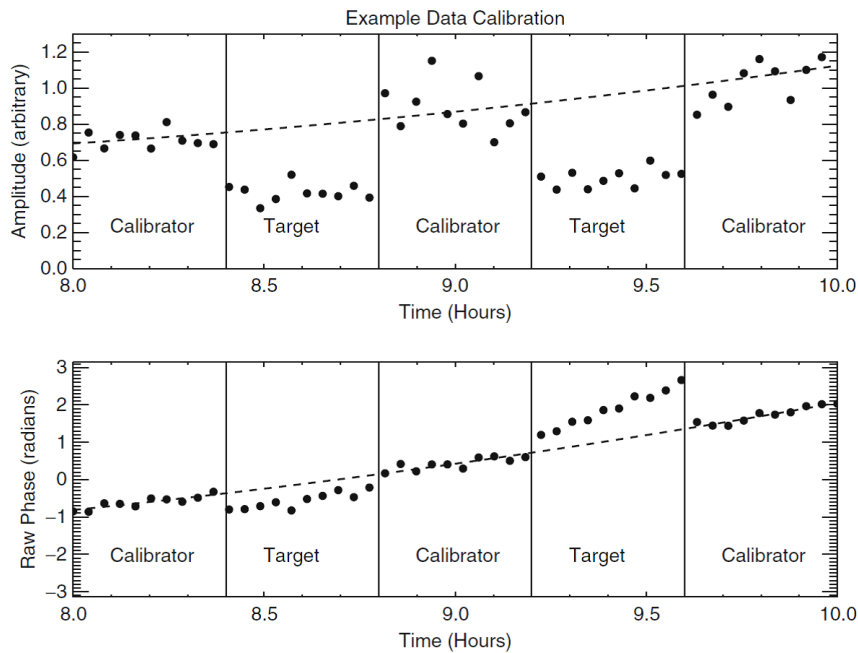


Figure 2.9: Observation sequence alternating between calibrator and target from Monnier & Allen (2013). A simple fit to the calibrator trends allows to correct the target amplitude and phase for environmental effects.

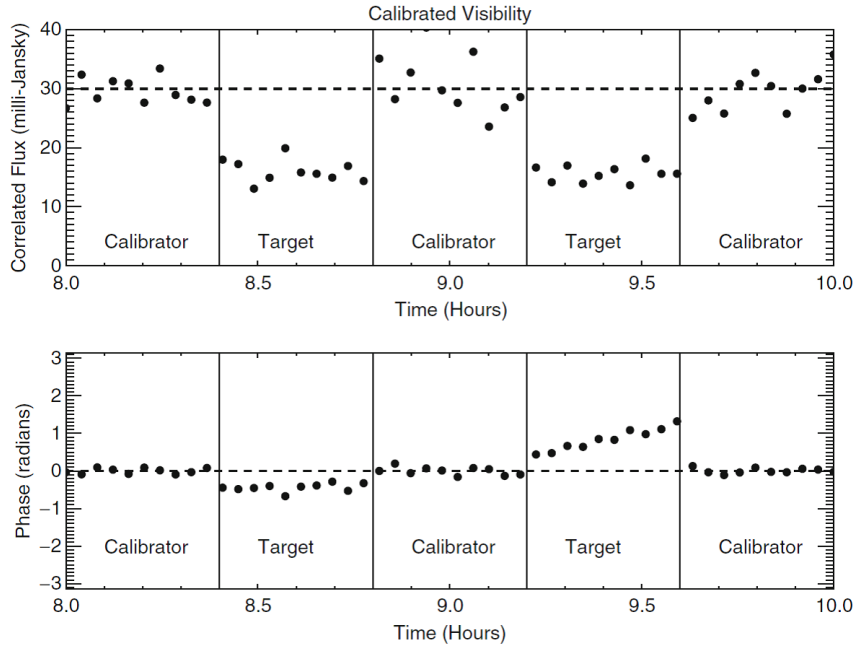


Figure 2.10: Calibrated data after subtraction of fitted trends from Monnier & Allen (2013).

deconvolution of the visibilities.

Before a dedicated section explains the imaging process, it shall be briefly mentioned that the visibility-model fitting in the (u,v) -plane works with the Fourier transform of certain model functions to describe the intrinsic source brightness distribution. At this level the fitted parameters are only limited by SNR and the model confidence. Consequently, this visibility-model fitting allows to determine source sizes smaller than the nominal beam size. Nevertheless, imaging can provide further insight into the source properties as discussed next.

2.2.3 Imaging

According to the van Cittert-Zernike Theorem in Equation (2.22), the intensity distribution $I_{source}(l, m)$, namely the clean image, can be calculated by a Fourier transform of a visibility distribution. The aperture function which considers the ideal response of the antenna array to a point-source is called primary beam $B_{primary}(l, m)$.

Together with the intrinsic intensity distribution of the target, the primary beam determines the visibility measurements $\mathcal{V}(u, v)$ of an ideal interferometer:

$$\mathcal{V}(u, v) = FT\{B_{primary}(l, m) \times I_{source}(l, m)\} \quad . \quad (2.24)$$

The reality introduces additional perturbations, however, such as noise, imperfections and incomplete sampling of the (u,v) -plane. The calibration tries to catch a variety of instrumental and atmospheric effects and to correct the raw visibilities for them. The remaining

noise terms nevertheless leave the observers with so called “dirty” quantities such that the inverse Fourier transform of the calibrated visibilities only leads to a dirty map I_{dirty}

$$I_{dirty} = B_{dirty} * \{B_{primary} \times I_{source}\} + N \quad . \quad (2.25)$$

Thermal noise is denoted N and $*$ represents a convolution. B_{dirty} corresponds to the dirty beam given by the inverse Fourier transform of the sampling function S . The sampling function consists of delta functions where the visibility space is probed by the observations, and zero elsewhere. The dirty beam comes from the incomplete (u,v)-coverage. Equation (2.25) therefore can also be written as $I_{dirty} = FT^{-1}\{S \times \mathcal{V}\}$. Although the dirty map and dirty beam are known a priori, the underlying unknown real intensity distribution cannot be derived from their ratio because of the incomplete sampling leading to zero values in the denominator.

Therefore, the main difficulty of the imaging process is to also recover points that are in between the measured ones, since an observation cannot easily fill the entire (u,v)-plane and by that the sky plane. As such, interferometric imaging is not simply build on the inverse Fourier transform from visibilities to intensities, but instead a simple brightness model is assumed to reproduce the measured visibility values. Iteratively, this model is adjusted until the difference between it and the data reaches the noise level.

CLEAN

A standard non-linear deconvolution algorithm called CLEAN was pioneered by Högbom (1974).

The main idea behind is to create the so called dirty image by a Fourier transform of the visibilities without modeling the unmeasured visibilities. An example is shown in Figure 2.11. For attributing a physical interpretation to the latter, which is neither given by setting them to zero nor by the influence of the dirty-beam sidelobes from the measured points, the following cleaning procedure is undertaken to compute the clean image.

Essentially, the dirty image is re-built by the means of multiple point-source responses, which means dirty beams effectively. This process is performed iteratively such that every step defines a response which is subtracted with the peak amplitude being a fraction of the total image amplitude known as loop gain of typically a few tenths. The iterations can be stopped when the source structure has been removed. A possible criterion to define this point can be the highest intensity peak being at the noise level of the subtracted map, which then is the final residual map. Recording the positions and amplitudes of the responses in every step in the form of delta functions delivers the clean image model.

The clean image results from convolving each of the delta functions with a clean beam for interpolating between them. This step allows for re-introducing a finite resolution and is known as a posteriori regularization. A clean beam can be modeled by a Gaussian beam with Full Width at Half Maximum (FWHM) of the dirty beam in order to create a beam free of the dirty-beam sidelobes. The final clean image is produced by adding the residuals such that the Fourier transform of it re-produces the measured visibility distribution. An example for the clean products is displayed in Figure 2.12.

The practical realization of this cleaning process usually involves the use of a Fast Fourier Transform (FFT) algorithm and gridding. The FFT reduces the number of computations compared to a simple direct Fourier transform, because it applies a so called discrete Fourier transform on the data divided into samples by defining a grid.

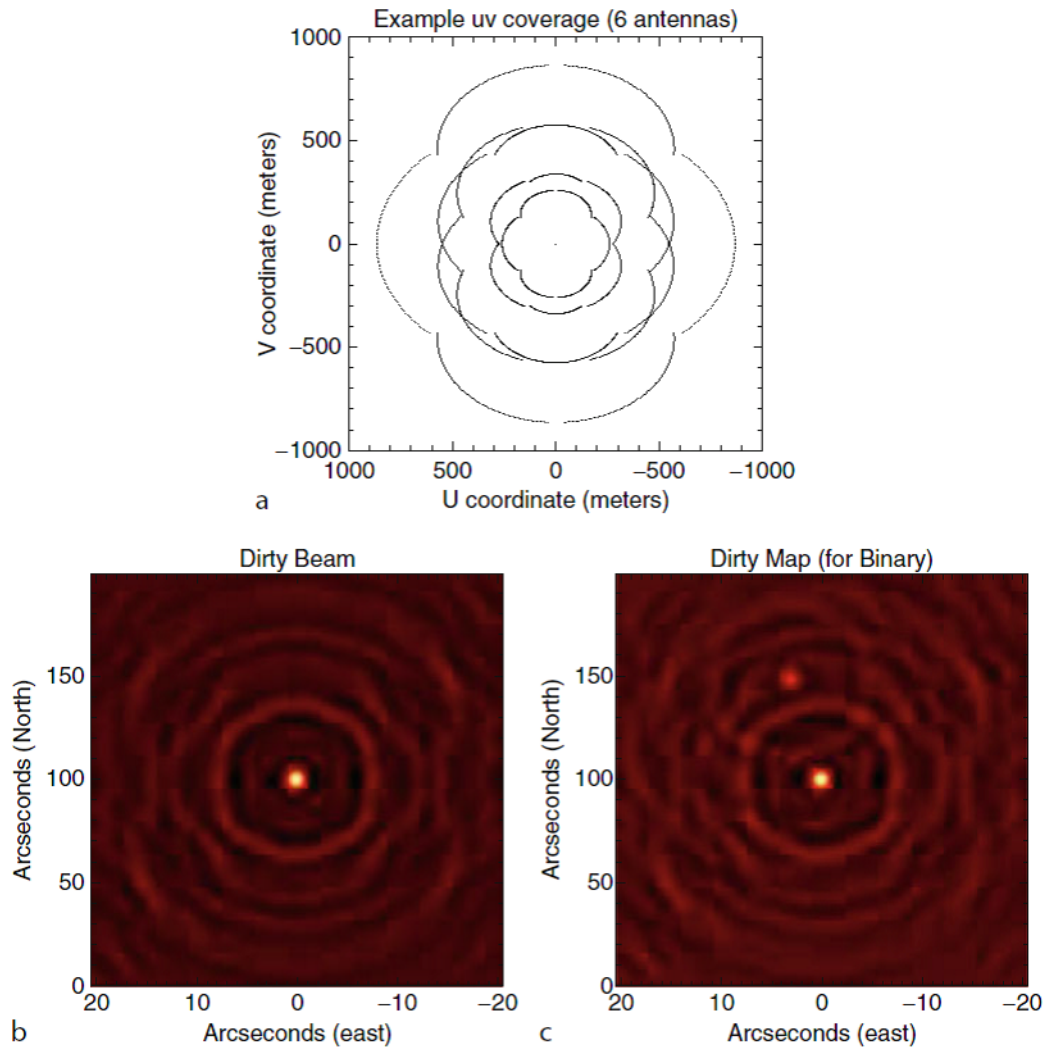


Figure 2.11: Dirty components used in the CLEAN algorithm from Monnier & Allen (2013): panel a shows the (u,v) -coverage used with six antennas. The lower panels b and c picture the resulting dirty beam and the dirty map of the observed binary from a Fourier transform of the (u,v) -sampling and the observed visibilities in (u,v) -space.

Weighting

In this process the visibilities can be weighted differently to obtain an optimum SNR or depending on specific observation goals.

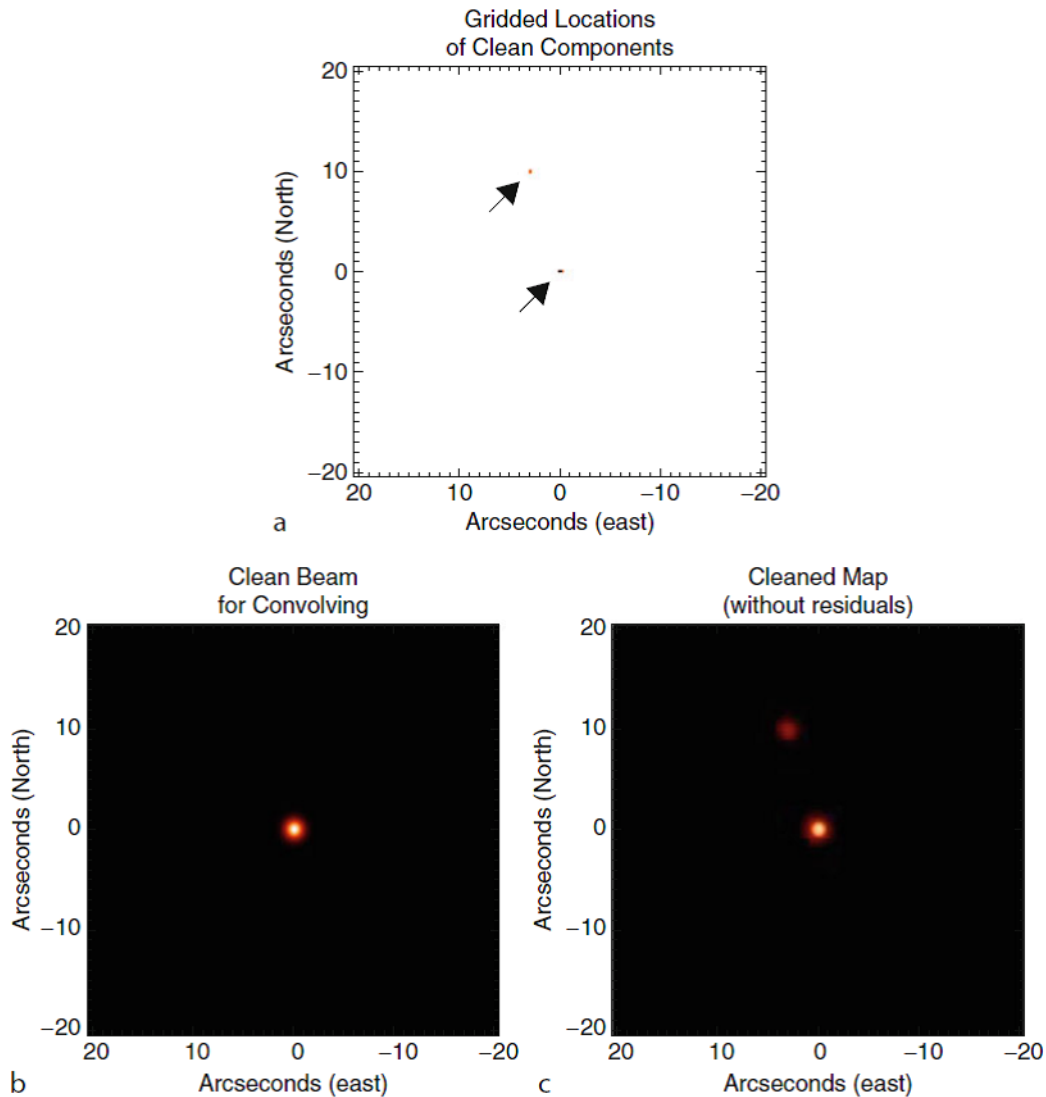


Figure 2.12: Clean components determined with the CLEAN algorithm from Monnier & Allen (2013): the point-source responses as found in the dirty map are plotted in panel a, while the panels b and c show the applied clean beam and the derived clean map prior to the addition of the residuals.

The best SNR is given when the visibilities have weights inversely proportional to their variances, which is known as natural weighting because it does not require introducing a dedicated weight function, but is given naturally. This method implies that small baselines get more weight than longer ones because they trace smaller (u,v) -plane areas per unit of time. As a consequence the focus is set on larger scales of the intensity distribution and the resulting beam shape has wide sidelobes.

For the cases where this is not wanted, one can apply uniform weighting instead, which

increases the influence of larger baselines and smaller scales as well as produces a cleaner, narrower beam shape at a cost of SNR. Uniform weights inversely relate to the area density of visibility points in the (u,v) -plane. The weights can be further adjusted according to the preferences and science questions posed. The weight function is introduced in the computation of the dirty map and beam.

Imaging Spectroscopy

The data product for scientific analysis are known as so called cubes consisting of intensities as given in a three-dimensional space (l, m, ν) , spanned by two spatial coordinates and a frequency axis.

The frequency dimension is divided into channels of a certain width $\Delta\nu_{ch}$. In addition to the analysis of the spectral information, it is possible to create a single image corresponding to the total line emission of the observed source, also known as integrated line map. As this name already suggests, the intensity I originating from line emission for instance is integrated over the frequency channels i in this manner

$$I = \Delta\nu_{ch} \sum_i I_i(l, m) \quad . \quad (2.26)$$

The reason for spectral lines being spread over a finite bandwidth is the Doppler shift $\Delta\nu = \frac{v_r}{c}\nu_0$ of the emitted light frequency ν_0 of matter moving with the velocity v_r relative to the observer. Different parts of a galaxy moving with different radial velocities v_r along the line of sight therefore produce spectral lines covering multiple frequencies. This relation also allows for mapping kinematic properties of the emitting material.

Kinematics The intensity-weighted mean velocity $\langle v_r(l, m) \rangle$ is a measure of large-scale motions in the line of sight and can be derived for every pixel with line emission by:

$$\langle v_r(l, m) \rangle = \frac{\sum_i I_i(l, m) v_{r,i}}{\sum_i I_i(l, m)} \quad . \quad (2.27)$$

Random motions are measured by the intensity-weighted velocity dispersion $\langle \sigma_r(l, m) \rangle$:

$$\langle \sigma_r(l, m) \rangle = \sqrt{\frac{\sum_i I_i(l, m) (v_{r,i} - \langle v_r(l, m) \rangle)^2}{\sum_i I_i(l, m)}} \quad . \quad (2.28)$$

As this thesis includes the kinematic analysis of galaxies which show relatively symmetric rotation, the velocity scale usually is defined to be zero at the symmetry center as seen in the kinematics. This point corresponds to the dynamical galaxy center and can be offset from the theoretical rest line frequency of the measured tracer. The offset consists of multiple effects as the cosmological shift due to the expansion of the Universe plus the systemic velocities of observer and emitter relative to a defined reference frame, for instance given by the cosmic microwave background.

Radio Units

While most interferometric concepts up to here were presented in terms of intensity, radio astronomy often deals with signal strength measured as flux density or formally spectral flux density S_ν , with a dedicated unit “Jansky” $1 \text{ Jy} = 10^{-26} \text{ W m}^{-2} \text{ Hz}^{-1}$. This unit ensures an easier handling of the very low energies traced in the radio regime, especially for signals originating from the cold parts of the cosmos as presented here. As the unit shows, the flux density S_ν describes a power P per area element ΔA and per bandwidth $\Delta\nu$:

$$P = \iint S_\nu \, d\nu \, dA \quad . \quad (2.29)$$

Depending on the point of perspective, the area element can describe the emission from, the propagation through or the reception by a surface.

In radiometry, the difference between spectral flux density and the spectral intensity I_ν is that the latter has an additional reference to the solid-angle element $\Delta\Omega$ under which the light is emitted or received accordingly as shown in Figure 2.13:

$$P = \iiint I_\nu \, d\Omega \, d\nu \, dA \quad . \quad (2.30)$$

The solid angle is measured in the dimensionless unit steradian (sr).

Flux density S and intensity I are given by integrating the respective spectral quantity over frequency. These definitions specific for radio astronomy deviate partially from photometric measures or the *Système International d’unités* (SI) convention, which would attribute the term radiance to what is called intensity here. In summary, different measures become applicable to describe radiant energy in electro-magnetism, preferably as flow, which means energy per unit time, characterized as power or flux. On this basis, additional constraints as area, frequency and solid angle can be adapted for a suitable description of the underlying experiment.

In addition, the radio regime also relates the measure of intensity I_ν to a surface-brightness temperature T via the Rayleigh-Jeans approximation of Planck’s law (Carilli & Walter, 2013; Thompson et al., 2017). The latter writes as

$$I_\nu = \frac{2h\nu^3}{c^2} \frac{1}{e^{h\nu/kT} - 1} \quad . \quad (2.31)$$

An ideal black body, which absorbs all incident radiation, emits such a Planck spectrum when in thermal equilibrium, with the Planck constant $h \approx 6.63 \times 10^{-34} \text{ Js}$ and Boltzmann constant $k \approx 1.38 \times 10^{-23} \text{ J/K}$. In the Rayleigh-Jeans approximation of low frequencies $h\nu \ll kT$ such that $e^{h\nu/kT} \approx 1 + h\nu/kT$, the spectral intensity becomes directly proportional to the temperature:

$$I_\nu \approx \frac{2kT\nu^2}{c^2} \quad . \quad (2.32)$$

As such, the physical temperature of radiating matter becomes a measure for brightness for thermal radiation, known as brightness temperature T_B . Strictly speaking this approach

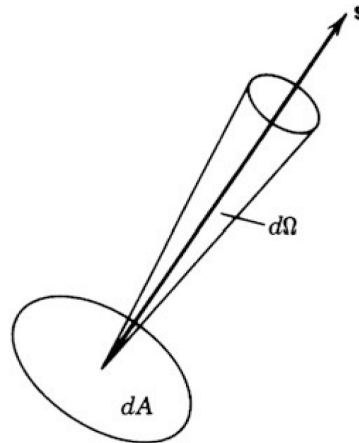


Figure 2.13: Definition of intensity from Thompson et al. (2017), which corresponds to the power emitted from the area element dA in normal direction \mathbf{s} within the solid angle $d\Omega$.

is valid at centimeter-wavelengths and less for the millimeter-regime, but the formalism is used nevertheless, while being cautious with interpreting the brightness temperature as a physical one. Related to this Rayleigh-Jeans approximation, the system noise mentioned in the section about offline calibrations is usually given as temperature. The minimum system noise is thus given in terms of the receiver temperature, the noise power of a resistive load matched to the receiver input.

After introducing the general extraction of maps and kinematics in radio interferometry, the next section briefly discusses the specific realization at the IRAM interferometer, before switching the focus to the optical regime.

2.2.4 The IRAM Interferometer

The IRAM interferometer is the most advanced array which is operated at millimeter wavelengths in the Northern hemisphere. Next to the French contribution, the German “Max-Planck-Gesellschaft” is one of the founding members of the IRAM institute with headquarters in Grenoble. Located in the French Alps above 2500 m, the interferometer originally consisted of six antennas with diameters of 15 m known as the Plateau de Bure Interferometer (PdBI). Figure 2.14 shows an image of this array.

In the meantime this system has been undergoing upgrades towards the Northern Extended Millimeter Array (NOEMA) of twelve antennas. This facility will provide 66 baselines until 2019 with a current status of nine antennas at the time of writing. This upgrading will improve the spatial resolution by a factor of four and the sensitivity will increase by factor ten thanks to a total collecting surface of 2120 m². These telescopes can be positioned along two tracks oriented in T-shape with a maximum separation of 760 m, which will be extended to 1600 m. On this basis 32 stations allow for different antenna configurations for filling the (u,v)-plane according to the scientific needs.

The highly-developed facility shows a certain complexity such that observations typi-

cally are performed by trained IRAM operators. The main building blocks of this interferometers are described next (Guilloteau et al., 1992; IRAM, 2017).



Figure 2.14: The IRAM interferometer in extended configuration located in the French Alps, from IRAM (2017).

Observations

The antennas are made of parabolic surfaces, which gather the astronomical signals and focus them at the sub-reflectors. From there, the waves are further propagated to the receivers inside the antenna cabins. Three bands are realized there according to atmospheric windows at 3 mm, 2 mm and 1.3 mm. The mixing is performed by a super-conducting junction as active element. The created intermediate frequency is then amplified and routed to the main building via low-loss cables in the underground.

There, the correlator filters out smallest signals out of background noise performing thousands of billions of operations per second. In addition, the device is also responsible for the delay compensation. For this reason the cable lengths of the interferometer are measured with a millimeter-accuracy. In total, two correlators are available covering a wide and a narrow band for nine and six antennas respectively (36 and 15 baselines). The observatory works in dual-polarization mode.

The antenna array is used in four different configurations called A, B, C and D. The D array is the most compact option delivering a spatial resolution around $1.6''$ for a source at a declination of 20° . The D configuration allows for a maximum sensitivity and the lowest phase noise such that it is best suited for the detection and coarse mapping of sources. Less compact is the C configuration that provides a good (u,v)-coverage and a spatial resolution of $0.85''$.

B and A are the most extended configurations and therefore allow for the best spatial resolutions of $0.43''$. This option is well suited for resolving small-scale structures, but at the price that fluxes coming from larger scales are washed out in the observations if they are not caught by additional more compact configurations.

Calibrations

As explained above, interferometric radio observations need calibrations. The typical IRAM observation spends a series of 45-seconds long integrations for every correlation to obtain the line spectrum with online calibrations in between, each in blocks of minutes. The interferometer electronics have variable gains in amplitude and phase versus frequency and time due to atmospheric absorption and path length fluctuations by other imperfections and unknowns. Typical distortions at the antenna level are present in the surface accuracy, focus and pointing, intrinsically or by thermal and gravitational effects.

In real-time pointing, focus, bandpass, atmospheric phase and absorption correction, antenna positions and delay are calibrated, but the latter three can be re-adjusted offline as well. A not-applied phase correction is also stored.

The bandpass is calibrated in amplitude and phase versus frequency on the basis of a strong quasar, which is observed at the beginning of the observation. As a continuum point source at these frequencies, a quasar provides zero phase and constant amplitude and therefore serves as appropriate calibration source.

One of the main error sources for the measured phases is the water vapor in the atmosphere that absorbs and re-emits parts of the flux. Since the typical flux-versus-frequency function is a power law for a quasar, any deviations can be treated as water-vapor induced errors. Typical flux variations are 5% for the 3 mm band up to 20% for the 1 mm band, which is close to the wing of a water-vapor band.

Once the data is acquired, further data calibration and reduction can be performed with the GILDAS software. The offline calibration is done with CLIC. Mainly, the varying phases and amplitudes are fitted and the fit is applied to flatten those quantities. Remaining phase discontinuities and ambiguities can be fixed by manually removing the corresponding data points. The final data product of CLIC is a (u,v) -table of calibrated visibilities. For the data analysis in the (u,v) and image plane the MAPPING software is used.

Visibility Modeling

Visibility-model fitting avoids the problem of “modeling the model”, appearing when model functions are fitted to the synthesized image. The corresponding (u,v) -fit of the software allows for different functions as displayed in Figure 2.15. In the framework of this thesis the applied models are a point source and a circular Gaussian distribution with the parameters offset from center, flux plus diameter in the case of the Gaussian function. The point-source model can be used for defining the source position while the Gaussian gives a size and first flux estimate for extended objects.

Sizes smaller than the beam can be determined in (u,v) -fitting. But talking of fluxes, high-resolution data of cold matter often reveal more complex structures than what can be described by a circular Gaussian. Either the model is extended accordingly or the further step to imaging can be taken for additional estimates.

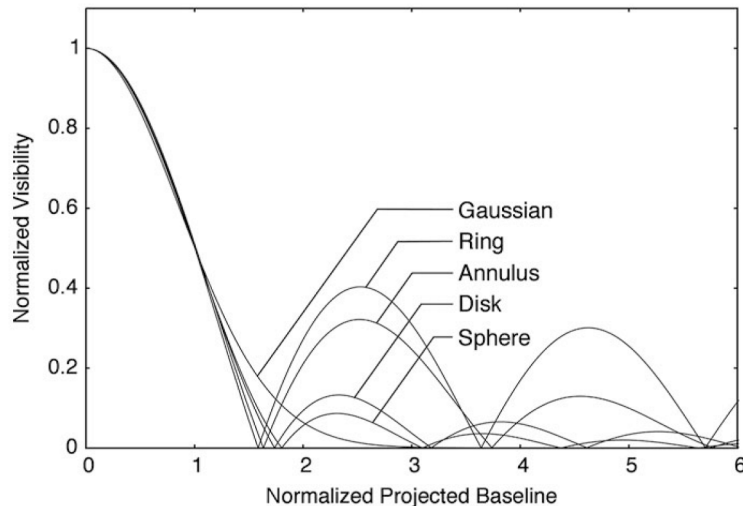


Figure 2.15: Azimuthally symmetric visibility models plotted in normalized form versus the projected baseline length, from Thompson et al. (2017).

Imaging

The deconvolution of the measured visibilities for a synthesized image is started from what is called dirty map or image and dirty beam. These quantities represent the known distributions in the deconvolution problem with the unknown intrinsic source intensity map as explained in the previous section. The computation of both is done in MAPPING by gridding the (u,v) -data using a convolving function, for instance a spheroidal one, and FFTs of the individual channels.

The user input mainly consists of the chosen weighting method as well as pixel and map size. The image size should amount to at least twice the primary-beam size to avoid artifacts. The image cleaning is performed in form of a CLEAN algorithm, which consists of identifying the individual intensity components in the dirty map and convolving them with the clean beam. The clean map produced consists of the convolution between the searched intensity distribution and the primary beam of the interferometer, as explained in 2.2.3, with additional noise components not caught by the calibrations. Some cleaning algorithms only restore the inner quarter of the map properly such as the CLARK version.

Cleaning with the CLARK Algorithm For the analysis presented in the chapter about galaxy evolution, the CLARK version of CLEAN was used with a maximum iteration limit of 100 (Clark, 1980). This cleaning method works with minor and major cycles

involving truncated beams and performs the subtraction of the point-source responses in the (u,v) -plane instead of on the dirty image. The conversion to the image plane is then realized through a FFT. The advantage of this approach lies in the reduction of calculations by order of factor 2 to 10. The default gain value is 0.2 and the iterations are stopped when the residual map reaches a noise level of 0.025 times the peak flux.

Measuring the Spectral Flux Density The cleaned cube has three dimensions with two spatial coordinates and a spectral one, in the form of flux density in units Jy/beam. This image cube can be inspected in MAPPING and further analysis in the image plane can be done. As mentioned previously, further estimates of the source flux density can be calculated here in addition to the visibility-model fitting.

On the one hand, this computation can be performed interactively in the MAPPING visualization of the cube. By applying manual and iterative restriction of the spatial and spectral areas, the integrated spectral flux density can be constrained.

The other method for its determination starts by first integrating over the relevant spectral channels and creating the integrated line map. The effective averaging of the source channels is done in the (u,v) -space. After cleaning, the source area can be defined manually by a polygon on the resulting image, for computing the contained flux density and the noise level in units mJy. Dividing by 1000 and multiplying with the total velocity width of the source channels allows for comparison to the integrated spectral flux density from above in units of Jy km/s.

2.3 Optical Interferometry

Visible and infrared light cannot be interfered as easily as the longer radio waves. Switching wavelengths from meter and millimeter to the micro- and nanometer regime involves the application of different techniques as previously shown in Table 2.1 although the basic principles remain the same.

Instead of measuring electric fields and making cross-correlations, the shorter wavelength beams are first directly combined and then detected in homodyne mode. Practically speaking, the optical combination works without any amplification or frequency shift as shown in Figure 2.5, because otherwise a large noise term would be introduced at high frequencies strongly degrading the SNR.

Instead of antennas, mirrors are used as collecting surfaces of the telescopes. Furthermore, the received beams are not transported via cabling but by free-space relay optics including the variable internal delay. However, due to the shorter wavelengths and coherence length, an increased measurement precision is required to control the geometrical delay for temporal coherent interference of the beams. Observations of extended objects also are affected by the more restrictive spatial-coherence criterion, decreasing the visibility contrast as the emission from the different parts of the source interfere destructively.

The typical realization as Michelson interferometer uses phase modulation for either spatial or temporal decoding of the fringe pattern created in the pupil plane. In contrast,

the Fizeau configuration performs the beam combination in the image plane. While the light beams usually are focused in the image plane, the pupil is defined by the image of the aperture as seen through the optical system. The comparison of both combination principles is shown in Figure 2.16.

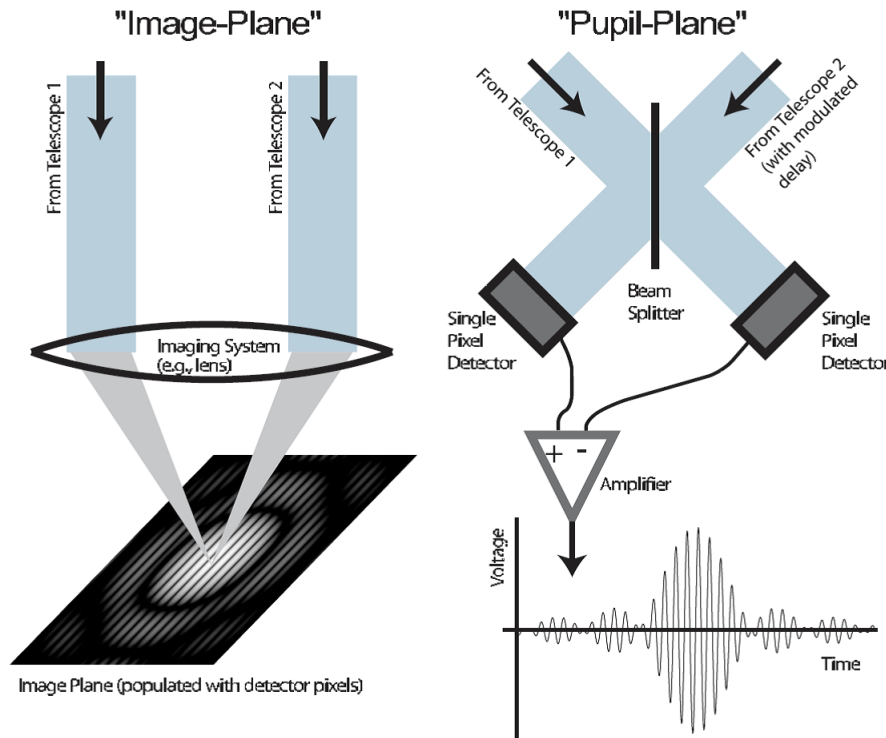


Figure 2.16: Comparison of the Fizeau and Michelson configuration of an optical interferometer from Monnier (2003): the Fizeau realization on the left performs the beam combination in the image plane. The interference in the pupil plane is known from the Michelson-Morley experiment and therefore is called Michelson configuration. In the classic setup of the latter, a beam splitter serves as the point of combination for two collimated beams. For the detection on a single pixel, the fringe pattern is scanned by temporally modulating the phase of one beam length.

In addition, the overall infrastructure has to be optimized for the optical-wavelength regime, from the construction of the telescope optics to the handling of atmospheric aberrations. In the following discussion of the corresponding details, the focus is set on Infrared (IR) light, on which GRAVITY operates, but the fundamental principles apply to the visible range as well.

2.3.1 Adaptive Optics

The random atmospheric fluctuations causing changes of the refractive index show different characteristics in the infrared than in the radio. In the IR, temperature and density fluc-

tuations of the air are the dominant factors which lead to differences in path length and as such to distortions in the wavefronts. These variations result in changes of the fringe phase reducing the visibility contrast for exposure times larger than the atmospheric coherence time. In addition, the imaging is corrupted, as the fringe phase no longer corresponds to the Fourier phase of the intrinsic sky brightness distribution. These effects limit the sensitivity and accuracy of observations by restricting the integration time and smearing the signal.

Adaptive Optics (AO) can be introduced at the telescopes to even out the light wavefronts distorted from traveling through the turbulent atmosphere. In three steps, the aberrations can be measured, analyzed and corrected by means of a Wavefront Sensor (WFS), real-time computing and a Deformable Mirror (DM) as pictured in Figure 2.17. A Very Large Telescope (VLT) equipped with such a system reaches a resolution of a few tens of milli-arcseconds instead of the typical limit of $1''$ without AO. The AO facility needs to be optimized for the characteristics of the atmospheric turbulence on the relevant temporal and spatial scales (Glindemann, 2011).

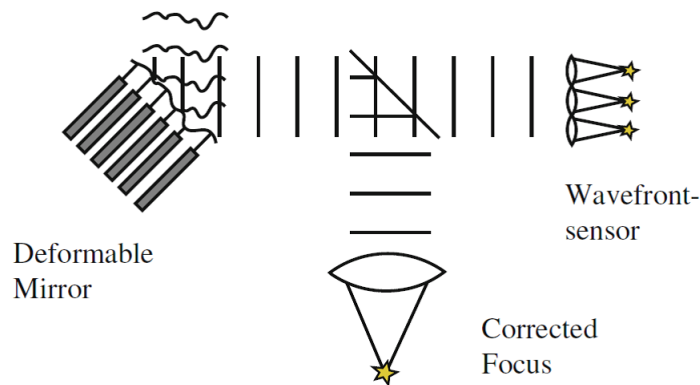


Figure 2.17: The working principle of adaptive optics from Glindemann (2011): a wavefront sensor detects the wavefront distortions, which can be flattened by a deformable mirror such that the astronomical object can be imaged with a diffraction-limited resolution.

Atmospheric Turbulence

The Fried parameter $r_0(\lambda)$ characterizes the maximum aperture which gives nearly diffraction-limited observations (Fried, 1965). Above this limit the retrieved images are limited by the turbulence called seeing and suffer from significant degradation. The seeing produces blurring and twinkling of astronomical objects in their observations. The attributed root mean square (rms) phase error for apertures corresponding to the Fried parameter is $\sigma_\phi \approx 1$ rad.

Following the Kolmogorov model as an adequate description of the atmospheric turbulence, the Fried parameter depends on the observed wavelength λ as (Kolmogorov, 1941, 1991)

$$r_0(\lambda) \propto \lambda^{\frac{6}{5}} \quad . \quad (2.33)$$

In the millimeter-regime, this parameter amounts to several hundreds of meters and the resulting phase error can be corrected by occasional calibrations. In contrast, the IR bandpass gives Fried values in the centimeter-range. Large telescopes have apertures far above these scales, which results in seeing-limited measurements. In addition to these differences on spatial scales, fast temporal variations introduce another difficulty.

On the basis of Taylor’s model of “frozen” atmosphere, a time scale of quasi-static spatial structure can be defined. Assuming that the structure moves parallel to the Earth surface with the wind speed v_s the coherence time in which the rms phase error amounts to $\sigma_\phi = 1$ rad is given by

$$t_0(\lambda) \approx r_0(\lambda)/v_s \quad . \quad (2.34)$$

For typical wind speeds of $v_s \sim 10$ m/s, micrometer-wavelengths show coherence-time scales of order milliseconds. In comparison, millimeter-observations deal with seconds in this respect. Short exposures in this regime therefore allow for nearly-sharp observations.

In summary, the knowledge of the Fried parameter as spatial limit and the coherence time as temporal one is needed to cope with atmospheric effects in optical interferometry. The better the perturbations can be corrected in real-time on these scales, the more sensitive the facility operates on faint objects requiring long integration times. Pushing this limiting magnitude to higher levels is one of the main goals (Monnier, 2003; Monnier & Allen, 2013).

Adaptive Optics System

With these concepts in hand, the atmospheric fluctuations can be measured by wavefront-sensing in the telescope pupil. A high rate of measurements ensures capturing the significant OPD variations.

Wave-Front Sensor In astronomy, there are three types of WFSs: the Shack-Hartmann (SH), curvature and pyramid realization namely. The widely used concept of the SH WFS is implemented in GRAVITY and therefore shown in more detail here. The idea behind is to divide the aperture into sub-apertures corresponding to the relevant spatial dimension of the turbulence. An array of lenslets creates images for all those sub-apertures on a photon sensor. For perfectly plane wavefronts the focused images would align in the cell centers of the detector grid. Since the light waves are distorted, displacements from the centroid positions can be observed, which are proportional to the wavefront slopes. The function of the SH is to measure the average wavefront slopes over each sub-aperture.

The observed differences from a ideal plane wavefront can be expressed by means of Zernike polynomials, a set of orthogonal functions defined on a unit disk and therefore suitable for circular pupils. The lowest-order modes of the polynomials describe distortions in piston, tip and tilt. Piston describes a general phase shift of the wavefront and as such cannot be sensed neither by a single telescope nor by the SH WFS. Tip and tilt affects both types of observations as they describe the tilt of the wavefront around one of the two orthogonal axes defining the two-dimensional pupil plane. Accounting for tip, tilt and piston

distortions is crucial for stabilizing the observed object within the Field of View (FOV) and coherent beam combination. Varying tilts of the wavefront lead to image jitter.

Real-Time Computation The offsets of the images formed by the lenslets quantify the average tips and tilts of the wavefront within the cells. An interaction matrix Θ is computed which in good approximation linearly connects the measured slopes \mathbf{M} with the corrections \mathbf{a} that need to be performed by the DM in order to improve the observations in the direction of the diffraction limit according to

$$\mathbf{M} = \Theta \mathbf{a} \quad . \quad (2.35)$$

Practically speaking, Zernike modes can be applied to the mirror to see the effect on the sensed wavefronts. This step allows for computing the reconstruction matrix, the inverse of the interaction matrix. On this basis, the real-time computing treats the measurements of the WFS to give the correcting instructions to the DM. This wavefront-sensing also works using achromatic and extended sources not exceeding the sub-apertures in their images (Roddier, 1999).

Deformable Mirror The DM typically has a variable surface shape using piezo-electric elements roughly of the amount of sub-apertures of the WFS. These piezo crystals can expand with applied voltage. With adequate corrections being implied, the distorted wavefronts are reflected in approximately plane form. Frequently, the secondary mirror of the telescopes, which captures the light collected and reflected by the primary mirror, serves as DM.

Performance

During observations the AO system is driven in closed loop between its three components of sensing the wavefronts, computing the matrix and applying the deformation. This technique requires a bright guide star, either a natural one or laser-induced.

This object needs to be located within the isoplanatic angle of $\theta_{iso} < 10''$, in which roughly the same atmospheric aberrations result as for the light of the primary target. The lower atmospheric layers cover the largest areas in the air cone between aperture and FOV and as such have a strong influence on the size of the isoplanatic patch. In addition, the ground layer introduces the dominant distortions in the wavefronts. High altitudes with stable temperature conditions therefore are the preferred observing sites for astronomical measurements.

Typically, AO cannot correct 100% of the atmospheric effects of turbulent mixing. The quality of AO performance can be expressed in terms of the Strehl Ratio (SR) as it defines the ratio of the PSF peak between observed and perfectly diffraction-limited case (Stehl, 1902). For random wavefront errors the Maréchal approximation applies, where

$$SR = e^{-\sigma_\phi^2} \quad , \quad (2.36)$$

with the variance of the phase aberration σ_ϕ^2 (Marechal, 1947). A phase error of 1 rad gives an SR of 37%. Typical AO corrections in the Near-Infrared (NIR) reach moderate levels of 40% to 60% and only rarely above 80%, which is considered as quasi diffraction-limited case (Boffin et al., 2016). As a consequence, interferometric observations still are affected by random OPD fluctuations induced by atmospheric fluctuations.

Additional Methods

Spatial filtering allows for an additional rejection for distorted wavefronts by the use of Single-Mode (SM) fibers. The SM fiber sets boundary conditions to the propagation of the light wave such that it only transmits one fundamental mode with a single phase. Since the coupling efficiency to the fiber depends on the shape of the wavefront focused to and accepted by the fiber entrance, varying wavefront distortions convert to intensity fluctuations. These photometric fluctuations are easier to calibrate in optical interferometry than the random phase distortions due to the atmosphere (Perrin et al., 2000; Coudé du Foresto et al., 1998; Quirrenbach, 2001; Monnier, 2003; Glindemann, 2011).

Another method is the closure-phase principle. This concept relies on the use of three telescopes, visualized in Figure 2.18. The closure phase is given by the sum of the fringe phases from the three baselines

$$\phi_{closure} = \phi_{12} + \phi_{23} + \phi_{31} \quad . \quad (2.37)$$

An atmospheric delay above any of the telescopes cancels out in that term as the interference results in a phase $\phi_{ij} = \phi_i - \phi_j$ for $i, j = \{1, 2, 3\}$ (Monnier, 2003; Monnier & Allen, 2013). This technique not only captures atmospheric phase shifts but general telescope-specific influences also by optics. The recovered Fourier phase allows for imaging.

While AO systems and spatial filtering works for the signals of individual telescopes, the beam combination in interferometers poses an additional challenge due to varying internal and atmospheric OPDs, which cause the fringes to jitter. Modern optical interferometers therefore include dedicated additional sub-system taking care of OPD jitter blurring the fringes, namely the fringe tracker. Fringe tracking especially is needed to record longer exposures as is briefly summarized in the following section.

2.3.2 Fringe Tracking

The technique of fringe tracking can follow random OPD motions of the science target. For very faint sources the fringe tracking can be performed on a bright reference object, analogous to the calibrator concept in the radio regime, but with the more limiting condition of a rather narrow isoplanatic patch as explained previously. Also in contrast to the radio technique, due to the small coherence time of milliseconds the reference phase is tracked in simultaneous observations instead of alternating between target and calibrator (Glindemann, 2011).

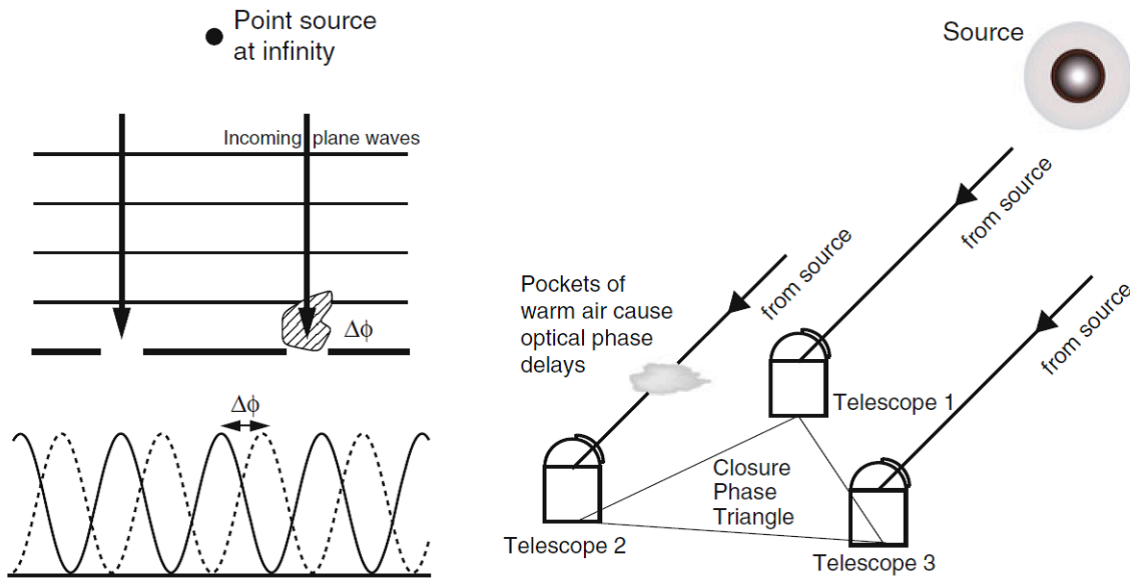


Figure 2.18: The closure-phase technique as shown in Monnier & Allen (2013). It is insensitive to phase shifts $\Delta\phi$ from atmospheric path length variations by adding up the three phases from three baselines. By that, the phase shift above one telescope cancels because of the opposite sign in the two involved baseline phases.

Fringe Stabilization

In a corresponding servo-loop, the fringe pattern of the reference object can be quickly scanned, centered on its WLF for maximum visibility and its measured phase jitter allows to stabilize the WLF of the science fringes on a fixed position. In this way, the fringe tracker measures and corrects for the geometrical OPD and for the atmospheric and internal differential piston. The tuning parameters of the fringe tracker are usually optimized to reduce the fringe jitter to a level much smaller than the fringe spacing. In this respect, the required scan rate depends on the frequencies of the dominant OPD fluctuations as can be determined in their power spectrum. The corresponding OPD adjustment of geometrical delay and low-frequency jitter is realized in the form of the main optical delay lines in the beam trains. A common opto-mechanical realization of Delay Lines (DLs) are cat's eye retro-reflectors movable on rails. High frequencies can be corrected by piezo-mirrors.

Measurements of the reference phase in the fringe tracker channel allows for a real-time adjustment of the internal path lengths in the interferometer in order to compensate for the atmospheric fluctuations of the fringes. Similarly as in radio mode, the corresponding reference star should be a bright point-source or a source of well-known extended structure and in addition located in the vicinity of the astronomical target on sky within the isoplanatic patch. Typical limits in the state of the art prior to GRAVITY were limiting K-band magnitudes of $m_K \leq 12.5$ (Kishimoto et al., 2011; Weigelt et al., 2012; Woillez et al., 2014) and distances $< 10''$.

ABCD Sampling

Dedicated control theories have been developed in order to correct for the random phase errors induced by atmospheric and internal effects. An example is the Kalman algorithm realized for GRAVITY as explained in the next chapter. A way to reach fast scanning rates is to sample the fringe intensity at only four points separated by $\pi/2$ and denoted by A, B, C and D (Wyant, 1975; Shao & Staelin, 1980). This so called ABCD approach allows for a fast fit of the fringe by the phase shifts $\alpha_i = \{0, \frac{\pi}{2}, \pi, \frac{3\pi}{2}\}$. The fringe phase ϕ can then be calculated from the individual intensities I_i with $i \in \{A, B, C, D\}$ via

$$\phi = \arctan \left(\frac{I_A - I_C}{I_B - I_D} \right) , \quad (2.38)$$

as can be calculated from the four equations based on the interference pattern between two beams of intensities I_1 and I_2 on a plane with coordinates x and y :

$$I_i(x, y, \alpha_i) = I_1 + I_2 + 2\sqrt{I_1 I_2} \sin(\Phi(x, y) + \alpha_i) . \quad (2.39)$$

Long Exposures

Only by such fringe tracking long integration times become feasible. Long exposures are particularly important since the beam combination between more than two telescopes requires the splitting of the individual telescope signals meaning a loss of sensitivity for the actual science target. The sensitivity scales with the integration time t_{int} as $\sqrt{t_{int}}$. Therefore, the duration of the exposure also defines the limiting magnitude at which astronomical targets are still observable for the interferometer. By this method the sensitivity of the interferometer can be increased by several stellar magnitudes.

With stabilized fringes, not only long integration times become feasible for interferometric observations but also visibility-phase measurements for imaging as well as for astrometry. The basic principles of such phase referencing are introduced next.

2.3.3 Phase Referencing

The phase-referencing technique relies on observing two objects simultaneously. Such a dual-feed system requires separating the beams of the light sources and forming individual fringe patterns (Monnier, 2003; Glindemann, 2011; Monnier & Allen, 2013).

Phase-Referenced Visibilities

The simultaneous, phase-referenced detection of both fringe patterns requires to correct for the dOPD resulting from the different positions in the sky as demonstrated in Figure 2.19. This quantity is given by the scalar product

$$dOPD = \Delta \mathbf{s} \cdot \mathbf{B} \quad (2.40)$$

of the angular separation vector between the objects $\Delta \mathbf{s}$ and the baseline vector \mathbf{B} . The dOPD results in a phase difference of the WLFs, which can be determined in order to derive the angular separation by the relation above. However, similar as in the case of the OPD, instrumental and atmospheric effects also influence the dOPD, such that for measurements of the real dOPD on sky they need to be measured and corrected.

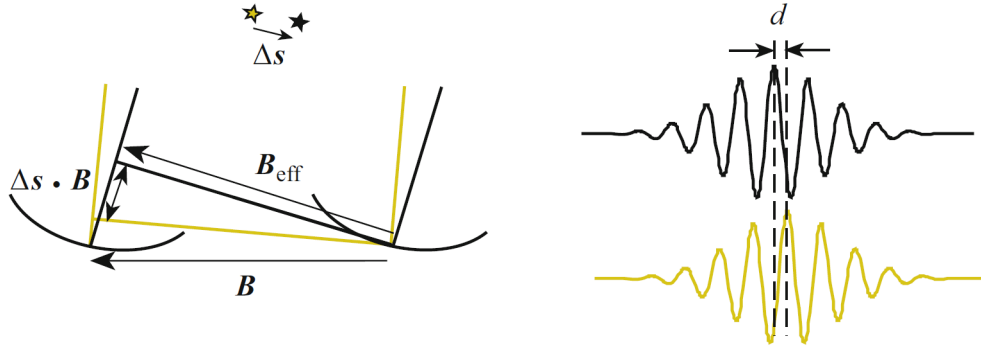


Figure 2.19: Dual-feed operation of an interferometer results in a differential delay, the dOPD, between the two observed objects, as shown in this figure from Glindemann (2011). This quantity encodes the angular separation $\Delta \mathbf{s}$ on sky with the baseline vector \mathbf{B} : $dOPD = \Delta \mathbf{s} \cdot \mathbf{B}$. The detected fringes experience a corresponding phase difference d , from which the separation can be determined. Corrections for internal and atmospheric dOPDs need to be subtracted from the measured dOPD for this purpose.

A metrology system can determine and subtract the internal effects in the interferometer, which is the central aspect of the instrumental part of this thesis. The optical adjustment of the dOPD is done via a Differential Delay Line (DDL). By this method, the visibility phase of the astronomical source can be determined, a technique known as phase-referenced imaging.

Compared to the radio regime, optical interferometry cannot provide spectroscopic measurements as in the radio regime by cross-correlating the signals with a set of different geometrical delays applied. Therefore, a dedicated dispersive element needs to be included instead. In contrast, imaging can be performed as known from classical aperture synthesis by means of algorithms such as CLEAN.

Narrow-Angle Astrometry

The dual-feed approach allows to perform astrometric measurements of the relative positions between nearby objects as outlined next. This technique is known as dual-star narrow-angle astrometry.

The astrometric precision $\Delta \Phi$ is proportional to the wavelength over the baseline and SNR:

$$\Delta \Phi \propto \frac{\lambda}{B \times SNR} \quad . \quad (2.41)$$

A fringe spacing of the order $\lambda/B = 2 \mu\text{m}/200 \text{ m}$ with an SNR of 200 results in a precision of roughly $10 \mu\text{as}$.

A famous target related to this scale is the event horizon of the SuperMassive Black Hole (SMBH) in the Galactic Center (GC). Investigating this environment not only requires a precise determination of the baseline vector (Woillez & Lacour, 2013; Lacour et al., 2014) but also controlling systematic effects within the interferometer as mentioned previously. Especially the influence of atmospheric turbulence needs to be minimized by techniques such as AO, spatial filtering and fringe tracking (Shao & Colavita, 1992). Furthermore, the desired astrometric precision requires internal dOPD measurements on a nanometer-level by the metrology system.

Recently, one of the largest optical interferometers, the VLTI, “opened its second eye”, when GRAVITY introduced the first realization of a fully-equipped dual-feed system. Before describing the GRAVITY instrument and its novel metrology system in more detail, the general VLTI infrastructure is explained.

2.3.4 The Very Large Telescope Interferometer

The VLTI run by the European Southern Observatory (ESO) consists of eight telescopes in total (Haguenauer et al., 2012; ESO, 2017). The four large Unit Telescopes (UTs) have primary mirrors with a diameter of 8.2 m. While these telescopes stand on fixed positions, the smaller Auxiliary Telescopes (ATs), with primary mirrors of 1.8 m in size, can be located on 30 different locations on the mountain platform as visualized in Figure 2.20. The AT-stations are enclosed by a circle with 200 m in diameter, which limits the maximum baseline. Most of the time, the UTs perform observations as individual telescopes, as VLT, being equipped with various near-UV to IR instruments. In contrast, the ATs are only used for interferometry.

Located in the Atacama desert in Chile, VLTI observations profit from dry and stable weather conditions. Day-night differences in the ambient temperature are suppressed by thermal control within the telescopes. The thin UT primary mirrors have a flexible shape, which needs to be controlled by actuators on the rear side. This technique is called active optics. This correction also includes the re-positioning of the secondary mirror. Following the further beam path from the active optics, the deformable mirrors of the AO system MACAO provide the high-frequency correction of atmospheric wavefront distortions. The MACAO mirrors are of bimorph design using two piezo-electric layers (Arsenault et al., 2003). The deformable mirrors are installed behind the Coudé foci of the VLTs, which are used for interferometry.

Beam Combiner Instruments

Nowadays, four telescopes of the VLTI can be combined for interferometric observations. This was first achieved in 2010 with the beam combiner named PIONIER (Le Bouquin et al., 2011), which is still operational, but comes with a rather low spectral resolution of $R = \lambda/\Delta\lambda = 40$, where $\Delta\lambda$ denotes the smallest distinguishable difference in wave-

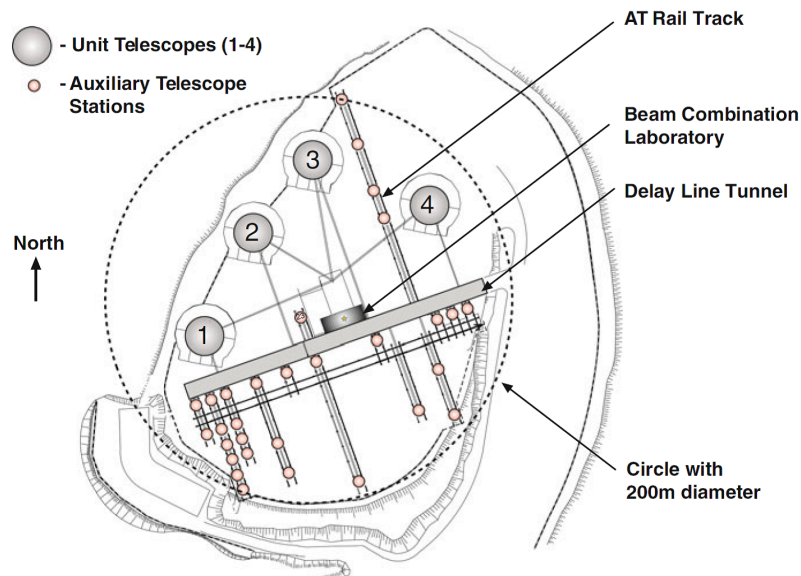
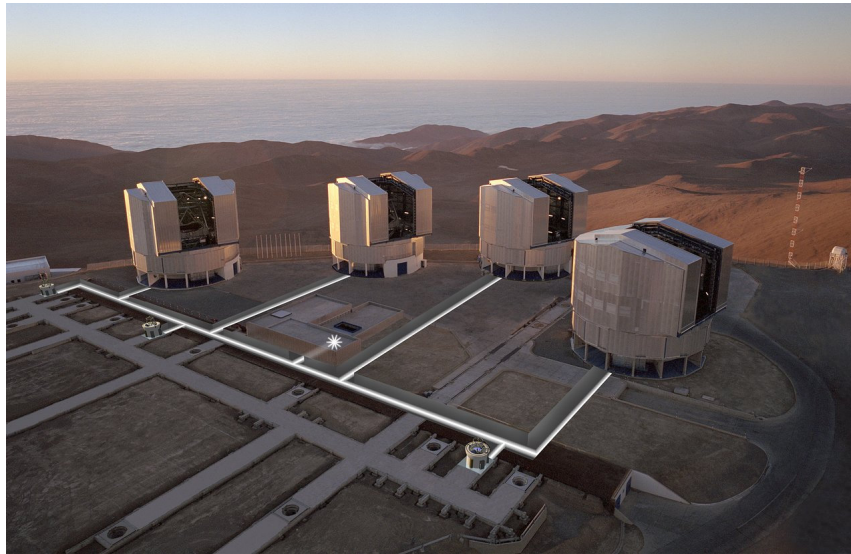


Figure 2.20: The VLTI facilities are installed on top of the Paranal mountain close to 3000 m in height. Four fixed 8.2 m Unit Telescopes and four movable 1.8 m Auxiliary Telescopes can be combined for interferometric observations with maximum baselines of 130 m and 200 m, respectively. Rail tracks allow to position the auxiliary telescopes on 30 different stations. The white lines show the light paths for beam combination, which are realized in the underground, for better thermal stability. The bottom image is taken from Glindemann (2011) and the one at the top from ESO (2017).

lengths. With a limiting H-band magnitude of 7 at the ATs this instrument pioneered the combination of beams on an Integrated Optics (IO) chip at the VLTI with implemented ABCD sampling but still by fringe scanning. Also GRAVITY picks up this technique but

with improved and more capabilities covering the K-band, from 2.0 to 2.4 μm (Gravity Collaboration et al., 2017b).

The way towards this more and more complex systems started with the first fringes at VLTI in 2001 measured by the test instrument VINCI on a single baseline (Kervella et al., 2000). Also on the basis of two telescopes, the science instrument MIDI (Leinert et al., 2003) worked in the mid-infrared N-band from 8 to 13 μm delivering a typical spatial resolution of 20 mas.

AMBER was the first instrument to combine three telescopes beginning in 2004 (Petrov et al., 2007). Its spectral resolution up to $R = 12000$ made AMBER a versatile instrument providing J, H and K-band (1.0 to 2.5 μm) spectroscopic and photometric observations with milliarcsecond-resolution. AMBER also brought the first implementation of single-mode fibers in a VLTI beam combiner. In H-band this instrument can be operated with the first fringe tracker at VLTI, FINITO (Gai et al., 2004).

MIDI was operated very successfully until 2015 when it was decommissioned for the new generation of beam combiners. These are MATISSE (Matter et al., 2016) with increased spectral resolution for the Mid-Infrared (MIR) bands L, M and N (2.8 to 13 μm) and GRAVITY for the NIR. While AMBER shows a limiting magnitude of ~ 9 in the K-band using the UTs, GRAVITY puts this limit to a higher level, as described in the next chapter.

Supporting Infrastructure

Currently, MATISSE, PIONIER and GRAVITY are operational at the VLTI. The step to GRAVITY was supported by the intermediate instrument PRIMA, which provided a Star Separator System (STS) (Delplancke et al., 2004). This subsystem extracts two separate fields out of the observed one. GRAVITY makes use of this system by picking up two fields for the wavefront-reference star and the dual-feed targets. The WFS star is sent to CIAO.

The development of GRAVITY included the construction of the WFSs CIAO to work in the H- and K-band, operating together with the MACAO mirrors. In the near future also the ATs will be supported by SH AO with the NAOMI system (Gonté et al., 2016). In addition, the use of the fringe tracker in GRAVITY for MATISSE observations is prepared in the GRAV4MAT project.

Another central structure of the VLTI are the DLs compensating for the OPDs between the different telescopes (Derie, 2000), which change during Earth's rotation. The compensation is performed by a typical cat's-eye system on rails using the reflection of the light beam within at a variable distance. A laser metrology system is used to measure the path length. The beams from the telescopes are received by the various beam combiners at underground level in the Combined Coudé Laboratory.

The power of radio and optical interferometry, with the PdBI and VLTI as two of the leading facilities, covers increased spatial resolution and additional capabilities such as imaging spectroscopy, phase-referencing and narrow-angle astrometry. For millimeter-observations this means subarcsecond-resolutions while NIR signals are resolved on a level of few milliarcseconds. The next chapters present related work in the field of galaxy evolution by imaging spectroscopy from the PdBI and the development of a metrology system

enabling the VLTI to perform phase-referenced imaging and narrow-angle astrometry.

Chapter 3

The GRAVITY Metrology System

The GRAVITY metrology is a laser system designed to control the differential OPDs with a nanometer-precision for operating the VLTI with the beam combiner instrument GRAVITY. Such measurements allow for phase-referenced imaging on the one hand and astrometric observations on the other. Therefore, the metrology system is one of the central innovations that were made with GRAVITY to realize its advanced capabilities.

The work presented in this thesis substantially contributed to designing and implementing the final metrology system. This development involved solving highly complex problems. Not only had the metrology system no precursor in this form, but it is also strongly related to all other GRAVITY subsystems as well as the overall telescope infrastructure. The work of this thesis started with implementing and testing the original dual-beam principle as planned in the first stages of the GRAVITY development. However, when the original metrology concept was first tested together with the full instrument, unexpected backscattering of the metrology light onto the science detectors was found. This main culprit of the first metrology realization then was diagnosed and mitigated by the implementation of a three-beam metrology concept.

Therefore, this section about the metrology system is split in three parts. First, the overall design of GRAVITY is presented as basis for the description of the metrology development. In the next step, the original dual-beam principle of phase-shifting interferometry is introduced, as well as the related advanced calibration scheme developed as part of this thesis. The third part describes the analysis of the backscattering of the metrology light found in the assembly of the beam combiner instrument of GRAVITY and the metrology upgrade to a three-beam scheme as the best mitigation principle among several evaluated concepts.

The calibration routine for the phase shifter and the final three-beam realization of the metrology were published in Lippa et al. (2014) and Lippa et al. (2016). The backscattering is one of the topics in the planned publication by Lippa et al. (2018) about learnings from the use of fiber optics in GRAVITY.

3.1 The VLTI Instrument GRAVITY

GRAVITY is an international project driven by several institutes under the lead of the Max Planck Institute for Extraterrestrial Physics (MPE) located in Garching, Germany. GRAVITY was delivered by the consortium to ESO in exchange for observing time with this new system. This advanced beam combiner brings a wide range of new and progressed capabilities to the VLTI and as such it is called a second generation VLTI instrument.

GRAVITY provides phase-referenced imaging and narrow-angle astrometry. For both the imaging and astrometric mode, sensitivity and accuracy are pushed towards new limits of few milliarcseconds and $\sim 10 \mu\text{as}$, respectively. Before the main science goals are summarized, the general design of GRAVITY is presented.

The instrument is built for the simultaneous usage of four VLTI telescopes, either the UTs or ATs. In this operation scheme the beams of the individual telescopes are combined interferometrically producing interference fringes of the observed object. This method overcomes the resolution limit of the single telescope as illustrated in chapter 2. Figure 3.1 shows the overall design of the GRAVITY system. The instrument consists of three main components: the beam combiner, the wavefront-sensors and the metrology system. The working principle of the latter will be discussed separately later on, since its development is one of the two main topics of this thesis.

The wavefront-sensing in the IR introduced by the CIAO system in the GRAVITY project allows for the observation of object that are highly extinguished in the visible spectrum due to dust obscuration (Scheithauer et al., 2016). The WFSs are installed in the Coudé laboratory of each UT telescope. The SH WFS of CIAO works in the H- and K-band with 68 sub-pupils, while the corrections are performed with the existing DM of the MACAO system operating 60 elements. CIAO typically delivers SRs between 10% and 60% depending on the seeing conditions. In the best cases, guide stars as faint as $m_K \approx 11$ can be used. CIAO was developed at the Max Planck Institute for Astronomy in Heidelberg, Germany.

3.1.1 The Beam Combiner Instrument

The GRAVITY beam-combiner instrument operates in the astronomical K-band centered at around $2.2 \mu\text{m}$. The beam combination of four telescope beams delivers a total of six baseline measurements. The light of two objects, science and reference target, within a large FOV of $2''$ for the UTs can be fed to the instrument for beam combination. The Beam Combiner Instrument (BCI) consists of several subsystems, most of them located within a big cryostat as shown in Figure 3.2. The cryogenic environment with temperatures between 80 and 290 K ensures a high degree of stability, cleanliness and low thermal background. The cooling is achieved by fueling the vacuum vessel with liquid nitrogen (Haug et al., 2014).

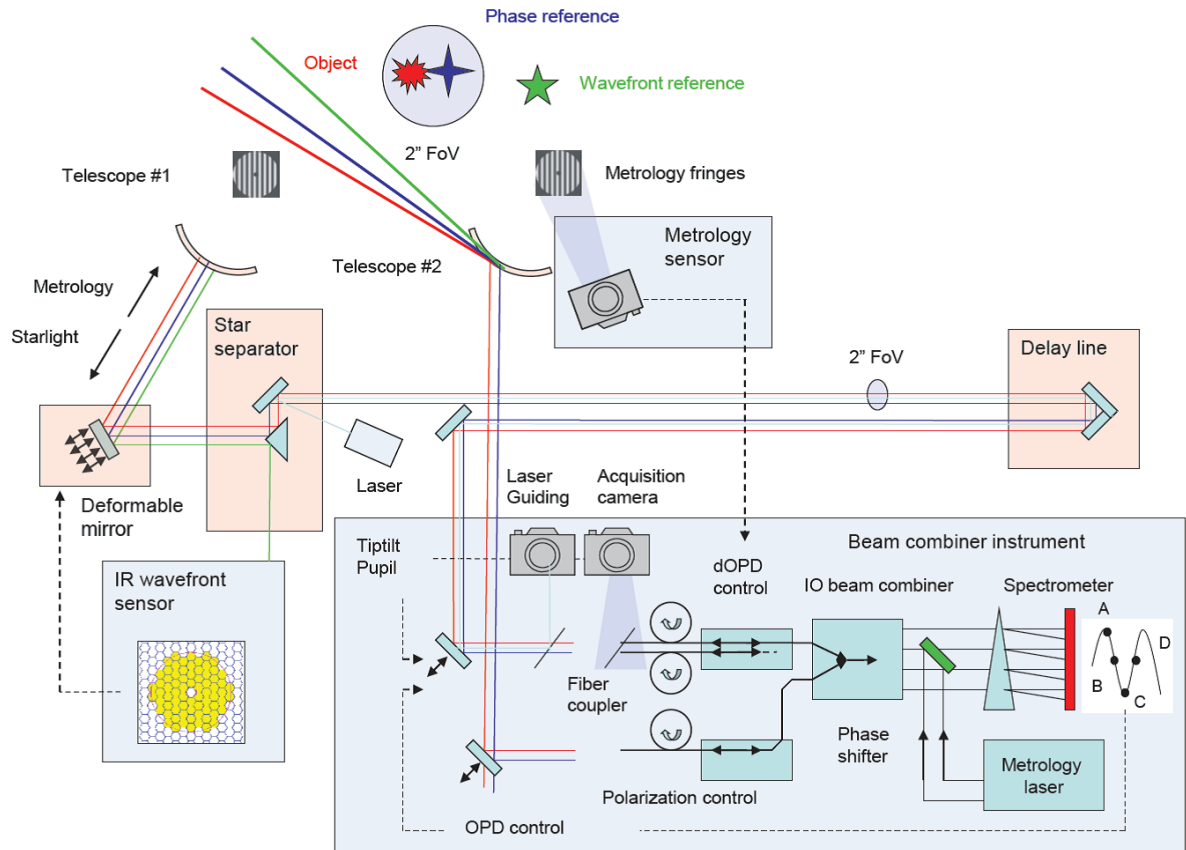


Figure 3.1: Working principle of GRAVITY at the VLTI illustrated with two out of four telescopes as in Gravity Collaboration et al. (2017b). Two objects (red and blue) can be observed simultaneously within the large FOV for phase-referencing with the GRAVITY components in the blue-shaded boxes. The atmospheric seeing is corrected by CIAO, operating on a wavefront reference in green, for the use of adaptive optics in the near-infrared. Another main component of the system is the metrology system for measuring internal differential OPDs between the observed objects and as such needs to cover most of the interferometer paths. The heart of GRAVITY lies in the beam combiner instrument, where the interference of the telescope beams takes place. The VLTI structure already existing prior to GRAVITY is shown in the boxes shaded in orange.

Fiber Couplers

Within the four Fiber Couplers (FCs), the light for the Fringe Tracker (FT) and Science (SC) channel is separated and injected to single-mode fibers (Pfuhl et al., 2014). Before, optics, partly motorized, perform various adjustments such as de-rotating the field given by the VLTI beam train. In addition, the linear polarization of the light can be rotated by a half-wave plate. Piezo-driven mirrors adjust internal tip, tilt and atmospheric piston and control the lateral pupil.

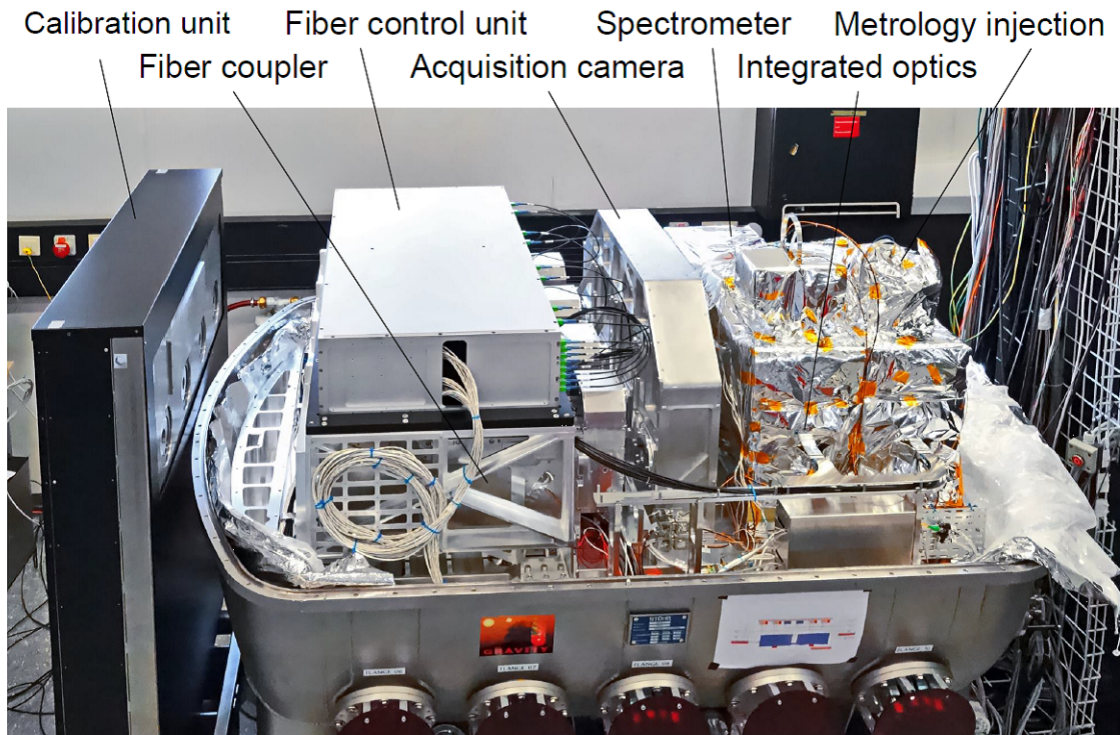


Figure 3.2: Beam combiner instrument of GRAVITY with open cryostat showing the individual subsystems, from Gravity Collaboration et al. (2017b). The scientific light enters the instrument from the left. The four fiber couplers feed the light from the telescopes in fibers, separately for the simultaneous observation of two objects. The compensation of dOPDs happens in the fiber control unit. Another controlling element is the acquisition camera, which observes the motion of the field, pupil, tip and tilt in the beam trains. The output from the fiber control unit is routed to the two integrated optics, of which each combines the four beams from one object. The IO outputs feed the spectrometers under the shiny super isolation, where the light is spectrally dispersed and detected. The laser metrology is injected on top of the spectrometers.

The object separation is achieved by means of a roof-prism with a fully reflective part. The other prism half serves as a beam splitter to feed the fringe tracker and science channel in so called on-axis operation when only one object is observed. The position of the fibers are controlled with piezo-driven three-axis stages. A dichroic beam splitter transmits the short wavelengths of $< 1.85 \mu\text{m}$ to the Acquisition and Guiding Camera.

Acquisition and Guiding Camera

This device, developed at Centro Multidisciplinar de Astrofísica Lisbon and Porto in Portugal, serves the beam analysis and images the field of view on sky (Amorim et al., 2012). Multiple images need to be measured by the corresponding detector, namely for the mo-

monitoring of the field, the pupil, wavefront aberrations and pupil motions, each for all four telescopes.

Aberration Sensor While the AO system is responsible for measuring atmospheric disturbance in the light waves, the internal SH WFS measures aberrations within the VLTI at low frequencies.

Pupil Imager Low-frequency image drifts can be compensated on the basis of the imaged pupils of the full telescopes.

Field Imager Higher frequencies produced by air turbulence in the VLTI beams are covered by the use of the laser beacons for tip and tilt and the field imager. Dedicated laser-guiding beams launched at the telescope spider arms, holding the secondary mirror, for pupil tracking. The light is measured by the camera to trace tip, tilt and pupil motion within the VLTI train (Pfuhl et al., 2014). The adapted corrections minimize the astrometric error and maximize the coupling efficiency leading to high measurement precision and throughput.

Pupil Tracker The pupil tracker consists of a lenslet array receiving the pupil guiding lasers from primary space. In this manner, lateral and longitudinal, corresponding to the focus, pupil motion can be tracked, which is essential for narrow-angle astrometry. The lateral correction happens in the FC and longitudinally by the variable curvature mirrors in the main DLs of the VLTI.

Behind the FC dichroic not only the beams for acquisition and guiding are captured, but also the metrology laser light is picked up by multi-mode fibers glued to a lens as feedback signal for the dOPD control. The scientific K-band light picked-up by the fiber couplers is transported in fibers first passing the fiber control unit.

Fiber Control Unit

The Fiber Control Unit (FCU) consists of two functionalities, the Fiber Polarization Rotators (FPRs) and the Fiber Differential Delay Lines (FDDLs), which allow to rotate the polarization axis of the light for maximum fringe contrast and to compensate for all dOPDs. The mechanisms used for these modifications are based on twisting and stretching the fibers. The fibers are made from fluoride glass and used to route the beams from the FCs to the actual Beam Combiners (BCs) (Gravity Collaboration et al., 2017b). As SM fibers, they provide spatial filtering of wavefront distortions induced by the atmosphere as described in 2.3.1.

These fluoride fibers in GRAVITY have matched lengths to introduce a maximum OPD of 0.9 mm. The FDDLs consist of > 16 m of wrapped fiber around two half spools stretched by a piezo-mechanism for maximum delays of 6 mm. The absolute accuracy using the feedback from strain gauges is few 10 μm . The relative precision is that of the metrology

feedback of few nanometers. The FPRs have a length of 1 m and are twisted by a stepper motor. The FCU system was developed by the company Le Verre Fluoré (LVF) and the French partners in the GRAVITY consortium LESIA and IPAG in Meudon and Grenoble, respectively.

From the FCU the light is guided to the actual beam combiners.

Integrated Optics

The beam combination in GRAVITY is realized by two IO chips as demonstrated in Figure 3.3 (Jocou et al., 2014; Perraut et al., 2018). As optical equivalent to electronic integrated circuits, IO allows to combine multiple functions in a single component. The chip is based on a silicon wafer with waveguides implemented by doped silica. Frequently used in telecommunication for shorter wavelengths, this technology was ported to the K-band for GRAVITY in a dedicated development project led by IPAG.

For the beam combination on six baselines, the incoming light needs to be split in beams of same intensity. Achromatic beam splitters in the IO perform this splitting. X-couplers then combine the beams. Each beam combination is performed four times with different phase shifts for instantaneous fringe sampling. This ABCD coding uses relative phase shifts of roughly 0° , 90° , 180° and 270° . These functions lead to 24 outputs (six baselines times four phase shifts for each of them). The complex visibilities of the observed fringes are derived using the so called P2VM formalism (Chelli et al., 2009). The P2VM describes the relation between the four inputs and 24 outputs of the IOs in terms of photometry, coherence and phase.

Before the detection of the fringes, GRAVITY includes spectrometric and polarimetric analysis of the light. All three steps are implemented in the spectrometer units.

Spectrometers

While the integrated-optics chips are of identical design for the science and the fringe tracker channel, the spectrometers are optimized for their specific purpose. These subsystems were built at the University of Cologne, Germany (Straubmeier et al., 2014).

In the FT spectrometer each output is spectrally dispersed with low resolution onto only six pixels, while the science spectrometer allows for three different spectral resolutions of $R = 22$ (ten pixels), 500 and 4500. A high readout frame rate in the kilohertz-range allows fast phase-referencing with the FT. Furthermore, each channel can be split into two polarization states by Wollaston prisms.

Detectors Another highlight triggered by the GRAVITY project is the use of new detector technology. The FT is equipped with a Selex SAPHIRA electronic avalanche photodiode array (Finger et al., 2016). This technique of the avalanche amplification of photoelectrons in a detector pixel allows to overcome the noise barrier of the previously used NIR sensors for high frame rates. In this manner, for the first time an effective read noise below one electron rms can be achieved in the K-band. Also the CIAO WFSs use these SAPHIRA

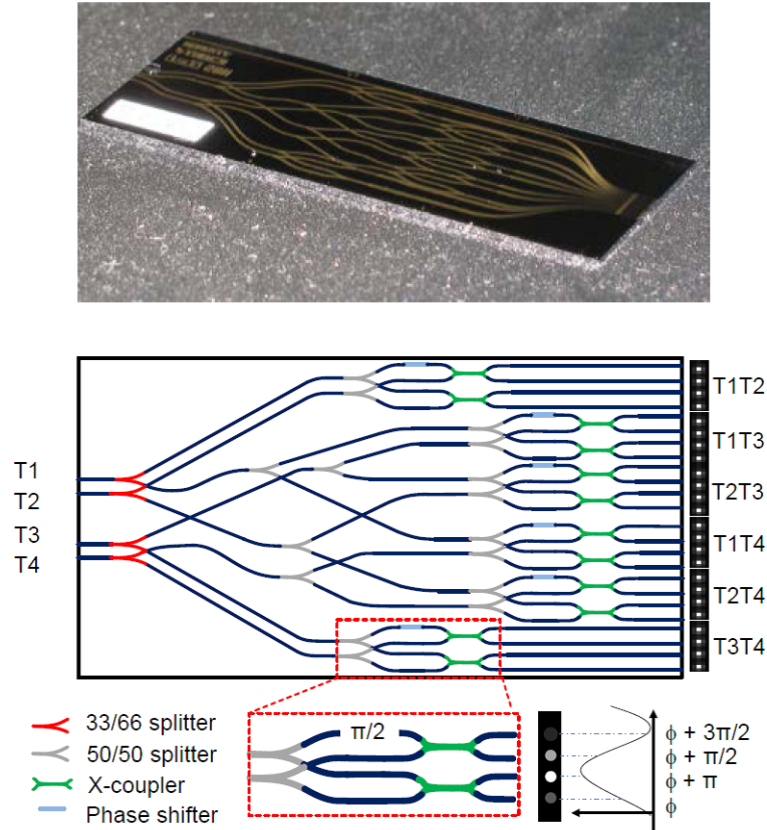


Figure 3.3: Integrated-optics chip made of a silicon wafer with waveguides from doped silica, as shown in Gravity Collaboration et al. (2017b). The photograph shows the component as built-in in GRAVITY. The scheme in the lower panel explains the individual functions connected by the waveguides in dark blue. Splitters split the light beams from the four telescopes T1, T2, T3 and T4 such that six baselines can be combined simultaneously in the green couplers. In addition, instantaneous fringe sampling is realized by performing each of the six combinations four times with induced phase shifts in blue as multiples of $\pi/2$, which results in 24 outputs in total.

detectors. The science detector and the acquisition camera come with a Teledyne HAWAII2RG detector. This receiver is optimized for a low dark current and has a read noise of down to three electrons for long exposures (Finger et al., 2008).

The interferometer beam train ends with the detection of the fringes. But in order to control, calibrate and analyze the fringes other subsystems are needed such as fringe-tracking control, a calibration unit, a software system and a data-reduction pipeline.

Other Subsystems

Fringe Tracking The data received by the FT detector allows to compute the delays to correct the OPDs introduced by the atmosphere and vibrations. The correction is done

with the mirrors in the fiber couplers for high frequencies and with the main DL for low ones.

The OPD control in GRAVITY is done with a so called Kalman algorithm, which predicts the near-future OPDs by a model of their previous evolution. Furthermore, the Kalman implicitly corrects vibrations. The algorithm is optimized to provide the required corrections and mitigates flux dropouts which can occur due to fluctuations in the fiber injection (Menu et al., 2012; Choquet et al., 2014).

The FT performance depends on the atmospheric coherence time τ_c and the K-band magnitude of the reference star. Under good observing conditions with $\tau_c > 4$ ms the limiting magnitude amounts to $m_K = 8$ for the ATs and > 10 for the UTs in the on-axis mode and fainter by 0.5 for the off-axis case. The OPD residuals within a few minutes are around 200 to 300 nm in rms. Typically, the UT operation produces larger values than for the ATs, due to uncorrected vibrations of the telescopes and further optics.

Calibration Unit To use GRAVITY without telescopes, a subsystem is installed at the cryostat entrance, namely the Calibration Unit (CU) (Blind et al., 2014a). This part of the instrument serves as simulator of two stars as observed by four telescopes, which allows for testing and calibrating the BCI without VLTI operation.

Computing The software for operating GRAVITY includes instrument control, detector control and real-time algorithms with a total of six Linux workstations, seven VxWorks computers and two programmable logic controllers (Ott et al., 2014; Burtscher et al., 2014).

A data-reduction pipeline helps the observer to calibrate and reduce GRAVITY data (Lapeyrere et al., 2014). This software provides calibrated complex visibilities, reconstructed images and astrometric data. The calibration routine works with each Pixel-to-Visibility Matrix (P2VM) (Tatulli et al., 2007) of both BCs, the map of the spectral profiles of the science fringes, the wavelength calibration of the FT and SC channel as well as dark frames and bad-pixel maps for the detectors, all of which determined from CU measurements.

GRAVITY Operation

The development of the GRAVITY instrument started at the end of 2007, following a proposal in 2005. The beam combiner instrument was shipped to Paranal in mid 2015 and the WFSs followed 2016.

The commissioning phase of the BCI began with the first light at the ATs in November 2015, and UT operation followed in May 2016. In September 2016 the four UTs were used for the first time together with all four CIAO WFSs. One month later science operation of GRAVITY started at the ATs. For the UT science, operations started in April 2017. A summary of the present and future scientific achievements follows in the next section, illustrating the current performance of GRAVITY and further goals.

3.1.2 Science Cases

The spatial resolution of a few milliarcseconds and astrometric precision in order of ten microarcseconds opens up a wide range of new science cases for GRAVITY. Furthermore, the instrument is able to perform minute-long integrations on faint objects. The primary goals for GRAVITY lie in the vicinity of the super-massive black hole (SMBH) in our Galactic Center (GC).

The Galactic Center

The physics around the SMBH in the GC are of extraordinary interest (Genzel et al., 2010). The black hole is associated with the radio source Sgr A*, which traces an emission from hot, ionized plasma in the inner accretion zone. Stellar orbits of the so-called S stars, partially a full orbit or more, reveal a mass of $4 \times 10^6 M_\odot$, with $M_\odot \approx 1.99 \times 10^{30}$ kg. The mass is located in such a small region that no other object than a Black Hole (BH) could explain these observations.

One fascinating aspect is the extremely strong gravitational potential of such a SMBH. GRAVITY basically was designed with the primary goal of observing scales similar to the Schwarzschild radius of the SMBH. For non-rotating black holes, the Schwarzschild radius R_S is fully set by the mass M :

$$R_S = \frac{2MG}{c^2} \tag{3.1}$$

$$= \frac{2 \times (4 \times 10^6 M_\odot) \times (7 \times 10^{-11} \text{ m}^3 \text{ kg}^{-1} \text{ s}^{-2})}{(3 \times 10^8 \text{ m/s})^2} \tag{3.2}$$

$$\approx 10^{10} \text{ m} \tag{3.3}$$

with G the gravitational constant. At the distance of roughly 8 kpc, this radius has an angular size of 10 μas , which sets the goal for the astrometric precision of GRAVITY. This corresponds to the scale a coin would have at the distance of our moon.

Testing Flare Models GRAVITY will allow for distinguishing between different models that would explain the observed flaring of the otherwise dark mass concentration (Baganoff et al., 2001; Genzel et al., 2003; Eckart et al., 2004; Eisenhauer et al., 2005). These flares typically occur a few times per day for a few hours in X-rays and the IR, due to heated electrons in the inner accretion zone and outflow region of the SMBH (Dodds-Eden et al., 2009). The infrared-millimeter department of the MPE, in which this thesis work has been done, is one of the leading expert groups in this field.

Mainly, three models for the flare activity of the BH are considered, which are visualized in Figure 3.4. Either jet outflows, individual hot spots close to the last stable orbit or statistical fluctuations in the accretion disk around the SMBH lead to flaring material.

Statistical variations would show up as no or random motions in the GRAVITY observations (Vincent et al., 2014). If the emission is dominated by a hot-spot, GRAVITY has the potential to probe the spacetime metric in the inner GC, because the flares would then

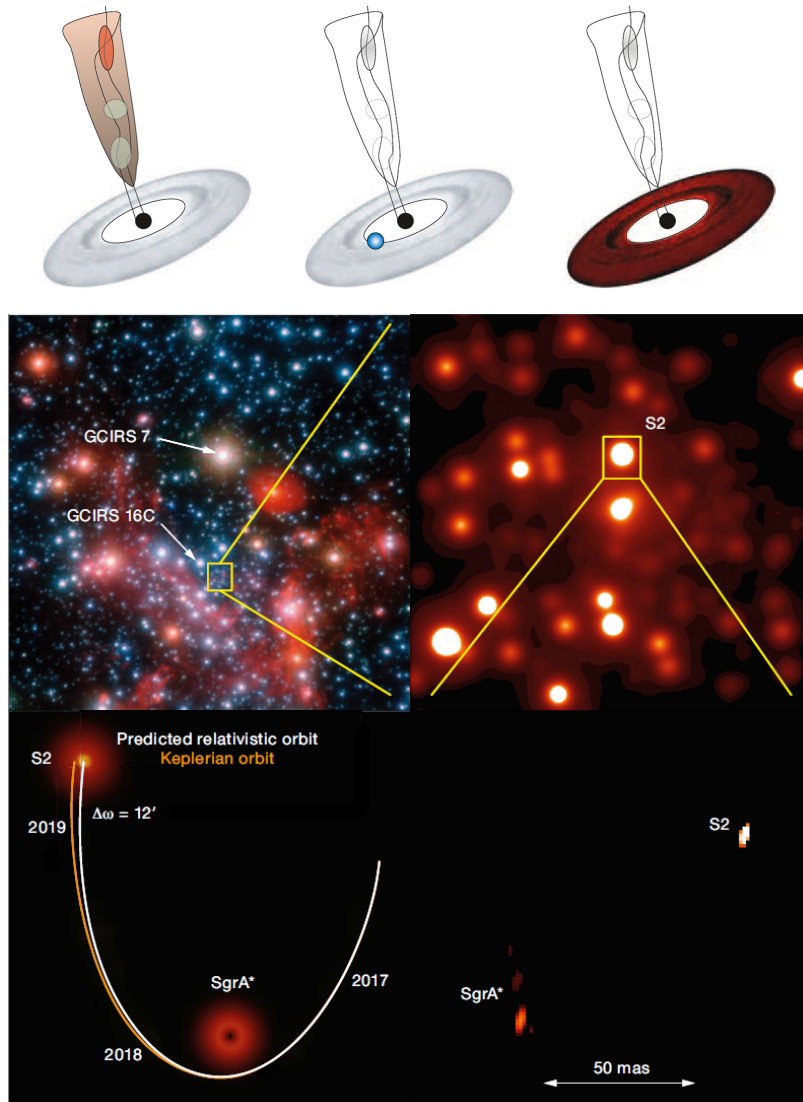


Figure 3.4: Top: flare models for the Galactic Center draw three different scenarios as illustrated in Eisenhauer et al. (2011). On the left a jet causes the flaring, in the middle an orbiting hot spot is responsible, while on the right statistical fluctuations in the accretion disk are the origin. GRAVITY will be able to distinguish between these cases. Bottom from Gravity Collaboration (2017), from left to right: the central $20''$ of the GC contain objects suitable for AO with CIAO and fringe tracking such as the supergiant stars GCIRS 7 and GCIRS 16C ($m_K = 9.8$) respectively. AO observations with an UT show the central arcsecond with the yellow box marking S2 and Sgr A*, the primary science targets for GRAVITY. The orbit of S2 around Sgr A* is expected to follow a relativistic path in white compared to the yellow Keplerian motion corresponding to the shift $\Delta\omega = 12'$. The lower right shows the imaging of the first Sgr A* detection, achieved by GRAVITY in September 2016. The apparent elongation of the sources is not intrinsic but resembles the geometry of the observatory projected on sky.

be linked to the mass and the spin of the BH. The short timescale and the large variations in brightness of the flares hint towards a origin within a few Schwarzschild radii, which would allow to probe a region close to the event horizon of the SMBH.

Tests of General Relativity GRAVITY will reveal effects of general relativity in the strong-field limit as present close to BHs but nowhere on Earth. Deviations from the classical Keplerian orbits are expected to occur due to the strong gravitation. A relativistic shift of the periastron of S2 as in Figure 3.4 is expected, which is the point of the smallest distance to the gravitational center. A hot spot orbiting the GC close to the last stable orbit will be affected by gravitational lensing and gravitational redshift.

GRAVITY could already demonstrate phase-referenced dual-beam observations with use of the IR WFSs CIAO in the Galactic Center on one of the S stars, S2. This object has the shortest known orbital period of 16 years and reaches a velocity up to 7600 km/s, 2.5% of the speed of light (Schödel et al., 2002; Ghez et al., 2008; Gillessen et al., 2017). With a K-band magnitude of $m_K = 14.1$, S2 had been too faint to be observed by the VLTI before GRAVITY. S2 shows motion measurable day to day and its monitoring is ongoing.

Monitoring Sgr A* Moreover, the use of GRAVITY allowed for the first detection of Sgr A* in IR interferometry, which usually is detected as compact radio source at the position of the SMBH. At that time, a moderate flare of $m_K = 15$ occurred. This IR counterpart can always be detected now, no matter if flaring or not. Since light of S2 is entering these observations of Sgr A* as well, typical binary signatures are visible in the visibilities and phases. This feature allows for astrometric measurements in single-field mode.

GRAVITY Performance Prior to GRAVITY, the faintest objects observed with NIR interferometers in dual-field phase referencing have magnitudes of $m_K = 12.5$, demonstrated at the Keck Interferometer (Woillez et al., 2014). Science results are published for objects as faint as $m_K = 10.2$ and $m_K = 10.1$, in Kishimoto et al. (2011) and Weigelt et al. (2012), respectively.

Limiting magnitudes of $m_K \approx 17$ for phase-referenced interferometry and $m_K \approx 10$ for fringe tracking could be reached by GRAVITY (Gravity Collaboration et al., 2017b). Clearly, GRAVITY offers a new level of detecting faint sources in optical interferometry. In this way, the observations of S2 and flare activity could exclude the presence of field stars brighter than $m_K = 8$ near S2, which makes this star a suitable test particle to trace the GC.

Future GRAVITY observations of the GC will be able to explore relativistic effects, with additional measurements of the VLT spectrograph SINFONI (Grould et al., 2017; Waisberg et al., 2018). Depending on the effect, the star S2 needs to be monitored for a few months or years in this respect. The pericenter flyby in spring 2018 is particularly important in this respect. This event potentially allows for the detection of the Schwarzschild precession of the S2 orbit in the next two years.

Another ultimate goal would be the optimization of the GRAVITY sensitivity to detect faint stars on even smaller orbits with periods of a few years or even months. The stellar-density profile hints towards the presence of such objects. Then, not only the monitoring of the smallest orbit would be shorter, but also higher-order relativistic effects could be observed, for example the Lense-Thirring precession of the stellar orbits around the spin axis. According to the no-hair theorem a BH is fully characterized by its spin and mass. In this respect, a very fundamental and spectacular measurement could become possible for the first time by the use of GRAVITY. By measuring the quadrupole moment, the BH spin could be probed.

Other Science Cases

Other dynamical measurements will also be revolutionized by GRAVITY. Similar as for the SMBH in the Milky Way, accretion and disk phenomena are of particular interest. These span from Active Galactic Nuclei (AGN) found in galaxy centers to young stellar objects. Rapid accretion to such sources results in outflows and jets. The formation mechanism of jets are not fully understood and therefore high-resolution measurements as done by GRAVITY are needed. Young stellar sources also host planet formation in their disks. In general, such sites are already analyzed by radio interferometry, but the IR range offers the possibility of resolving these objects on smaller scales and disk radii.

In the case of the AGN the geometry of its structure is still debated. Imaging those inner regions could shed light on the open questions about the standard unified model that assumes a SMBH surrounded by a torus of obscuring material. GRAVITY might also be able to dynamically measure the masses of such SMBHs.

In addition to SMBHs in galaxy centers, intermediate-mass black holes are also of interest for GRAVITY observations. Accumulating evidence shows that those objects might be present in star clusters. The small influence region of the BHs can be more frequently probed by the resolution capabilities of this new beam combiner instrument.

Also classical topics for interferometry such as binary stars will be analyzed with GRAVITY. Not only the components and their orbits can be observed but also winds due to their interaction are of special interest.

GRAVITY Performance GRAVITY already could show its capabilities on different types of sources. The precision of the complex visibilities of long exposures is a function of the source brightness and FT residuals. Measurements on bright calibrator stars show a typical precision of 0.5% for the visibility amplitude and 1° for the phase. The high accuracy of the GRAVITY visibilities could also be demonstrated by the observation of resolved stars with results better than 0.25% - a level reachable only with the help of spatial filtering through SM fibers (Perrin et al., 2004). Spectro-differential and closure phases can be determined by GRAVITY with accuracies better than 0.5° . Also interferometric imaging is brought to the next level by GRAVITY due to high sensitivity and spectral analysis such that detailed morphologies can be studied, as for the binary star η Car (Gravity Collaboration et al., 2018).

Spectro-Differential Astrometry Spectro-differential astrometry of 10 μas precision allowed to trace the gas stream in the X-ray binary BP Cru (GRAVITY Collaboration et al., 2017) and jet emission in the microquasar SS433 (Gravity Collaboration et al., 2017a). Differential means that visibilities or phases are analyzed in difference to each other with respect to the spectral channels. In the differential phase, the position and potential changes of the photocenter of an object can be traced across the different wavelengths, which allows for astrometric measurements without referencing to another object. By this technique, asymmetries can be resolved in small scale structure, for example giving an insight into the inner accretion and ejection processes in the young stellar object S CrA.

Dual-Beam Astrometry Dual-beam astrometry is still under commissioning, but first results on the basis of a few binaries already show an accuracy 50 μas in measurements repeated over several months. The results for the binary GJ 65 AB at 2.68 pc from the Sun is plotted in Figure 3.5. The differential nature of dual-beam astrometry minimizes astrometric errors. The ultimate limit comes from residual atmospheric perturbations, but even these average out to 10 μas within minutes. Such levels of astrometric accuracy allow for measuring the reflex motion of a low-mass star caused by an Earth-mass planet with orbital period of one year. The current performance of GRAVITY will allow detecting Jovian planets, which are more massive roughly by a factor 300 requiring astrometry of 3 mas. The detection of Earths requires further progress in modeling and correcting systematic errors (Gravity Collaboration, 2017).

One of the big challenges for this new capability of the VLTI is the measurement of dOPDs will be the laser metrology system developed at MPE. This subsystem is presented in the next sections focusing on the work that was done in the frame of this thesis, starting from the original dual-beam scheme and leading towards the required design change to the three-beam concept including the results published in Lippa et al. (2014) and Lippa et al. (2016).

3.2 Dual-Beam Scheme

The metrology system is the basis for narrow-angle astrometry with the VLTI. The idea is to determine the angular separation on sky between two targets showing up in the interferometric observations by a phase difference between the individual fringe packets as demonstrated before in Figure 2.19.

The astrometric precision of GRAVITY aims at 10 μas , the angular size of the event-horizon radius of the black hole in our Galactic Center. This requires the measurement of internal dOPDs on a nanometer scale with a dedicated metrology system. The high-precision levels needed, the interferometric setup of GRAVITY at VLTI, and the need for differential length measures suggest the use of a laser-light metrology system performing phase-shifting interferometry.

The main idea is to use the interferometer to create laser fringes after the light has passed the way through the instrument and observatory. The dual-beam observations of

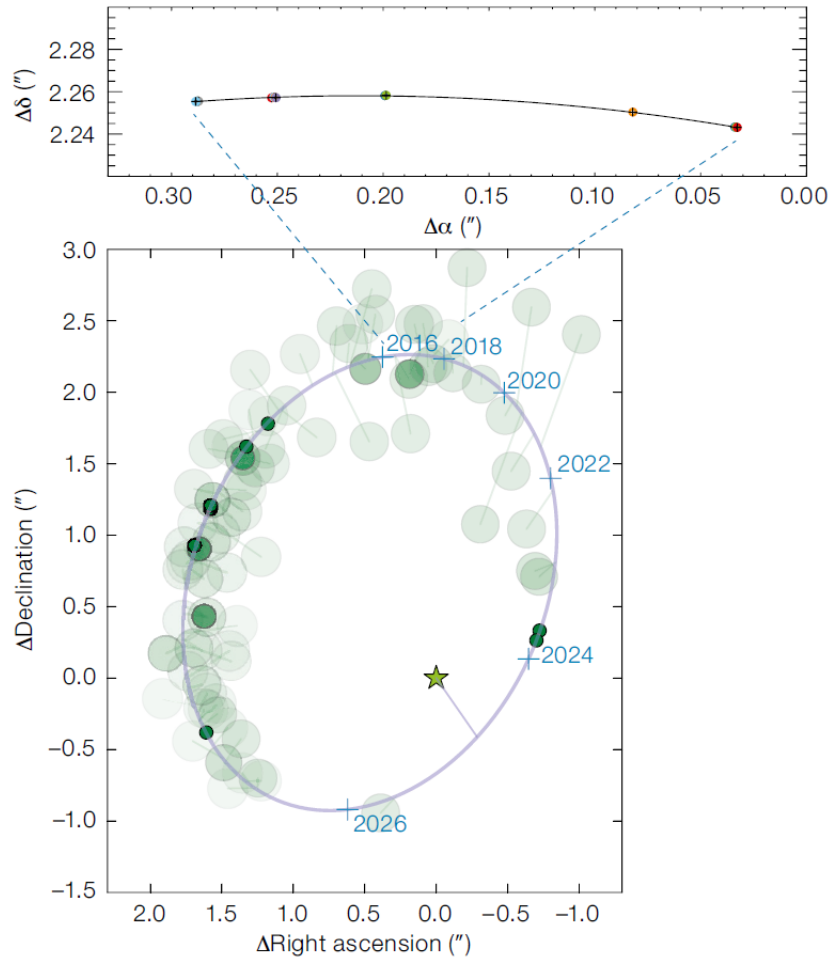


Figure 3.5: Dual-beam astrometry of the binary GJ 65 AB from Gravity Collaboration (2017) showing measurements from GRAVITY in the top panel with the best quadratic fit as black line compared to previous seeing-limited and AO results from Kervella et al. (2016) on the lower panel. The latter shows the orbit of one star with respect to the other fixed at the position of the stellar symbol. Higher accuracies are marked by darker shades and decreasing disk sizes show smaller uncertainties. GRAVITY took data points with the ATs in five epochs in 2016 and 2017 achieving an unprecedented accuracy of roughly $50 \mu\text{as}$ and measuring the orbital acceleration in less than a year (Gravity Collaboration et al., 2017b).

GRAVITY therefore naturally lead to a dual-beam metrology. The internal dOPDs are encoded in differences between fringe phases of the individual telescopes which can be measured by ABCD sampling of the fringes as described previously.

3.2.1 Phase-Shifting Interferometry

The original metrology concept of the GRAVITY instrument is displayed in Figure 3.6 for the example of two telescopes. A laser beam is split in two equally bright ones and injected to the outputs of the IO beam combiners of the fringe tracker and science channel, BC A and BC B. The metrology light then travels the interferometer up to the two telescopes. There, above the primary mirrors, they interfere and form fringes, which are sampled by four metrology receivers per telescope and using a phase shifter in one of the injected beams. The fringe scanning is implemented in the form of ABCD sampling at a kilohertz-rate which delivers four intensity measurements at four controlled phase shifts.

Narrow-Angle Astrometry

The dOPD between the two objects observed by GRAVITY is a measure for their angular separation on sky and mathematically is encoded in the difference between the fringe phases Ψ_A and Ψ_B of both objects measured at detectors A and B. Internal dOPDs need to be subtracted however as given by the difference of the fringe phases Φ_1 and Φ_2 at the telescopes T1 and T2 formed by the interfering metrology beams:

$$dOPD = \frac{\lambda_A}{2\pi} \Psi_A - \frac{\lambda_B}{2\pi} \Psi_B + \frac{\lambda_L}{2\pi} (\Phi_2 - \Phi_1) - \frac{\lambda_L}{2\pi} (\delta_2 - \delta_1) \quad (3.4)$$

with λ_A and λ_B denoting the effective wavelengths of the science light and λ_L referring to the metrology wavelength. The terms δ_1 and δ_2 consider the influence of the so called non-common paths that are only seen by the metrology light and not by the science contribution. These non-common paths occur in the parts labeled U_A and U_B in Figure 3.6 and arise from injecting the metrology light by two fibers per BC, not illustrated in the figure. The phase difference between the two fibers enters the dOPD budget for four of the six baselines.

The difference of the non-common paths, $\delta_2 - \delta_1$, can be measured prior to the observations by swapping the objects between the beam combiners A and B, which gives the zero points of the metrology phases. The adjustment of the metrology zero does not need to be applied online but can be integrated in the data reduction. The described extraction of the dOPD can be applied to all six baselines of the VLTI.

As a consequence, the desired quantities for the metrology measurements are the fringe phases at the telescopes which in difference are a measure of the internal dOPD between the two beam paths of the two science targets. Using Equation (3.5), this phase can be computed from four measured intensities I_A , I_B , I_C and I_D separated by $\pi/2$ by controlled phase shifts:

$$\phi = \arctan \left(\frac{I_A - I_C}{I_B - I_D} \right) . \quad (3.5)$$

Therefore, next to the detection of the science light also the metrology concept relies on phase-shifting interferometry. Since this phase extraction is an ambiguous measurement for changes $> \pi$ due to the arctangent function, the metrology phases at the telescopes Φ_1 and Φ_2 need to be reliably tracked in real-time during the observations starting from the

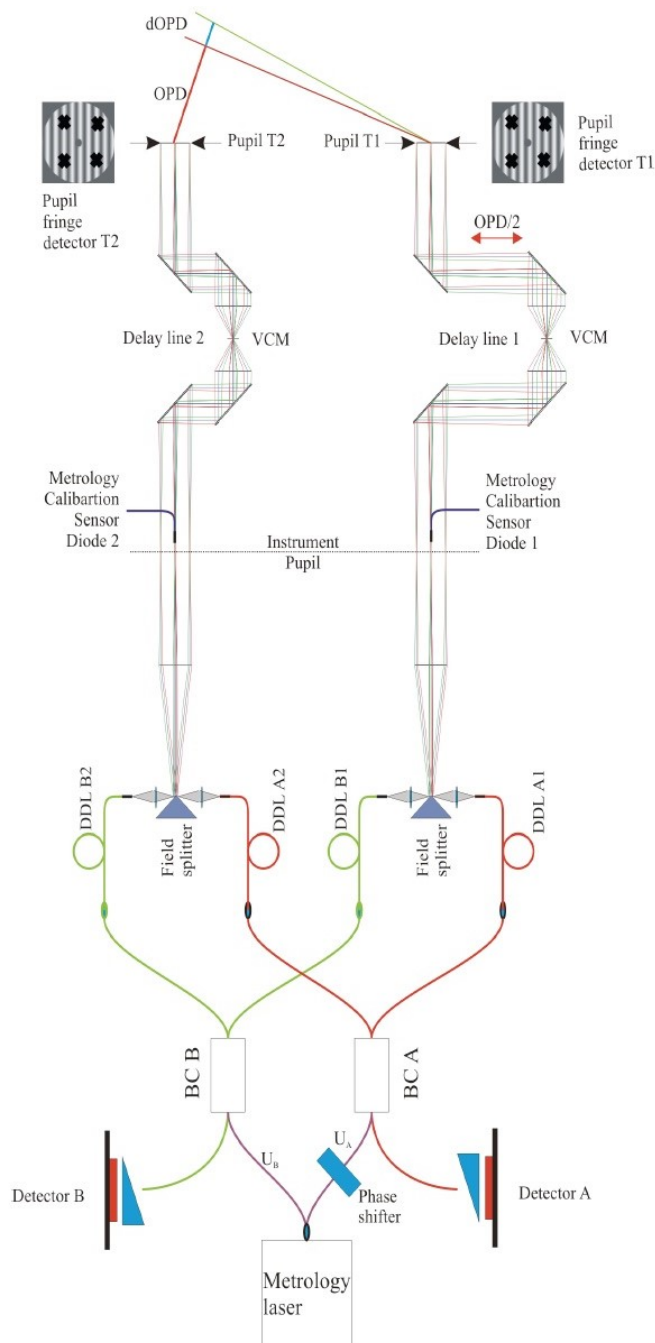


Figure 3.6: The original dual-beam concept of the GRAVITY metrology as published in Gillessen et al. (2012). A laser beam is launched, split in two and injected to the outputs of both beam combiners BC A and B. In reverse direction to the science light the metrology beams travel to the telescopes, where they interfere in the pupil plane above the primary mirror. For demonstration of the concept only two of the four telescopes are shown as T1 and T2. The fringes detected by four metrology receivers per telescope can be scanned by means of the phase shifter in one of the injected beams.

zero-point calibration. Only then the internal dOPDs can be determined and subtracted from the science dOPD. For this reason the four phase shifts $0, \pi/2, \pi$ and $3\pi/2$ need to be applied online at a fast rate in the kilohertz-regime. The phase measurement per telescope results from the average phase seen by the four receivers.

Astrometric Error Budget The uncertainty in the accuracy of the applied phase shifts goes into the astrometric error budget among other factors. Error propagation from Equation (3.5) relates the resulting phase uncertainty $\delta\Phi$ to the SNR of the measured intensities by

$$\delta\Phi^2 = \left(\frac{\partial\Phi}{\partial I_A}\delta I_A\right)^2 + \left(\frac{\partial\Phi}{\partial I_B}\delta I_B\right)^2 + \left(\frac{\partial\Phi}{\partial I_C}\delta I_C\right)^2 + \left(\frac{\partial\Phi}{\partial I_D}\delta I_D\right)^2 \quad (3.6)$$

$$= \frac{(\delta I_A^2 + \delta I_C^2)(I_B - I_D)^2 + (\delta I_B^2 + \delta I_D^2)(I_A - I_C)^2}{((I_A - I_C)^2 + (I_B - I_D)^2)^2} \quad (3.7)$$

$$= \frac{2\delta I^2}{(I_A - I_C)^2 + (I_B - I_D)^2} \quad (3.8)$$

$$= \frac{2\delta I^2}{4I_1 I_2 (\sin(\phi) - \sin(\phi + \pi))^2 + 4I_1 I_2 (\sin(\phi + \frac{\pi}{2}) - \sin(\phi + \frac{3\pi}{2}))^2} \quad (3.9)$$

$$= \frac{\delta I^2}{2I_0^2 (\sin(\phi)^2 + \cos(\phi)^2)} \quad (3.10)$$

$$= \frac{\delta I^2}{2I_0^2} \quad (3.11)$$

$$= \frac{1}{2 \times SNR^2} \quad , \quad (3.12)$$

when the four intensity measurements have equal uncertainties $\delta I := \delta I_A = \delta I_B = \delta I_C = \delta I_D$ and beams are of equal brightness $I_1 = I_2 = I_0/2$.

This uncertainty in the phase shifts enters the total error in the measurement of the metrology phase and by that the total GRAVITY OPD error and astrometric error as shown in Table 3.1.

In the theoretical error budget prior to the development of the phase-calibration routine, the total metrology error was budgeted to 1 nm, such that the calibration of phase shifts should have an uncertainty equal or smaller than this value. In my master thesis a calibration by a linear scan through $[0, 2\pi]$ resulted in an error of 2 nm dominating the total phase-extraction error of the estimated metrology budget, which would make up the second largest term in the computation of the astrometric error (Lippa, 2012). But since the error on the phase calibration is only one of several terms of similar order, for instance depending on the laser and receiver performance, differences by a factor of two have no strong effect on the astrometric error in the end as demonstrated in Table 3.1.

However, as the calibration method of Lippa (2012) relies on a rather complex model with many assumptions, I made another attempt to further reduce the calibration error

Error term	Case 1	Case 2	Case 3
Phase shifter calibration error	$\lambda_L/4000$ 0.5 nm	$\lambda_L/2000$ 1 nm	$\lambda_L/1000$ 2 nm
Total metrology phase extraction error	0.94 nm	1.22 nm	1.81 nm
Total GRAVITY OPD error	6.83 nm	6.87 nm	7.00 nm
Astrometric error	10.27 μ as	10.34 μ as	10.53 μ as

Table 3.1: Role of the phase-shift calibration within the astrometric error budget of GRAVITY for observations with four UTs during a period of 5 min demonstrated on basis of three example cases, as shown in Lippa et al. (2014).

by implementing another routine. This phase-step insensitive method is more elegant, because it involves fewer assumptions and measures the phase shift unambiguously with simple modeling. The calibration scheme is explained in the following after introducing the general design of the dual-beam metrology system.

Dual-Beam Design

In the first stages of this thesis work I assembled and tested the final dual-beam metrology in the GRAVITY cryostat based on the previous characterization of various prototypes. Figure 3.7 illustrates the chain of components for the dual-beam scheme.

Metrology Laser The laser from Sacher Lasertechnik and Keopsys produces light with a single frequency, high power level and linear polarization. The metrology wavelength (1908 ± 1) nm is chosen to lie slightly below the astronomical K-band light in order to not interfere with the observations but large enough to be single mode, still tracking dOPDs similar as seen by the science light. The output of > 1 W is fed into a SM fiber which is also Polarization-Maintaining (PM).

Polarization-Maintaining Fibers The metrology system is based on the fiber type Fujikura SM15-PS-U25A or the equivalent Corning PM15-U25A with a nominal wavelength 1550 nm. This choice allows for highly transmissive, single-mode operation at the metrology wavelength and at the same time opens up a wide range of various fiber components from telecommunication industry which frequently operates at 1550 nm. In this respect, FC/APC connectors are used at the ends of the fiber cables, which have angled end faces to minimize back-reflections, shown in Figure 3.8.

A non-PM single-mode fiber easily produces a variable polarization of the injected light due to stress or asymmetries in the circular core (Noda et al., 1986; Fujikura, 2017). Linear polarization is maintained in the metrology fibers due to the PANDA design, which includes two stress-applying rods in the fiber cladding surrounding the fiber core as shown in Figure

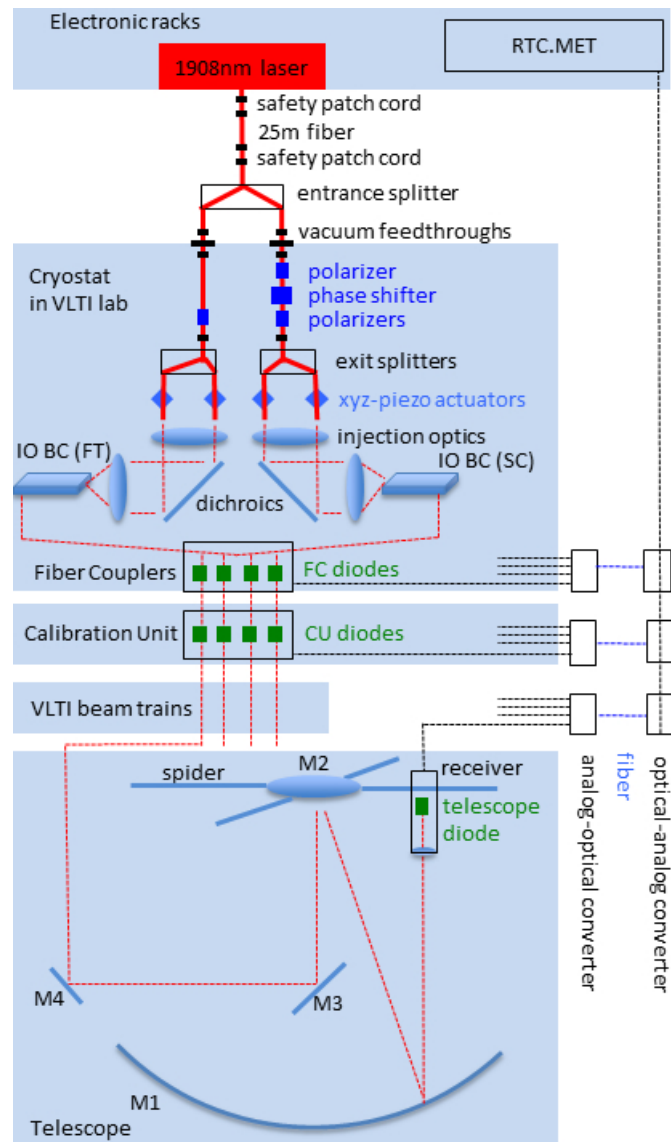


Figure 3.7: Design of the dual-beam metrology: on the top a laser beam is launched and split for injection to the IO outputs. The red solid lines denote the metrology fibers guiding the laser light, which transfer to dashed lines, where the propagation continues as free-beams and joins the science path after the reflection from the dichroics. More details are given in the text.

3.8. The induced stress creates birefringence, which means the refractive index depends on the polarization state (Folkenberg et al., 2004). If light is injected with linear polarization aligned to the vertical or horizontal symmetry axis of the fiber, the polarization state is maintained.

The PANDA fiber has a so called fast and slow axis. The metrology design is aligned to the slow axis. The orientation is marked at the fiber connector by a feature called key.

The mating adapters for the connection of patch cords come with receptors for these keys such that the fibers are oriented correctly at their interface. Special mating adapters from Thorlabs for PM applications were used to minimize alignment errors. The polarization leaving the fiber at the laser output is linear with an amplitude ratio of $> 100 : 1$ in the orthogonal polarization axes. This value corresponds to a polarization Extinction Ratio (ER) of > 20 dB, which is typical for the fiber connectors as well as their mating. The ER can be as good as 30 dB while the fiber itself shows high values of > 50 dB (Penninckx et al., 2006).

Fiber Patch Cords From the laser, the metrology light is routed via the PM fiber in the form of patch cords from FCC Fibre Cable Connect with metal-housing for protection of the fragile fused silica fiber. Since the electronic racks and the GRAVITY cryostat are located in separate rooms a patch cord with a length of 25 m is used.

Since high power levels can melt the fiber by heat excess of absorbing dust residuals on the fiber end faces, I introduced a set of short safety patch cords to the chain. The idea behind is to allow disconnecting the long fiber from the expensive laser and the following built-in splitter component from each other without risking damage of these components. Instead, two short patch cords are installed after the laser output fiber and in front of the entrance splitter, such that connections can be opened and closed, which are easier to replace in the case of any damage.

Entrance Splitter The first component in the fiber chain is the entrance splitter by OZ Optics, which performs a roughly equal split in two beams to feed the science and fringe tracker channel of GRAVITY. The splitter is fabricated by the Fused Biconical Taper (FBT) process (Kawasaki & Hill, 1977). For FBT, two fibers are brought together, twisted, heated and stretched such that their cores end up being very close forming a coupling region. There, the light from one core can leak into the other, while the coupling ratio depends on the length and diameter of the tapered region.

Originally, this splitter was implemented within the cryostat, where it witnessed a drastic reduction of its transmission probably due to mechanical stress of the integrated fiber in the cooled environment. Therefore, the entrance splitter was then installed outside the cryostat and as a consequence two fibered vacuum feedthroughs from Schäfter + Kirchhoff were implemented for the metrology light instead of a single one.

Vacuum Feedthroughs The vacuum feedthrough essentially consists of a fiber glued into a flanch. Except for the entrance splitter, which initially was placed inside the cryogenic environment, all the fibers between laser and cryostat are protected by a step-proof metal housing to prevent any damage as they are easily accessible.

Phase Shifter with Polarizers Within the GRAVITY cryostat at 280 K, one of the fiber paths is equipped with a phase shifter from Photline Technology for scanning the metrology fringes. Due to the many fiber connections in the previous fiber chain, small

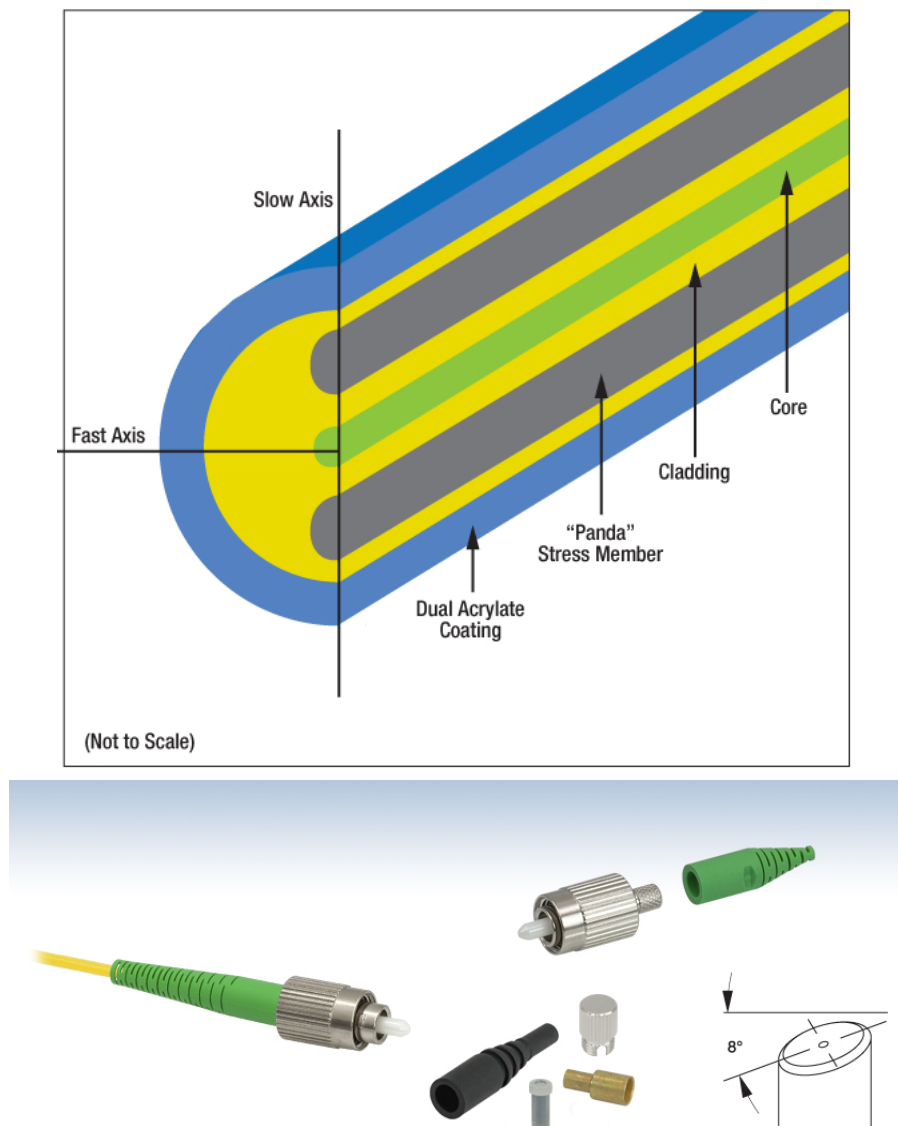


Figure 3.8: Polarization-maintaining fiber of PANDA type as shown by Thorlabs (2017), in its cross sections (top) and FC/APC connectors with angle ferrule for minimizing back-reflections (bottom). Injected light travels through the fiber core by reflection from the cladding. A coating protects the fragile wave-guiding material. The stress rods induce a high birefringence such that the two polarization components of the wave are affected by different refractive indices in the slow and fast axis. The connector typically is aligned with the slow axis marked by a key on the metal housing surrounding the ceramic ferrule. Different strain-relief boots and dust caps are offered on the market.

misalignments of the polarization occur which are corrected by fibered polarizers from Thorlabs. This is particularly important in front of and behind the phase shifter for a better control of phase shifts. The detailed background of this step is discussed in section 3.2.2.

Exit Splitters In the next step both metrology beams need to be equally split another time by the exit splitters from LEONI. This split is necessary to feed two of the 24 IO outputs of each IO BC chip, such that all four inputs of the IOs are illuminated. The splitting is integrated on a small IO chip.

The splitter outputs are bare fibers without cables and connectors. The exit fibers are mounted in V-grooves held by **xyz-actuators** from SmarAct, for coupling the metrology light to the IOs in the fiber positioner units built at MPE. The SmarAct devices allow for a sub-micron positioning accuracy to optimize the coupling prior to the observations. In stable operation of the instrument, the coupling only needs to be adjusted once. Only interventions or incidents like power cuts or earth quakes can require re-adjustment of the laser coupling to the IOs.

The output fibers are 5 cm short and of equal lengths with a difference of at most 1 mm. This specifications ensure that non-common paths do not lead to significant error terms in the metrology measurements. The polarization direction can vary due to bending when positioning the fibers. To mitigate this scenario, SM fibers instead of a PM realization is implemented. In tests, these fibers showed smaller changes in the output polarization state. The short fiber length maintains the polarization in this configuration, because it is much smaller than the beating length. The latter describes the phase difference of a full wave between the two polarization modes. Since the beating length is inversely proportional to the birefringence, the polarization alignment in highly-birefringent PM fibers is much more sensitive to the stress from bending (Noda et al., 1986).

Injection Optics Injection optics including **dichroics** in the spectrometers feed the metrology light from the splitter outputs to the paths of the science light. The fiber positioner units are equipped with two thermal control loops to maintain the temperature while being mounted on top of the cold spectrometers and for the warm-up of the instrument. The science light travels in opposite direction through the system compared to the metrology and is transmitted by the dichroics to the detectors. The metrology light in contrast is reflected by the dichroics in the directions of the IOs. The small fraction of light transmitted through the dichroic is captured in a beam dump with zero back-reflection and less than a few percents backscattering. The injection optics image the fiber exits to the IO outputs including a demagnification to match the Gaussian modes. The IOs have an anti-reflection coating at their outputs in order to maximize the throughput.

Metrology Detection After the injection to the IOs, the metrology light travels backwards through the instrument, along the paths of the science light in reverse order over the FCUs, containing the polarization rotators and the differential delay lines, to the **fiber**

couplers. Here, the metrology beams interfere for the first time, such that fringes can be detected. The detection happens at three places: the fiber coupler, the **calibration unit** and the telescopes. While the telescope signals are used for the actual dOPD measurement, the calibration unit serves for simulating the telescopes for test and calibration purposes. The fiber coupler signals are the strongest in the chain and therefore used to command the DDLs.

Diode Boxes The key element of the metrology receivers are **photodiodes** from Teledyne based on extended InGaAs. The size of the photosensitive area in the diodes is 0.5 mm. The diodes are integrated into housings designed and built at MPE. The diode boxes are equipped with optics which focus the metrology light onto the photosensitive area of the diodes. Furthermore a circuit board built at MPE amplifies the electrical signal in three stages. The first stage has different amplification levels of which one can be chosen from 10^4 to 10^7 , in steps of factor of 2. The second and third stage provides an amplification by a factor of 10^3 each.

Fringe Detection in Pupils In each of the four fiber couplers, a small fraction of the metrology light is picked up in the pupil plane by a Multi-Mode (MM) fiber from Thorlabs glued to a lens surface. The lens is part of a retroreflector behind the dichroic to image the fibers on the acquisition and guiding camera. On its other end, the pick-up fiber has a connector which is mounted to a fiber-to-diode coupler made by OZ Optics. The coupler consists of a lens with tilt adjustment designed for the metrology wavelength.

The same type of arrangement is found in the four diode boxes of the calibration unit. There, the pick-up fibers are mounted in the collimated beam. Each **telescope** is sampled by four receivers on the **spider arms** holding the **secondary mirror M2** above the **primary M1**. The receiver schemes of the fiber couplers and telescopes are visualized in Figure 3.9.

Telescope Receivers For the GRAVITY operation the metrology light exits the calibration unit at the four beam inputs for the science light coming from the telescopes. Via the **VLT beam trains** it reaches the **mirrors M4, M3, M2** and **M1** with final reflection onto the telescope diodes, as shown in Figure 3.7. The telescope receivers work with lens optics instead of pick-up fibers in order to capture a larger portion of the widely spread light above the big primary mirror.

The maximum diameter of the focusing lens from Thorlabs depends on the fringe spacing. The UT FOV of $2''$ contains less than 41 fringes, and less than 17 fringes are found in the AT case with a FOV of $4''$. The minimum fringe spacing is 20 cm and 11 cm, which limits the lens diameter to 5 cm and 2.8 cm, respectively. The diameter of the implemented lenses are 5 cm and 1.25 cm for the UT and the AT case. The lenses were coated for the 1908 nm wavelength. In order to suppress background light, the receiver optics at the telescopes also include line filters from Filtrop. The focus of the optics can be mechanically adjusted by a few millimeters. The focal length is 40 mm and 10 mm, respectively.

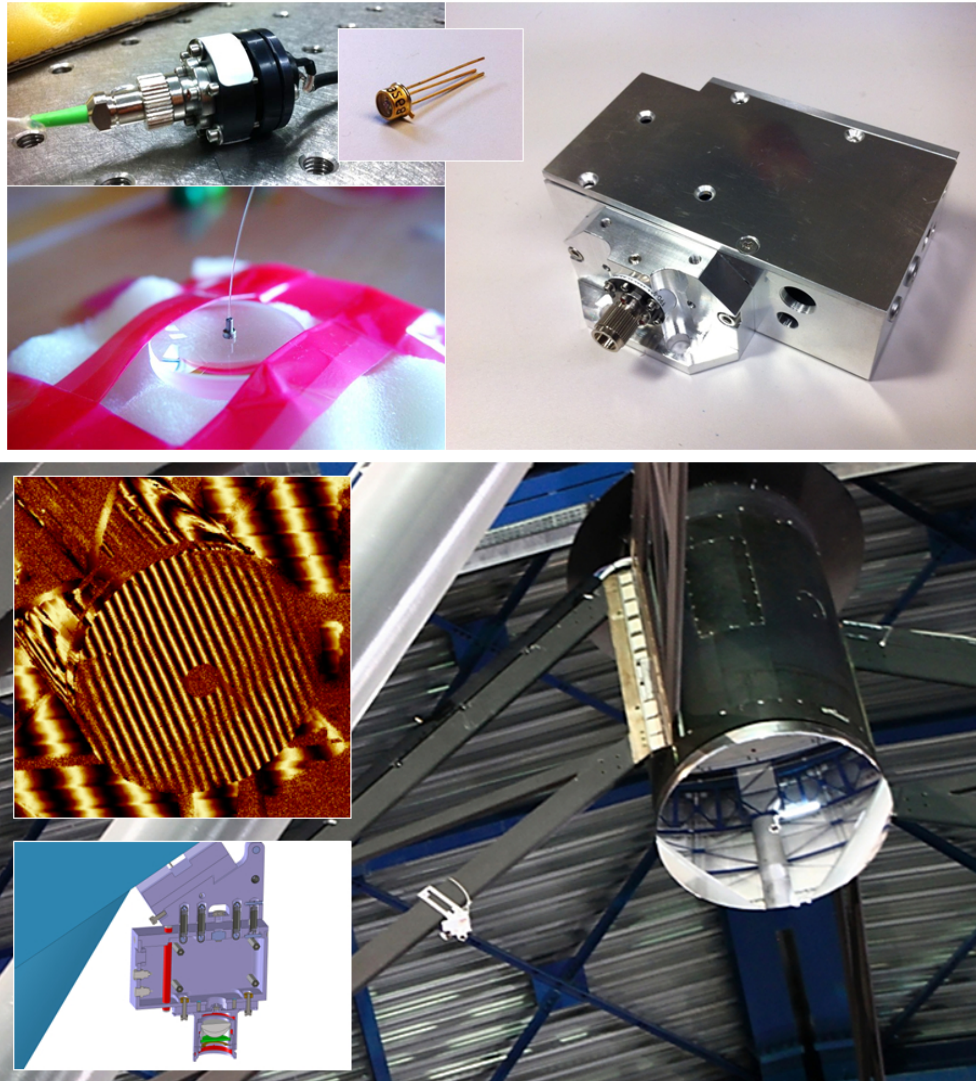


Figure 3.9: Metrology receivers in the fiber couplers (top) and at the telescopes (bottom). The metrology light is picked up by the shown fiber glued to a lens in the fiber couplers. The fiber feeds a fiber-to-diode coupler in the top left which contains the photodiode displayed on the right. The coupler is mounted to the metrology receiver on the right side. For the telescopes, similar diode boxes, but with lens optics, are mounted to the spider arms of the secondary mirror M2. The opto-mechanical design is shown in the lower left. During a test campaign in 2010 a prototype was installed at a UT to verify the detection scheme. Fringes were measured on M2 by an infrared camera.

The choice of the mounting radius for the receivers eliminates the dependence on the differential focus. The accuracy of the receiver positions at the telescopes needs to lie at ≤ 1 mm. Therefore, the boxes are equipped with a mechanism for radial and tangential direction with sub-millimeter fine adjustment. To optimize the coupling, angular adjustment

is possible in both directions by a few degrees.

Signal Conversions The analog signals from the telescope diode boxes are digitized for the transport in glass fibers down to the electronic racks in the VLTI laboratory. This **analog-to-optical conversion** takes place in dedicated electronic boxes built by M.K. Electronic and mounted to the telescope centerpieces. The power supply for the receivers is also located in this box as well as the lasers of the pupil guiding in GRAVITY.

The electronics of this system has a low power consumption such that the surface temperature is not higher than 1° above the ambient temperature in the telescope domes for not adding turbulence seeing to any observations. The conversion systems from mk-messtechnik allow processing four signals per **fiber** link including a digital link that can be used for switching the electronic boxes on and off. The output of the receivers in the fiber couplers and the calibration unit are treated similarly.

In order to operate this system at any of the available AT stations, a switch box also from mk-messtechnik allows to select the correct AT optical signals. The switch box provides 36 optical inputs covering the 35 fiber links from the four UTs, the 30 AT stations and the calibration unit.

Real-Time Computing In the electronics racks the received signals are processed. The real-time computing of the metrology **RTC.MET** not only involves this real-time recording and related online calculations but also controlling three devices namely the laser, the xyz-actuators and the switch box. The calculations include the subtraction of the offset voltages in the diode boxes, time-averaging of the signals, determination of the SNRs and phases as well as flagging of values that indicate problems occurring. In addition, the laser power and wavelength is monitored.

In this way, the metrology system can measure internal dOPDs by forming and detecting laser fringes at telescope level. The scanning of the fringes is realized by phase shifting at kilohertz-rates. The development of the calibration scheme for the required phase shifts is described next. In contrast to a previous method, the advantage of this concept is that the accuracy of the calibration does not depend on the phase step. As such, the calibration is labeled phase-step insensitive.

3.2.2 Phase-Step Insensitive Calibration of the Phase Shifter

The key device for the scanning of the metrology fringes is the phase shifter. The prototype and final component for this purpose is the device MPX2000-LN-0.1 in Figure 3.10 produced by Photline Technologies. The core of this modulator is a lithium niobate crystal (LiNbO_3). Applying an electric field to this material alters its refractive index, leading to a phase change at the output. The light is fed by optical fibers and passes the crystal on its surface within a waveguide made by a titanium diffusion. This dopant increases the refractive index to a level such that the light follows the waveguide through total internal reflection (Wooten et al., 2000).



Figure 3.10: Phase shifter of type MPX2000-LN-0.1 by Photline Technologies. Optical fibers serve as input and output for a lithium niobate crystal. This material changes its refractive index depending on the strength of electrical field applied to it.

The specifications of the phase shifter give a wavelength band centered on 2000 nm covering the metrology wavelength and an electro-optic bandwidth of 150 MHz meeting the kHz-rate of the metrology operation. This and other properties of the phase shifter are compared to the metrology requirements in Table 3.2. The optical input power is specified for a much lower power level of 0.1 W than what the original transmission budget of the metrology foresaw. But long-term tests in the laboratory showed the high laser power of 2 W is withstood by the phase shifter. The range of 10 V covers shifts by a full metrology wavelength.

Parameter	Photline specification	Metrology requirement
Operating wavelength	1900 nm – 2200 nm	1908 nm
Electro-optic bandwidth	150 MHz	4 kHz
RF input power	-20 V – +20 V	0 V – 10 V
Optical input power	0.1 W	0.85 W

Table 3.2: Specifications of the phase shifter as shown in Lippa et al. (2014)

Modifications at the Phase Shifter

In the course of developing the first calibration routine based on a linear scan covering one wavelength, I modified the phase shifter for better performance (Lippa, 2012). As mentioned before, fiber polarizers had to be added in front and behind the phase-shifting

device to correct for the misalignment of the polarization, for instance introduced by fiber connections.

Birefringence of the Phase Shifter Since LiNbO_3 is a birefringent material, the modulator crystal comes with different refractive indices depending on which of the two orthogonal polarization axis, fast axis x or slow axis y , is fed with light. Ideally, linearly polarized light aligned to one of these axes is injected to the phase shifter, but due to the mentioned misalignments in fiber connections and components the light travels both axes. As a result of this asymmetry, different phase shifts occur in the two axes per applied voltage. Overall, the general phase response to voltages is described by different functions depending on the fed polarization axis. In the phase-shifting device used here, the phase-shift difference between the axes can be up to factor of three.

As a further consequence of both axes being fed with light, the output signal of the phase shifter is elliptically polarized. Due to variations of the misalignments the two polarizations with power P_x and P_y show varying power ratios. As a result, the contrast changes in the measured fringe signal as the amplitude of interference is proportional to the product of the powers, which varies in this scenario. This variation of contrast can be interpreted incorrectly as a phase shift. The amplitude ratio between the polarization modes measured for the phase shifter ranges from 1 : 10 to 1 : 5.

Fusion Splicing Therefore, a linear fiber polarizer is added to the setup in front of the phase-shifter input. In order to reduce misalignments in the connection between polarizer and phase shifter the components are fusion-spliced using a splicer from Fujikura shown in Figure 3.11 providing an ER of > 55 dB with

$$ER = \frac{P_x}{P_y} \quad . \quad (3.13)$$

At the same time the fiber length can be shortened to minimize the losses and for better polarization alignment. First a polarizer was spliced to the input fiber of the phase shifter. After this step, still elliptical polarization was observed to a level larger than the specified ER of the polarizer ≥ 26 dB would imply, which means there are internal misalignments within the phase-shifter component itself.

I therefore also spliced a fiber polarizer to the output fiber to at least project the elliptical polarization induced by the phase shifter back to a linear state for further propagation. In this way, the polarization effects are transformed to intensity modulations in the phase-shifter arm, which can be included in the modeling of the calibration procedure. The calibration routine is based on linearly scanning through a voltage range covering a full wave and was established in the master thesis Lippa (2012). This method of a linear scan should briefly be summarized in the following as basis for the advanced phase-step insensitive calibration developed in this thesis work.



Figure 3.11: Fusion splicer from the company Fujikura: the device is shown in the middle with its lid open surrounded by three close-ups, namely of the two displays showing the result of a successful splice as well as of the electrodes which perform the fusion splice in between the two fiber holders with open lids where the fibers are inserted. In the close-ups the left display shows the camera inspection of the spliced fiber as seen from the perpendicular x and y view, while the right display shows the parameters describing the quality of the splice estimated by the device starting with the angle of alignment and the corresponding extinction ratio.

Linear scan

For the phase shifts in the metrology system the aim was an accuracy of roughly 1 nm for determining internal dOPDs in the GRAVITY interferometer. In order to establish the relation between voltages applied to the phase shifter and the resulting phases on this level I build an interferometric setup in the laboratory schematically shown in Figure 3.12 (Lippa et al., 2014).

Laboratory Measurements The illustration also plots the linear voltage ramp from 0 V to 10 V applied by a function generator to scan a full fringe detected as voltage by a metrology receiver. The split and combination of beams is performed by fiber splitters. The

phase shifter is spliced to polarizers on both sides and the parallel arm is also equipped with such a fiber polarizer. In front of these components, I installed beam shutters in both arms to be able to measure the intensity of each arm separately to calibrate the contrast modulation mentioned above. In addition, both shutters can be closed for a measurement of an intrinsic signal offset and the noise level. This setup is fed by the metrology laser and the input and output voltages are measured by an oscilloscope.

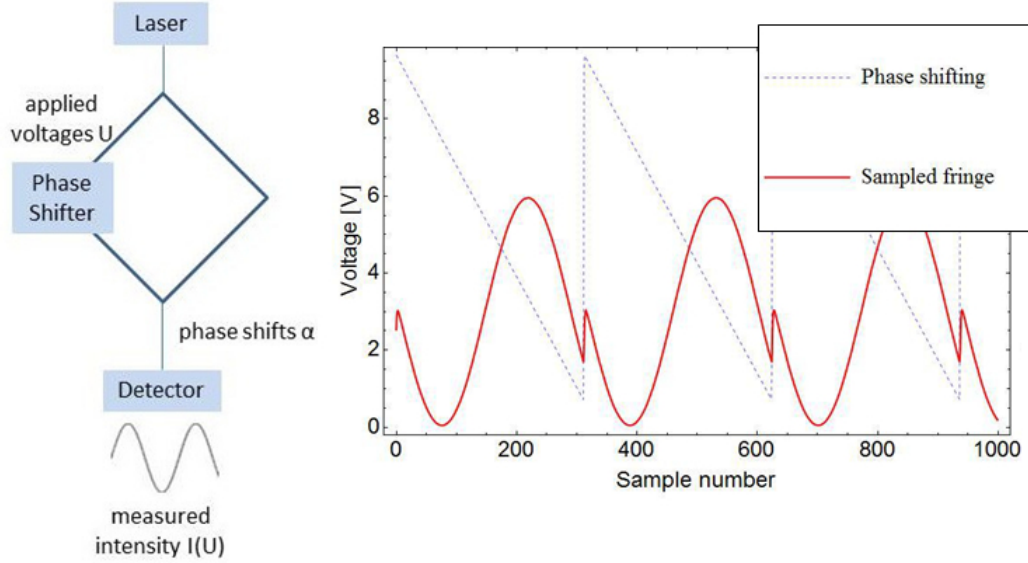


Figure 3.12: Calibration of the phase shifter by a linear scan with the schematic setup on the left and the measured voltages on the right adapted from Lippa et al. (2014). The laser is split into two beams of which one is phase-shifted by a linear scan through the voltages U corresponding to more than a full wave and applied to the phase shifter. By that, the fringe intensity distribution $I(U)$ can be measured at the detector in the beam combination including the relation of interest, namely phase shifts $\alpha(U)$ depending on the applied voltage U .

The scans are repeated a few hundred times at a maximum rate of 500 Hz which guarantees proper response of the detector. The averaged intensity distribution I of the measured fringes is best fitted by the following function relating I to the voltage U which sets the phase shift α :

$$I(U) = \xi + I_1 + I_2(U) + 2\nu\sqrt{I_1 I_2(U)} \sin(\Phi + \alpha(U)) \quad . \quad (3.14)$$

The individual intensities of the interfering beams I_1 and $I_2(U)$ are measured by closing one of the beam shutters, respectively. The modulated beam shows a dependence of transmission on the applied voltage due to the birefringence of the phase shifter as described previously. Nevertheless, an additional contrast-adjusting fit parameter ν needs to be included for the fit as well as the bias parameter ξ .

The quantity of interest in this calibration scheme is the response of the phase shifter $\alpha(U)$. In the fitting a non-linear function, namely a polynomial of 4th order, describes the measured data the best. This description allows to extract the three voltages to shift the metrology fringes by steps of $0, \pi/2, \pi$ and $3\pi/2$ for the ABCD method. With this calibration routine I was able to determine the phase shifts with an accuracy of 2 nm.

Limitations However, the non-linear phase-voltage relation and other environmental effects when calibrating by linear scans require a rather complicated routine for the use in GRAVITY and in the end limit the accuracy of the calibrated phase steps. The limiting factors are:

- The phase shifts α resulting from the applied voltages U follow a non-linear relation.
- During the calibration measurements the fringes drift with 0.2 nm per full wave due to temperature fluctuations, which let the fiber lengths vary and by that the fringe phase.
- Vibrations as found in the Fourier analysis of the data also affect the calibration precision.
- Fluctuations of the laser power by a few percent influence the calibration at frequencies from 0 Hz to 50 Hz.
- Contrast variation of the measured fringes is generated by polarization misalignments in the birefringent phase shifter.
- The phase shifter has a transmission function depending on the input voltage and therefore showing a peak-to-peak modulation of around 10^{-3} with respect to the average signal displayed in Figure 3.13 and leading to a fringe contrast modulation of order 10^{-2} . A likely origin of this variation is low-finesse Fabry-Perot interference of Fresnel reflections in the phase shifter.

Considering this variety of effects that enter the calibration two main concerns arose:

- Is the applied model of the measured intensity distribution $I(U)$ and the phase relation $\alpha(U)$ an adequate description for well-calibrated phase shifts within the specifications?
- Can the four ABCD phase values extracted in the calibration really be attributed to shifts of $0, \pi/2, \pi$ and $3\pi/2$ as they are not determined instantaneously but in a linear scan across many more values in the presence of environmental instabilities and laser power fluctuations?

On this basis I investigated the possibility of an alternative calibration method less influenced by the found non-linearities in this work. In the following I discuss the developed algorithm, which is phase-step insensitive.

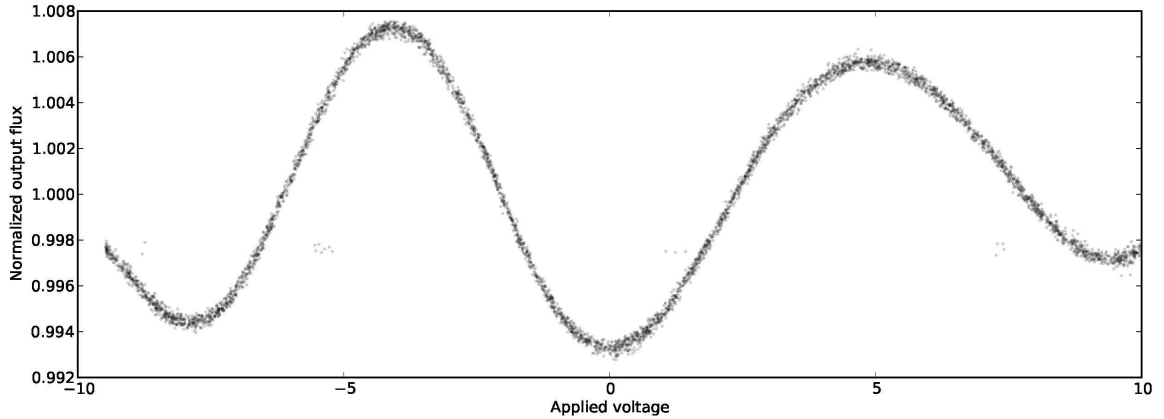


Figure 3.13: Transmission modulation of the phase shifter measured in a purely photometric setup of one beam without any beam combination involved, from Lippa et al. (2014). Voltages between -10 V and +10 V were applied.

Phase-Step Insensitive Algorithm

In order to make the calibration routine for the phase shifter less affected by the environmental effects explained above, an approach is followed in which the required ABCD phase shifts are applied instantaneously one after another instead of using a linear scan through the entire phase shift range. In this way, a fixed correlation is conserved between the phase steps in a quasi-static environment where the observed fringe drift becomes negligible.

In a setup as drawn schematically in Figure 3.14 the ABCD shifts are constantly repeated on the phase shifter to be calibrated, while another phase-shifting component in the parallel beam serves as delay line scanning the fringes through a full wave, either randomly or by some function, for instance by a linear scan. Scanning linearly has the advantage that this function can also be used to measure and include the transmission variation of the phase shifter in the calibration routine. For each shift in the delay line, one cycle of ABCD values is applied. The delay-line phase shifter also is spliced to linear fiber polarizers on both ends.

Since the ABCD shifts α_i are applied subsequently faster than environmental disturbances at a fast kilohertz-rate, their correlation remains independently of the environment and the current delay line phase. The measured quantities in this approach are the four intensity distributions I_i with $i \in \{A, B, C, D\}$ as a function of the delay line phase β :

$$I_i(\beta) = a_i + b_i \sin(\beta + \alpha_i) \quad (3.15)$$

with a_i corresponding to the intensity offsets and b_i to the amplitudes of the intensity modulation.

This set of four functions correspond to Cartesian coordinates of an ellipse in its parametric form. In this respect, couples of these intensity distributions, I_i and I_j can be plotted versus each other resulting in elliptic graphs with shapes depending on different parameters in the experiment such as flux and phase shift $\Delta_{ij} = \alpha_i - \alpha_j$.

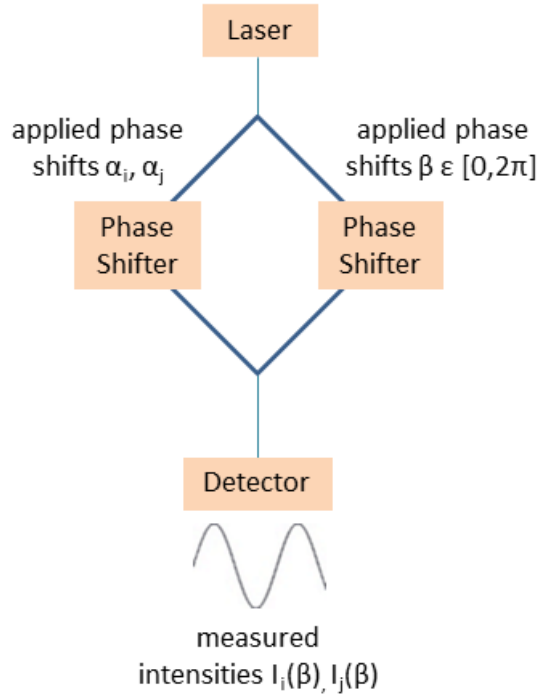


Figure 3.14: Schematic setup for the phase-step insensitive calibration of the phase shifter from Lippa et al. (2014): two phase shifters are implemented into both beams of the interferometric scheme. One device is calibrated for the phase step from i to j , while the other serves as delay line that continuously induces random phase shifts β at a slow rate. For every β a controlled phase step $|\alpha_i - \alpha_j|$ is performed by the other phase shifter through the applied voltages U_i and U_j . This induced phase step can be calibrated by the measurement of the corresponding intensities I_i and I_j as a function of β .

Ellipse Fitting Fitting of these data can be performed by the ellipse equation in Cartesian coordinates:

$$EI_i^2 + FI_iI_j + GI_j^2 + HI_i + KI_j + L = 0 \quad . \quad (3.16)$$

In this description, the coefficients (E, F, G, H, K, L) can be used to calculate the phase step Δ_{ij} by (Farrell & Player, 1994):

$$\Delta_{ij} = \arccos\left(\frac{-F}{\sqrt{4EG}}\right) \quad (3.17)$$

with

$$\kappa = (a_i b_j)^2 + (a_j b_i)^2 - 2a_i b_i a_j b_j \cos(\Delta_{ij}) - b_i^2 b_j^2 \sin^2(\Delta_{ij}) \quad (3.18)$$

$$E = \frac{b_j^2}{\kappa} \quad (3.19)$$

$$F = \frac{-2b_i b_j \cos(\Delta_{ij})}{\kappa} \quad (3.20)$$

$$G = \frac{b_i^2}{\kappa} \quad (3.21)$$

$$H = \frac{2(a_j b_i b_j \cos(\Delta_{ij}) - a_i b_j^2)}{\kappa} \quad (3.22)$$

$$K = \frac{2(a_i b_i b_j \cos(\Delta_{ij}) - a_j b_i^2)}{\kappa} \quad (3.23)$$

$$L = 1 \quad , \quad (3.24)$$

where L is fixed to be 1. This constraint is put such that (3.16) is fulfilled in a χ^2 -minimization run to determine the parameters a_i , a_j , b_i , b_j and Δ_{ij} other than by the coefficients shrinking to zero.

Alternatively, direct analytical methods can be used to fit the coefficients as by Fitzgibbon et al. (1996), but the drawbacks are:

- The computation of the parameters requires a complex inversion process.
- Any flux, transmission or contrast variation during the fringe scan can lead to a calibration result biased by up to several degrees in phase.
- The success rate and stability as shown in simulations and experiments are only moderate compared to a standard χ^2 -minimization.

After comparing different solutions from literature in theory and simulation, such as the direct analytical approaches or the matrix inversion by Halir & Flusser (1998), the χ^2 fitting is implemented for the calibration of phase shifts as the most suitable and robust one.

Laboratory Measurements Since the modulation of a full wave for the metrology wavelength is realized with the Pholine phase shifter by applying approximately 8 V, the initial ABCD values are chosen to be $\{0 \text{ V}, 2 \text{ V}, 4 \text{ V}, 6 \text{ V}\}$ as first approximation of the phase values $0, \pi/2, \pi$ and $3\pi/2$. As the formula (3.5) can be generalized for metrology phase shifts α_i deviating from the nominal values $0, \pi/2, \pi$ and $3\pi/2$ for example as in Sahlmann et al. (2009), this basic approach does not necessarily need to be changed. On this basis, the phase shifts Δ_{AB} , Δ_{BC} and Δ_{CD} are measured applying the suggested formalism.

Linear voltage ramps of 1000 phase steps each by 4 nm are applied to the delay line. For every delay-line step the ABCD modulation is applied with different frequencies in the

range between 0.5 kHz and 1.5 kHz. Measurements were taken at different dates during a few months without specific control of the environment.

Using a 2x2 splitter for the beam combination allows to record two signals simultaneously for comparison. In order to operate the receivers at similar signal levels as in GRAVITY and to minimize variations in path lengths from heating by high laser powers, the laser is operated at the minimum stable power output of ~ 200 mW and an additional fiber attenuator is inserted in front of the beam splitter.

For an optimized synchronization between the two voltages applied to the two phase shifters and the read out of the fringe signals measured by the receiver, I implemented all functions in a single data-acquisition device from National Instruments. I developed a sophisticated routine in LabVIEW, for commanding the signal processing of writing and reading as well as immediate visualization of the measured ellipses for quick judgement by eye on the data quality. LabVIEW is a software platform for visual programming provided by National Instruments well-matched to the offered hardware products. The setup with the different devices is shown in Figure 3.15.

Results The resulting error on the measured phase shifts typically is $\pm 0.2^\circ$ or ± 1 nm on each individual measurement series and between the series. As such, the phase-step insensitive algorithm is able to calibrate the ABCD phase steps on a 1 nm-level as required for the phase measurements by the GRAVITY metrology. Figure 3.16 shows the determined phase steps Δ_{AB} of one series of ten measurements together with one of the respective ellipse plots including the data fit and residuals. The ellipses show very low dispersion which is dominated by systematics. The tests delivered consistent results for both diode boxes, within the error of $\pm 0.2^\circ$.

Comparing this scheme to the previously tested one of linearly scanning, the achieved calibration precision is by a factor of two better. But the fundamental difference is that the extraction of the phase angles is performed unambiguously as the modeling of the interference fringes is not required. The latter relies on various complex effects acting on the measured intensity distribution beyond the theoretical simple two-beam interference. The direct comparison of both phase-shifter calibration methods, tested for the GRAVITY metrology concept, is summarized in Table 3.3. The phase steps determined with the previous method are offset by several degrees from the unambiguous measurements of the new concept. Obviously, the applied modeling of the linearly scanned fringe is not capable of properly extracting the actual phase information due to the limitations presented above.

Before I conclude on the calibration results, I discuss the limitations of this phase-step insensitive method, also in comparison to the previously developed scheme of linearly scanning through all possible phase shifts.

Limitations Regarding the limiting effects in the previous method of linear scans, only three out of five have an influence in the phase-step insensitive scheme, namely those involving flux or contrast changes. The other limitations do not apply anymore by design:

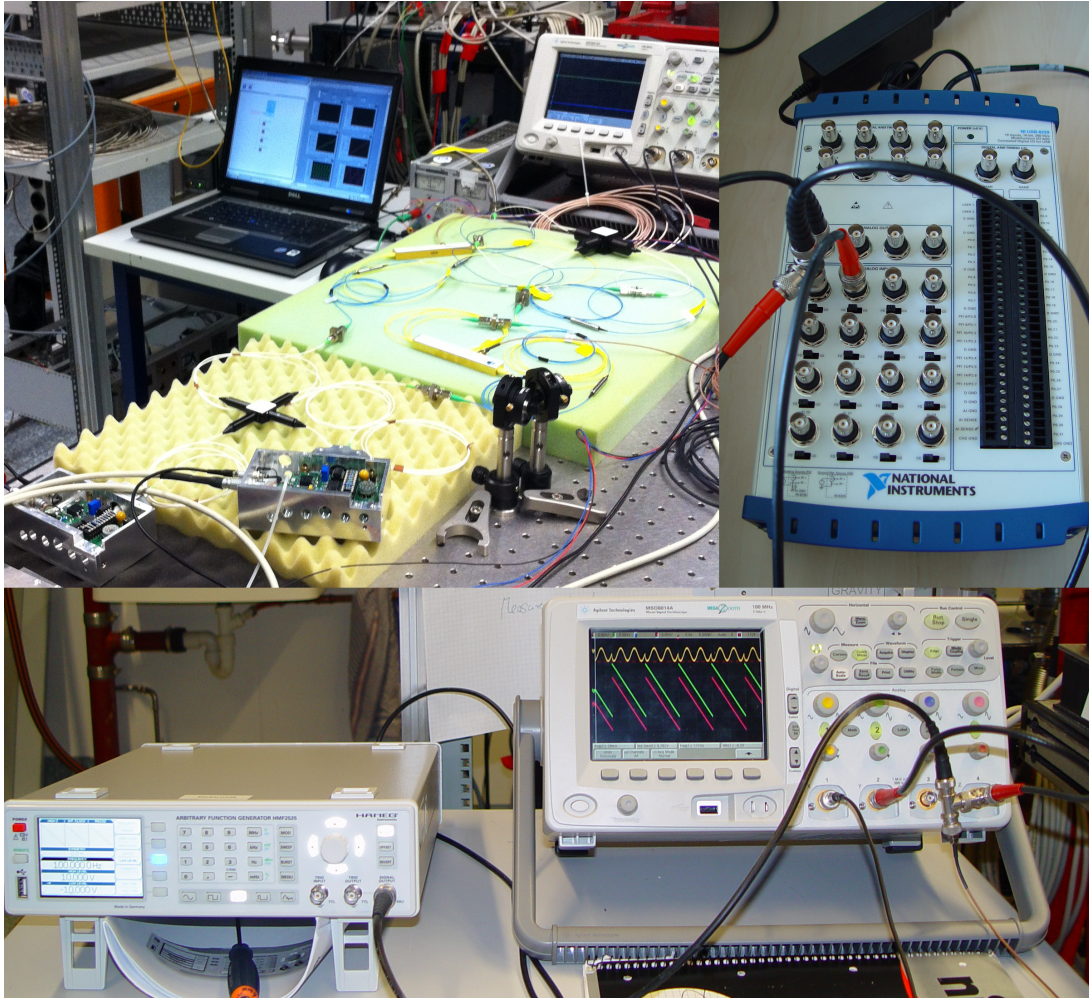


Figure 3.15: Laboratory setup for the phase-step insensitive calibration: the upper left shows the optical bench with the fiber chain fixed on foam material for minimizing vibrations and with a 2x2 beam combiner, the black cross, combining the two beams and feeding two metrology diode boxes as receivers. The laptop is used for controlling the measurements with a LabVIEW routine and the data acquisition device from National Instruments in the right picture for applying the phase-shift voltages and reading the signal voltages. The bottom picture shows the previous setup for these tasks, a function generator on the left and an oscilloscope on the right, which were replaced by the device from National Instruments for easier remote control and synchronization.

- No assumption about the detailed relation $\alpha(U)$ between phase shifts α and applied voltage U has to be made, which cannot be measured directly.
- The influence of environmental effects on the measurements is minimized by the applying the ABCD phase shifts to be calibrated subsequently at a rate close to 1 kHz, faster than what the temperature fluctuations and vibrations show.

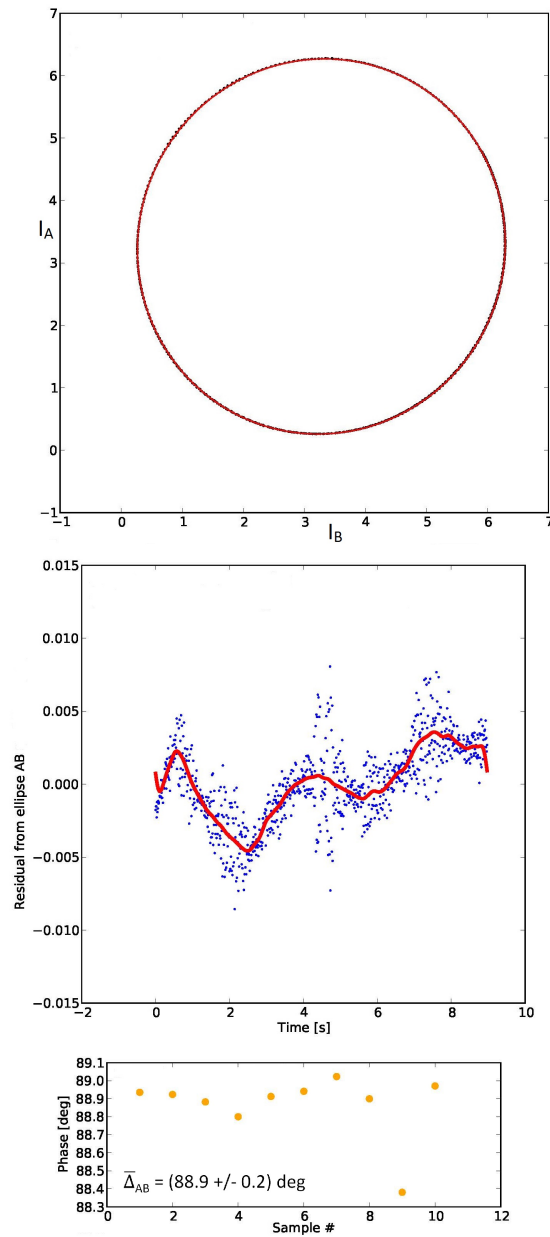


Figure 3.16: Measurements by the phase-step insensitive algorithm as shown in Lippa et al. (2014): the top shows an ellipse plot of the intensities I_A versus I_B for the phases A and B as a function of delay-line shifts measured by the receiver in units V acquired at a ABCD modulation of 700 Hz. In order to determine the phase step Δ_{AB} a fit using a χ^2 minimization is performed. Due to their small dispersion, the black data points are almost completely hidden by the red line of the fit. The middle panel shows the fit residuals relative to the data as a function of time. The bottom plot illustrates the determined phase step for a series of ten such measurements with a mean value of $\bar{\Delta}_{AB} = 88.9^\circ \pm 0.2^\circ$.

Results	Δ_{AB}	Δ_{BC}	Δ_{CD}
Applied voltage step	{0 V, 2 V}	{2 V, 4 V}	{4 V, 6 V}
Phase-step insensitive algorithm	$89.0^\circ \pm 0.2^\circ$	$89.2^\circ \pm 0.2^\circ$	$92.5^\circ \pm 0.2^\circ$
Linear scan	$87.0^\circ \pm 0.4^\circ$	$86.6^\circ \pm 0.4^\circ$	$87.1^\circ \pm 0.4^\circ$

Table 3.3: Calibration results of the phase-step insensitive algorithm compared to the linear scan. The phase-step insensitive method was used to measure the phase shifts Δ_{AB} , Δ_{BC} and Δ_{CD} in many series of measurements at different ABCD modulation frequencies and different dates during a time span of a few months. In voltage steps always +2 V were applied, resulting in different phase angles due to the non-linear behavior of the phase shifter. The linear scan clearly shows systematically different and less precise results probably by non-linearities in the phase shifting not being properly modeled. The phase-step insensitive method by design is less affected by those factors.

In addition, the setup was optimized to minimize vibrations by fixing the fibers and fiber components to foam material on the optical bench. The measurements show that in this stabilized setup, the dispersion of the data points from remaining vibrational perturbations average out and do not introduce a bias. The observed fringe drift typically is 0.1 nm/ms leading to values smaller than $0.3 \text{ nm} \simeq \lambda/6000$ during every individual ABCD cycle and therefore without significant influence on our measurement of the ABCD phase angles compared to the resulting calibration precision of $1 \text{ nm} \simeq \lambda/2000$.

Other than the factors above, the remaining limitations that influence the measurements can be tracked within the calibration routine of the phase shifter. These effects are the laser power fluctuations, the transmission function of the phase shifter versus applied voltage and the contrast variation by polarization changes. The contrast modulation of the interference fringes by polarization misalignments in the birefringent phase shifter is projected to transmission variations by the use of linear polarizers and therefore is translated in flux changes.

Flux Variations The laser fluctuations $P(t)$ with time t affect both beams and can be tracked by a Fourier transform of the interference signal measured during one delay-line scan:

$$I_A(t_1), I_B(t_2), I_C(t_3), I_D(t_4), I_A(t_5), I_B(t_6), I_C(t_7), \dots$$

In the obtained spectrum of frequencies, the laser fluctuations peak between 0 Hz and 50 Hz as mentioned previously. This approach will also capture the transmission variation of the delay-line (DL) phase shifter $T_{DL}(V(t))$ depending on the applied voltage V . The fringe model including both effects can be written as

$$I_i(t) = P(t) \left[a_i T_{DL}(V(t)) + b_i \sqrt{T_{DL}(V(t))} \sin(2\pi f t + \alpha_i) \right] \quad , \quad (3.25)$$

with $\beta = 2\pi f t$ where f corresponds to the modulation frequency of the delay line.

The transmission function can be modeled by

$$T_{DL}(V(t)) = T_0(1 + \nu \cos(2\pi f_1 t)) \quad , \quad (3.26)$$

with ν the modulation amplitude and T_0 as average transmission level including the normalization of the transmission function. As the delay line is used to scan through a voltage range of [-10 V, 10 V] with frequency f , the transmission modulation is twice as fast with $f_1 = 2f$. This was plotted in Figure 3.13, where for one full modulation of the DL, the transmission modulation shows roughly two full cycles. As the amplitude of the modulation is very small compared to the signal, $\nu \sim 10^{-3} \ll 1$, the Taylor series $\sqrt{1+x} = (1 + \frac{1}{2}x + \dots)$ can be applied:

$$\sqrt{T_{DL}(V(t))} \simeq \sqrt{T_0} \left[1 + \frac{\nu}{2} \cos(4\pi f t) \right] \quad . \quad (3.27)$$

Inserting this function $T_{DL}(V(t))$ to (3.25) and using the trigonometric identity

$$\cos \theta \cos \phi = \frac{\cos(\theta - \phi) + \cos(\theta + \phi)}{2} \quad , \quad (3.28)$$

the model becomes:

$$\begin{aligned} I_i(t) &\simeq P(t) T_0 \left[a_i + b_i \cos(2\pi f t + \alpha_i) + \nu \left(a_i + \frac{b_i}{2} \right) \cos(4\pi f t) \cos(2\pi f t + \alpha_i) \right] \\ &= P(t) T_0 \left[a_i + b_i \cos(2\pi f t + \alpha_i) + \frac{\nu}{2} \left(a_i + \frac{b_i}{2} \right) (\cos(2\pi 3f t + \alpha_i) + \cos(2\pi f t + \alpha_i)) \right] \quad . \end{aligned} \quad (3.29)$$

This relation demonstrates that including the transmission variation in the model creates an additional frequency of $3f$. As this frequency is higher than the one of the delay-line scans it will be captured in the Fourier analysis of the interference signals for each scan, as introduced previously for tracking the laser fluctuations $P(t)$. The according fringe model then can be written in the simplified form:

$$I_i(t) = P(t) [a_i + b_i \sin(\beta(t) + \alpha_i)] \quad . \quad (3.30)$$

In summary, the laser power fluctuations occur between 0 Hz and 50 Hz and the delay line scans by a full voltage range at $f \sim 1$ Hz in order to perform a few hundreds ABCD modulation at the phase shift to be calibrated with kilohertz-speed. Therefore, the transmission modulation with $f_1 = 2f$ occurs at a rate of ~ 2 Hz in the beam with the delay line.

After filtering out of the laser-power fluctuations and transmission modulation according to this model, no significant difference in the calibration results were found. Apparently, these limitations produce error well below the general level of uncertainties in the calibration routine.

Modulation Frequency Another method to improve the calibration method is to perform the ABCD modulation at a faster rate to further reduce the influence of instabilities in the setup and the environment. The real-time performance of the GRAVITY metrology requires kilohertz-measurements, which are also implemented in the calibration routine presented here with rates of order ~ 1 kHz for the ABCD modulation. Faster measurements are limited by the bandwidth of the metrology receivers.

As this bandwidth limitation of the receivers is a general one, which also applies to the metrology operation, the phase-shifter calibration should be performed under similar conditions, such that frequencies larger than ~ 1 kHz for the ABCD modulation are not investigated further at this point.

Cryostat Environment The presented results were achieved in a normal laboratory environment under normal air pressure and room temperature. The calibration within the GRAVITY instrument faces different conditions such as vacuum at 10^{-6} mbar cooled to 240 K, which might enable even higher precision if no severe vibrations occur. While the manufacturer of the phase shifter, Photline, confirmed the use down to 10^{-7} mbar, I performed calibration measurements at 240 K within a temperature test chamber in order to exclude reduced performance or even damage in a cold environment.

The setup withstood these tests without any damage, however, stronger vibrations from the chamber operation led to reduced calibration performance. A single small measurement series at 240 K, with the chamber switched off, delivered calibration results of $\Delta_{AB} = 89.0^\circ \pm 0.2^\circ$, $\Delta_{BC} = 89.3^\circ \pm 0.2^\circ$ and $\Delta_{CD} = 91.7^\circ \pm 0.8^\circ$. These results are consistent with the laboratory measurements. Only the CD step shows an offset and larger scatter. This was also observed in previous laboratory tests for individual measurement series and therefore is not of further concern for this quick validation of the general phase-shifter operation at low temperatures.

In summary, the calibration method developed here is not as sensitive to non-linearities within the phase shifter and the environmental drift as the simple scan of fringes. Instead, phases can be measured unambiguously on the basis of a robust fitting routine for ellipses, which is done by a χ^2 -minimization. The achieved calibration precision of 1 nm fulfills the specified requirement for 10 μs -level astrometry.

For the phase-shifter calibration in GRAVITY, the FDDLs can be used as delay lines. The FDDLs have the advantage that their transmission is independent of the phase shift. Before I could optimize and conclude on the calibration routine in GRAVITY, the original dual-beam scheme of the metrology system had to be transformed into an entirely new concept, which in the end did not rely anymore on a sophisticated, highly precise calibration of the phase shifter. The upgraded metrology scheme does not apply well-defined phase shifts to scan the fringes, but scans through the available phase-shift range with a characteristic frequency. A lock-in amplifier can be coupled to this frequency to extract the required phase difference between the science and fringe-tracker beam.

I outline this transition from a dual-beam to a three-beam concept in the next section, triggered by unexpected backscattering of the metrology light in the fluoride-glass fibers

of GRAVITY. This backscattering could be understood due to the analysis I performed as the second scope of this thesis work.

3.3 Three-Beam Scheme

During the integration of the GRAVITY beam combiner instrument at MPE end of 2013, the metrology system could be tested together with the other subsystems for the first time. In these tests the science detectors were severely overexposed by several orders of magnitude compared to the requirements. The origin of this polluting light is the metrology laser light, despite its wavelength outside the science band, which should be blocked by dedicated filters for this wavelength.

Two sources of contamination could be identified. On the one hand, diffuse stray light was observed. The blocking filters in the spectrometers were wrongly characterized during test measurements and blocked three orders of magnitude less than expected. But even after replacement of the filters, diffuse scattering was still observed from unexpected reflections of the metrology light in the spectrometers. As a result, the diffuse stray light on the detectors was a factor 10^4 larger than the requirement.

The more harmful backscattering came directly from the IO outputs, shining out the science light by a factor of $\geq 10^5$. This illumination at wavelengths up to $\approx 2.15 \mu\text{m}$ clearly was created by the backscattering of the metrology light by a component within GRAVITY. Since the scattered light measured on the detectors travels in reverse direction of the actual metrology path through the instrument, the term “backscattering” is used to denote this effect.

Figure 3.17 shows a detector image displaying the diffuse stray component and the backscattered light. The stray light in the end could be removed by a combination of better filters, improved shielding and the reduction of laser power with the three-beam concept. Therefore, the diffuse stray light is not further described in this work.

Dedicated experiments were necessary to trace the source of the backscattering. Measurements were performed with the metrology path interrupted at different locations within the chain of fluoride glass-fibers. The latter have several connections between the IOs and the FCUs. These experiments showed that the backscattering originates from the fluoride-glass fibers in the instrument.

As outlined next, I performed a dedicated analysis of the backscattering in those fibers, in order to mitigate this effect preventing the nominal GRAVITY observations. The new metrology concept for this mitigation is based on three beams instead of two.

3.3.1 Raman Scattering and Fluorescence in Optical Fibers

Optical fibers are commonly used in communication industry and increasingly more in astronomical instrumentation. The reason are the many advantages of fiber solutions such as high throughput, polarization control and compactness. However, the fibers also come

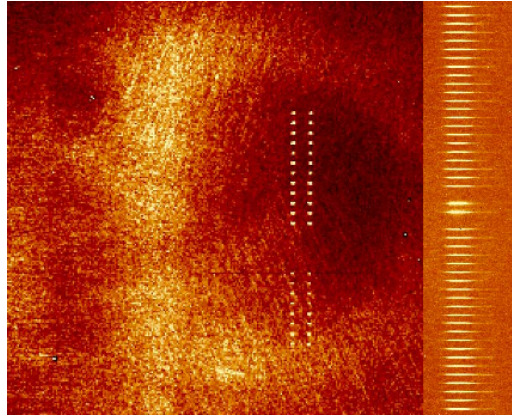


Figure 3.17: Backscattering of the metrology light on the science detectors. The left image from the fringe-tracking detector shows the backscattering as measured for 20 of 24 IO outputs. Also diffuse straylight is visible, originating from scattering of the metrology light in the spectrometers. The image on the right was recorded with the science detector in medium spectral resolution showing the K-band spectrum of the backscattering in 46 of the 48 channels, for polarization-splitting of the 24 IO channels, and the stray light in the background.

with certain weaknesses. Some of them were encountered during the GRAVITY project, as will be summarized in Lippa et al. (2018).

For the metrology system, which is largely based on fibers and fiber components, the challenges were high power levels inducing variations in temperature and by that also in path lengths corrupting the phase measurements. The phase-shifter calibration also showed problems within the polarization control despite the use of dedicated PM components. The most severe limitation, however, came from the fluoride-glass fibers used in the GRAVITY instrument, producing backscattering of the high-power metrology light. These fluoride-glass fibers were produced by LVF and are implemented for spatial filtering of atmospheric wavefront distortions.

One well-known origin of non-linear optical effects within fibers is Raman scattering. The comparison of the theory behind this effect and the actual observations in the GRAVITY context is described in the following.

Raman Scattering

Raman emission is inelastic scattering that originates from the interaction between condensed matter and photons. The effect can be described in the quantum interpretation by scattering of the photons with the quasi-particles called "phonons". The effect was predicted by Smekal (1923) and first observed in liquids by Raman (1928); Raman & Krishnan (1928) as well as in crystals by Landsberg & Mandelstam (1928). Due to this discovery Raman was awarded the Nobel Prize of 1930 (Nobel Media, 2018).

In the classical wave description, the Raman effect is linked to the interaction of an

electric field to vibrational transitions within molecules (Nakamoto, 2008; Singh et al., 2007; Boyd, 2008). When monochromatic light of the frequency ν interacts with molecular vibrations, the oscillating electric field acts on the vibrational displacement and hence on the polarizability of the molecules, resulting in an oscillating dipole emitting radiation. A short mathematical derivation is summarized in the following.

Classical Model A vibrational mode of a simple diatomic molecule can be treated as a harmonic oscillator of reduced mass μ inducing the displacement q with time t described by a force F :

$$F = \mu \frac{d^2q}{dt^2} \quad . \quad (3.31)$$

This model serves as a first approximation, but can be easily adapted towards a damped harmonic system. A solution for the harmonic oscillator equation is given by

$$q(t) = q_0 \cos(2\pi\nu_i t) \quad (3.32)$$

with amplitude q_0 and vibrational frequency ν_i .

Then, the polarizability can be approximated by a Taylor series for small displacement amplitudes around the equilibrium displacement $q = 0$ as

$$\alpha(t) = \alpha_0 + \left. \frac{\partial\alpha}{\partial q} \right|_{q=0} q(t) \quad , \quad (3.33)$$

where α_0 corresponds to the polarizability of the molecule in equilibrium displacement.

The induced dipole moment p is given by the product of this polarizability in (3.33) with (3.32) and the electric field $E(t) = E_0 \cos(2\pi\nu t)$ of the radiation:

$$p(t) = \alpha E(t) \quad (3.34)$$

$$= \left(\alpha_0 + \left. \frac{\partial\alpha}{\partial q} \right|_{q=0} q_0 \cos(2\pi\nu_i t) \right) E_0 \cos(2\pi\nu t) \quad (3.35)$$

$$= \alpha_0 E_0 \cos(2\pi\nu t) + q_0 \cos(2\pi\nu_i t) E_0 \cos(2\pi\nu t) \left. \frac{\partial\alpha}{\partial q} \right|_{q=0} \quad . \quad (3.36)$$

With the trigonometric identity (3.28), the oscillation of the second term in this dipole can be written as

$$\cos(2\pi\nu_i t) \cos(2\pi\nu t) = \cos(2\pi(\nu - \nu_i)t) + \cos(2\pi(\nu + \nu_i)t). \quad (3.37)$$

Thus, the dipole oscillates and emits radiation at three frequencies. The resulting elastic scattering at the intrinsic frequency ν is known as Rayleigh effect. In the case that coupling to an excited state takes place, the much weaker inelastic Raman scattering results in frequencies $\nu \pm \nu_i$, with ν_i the vibrational frequency corresponding to the difference between

the intrinsic energy state and the coupled one. As can be seen in (3.36), the selection rule for the Raman shift is

$$\left. \frac{\partial \alpha}{\partial q} \right|_{q=0} \neq 0 \quad (3.38)$$

meaning the polarizability needs to change with the displacements for the Raman scattering to take place.

One of 10^6 photons of incident radiation passing 1 cm of the material typically is scattered in the Stokes mode in spontaneous Raman scattering for small and moderate laser powers. Intense laser radiation can induce a stimulated process, in which the vibration at ν_i is reinforced by the beating of the laser frequency ν with the frequency $\nu - \nu_i$ of the scattered field. The stronger vibration then stimulates even stronger Raman scattering.

At $\nu_S = \nu - \nu_i$ the so called Stokes line appears, while $\nu_a = \nu + \nu_i$ corresponds to the anti-Stokes mode as illustrated in Figure 3.18 in the quantum interpretation, where the molecules are excited to a virtual energy state. The involved vibrational energy states can be described by phonons.

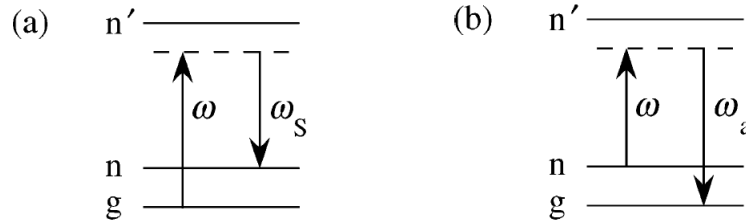


Figure 3.18: Energy transitions of Raman scattering from Boyd (2008). Panel (a) displays the Stokes mode, where light of the frequency ω excites the ground state of a molecule g to a higher level n . The scattered light has a reduced frequency ω_S going via a virtual intermediate energy level n' . Panel (b) shows the weaker anti-Stokes process from the level n down to the ground state g such that the light scattered has an increased frequency of ω_a compared to the incoming light.

For thermal equilibrium, the energy states are populated following the Maxwell-Boltzmann distribution, such that lower states are more populated. Therefore, the Stokes component usually is stronger than the anti-Stokes. For the Stokes scattering, the initial state uses a fraction of the incoming photon energy to populate a higher level while scattering a photon with reduced energy E and therefore reduced frequency $\nu_S = \nu - \nu_i$:

$$E = h \nu_s \quad (3.39)$$

As a consequence, Raman scattering results in a spectrum with two peaks at a distance of $\pm \nu_i$ from the exciting frequency ν with different peak intensities due to different populations of the involved states. The distance depends on the material and its characteristics. Due to these intrinsic properties varying within the material, for instance by interactions, the

scattering process does not necessarily result in a sharp line of a single frequency but can be a broader band around this central frequency (Singh et al., 2007).

With this theoretical background of Raman scattering in mind, the Raman spectrum as measured in the GRAVITY cryostat is discussed next.

Measurement in GRAVITY In the GRAVITY instrument the Stokes mode of Raman scattering is observed in the K-band, as the laser wavelength lies below this band and therefore showing a higher frequency or energy than the ones measured in the K-band. Thus, the stronger one of the two Raman modes is observed in this case.

Figure 3.19 shows the measured backscattering spectrum after the implementation of a K-short filter instead of the original K-band filter in order to suppress a dominant fraction of the backscattering at the lower wavelengths of the K-band.

This new filter was a first strategy tested in order to mitigate the backscattering in GRAVITY. The drawback of this adaption would be two-fold, as the scientific band would be narrower than on what the science cases of GRAVITY had been built on. On the other hand not all of the backscattering can be removed from the detector as can be seen in Figure 3.19.

The resulting backscattering spectrum in the K-short band displays a small peak at the wavelength $\lambda_S = 2150$ nm, which can be identified as Raman scattering of the laser line $\lambda = 1908$ nm. The comparison to respective literature studies of fluoride glass materials confirm that the observed wavenumber of the Raman shift, $\tilde{\nu}_i \approx 590$ cm⁻¹, is typical for Raman scattering within such samples. In spectroscopy the wavenumber $\tilde{\nu}_i$ is defined with respect to frequency ν , wavelength λ and speed of light c :

$$\tilde{\nu}_i = \tilde{\nu} - \tilde{\nu}_S \quad (3.40)$$

$$= \frac{\nu}{c} - \frac{\nu_S}{c} \quad (3.41)$$

$$= \frac{1}{\lambda} - \frac{1}{\lambda_S} \quad (3.42)$$

The characterization of the Raman shift by a wavenumber allows for the direct and easy comparison between studies performed at different laser wavelengths as in Figure 3.20. All of them show a dominating Raman peak at wavenumbers very similar to $\tilde{\nu}_i \approx 590$ cm⁻¹ for fluoride-glass fibers, independent of the detailed chemical compositions (Fortin et al., 2011; Agger et al., 2012; Yan et al., 2012; Saissy et al., 1985; Durteste et al., 1985).

This comparison to literature also shows that the dominant fraction of the backscattering measured in GRAVITY is not explained by the Raman scattering in fluoride-glass fibers. Therefore, at least two different effects cause the observed backscattering. This explanation also is supported by the Raman peak strength being polarization dependent while the other part of the spectrum does not depend on the polarization.

For the analysis and identification of the other part of the backscattering spectrum, further tests were necessary to find the origin in fluorescence from Rare-Earth Elements (REEs).

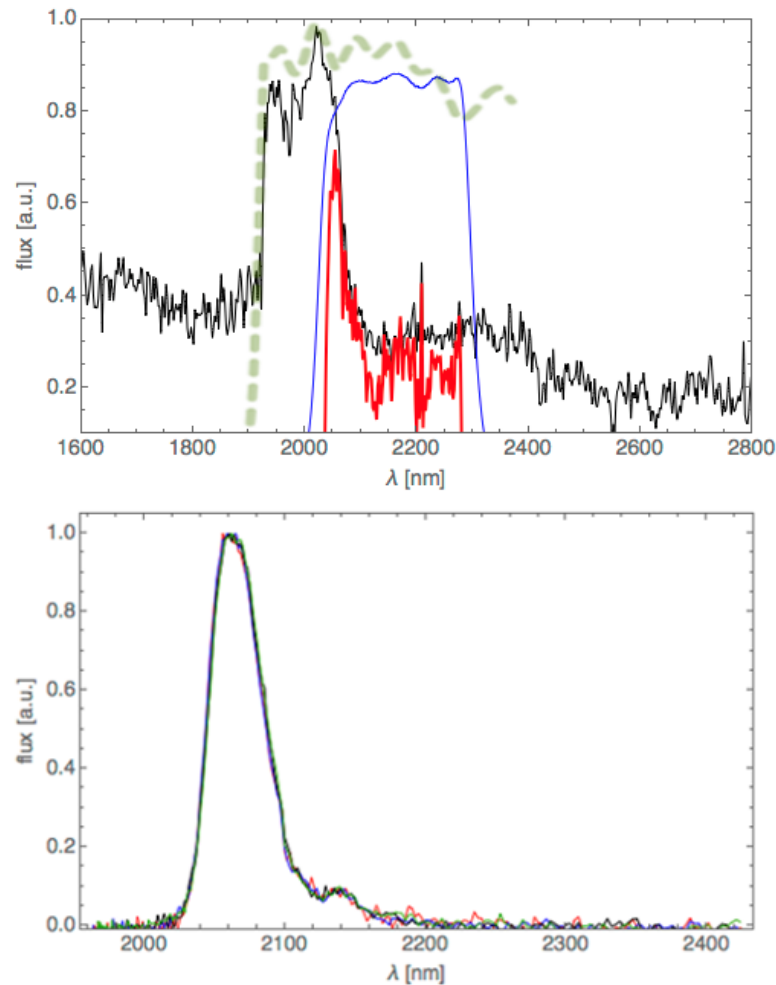


Figure 3.19: Backscattering spectrum measured in the GRAVITY cryostat with the flux in arbitrary units (a.u.) against the wavelength λ : the upper plot shows the full K-band spectrum (black) together with the bandpass of the K-band filter and two blocking filters (green, dashed). The transmission curve of the K-short filter is shown as blue line. The product of the spectrum and the K-short is visualized in red showing that K-short filters in the spectrometers could block a fraction of the backscattering. But more importantly, still backscattering photons remain, creating too high fluxes by several orders of magnitude. This implementation unfortunately also reduces the bandpass of the science light. The lower plot shows the resulting backscattering spectrum with two peaks, where only the lower one around 2150 nm can be attributed to Raman scattering.

Fluorescence from Holmium

Performing more detailed tests with the GRAVITY instrument itself to identify the physical processes behind the scattering in the cryostat, like varying the fiber length, would have been very time-intensive. Cooling down and warming up the instrument takes several

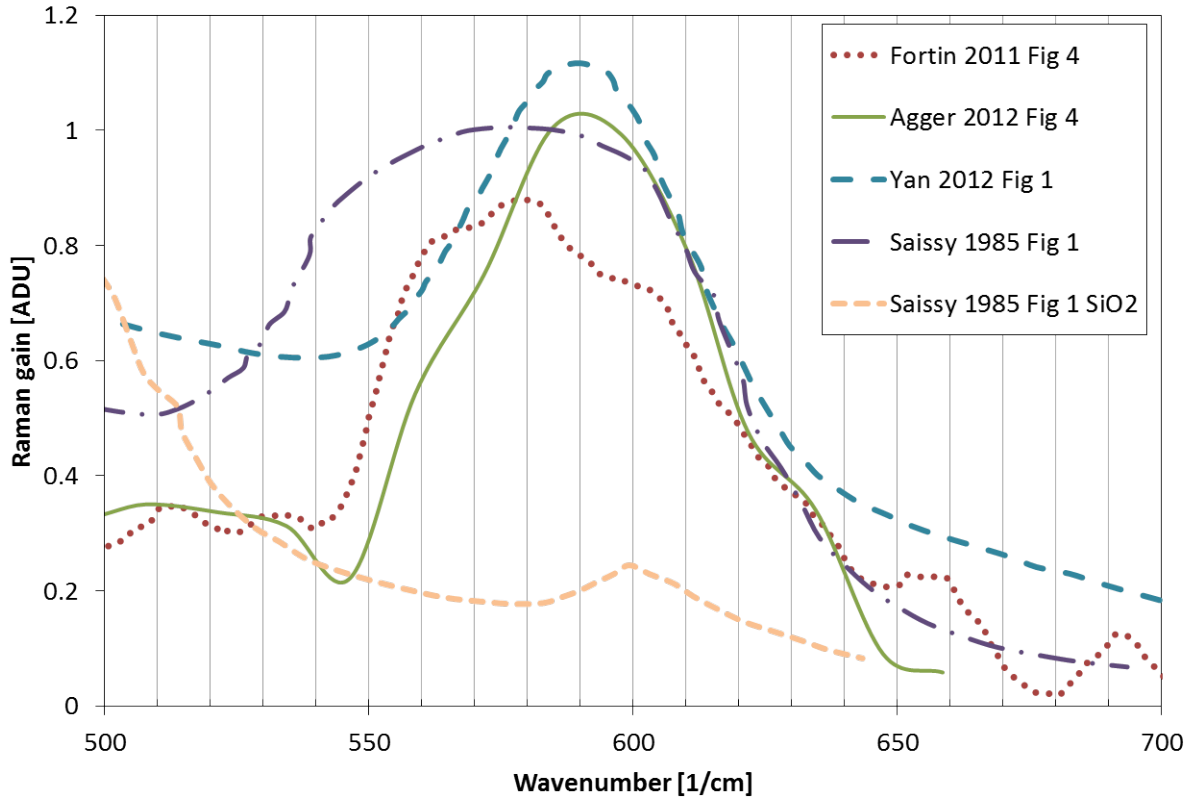


Figure 3.20: Raman spectra in fluoride-glass fibers from literature (Fortin et al., 2011; Agger et al., 2012; Yan et al., 2012; Saissy et al., 1985). The Raman gains of the studies are displayed in arbitrary detector units (ADU) as they are scaled to each other for comparison. Fluoride-glass fibers of different chemical compositions show a main Raman shift with wavenumber $\tilde{\nu}_i \approx 580 \text{ cm}^{-1}$ or $\tilde{\nu}_i \approx 590 \text{ cm}^{-1}$. The results of Saissy et al. (1985) also include the spectrum for a silica fiber (SiO_2), the same material as the metrology fibers are composed of. The metrology fibers do not cause the observed Raman scattering.

days. In addition, such tests would limit the access to the instrument for testing the other subsystems. Under these circumstances I built a mock-up setup in the laboratory that would allow for tests in a GRAVITY-like configuration but independent of the actual instrument.

Laboratory Measurements The mock-up consists of a GRAVITY-like configuration with the elements relevant for the backscattering. These parts include a metrology injection, a spectrometer and fluoride-glass fibers. The spectrometer setup was provided by the consortium institute IPAG in Grenoble as has been used there for the assembly and testing of the IOs. Similarly, test fluoride fibers and a proto-type FDDL were made available by the consortium partner Observatoire de Paris. Complementary to these components I built a metrology injection. The complete setup is drawn schematically in Figure 3.21 including

photographs of the spectrograph, the setup on the optical bench and the detector image.

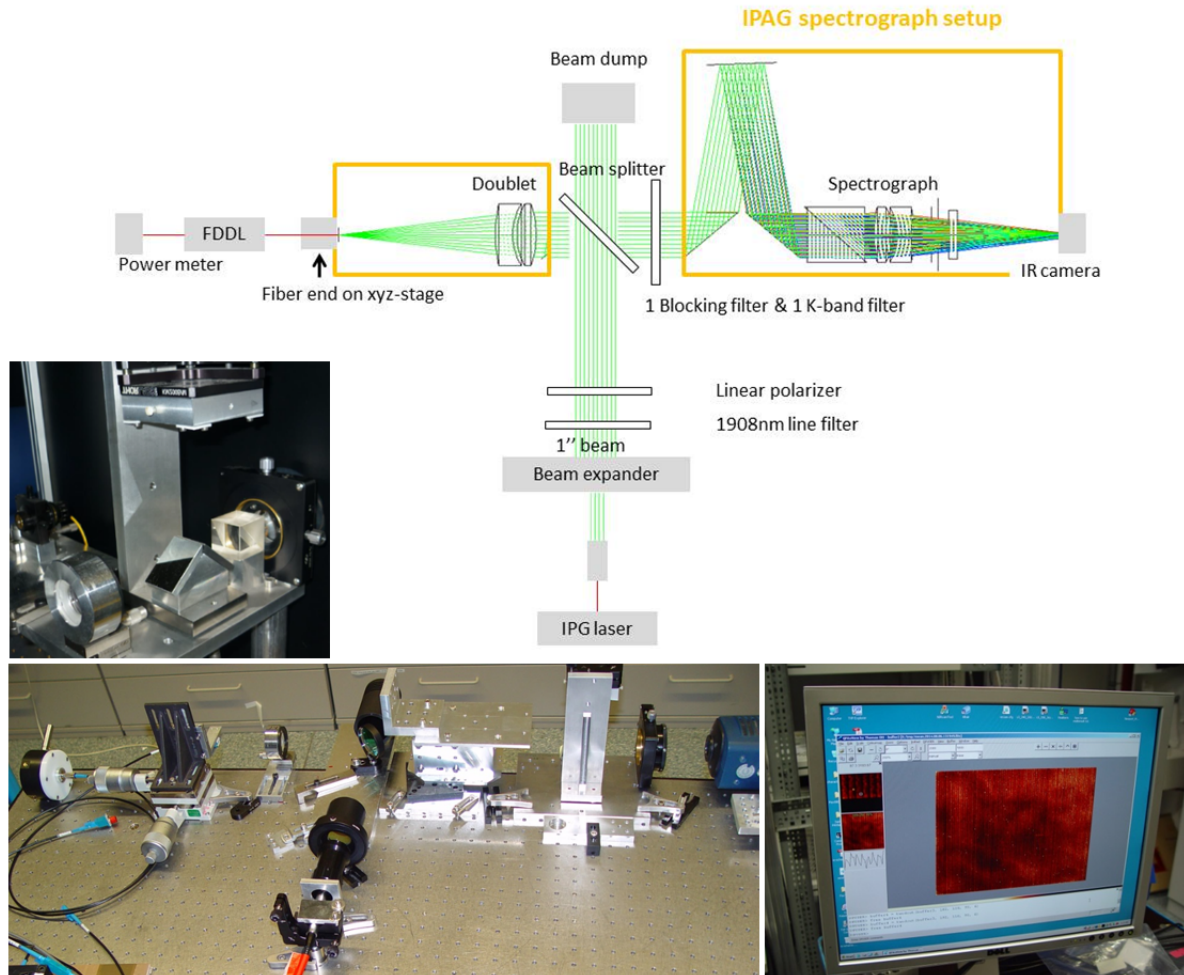


Figure 3.21: Laboratory setup for the analysis of the main backscattering component based on the GRAVITY configuration: the schematic drawing shows the metrology laser injection on the bottom, the coupling to fluoride-glass fibers via a beam splitter on the left and the spectral analysis of the backscattering from the fibers by the spectrograph from the consortium institute IPAG on the right. The photographs display the IPAG spectrograph, the setup on the optical bench and a detector image on the screen of the computer connected to the IR camera.

Setup The 1908 nm-laser light is injected on the bottom via the laser fiber and a collimator. The collimated beam is expanded to an 1-inch diameter in order to match the dimensions of the spectrograph, which are optimized for coupling to the mode-field diameter of the fluoride-glass fibers. Furthermore, a laser line filter is included to suppress

the broad background emission of the laser caused by asynchronous spontaneous emission. A linear polarizer is used to inject a defined polarization, for characterizing the polarization properties of the backscattering.

A beam splitter, at a 45° -angle to the optical axis, then reflects the laser light in the direction of the fluoride-glass fibers. A doublet lens focuses the laser light onto the fiber input mounted to a adjustable xyz-stage. A power meter is used to optimize the coupling. A proto-type FDDL can be connected in between the fiber and the power meter to increase the fiber length.

The backscattering from this fiber is transmitted by the beam splitter and passes a blocking and K-band filter to block the laser line. The spectral dispersion of the backscattering is performed by a grism. The squared block is a Wollaston prism for polarization analysis of the IPAG setup, but is not used. Another doublet lens focuses the light onto an IR camera. In between the doublet and the camera a linear polarizer can be inserted and rotated in order to analyze the polarization of the backscattering.

For the calibration of the wavelength scale I used a blackbody source and the filter bands known from the characterization for GRAVITY. I recorded separate blackbody spectra with only the K-band or blocking filter. The lower cut-offs of the filters and two further characteristic spectral features in the K-band filter were used to fit a linear function of wavelength versus detector pixel as plotted in Figure 3.22.

Results With two fiber patch cords and two proto-type FDDLs manufactured by LVF, I could test different fluoride fiber lengths ranging from 2 m to 16 m. For comparison, in GRAVITY four fiber chains of 20 m-length are implemented. So the laboratory setup allows to measure similar or shorter lengths. The backscattering has a lower cut-off at 1920 nm given by the blocking filter.

The main results of the performed measurements are summarized in the plots of Figure 3.23. The backscattering spectrum as known from the GRAVITY beam combiner instrument could be easily reproduced in the laboratory. The backscattering clearly scales with the fiber length and laser power also in the Raman peak, while the polarization analysis shows that the Raman peak is clearly polarized. No influence on the shape of the backscattering spectrum is found for varying the fiber positions, laser beam apertures, laser polarization and for the stretching of the FDDL.

The fiber position and laser aperture were varied in order to test whether the backscattering shape or strength depends on the coupling to the fiber. Similarly the variation of the backscattering strength with fiber length can be measured. If the backscattering originates from the fiber cores, its strength should decrease when decentering the core. In that case the backscattering flux should also vary with fiber length. The latter property is analyzed in Figure 3.24 and shows the entire backscattering spectrum scales similarly with fiber length.

All backscattering components also vary with fiber position and laser aperture. The spectrum being independent from these coupling properties as well as the flux variation with fiber length could exclude that the origin of the backscattering is linked to the fiber

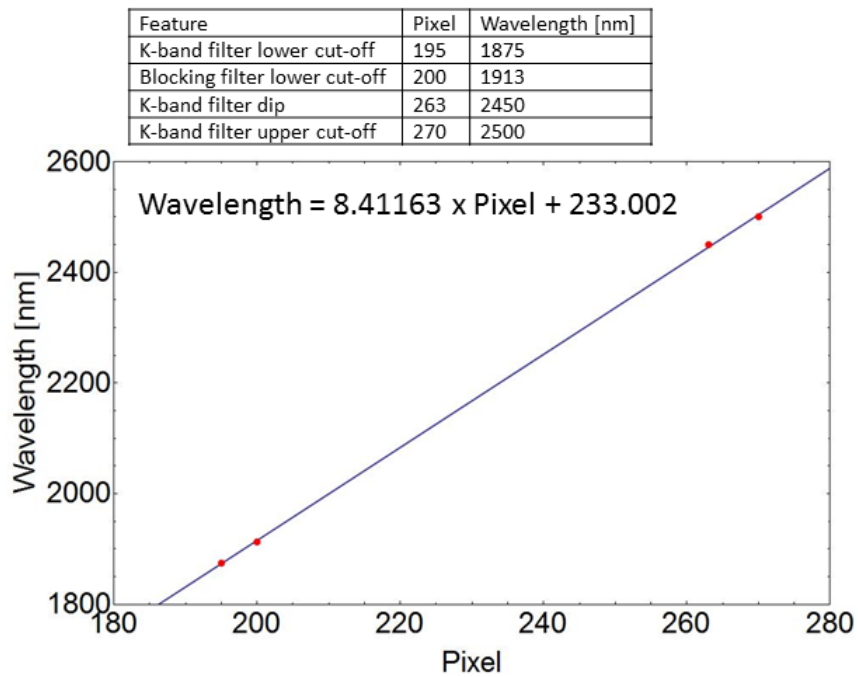


Figure 3.22: Wavelength calibration for measuring the backscattering spectrum in the laboratory: a blackbody spectrum was injected to the fluoride-glass fiber and measured with the backscattering setup separately with only the blocking filter or the K-band filter. Prominent features of the filter curves as known from their characterization for GRAVITY are used to link the detector pixels to the wavelength of the measured spectra by a linear fit.

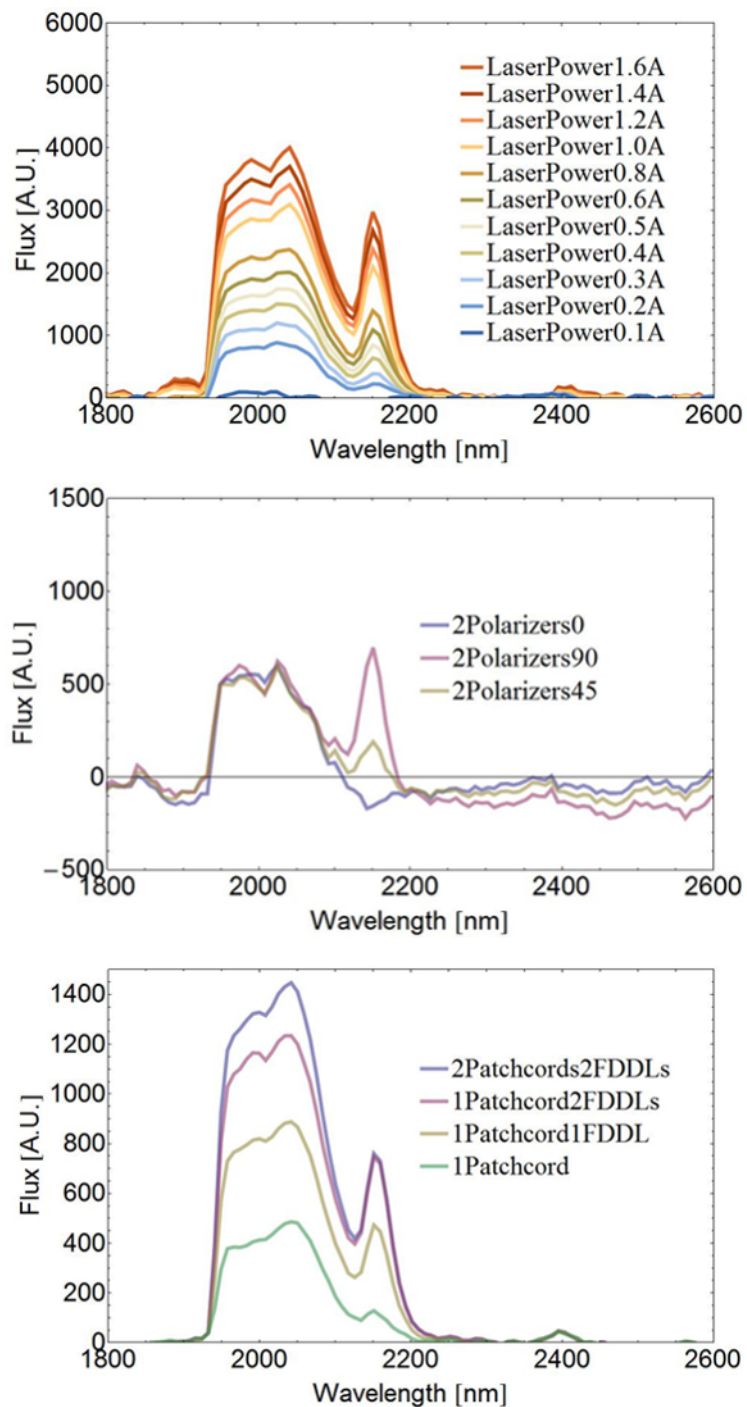


Figure 3.23: Main results from the laboratory measurements of the backscattering: the backscattering flux is measured in arbitrary units (A.U.) versus wavelength for different laser power levels (top), for two polarizers aligned to different angles with respect to each other (middle) and for different fiber lengths consisting of up to two patch cords and two FDDLs connected to each other (bottom).

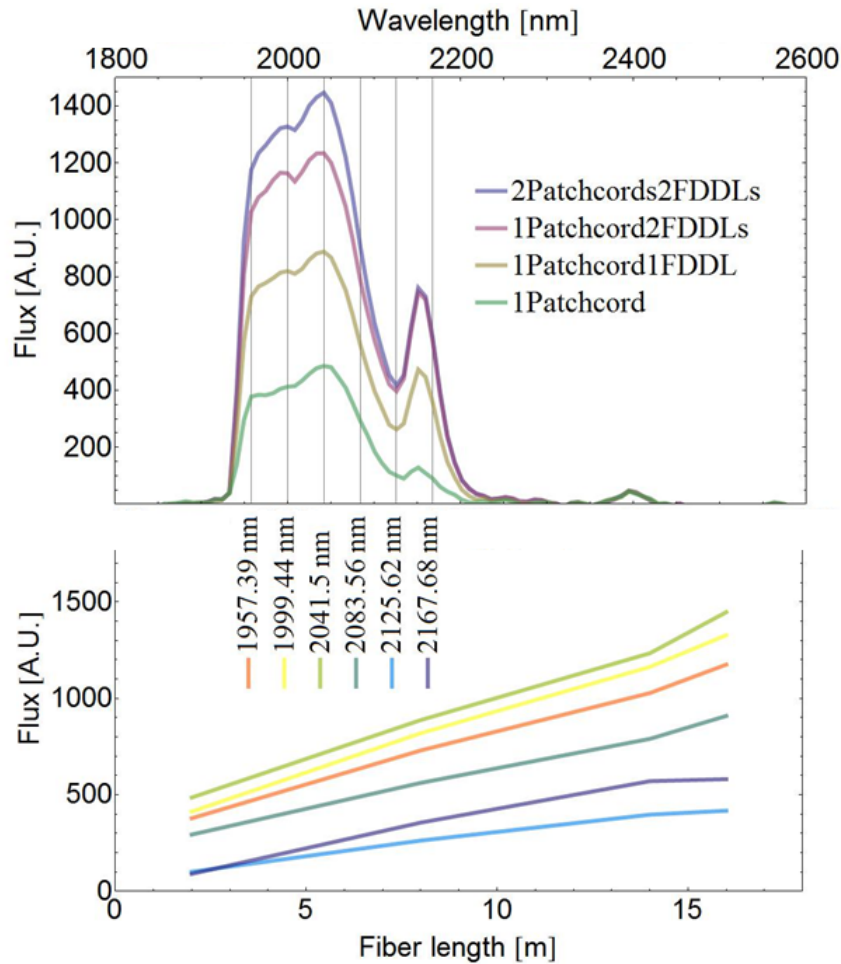


Figure 3.24: Backscattering strength for different fiber lengths (top). The bottom panel shows six wavelengths depicted across the spectrum for comparison of the strength from the Raman peak and the rest of the spectrum with varying fiber length. No prominent differences occur between the gradients of the six relations.

input, for instance by the connector ferrule holding the fiber. The backscattering thus is triggered within the fiber core as it scales with fiber length and coupling.

The manufacturer of the fluoride-glass fibers LVF recognized the fluorescence spectrum of the rare-earth element (REE) Holmium in the spectrum measured in the laboratory. The comparison of these results to literature studies is summarized in the next section.

Comparison to Literature and GRAVITY While the Raman radiation is induced by a scattering process, fluorescence is the absorption and, after some resonance time, emission of light by a material. The emission of REE ions in glass can occur in a broad spectral band above the exciting laser wavelength, due to Stark splitting of the energy levels into manifolds by local electric fields in the material (Stark, 1914; Kaminskii, 1996; Scholle et al.,

2010). The sublevel populations thermalize to a Boltzmann distribution through vibrational phonons faster than the resonance time (Simpson, 2008). Inhomogeneous distributions of the ions in the glass can lead to additional spectral broadening by differences in the local electric fields, producing different manifolds dependent on the environment. In such a setup, the lines from individual sublevels smear out to a continuous band.

The spectral shape of the fluorescence band is characteristic for the incident laser wavelengths of a corresponding broad absorption band, in contrast to the Raman effect. Raman scattering preserves a constant shift independent from the excitation wavelength.

Holmium Fluorescence in Literature The comparison of the measured backscattering spectrum to literature indeed matches the typical fluorescence spectrum of Holmium ions Ho^{3+} in glass. The involved energy levels are the ground state manifold $^5\text{I}_8$ and first excited-state manifold $^5\text{I}_7$ of the valence electrons in Ho^{3+} , in notation of LS or Russell-Saunders coupling typically used for REEs in contrast to the classical atomic orbital notation (Russell & Saunders, 1925). The strongest resemblance in terms of the spectral shape is found in the work of Zhang et al. (2009). The corresponding plots are displayed in Figure 3.25. In the work of Zhang et al. (2009), fluoride glass is doped with Thulium, Tm^{3+} , as well as with different Holmium concentrations and excited by a 800 nm laser.

Although the excitation wavelength is different than in GRAVITY and the studied process is the indirect excitation of Holmium via Thulium excitation, the plots show a spectral shape of Holmium emission as measured for GRAVITY. The absorption and emission spectra of both REEs show that the metrology laser can be absorbed by both elements leading to fluorescence. The emission in the K-band as observed in GRAVITY and the laboratory mock-up is clearly dominated by Holmium fluorescence. The absorption band of Holmium peaks close to the metrology wavelength, therefore triggering a maximum of fluorescence from Holmium.

The manufacturer of the fluoride-glass fibers stated that the Holmium is an unknown contamination in this case, and not a component of the fluoride glass put on purpose. The obvious question arises, whether there is also a contamination with Thulium, which could oppose the mitigation of the Holmium fluorescence by going to a shorter metrology wavelength.

Backscattering Level in GRAVITY Comparing the laboratory measurements to the ones in GRAVITY, the fluorescence measured in the cryostat seems to have a higher peak by a factor of seven in peak values, when scaling the spectra to have similar Raman peaks. Here I assume the polarization alignment in the cryostat is such that the Raman scattering measured shows a mean value between its maximum and minimum. Assuming the cryostat measurement shows the maximum Raman peak results in an upper limit of factor 17 in the fluorescence strength.

A factor of six is found by the comparison between the measured ratios of backscattered to injected light for the laboratory and cryostat, according to the integrated spectra. The instrument shows a ratio of 5×10^{-7} , while the laboratory setup results in 8×10^{-8} . This

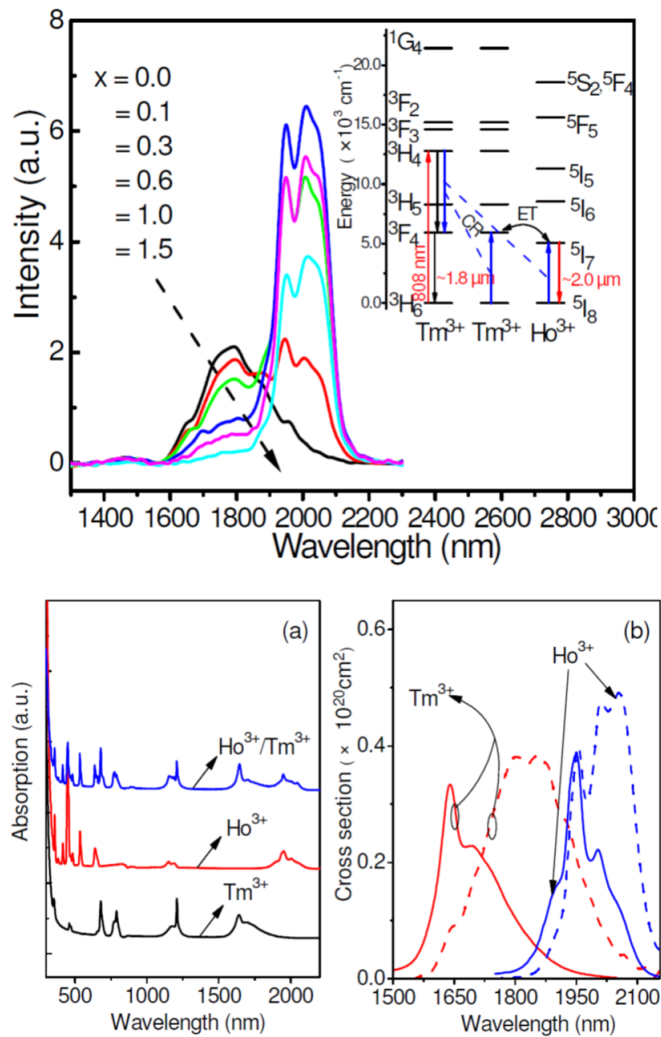


Figure 3.25: Absorption and emission spectra of Thulium and Holmium from Zhang et al. (2009): on the top fluorescence intensities in fluoride glass doped with Thulium and Holmium with a ratio $1/x$ together with a simplified energy level diagram. From left to right it shows the laser excitation of Thulium by 808 nm and the resulting de-excitation either directly or via cross-relaxation (CR), which results in two Thulium ions populating the same excited state. Via resonant energy transfer (ET) the Thulium is de-excited lifting the energy state of Holmium up. With increasing doping x , the fluorescence transforms gradually from being dominated by the direct Thulium de-excitation to reaching its maximum by the Holmium contribution. The bottom plot shows the absorption spectrum of 1/0.6 doping with Thulium and Holmium on the left together with the individual absorption spectra of these elements and on the right their absorption and emission cross sections are displayed. The latter enter the K-band and can be excited by the metrology wavelength relevant for this work.

comparison is done by integration over the K-band spectra of the fluorescence and considering the power levels in the fluoride-glass fibers as well as the individual integration times, gains and quantum efficiencies of the detectors. The laboratory value also was adjusted to represent a fiber length of 20 m as in the instrument by extrapolation of the measured dependence on fiber length. The calculations for the instrument and laboratory case are summarized in Table 3.4.

Quantity	Instrument	Laboratory
Integrated fluorescence [ADU]	2.2×10^7	2.9×10^4
/Integration time [s]	/10	/0.005
×Detector gain [e/ADU]	×2.4	×85.4
/Detector QE [e/ph]	/0.80	/0.3
/Transmission	/0.24	/0.22
=Backscattered fluorescence in fibers [ph/s]	$= 2.7 \times 10^7$	$= 2.2 \times 10^7$
/Laser power in fibers [ph/s]	$/5.4 \times 10^{13}$	$/9.6 \times 10^{16}$
Fluorescence in fibers/laser power in fibers	5.0×10^{-7}	8.0×10^{-8}

Table 3.4: Comparison of the fluorescence backscattered from the fluoride-glass fibers between the instrument and laboratory. In both cases the fiber length is 20 m.

In summary, the instrument fibers seem to be contaminated stronger by fluorescent elements producing a backscattering strength of at least a factor six more than in the case of the proto-type fibers used in the laboratory, which were manufactured by LVF at an earlier stage in a separate process. Due to this unexpected problem making GRAVITY not operational and a pressing schedule one year prior to the shipping of GRAVITY to Paranal, different mitigation scenarios were analyzed and tested in parallel as described in the following.

3.3.2 Mitigation Strategies

In order to mitigate the inelastic backscattering of the metrology light multiple routes were followed in parallel from 2014 to 2015 due to the tight schedule towards the installation of GRAVITY at the VLTI in July 2015. The corresponding strategies need to take into account the two effects found in the fluoride-glass fibers: Raman scattering and fluorescence by Holmium. As the latter is the dominating factor, the priority lies on routes which suppress, reduce or do not excite the Holmium fluorescence in the first place. There are three criteria to be considered:

- In the background-limited case of 100 s-exposure times, the backscattering should be

less than the background. Since the backscattered light occurs at $2\ \mu\text{m}$, the relevant background is only the instrumental background.

- For the shorter 10 s exposure times, the photon noise of the backscattering should lie below the read noise. For a 2×2 pixel region, the read noise is 10 e. Hence the number of photons over an integration should be lower than 100.
- The backscattering at $2\ \mu\text{m}$ adds similar in flux as the thermal background in a typical pixel. The reference value for the thermal background is at $2.2\ \mu\text{m}$.

These requirements are translated to the concrete cases of the low and medium resolution mode of the science spectrometer, since the high resolution mode is less affected due to the larger dispersion of the backscattering across the detector. This is not the case for the diffuse scattering, which in all cases is very similar. Table 3.5 summarizes the found specifications such that the backscattering levels do not violate the formulated conditions. Overall, the backscattering needs to be reduced by order 10^4 to 10^5 .

Resolution mode	Flux < background	Noise < read noise	Flux < thermal background
Medium, 100 s	5.5×10^{-5}	background limited	4.1×10^{-5}
Low, 10 s	read-noise limited	4.3×10^{-6}	2.9×10^{-5}

Table 3.5: Reduction factors for backscattering levels not restricting the GRAVITY operation with respect to the current backscattering strength.

The fringe-tracking spectrometer is less affected due to the shorter integration time in the millisecond-regime, compared to 10 s to 100 s for the science spectrometer. Recording the few-pixel wide spectra shows that the brightest channels have at most 1050000 e/s per pixel at 1 W of laser power. The typical exposure time on the FT channels will be 1 ms, which thus yields 1050 e per pixel and per detector integration time. Hence, a suppression of a factor 1000 already brings the backscattering down to a non-harming level, as the read noise of the FT detector is ~ 1 e.

On this basis, the mitigation routes followed are presented in the next section.

Evaluated Concepts

The above experiments and considerations indicate various ways to reduce of the backscattering. Possible concepts are:

- **Fiber length:** reducing the length of the fluoride-glass fibers in GRAVITY can reduce the backscattering strength.

- **Fibers:** the fluoride-glass fibers can be replaced by new ones with minimized contamination by Holmium.
- **Wavelength:** changing the metrology wavelength can move the Raman scattering to lie outside the K-band and triggers less or no fluorescence.
- **Laser power:** the laser power can be reduced for less backscattering.

Since the backscattering needs to be reduced by several magnitudes in the range of 10^4 to 10^5 , also a combination of the different concepts needed to be considered. The individual methods are outlined next.

Reducing the Fiber Length In the current FDDL concept the fiber length cannot be changed by a significant factor, since its length is needed to give enough differential stroke. The FDDLs and FPRs could be replaced by bulk optic elements. Motorized and piezo-driven mirrors can give sufficient stroke and precision to control the differential paths and motorized half-wave plates can be used to rotate the polarization. The volume available is sufficient to implement such a design.

Our engineering department has demonstrated that piezo stages in principle deliver sufficient precision in optical path direction and sufficient angular stability, but such a solution comes with expected transmission losses of order several 10%, and the implementation of a smooth, closed-loop operation needs to be developed. Also, fibers cannot be avoided completely, since the IO with some connected fibers is given. That means the maximum reduction of fiber length will be from ~ 25 m to 1 m, at most a factor few tens.

Replacing the Fibers A smaller effort would be to keep the concept, but replace the fibers with new ones that have less Holmium. This solution has a long lead time, and the actual level of Holmium contamination is hard to control according to the manufacturer. The expected gain thus is not predictable. The observed variation between the implemented LVF fibers, the LVF proto-type fibers and fluoride fibers from Thorlabs are factors of a few tens.

Another variant is to only remove the FDDLs of the science arm, where the backscattering is more limiting and giving up on FDDL stroke. In order to keep the stroke and remove the FDDLs from the science arm, one could put the fibers only on the FT arm, that means two in a row per telescope, and none on the science arm. This solution however would mean significant design changes within the beam combine instrument to guide the light directly from the IO fibers of the science combiner to the fiber couplers. Again only a few tens of reduced backscattering would be gained in this scenario.

Change of Laser Wavelength The choice of laser wavelength is strongly linked to overall properties of the GRAVITY instrument and cannot be chosen only according to reduction of the backscattering. The general basic requirement for the metrology laser is to emit outside the K-band and to correctly measure OPD in a single mode. The original design operates slightly below the band.

Longer Wavelengths Wavelengths above the band could move the Stokes mode of the Raman scattering beyond the K-band and the anti-Stokes component would potentially be faint enough to tune the instrument parameters such that it becomes irrelevant for science operations. No fluorescence is to be expected as this emission process results in bands similar or larger than the excitation wavelength.

However, components for a metrology working beyond 2500 nm are not commercially available. In addition, the noise of diodes increases for wavelengths above the K-band leading to less efficient detection. Also the transmission of the fluoride-glass fibers decreases in this range. In total, this would mean the already high metrology power would have to be even increased. Overall longer wavelengths than the K-band are not compatible with different instrument properties, such that wavelengths shorter than K-band are investigated, as they imply less severe changes to GRAVITY beam combiner.

Shorter Wavelengths A quick laboratory test was performed at the standard wavelength in telecommunication industry, 1550 nm, which lies outside of the absorption band of Holmium. The resulting backscattering spectrum is shown in Figure 3.26, which shows that this wavelength excites a Thulium contamination in the fluoride-glass fibers.

If indeed Thulium is the cause of the 2 μm backscattering for the 1550 nm laser, the strength of fluorescence should even increase by choosing another wavelength between the tested 1550 nm and 1908 nm according to the Thulium absorption spectrum in Figure 3.25.

With a tunable laser this range was scanned. The results are displayed in 3.27. Clearly, all tested wavelengths trigger fluorescence from Thulium, which becomes weaker with decreasing wavelength. This finding shows that going to shorter wavelengths for the metrology laser cannot fully eliminate the fluorescence, but a reduction of up to a factor 10^3 is possible.

The Raman shift of 590 cm^{-1} falls completely below the K-band for wavelengths $\leq 1700\text{ nm}$. A wavelength of $\leq 1650\text{ nm}$ was chosen at the time, where the lower level of backscattering together with a change of photo-detector material with increased sensitivity would lower the light level to the desired values. There was, however, one caveat: whether the fibers are still single-mode, or whether at least there is a stable phase relation between the scientific K-band and the $\leq 1650\text{ nm}$ laser light.

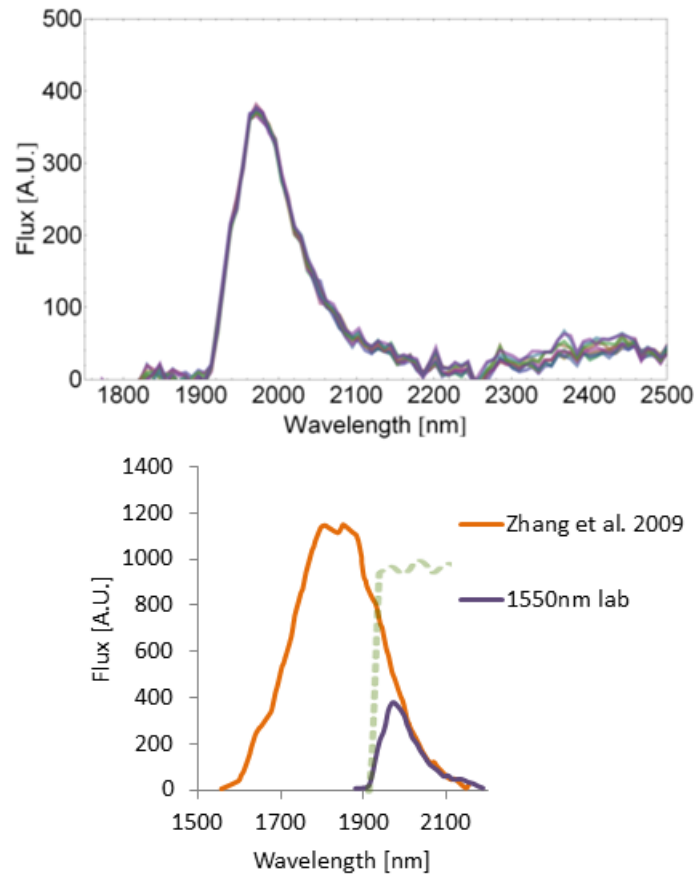


Figure 3.26: Backscattering spectrum from a 1550 nm laser measured in the laboratory (top) compared to the Thulium fluorescence band from Zhang et al. (2009) by appropriate scaling (bottom). The dashed green line indicates the product of the transmission curves from the K-band and blocking filter, responsible for the cutoff in the laboratory measurement.

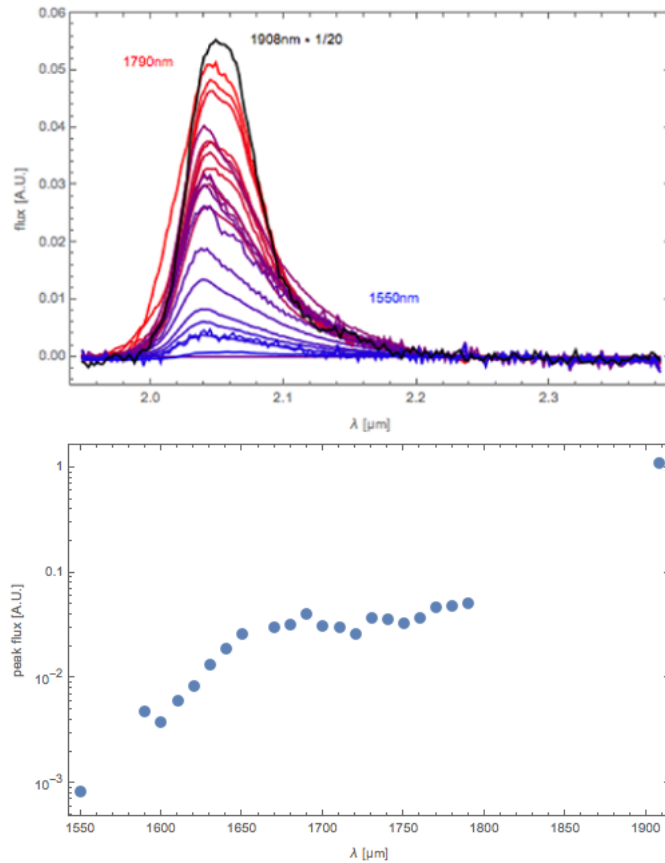


Figure 3.27: Backscattering spectrum measured in GRAVITY for different excitation wavelengths between 1550 nm and 1908 nm (top) and the corresponding peak flux of the observed fluorescence versus the excitation wavelength λ (bottom). The spectrum from the laser 1908 nm is scaled down by a factor of 20 in the top plot.

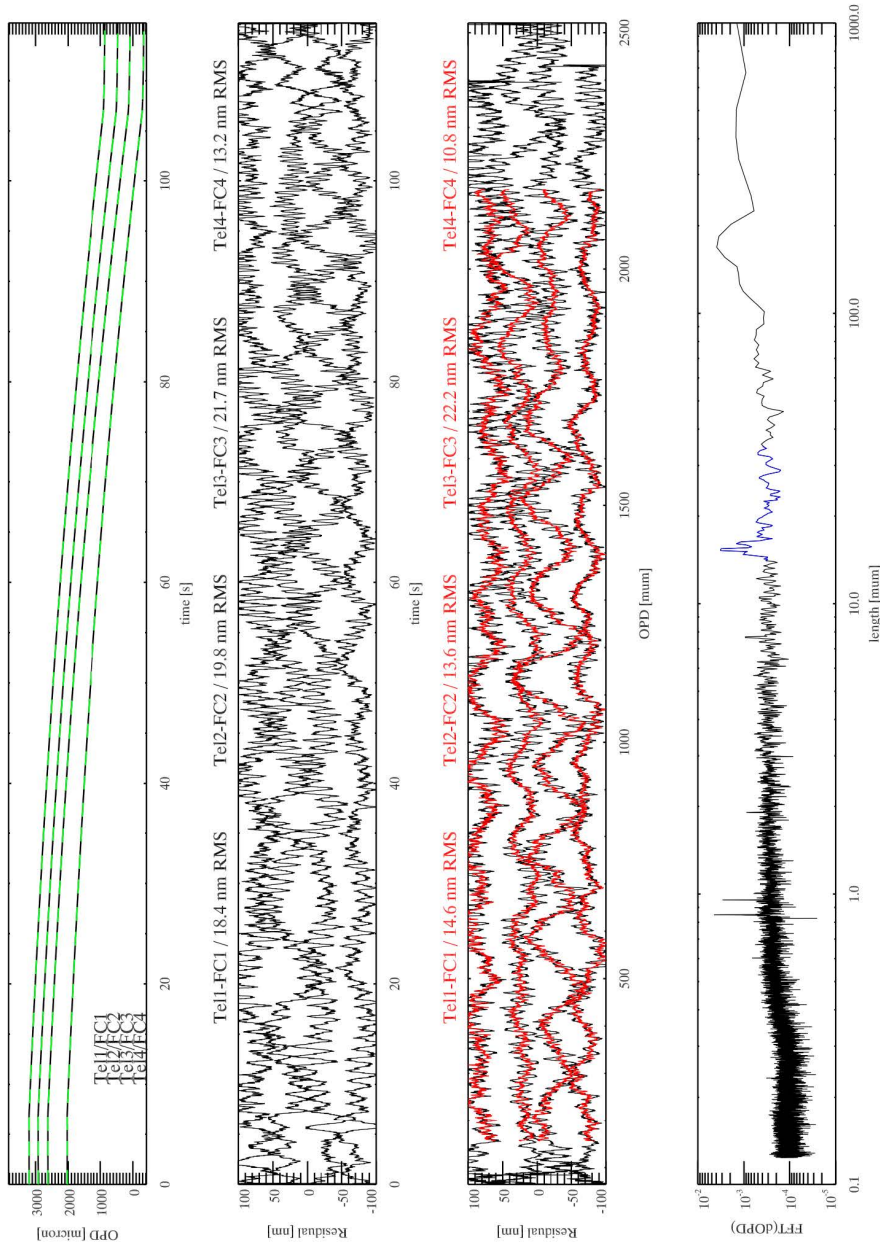


Figure 3.28: Tests to evaluate the metrology accuracy at a laser wavelength of 1700 nm. The metrology signal was recorded and analyzed simultaneously at 1700 nm and 1908 nm. Top panel: commanded and recorded optical path length (OPL). The difference of the two signals is shown versus time in the second panel and in the third one against OPD. The signal difference clearly shows the mode beating (red line) between first and second propagation mode as well as higher-frequency oscillations probably from vibrations. Bottom panel: FFT of the red part of the signal in the third panel.

Analysis of Fiber Modes Dedicated tests were performed to find out if the transmission of the metrology light through GRAVITY would still be confined in a single mode, which is necessary to perform reliable phase measurements. In particular, two tests were performed:

- The far field of the fiber output was observed, when moving the FDDLs. At 1650 nm a fundamental mode and the next higher mode are observed. The intensity distribution appears to jump back and forth between the modes.
- In a second test, the metrology was operated at different wavelengths. Here, the FDDL were moved as shown in Figure 3.28 and recorded the phases at the wavelength at test and 1908 nm simultaneously. Periodic changes of the phase could be noticed with an amplitude of up to 100 nm, and a period of 200 μm . The latter number matches the beating length between the first two fiber modes. The effect decreased with wavelength, but it was not possible to demonstrate that the system measures the OPD reliably.

As a result of these tests, the conclusion emerged that 1750 nm might be an acceptable compromise between low backscattering and almost single-mode operation.

Another route followed to mitigate the backscattering was reducing the laser power. There are several possibilities to run the metrology at lower power, which are presented in the following and lead to the successful development of the final three-beam metrology, which provided better results than the two-beam operation at 1750 nm.

Reducing the Laser Power Given the linearity of the backscattering strength with laser power, it is an obvious route to try to reduce the laser power in the fluoride glass fibers. More sensitive detectors and different injection schemes are the main themes for this route.

Different Injection Point The idea behind this class of concepts is to inject the laser behind the fluoride fibers such that a high-power beam travels to the telescopes and a low power beam along the instrument fibers. The beams need to originate from the same laser source for a fixed phase relation.

More Sensitive Detectors The following list of ideas might lead to a more sensitive detection scheme.

- **Smaller photodiodes:** The noise of a photodiode decreases with its diameter. In turn, one would need to check whether the optics still is sharp enough to focus the metrology light onto the photosensitive area. Our current diodes have an area of $(0.5 \text{ mm})^2$, but the same type of diodes are available also as $(0.25 \text{ mm})^2$ variants. The gain in SNR is roughly a factor 2.

- **Different detector material:** For the detection of 1908 nm laser light the best choice is extended InGaAs with a cutoff at 2200 nm. A significant improvement can be achieved if one would be able to use a different material, such as normal GaAs. Beyond a wavelength of 1700 nm, avalanche photodiodes are not readily available and would constitute significant research and development. For a shorter wavelength, this is a valid, although costly option.
- **Cooled photodiodes:** The noise of a photodiode can be reduced by cooling. The limitation here comes rather from practical considerations, e.g. no liquid coolant supply possible for ATs, such as there are limits how much cooling power dissipation one can dissipate at the diode locations, sitting above the primary mirrors.
- **Different location of detection:** one can think of changing the place where to detect the metrology light, if the metrology signals are transported with optical fibers to a place where sufficient cooling power can be made available. An obvious option would be cooled photodiodes with multi-stage Peltier coolers, each dissipating ~ 5 W. If the signals are already transported to a different location, one could even think of detecting the signals with a SELEX detector, yielding the ultimate sensitivity. This would imply, however, using eight additional detector systems for four UTs and four ATs.

In the end, smaller photodiodes and the injection of a third beam amplifying the then much fainter metrology beams could be implemented in the three-beam scheme presented in the final section.

Three-Beam Design

Here, the metrology consists of a three-beam laser system using phase-shifting interferometry in combination with lock-in amplifiers. The detection of the three-beam interference is realized by locking to the phase-shifting frequencies. The scheme allows using the original wavelength, which assures not only that the correct optical path is traced, but it also avoids the exchange of many optical elements, such as coatings and filters, which would have been needed for shorter wavelengths. This in turn means a smaller overall system impact and therefore smaller cost and shorter implementation time.

Concept The metrology laser is split into three beams instead of two. The two original beams are still injected backwards to the IOs but at a power level reduced such that only reduced backscattering is detected in the spectrometers. Instead, the high power necessary for detecting the metrology signals at the telescopes is carried by the third beam, which is overlaid on the faint beams after they have passed the fluoride-glass fibers within the BCI. The design is pictured in Figure 3.29. This new concept also reduces non-common path errors in the metrology injection by the reduced laser power. The dominating error from non-common paths is induced by differential temperature variations in the injection fibers, mainly by fluctuations in the high laser power (Kister, 2011; Gillissen et al., 2012;

Weber, 2014; Kok et al., 2014; Blind et al., 2014b). In addition, the problem of the diffuse stray light from the metrology in the spectrometers is solved as well.

Instead of two-beam interference, a three-beam interference is measured for every pair of FT and SC beams. The phase of interest is between the faint beams, which is undetectably faint. The third beam is used as amplification of the fringe pattern, such that its interference with each of the faint beams can be analyzed. To distinguish those two interference components, they are phase-shifted at different frequencies. Lock-in amplifiers coupled to those frequencies extract the phases of the respective interference. The difference of those phases cancels the phase of the third beam and results in the phase difference between the two faint beams, the metrology phase of interest.

In this scheme, only the oscillating part of the interference is of interest since it carries the phase information. The metrology receivers are adapted to AC coupling instead of DC, in order to prevent saturation of the subsequent amplifiers. In this way, they are only sensitive to the faint oscillating part of the signal and not to the high average signal level. Since the lock-in amplifiers are coupled to the frequencies corresponding to the modulation of the faint beams, this detection scheme is a homodyne scheme.

The mathematical description of the created three-beam interference and its analysis is summarized next.

Three-Beam Interference The three beams are called science, fringe tracker and carrier beam with the respective intensities I_{SC} , I_{FT} and I_C . The interference between these beams can be described by:

$$I(t) = I_{SC} + I_{FT} + I_C + 2\sqrt{I_{SC}I_{FT}} \cos(\theta_1 + \phi_{SC}(t) + \phi_{FT}(t)) \\ + 2\sqrt{I_{SC}I_C} \cos(\theta_2 + \phi_{SC}(t)) + 2\sqrt{I_{FT}I_C} \cos(\theta_3 + \phi_{FT}(t)) \quad (3.43)$$

with the beam phases

$$\theta_1 = \theta_{SC} - \theta_{FT} \quad (3.44)$$

$$\theta_2 = \theta_{SC} - \theta_C \quad (3.45)$$

$$\theta_3 = \theta_{FT} - \theta_C \quad . \quad (3.46)$$

The first part of this formula, consisting of the sum of I_{SC} , I_{FT} and I_C , is a DC term not affected by the phase modulations. Since the quantities of interest are the oscillating AC terms, which encode the phase information within the cosine, the metrology receivers are set to AC coupling. This receiver design helps to detect the small oscillating term and neglecting the strong underlying average signal.

This means the DC terms are not seen by the detectors. Therefore, the signal amplitudes as measured by this detection scheme are given as in terms of powers P_1 , P_2 and P_3

$$P_1 = 2\sqrt{P_{SC}P_{FT}} \quad (3.47)$$

$$P_2 = 2\sqrt{P_{SC}P_C} \quad (3.48)$$

$$P_3 = 2\sqrt{P_{FT}P_C} \quad . \quad (3.49)$$

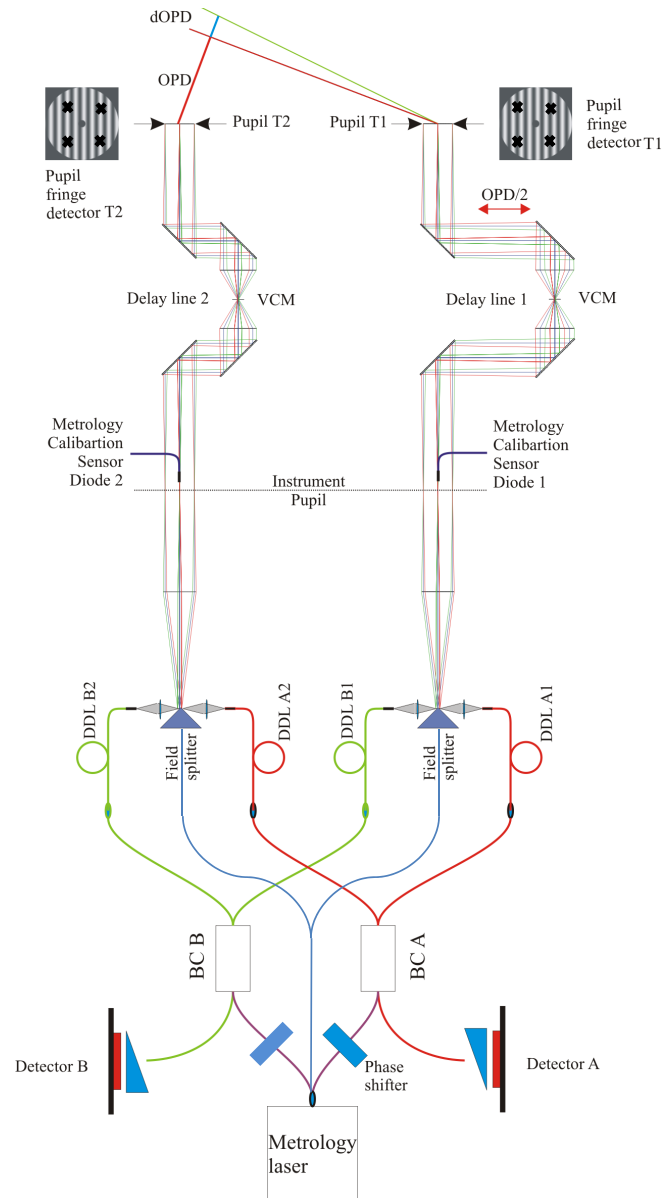


Figure 3.29: Scheme of the three-beam metrology shown for two out of four telescopes in Lippa et al. (2016): a laser beam is split into three, with two faint beams and one high-power beam. The faint beams are injected to the two BCs of GRAVITY, A and B, to reduce the high backscattering levels of the metrology light onto the science detectors. The beams follow all the optical paths back to the telescope pupils T1 and T2 where they interfere with the bright carrier.

while P_1 is undetectably faint. Thus, the actual phase of interest θ_1 cannot be measured directly. Instead, this quantity can be determined from the phase difference $\theta_2 - \theta_3$ in which the phase of the carrier beam cancels out leaving θ_1 . θ_2 and θ_3 are measured by means of lock-in amplifiers.

For the available laser power $P = P_C + P_{SC} + P_{FT}$ of ≥ 1 W, reducing the original metrology beams, SC and FT, in power by factor $\geq 10^4$ from the level of 0.5 W to 50 μ W, still leaves an amplifying carrier beam of roughly $P_C = 1$ W. In order to demonstrate the amplification process on this intrinsic power levels, I assume in the following that those beams interfere directly without passing the instrument.

Both the DC term $P_{SC} + P_{FT}$ and the AC term P_1 of an interference between the two faint beams only amount to a signal of 0.1 mW, according to (3.47). The AC term of the interference with the carrier beam leads to a signal P_2 and P_3 of 14 mW following (3.48) and (3.49). So the signal strength differs by a factor of 140. In reality this factor is of order 10^6 as the contrast between the faint beams and the high-power beam is even larger when they interfere. This is because the carrier beam witnesses fewer throughput losses omitting many instrument components.

Each lock-in amplifier is coupled to one of the frequencies of the periodic phase modulations $\phi_{SC}(t) = 2\pi f_{SC}t$ and $\phi_{FT}(t) = 2\pi f_{FT}t$. These frequencies are set to $f_{SC} = 9$ kHz and $f_{FT} = 11$ kHz in order to operate on a position of the bandpass where the noise level is at its minimum as shown in Figure 3.30.

The two outputs of our dual-phase lock-in amplifiers are of the form $X_{out} = V_{sig,i} \cos(\theta_i)$ and $Y_{out} = V_{sig,i} \sin(\theta_i)$ where $V_{sig,i} \propto P_i$ and $i = \{2, 3\}$. Therefore, both the signal and the phase can be derived by

$$V_{sig} = \sqrt{X^2 + Y^2} \quad (3.50)$$

$$\theta_i = \arctan \frac{Y}{X} \quad (3.51)$$

This means two lock-in amplifiers are needed per metrology receiver to measure the phase difference of each beam and the carrier. As there are 16 receivers at four telescopes plus four in the fiber couplers, this makes 40 lock-in amplifiers in total, which perform 80 measurements delivering the X and Y values. This detection scheme and the general implementation of the three-beam design required certain hardware changes described in the following.

Hardware Changes The altered metrology design is displayed in Figure 3.31. The main changes were:

- **Distribution box:** to split the laser beam and attenuate the two beams propagating through the beam combiner.
- **Vacuum feedthroughs:** to feed the third beam, which is split in the above distribution box and fed via four feedthroughs.

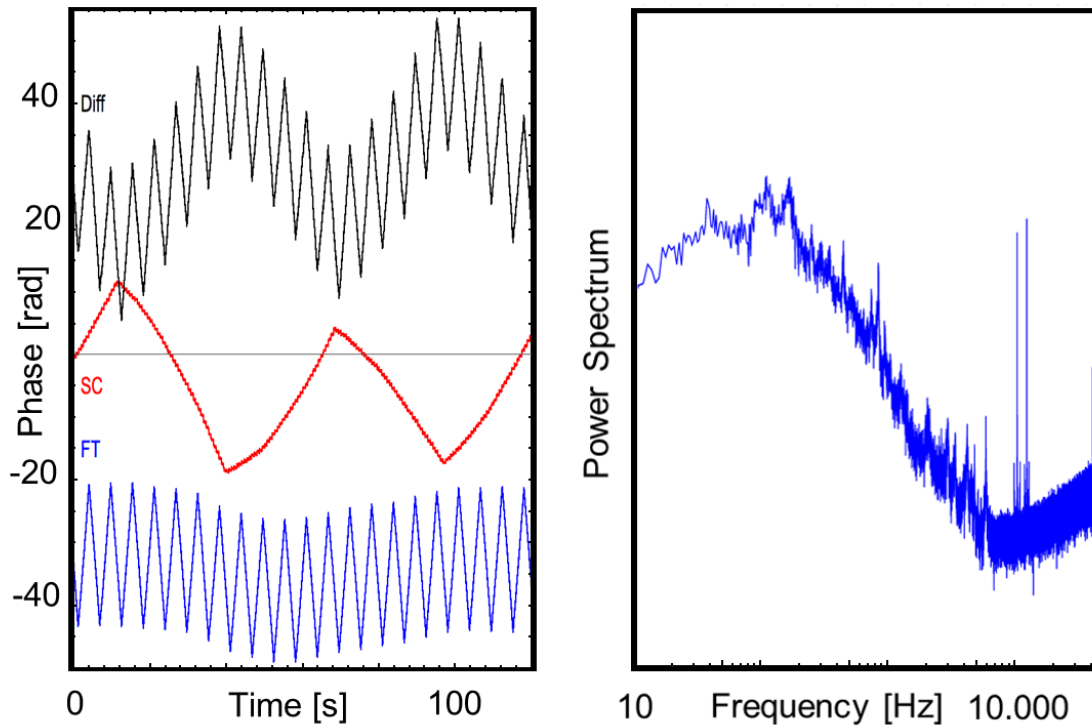


Figure 3.30: Detection by phase modulation at characteristic frequencies: on the left the science (SC) and fringe tracker (FT) metrology phases are measured continuously during an FDDL modulation. In this example, the FDDLs are moved up and down by a few micrometers, each at a different speed. The black signal is the phase difference between them, which is the quantity of interest to determine the internal dOPD. The power spectrum of the interference is shown on the right displaying the two frequency peaks at $f_{SC} = 9$ kHz and $f_{FT} = 11$ kHz, with which the beam signals are phase-shifted and locked for detection. These tests found that the new metrology concept can be operated stably.

- **Phase shifter:** to be able to modulate both beams in the instrument instead of only one.
- **Carrier injection optics:** to inject the carrier in free beams behind the four fiber couplers.
- **Receivers:** AC coupling was implemented in the receiver circuits after the first amplification stage, and the amplification factor from the second and third stage could be reduced from 1000 to 10 each.
- **Lock-in amplifiers:** to detect the phase-modulated interference between the two beams and the carrier.

- **Function generators:** to drive the phase modulation.

In the distribution box mounted to the outside of the cryostat, the laser beam is split into six beams: four carrier beams, one for each telescope, and two science beams, one for each spectrometer. Via a highly imbalanced fiber splitter only about 2% of the light is directed towards the science beams, while 98% are sent towards the carrier beams, which are equally split into four to cover all telescopes. In order to adjust the power of the two faint beams to the lowest level possible, two fiber attenuators are mounted to each fiber chain. The additional phase shifter is spliced to polarizers and installed within the cryostat in parallel to the other one. The four high-power beams are fed to the cryostat by vacuum feedthroughs. Prior to the injection, fiber polarizers are inserted to correct any previously induced misalignments.

The injection units for the carrier beams consist of an off-axis parabolic mirror as collimator. The fiber is focused by means of small, thin O-rings. The collimated beam is then superimposed onto the optical axis at the backside of the fiber coupler. There the beam is propagating from the fiber coupler to the acquisition camera. A dichroic splitter is used here, which transmits the H-band light to the acquisition camera, while reflecting the 1908 nm laser light towards the telescopes. The polarization state is adjusted by means of a quarter- and a half-wave plate between parabola and dichroic. This adjustment is performed once during initial alignment, to align the laser to a defined polarisation axis with respect to the fiber coupler dichroics. Doing so, 20% of the carrier beam is reflected towards the fiber coupler metrology pickups, and 80% is going in direction of the VLTI. The adjustment screws of the mount allow adjusting both pupil and field of the carrier beam.

The lock-in amplifier phase-analyzes the analog voltages received from the various receiver diodes. Each diode feeds two lock-in amplifiers, such that both fringe patterns modulated at different speeds can be detected. Each lock-in amplifier returns the sine and cosine voltages of the measured phase. The chosen lock-in amplifiers are of type FEMTO LIA-BVD-150-H.

The voltages for the phase modulations are set by two function generators. Commercially available devices were purchased from Keysight, model 33500B. They are set to linear scans with an amplitude of around 8 V peak-to-peak, matched to the full-wave voltage of the phase shifters.

Limitations The main limitations of this implemented scheme were found to be the laser fluctuations and the receiver sensitivity.

The short-term intensity fluctuations of the laser occur at > 30 Hz. They are a limiting factor, because at some point they will wash out the fringe modulation, when the power of the faint beams is further reduced. A possible solution would be to stabilize the laser. There are commercially available “noise eater”: a fast control loop that measures the intensity of the beam with a photodiode, and adjusts its intensity by some modulating element. However, none of the considered devices could be integrated to the existing metrology laser system.

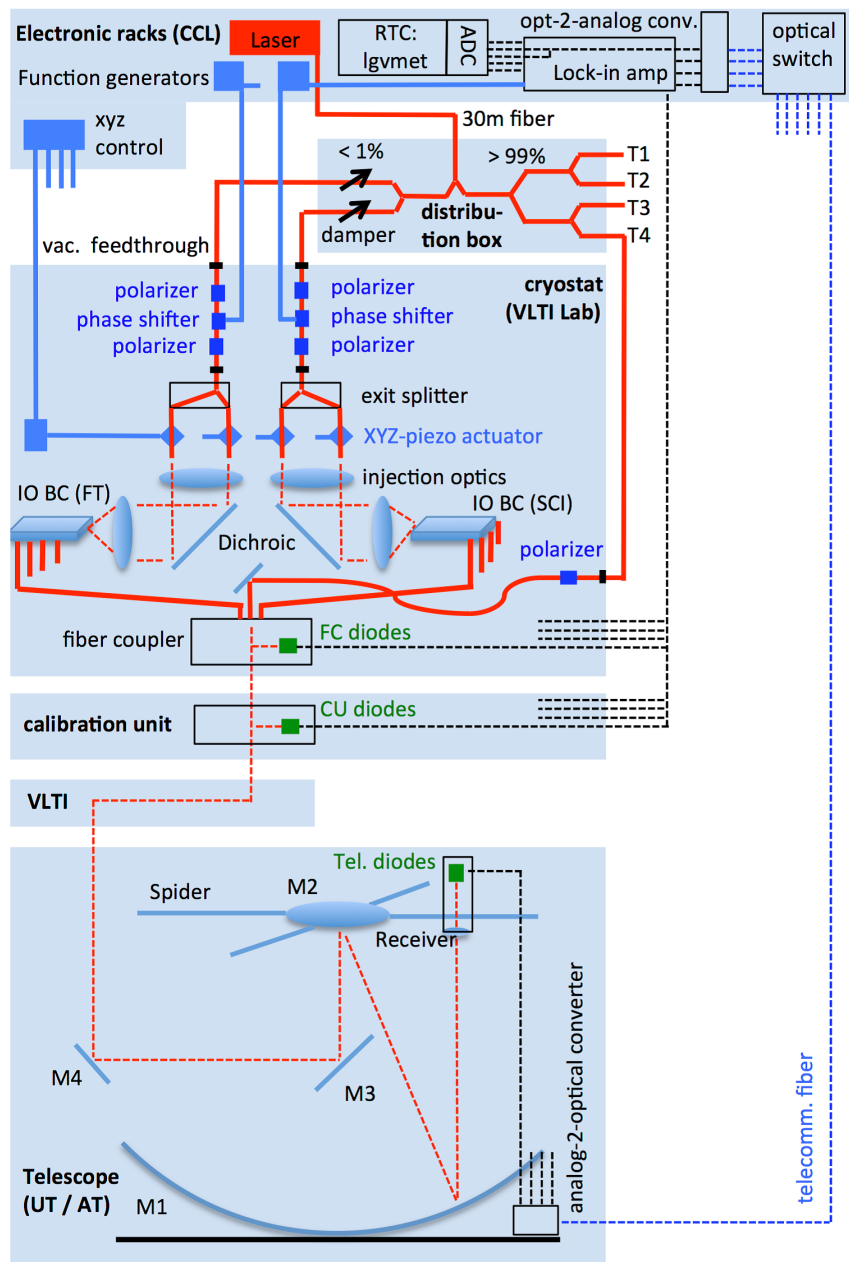


Figure 3.31: Hardware of the three-beam metrology as in Lippa et al. (2016): the main changes are the lock-in amplifiers added to the detection scheme in the top, which are coupled to the function generators driving the voltage modulation of the phase-shifters. Previously only one phase shifter was used. An additional distribution box splits the laser light in three beams effectively. Dampers are used to reduce the power level of the two metrology beams passing the fluoride-glass fibers. The third carrier beams is split for the four telescopes and superimposed on the two beams in the fiber couplers.

The other limiting factor comes from the sensitivity of the metrology detection. To improve the sensitivity, the lens diameters of the UT receivers were increased from 25 mm to 50 mm, increasing the sensitivity by a factor of four. Furthermore the diode sizes were decreased from 0.5 mm to 0.25 mm to lower the intrinsic noise. The signals focused by the receiver lenses are still sharp enough to create focus spots smaller than the active diode area.

By all these measures, the backscattering of the metrology could be dimmed by a factor $\sim 10^4$ to almost the level of the thermal background summarized in Table 3.6. The contrast between carrier and science beams is around 10^6 .

Detector	Backscattering	Thermal background
Science	180 e/s	40 e/s
Fringe Tracker	0.5 ADU/ms	0.2 ADU/ms

Table 3.6: Backscattering level of the three-beam metrology compared to the thermal background in January 2018. The science detector was used in low resolution mode. The values are measured at the respective brightest pixels, which for the thermal background is situated at the longest wavelengths and for the backscattering at the shortest.

The science detector is still affected by the backscattering, however only in the shortest wavelength range between 2.0 μm and 2.1 μm . The fringe tracker case is very close to the photon-noise limit.

The metrology has been constantly improved since then in hardware, software and data analysis to minimize the impact of the backscattering. The conclusions and outlook on the metrology performance are summarized in the last Chapter 5 after the following chapter about galaxy evolution with the IRAM interferometer as a different application of interferometry in astronomy.

Chapter 4

Galaxy Evolution with the IRAM Interferometer

Interferometry is widely used for astronomical observations in wavelengths longer than optical, reaching from sub-millimeter, millimeter to the radio regime. As outlined in the section about the principles of radio interferometry, the applied techniques of signal correlation allow both for imaging and spectroscopy. One of the leading facilities in this respect is the IRAM Interferometer, formerly known as Plateau de Bure Interferometer (PdBI) or now NOthern Extended Millimeter Array (NOEMA).

The long wavelengths often originate from cool, dense regions in the Universe, such as molecular gas clouds. In order to study those regions back in time with increasing redshift, the sensitivity, instrument stability and spatial resolution of single-dish observations need to be improved. Interferometric measurements do so due to larger collecting areas and instrumental features being averaged out in the correlation and long baselines. In comparison, optical light traces warmer gas such as the ionized component, which can be observed with individual telescopes in large detail out to redshifts of $z > 2$. The radio and related regimes rely on the use of multiple apertures. Despite the fact that larger single telescopes can be built for radio than for the optical observations, this difference in resolution due to wavelength cannot be adjusted with single dishes.

This chapter illustrates the power of radio interferometry for a small sample of star-forming galaxies at high redshifts. The corresponding work also includes optical data from single telescopes. Tracing galaxy evolution at past epochs requires such a synthesis between multi-wavelength observations. The state of art in this research field is outlined in the first section, followed by the study of the galaxy sample and the highlighting of a particularly interesting object within the latter. These contents also serve as basis for two publications planned.

4.1 Molecular Gas as the Fuel of Star Formation

The build-up of galaxies is driven by the accumulation of baryonic matter. This gravitational concentration is embedded within the structures of Cold Dark Matter (CDM). The latter does not show electromagnetic interaction but only gravitational collapse, as described by the standard model of cosmology (Kauffmann et al., 1993; Komatsu et al., 2011; Planck Collaboration et al., 2014). The web of growing dark-matter structures, the halos, and the connecting filaments in between span the foundation for galaxy evolution (White & Rees, 1978). The gravitational potentials of this hierarchical clustering attracts the baryonic matter. The baryons cool onto forming galaxies and by disk instabilities the matter fragments to clumps of molecular gas forming stars. In this basic process, the luminous parts of galaxies are formed within the framework of the so called standard CDM model.

Initiated by density fluctuations in the primordial plasma of the Universe, this formation of galaxies went through different epochs. The gas component dominated by hydrogen was gradually enriched. The enrichment happens through the fusion processes in stars, up to the element iron, as well as in stellar feedback such as explosions for higher atomic numbers. During this enrichment and further gas inflow to the galaxies, the star formation density increased. Between redshift $z = 1$ and $z = 2$ a peak was reached, followed by the winding down to the current status at $z = 0$ as shown in Figure 4.1 (Madau & Dickinson, 2014).

Simulations help understanding the involved processes. These mainly consist of gas accretion and cooling, star formation, its feedback in the form of stellar winds, explosions as well as radiation pressure and resulting turbulent gas motions and outflows. In their interplay they lead to gas replenishment and depletion (Bouché et al., 2010; Davé et al., 2011, 2012). In this cycle of baryonic flows, Star-Forming Galaxies (SFGs) evolve growing in stellar mass and increasing their Star Formation Rate (SFR). In this respect, a near-linear relationship called Main Sequence (MS) is observed for the SFGs between the logarithms of stellar mass and SFR. In Figure 4.2 this relationship is demonstrated for redshifts $z = 0$ to $z = 2.5$ (Wuyts et al., 2011a; Speagle et al., 2014; Whitaker et al., 2014).

The star-forming MS is dominated by disk-like systems out to $z \sim 2.5$. The slope of this relationship is roughly constant throughout those redshifts, only the zero point goes up with lookback time indicating increasing SFRs (Wuyts et al., 2011a). While the star formation density is dominated by galaxies of $SFR \leq 100 M_{\odot}/\text{yr}$ at $z \sim 2$, at $z \sim 0$ the value is $SFR \leq 10 M_{\odot}/\text{yr}$. The growth of these galaxies suddenly stops at the Schechter mass of $\sim 10^{11} M_{\odot}$ (Conroy & Wechsler, 2009). The mechanisms causing this rather abrupt limit, at which the growth of galaxies is quenched, are not yet entirely understood. In order to analyze the shown growth of galaxies across cosmic time, measurements of the involved parameters at all epochs are necessary, such as SFR, stellar mass and molecular gas.

By a comparison of the extent of different distributions, previous studies showed that the ionized-gas components of similar galaxies have larger effective radii than the stellar distribution (Wuyts et al., 2013; Tacchella et al., 2015; Nelson et al., 2016). A possible explanation for this observations could be an inside-out growth of the galaxies, proposed by simulations and models as in Mo et al. (1998). This model describes the galaxy build-up within the potential of dark-matter halos. The latter grow over time, inducing a

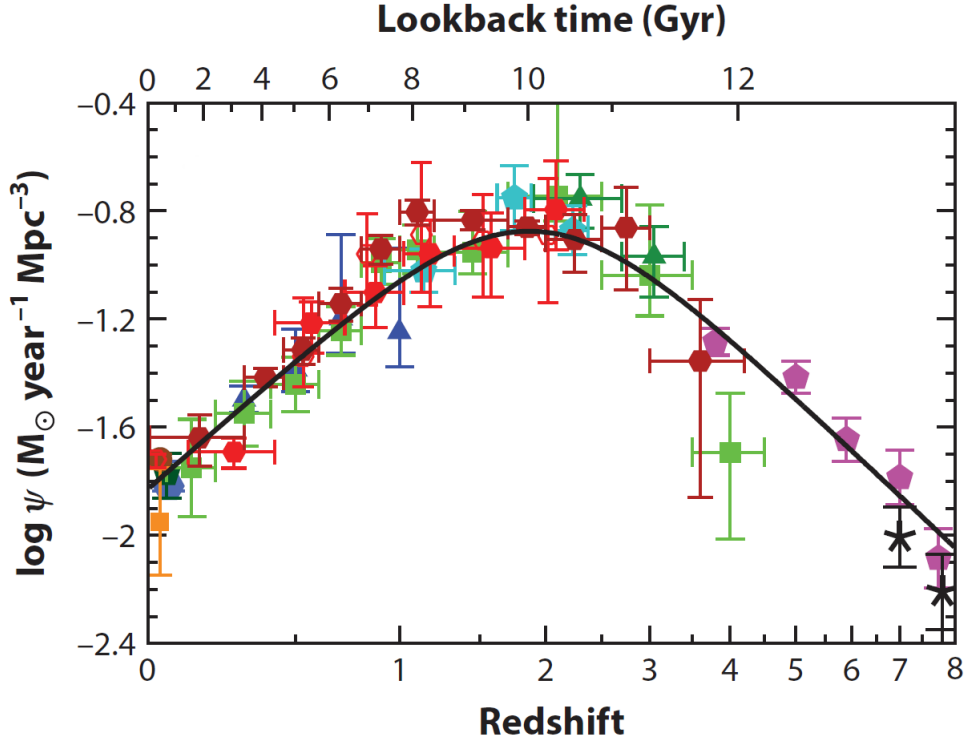


Figure 4.1: Star-formation history plotted as the star-formation density ψ versus lookback time and redshift from Madau & Dickinson (2014), based on far-UV and IR measurements. The symbols denote the different references that delivered the individual data points.

larger gas extent in disks of exponential profile. The bulk of the formed stars resides in the center. While star formation continues in the outer disks, the inner part is quenched. Possible quenching mechanisms are the depletion of gas by regular star formation, starbursts, outflows or by bulge formation.

Many studies have already thoroughly shed light onto the properties of stars, star formation and the ionized-gas component out to redshifts of $z > 2$. Only since recently, the molecular gas in the galaxies can be addressed in a similar manner and detail, due to observational difficulties for tracing the longer emission wavelengths of the cold, dense medium. The main focus of this work lies in spatially resolving molecular gas at the peak of star formation, as it serves as the fuel for the star formation. In addition, other multi-wavelength data sets are used to link the observations to other galaxy properties, such as stellar mass and star-formation rate. In two preparatory sections, the role of molecular gas in galaxies is outlined and the PHIBSS surveys are introduced. These surveys delivered a first big census of the molecular gas content in SFGs at high redshifts (Tacconi et al., 2013; Freundlich et al., 2018).

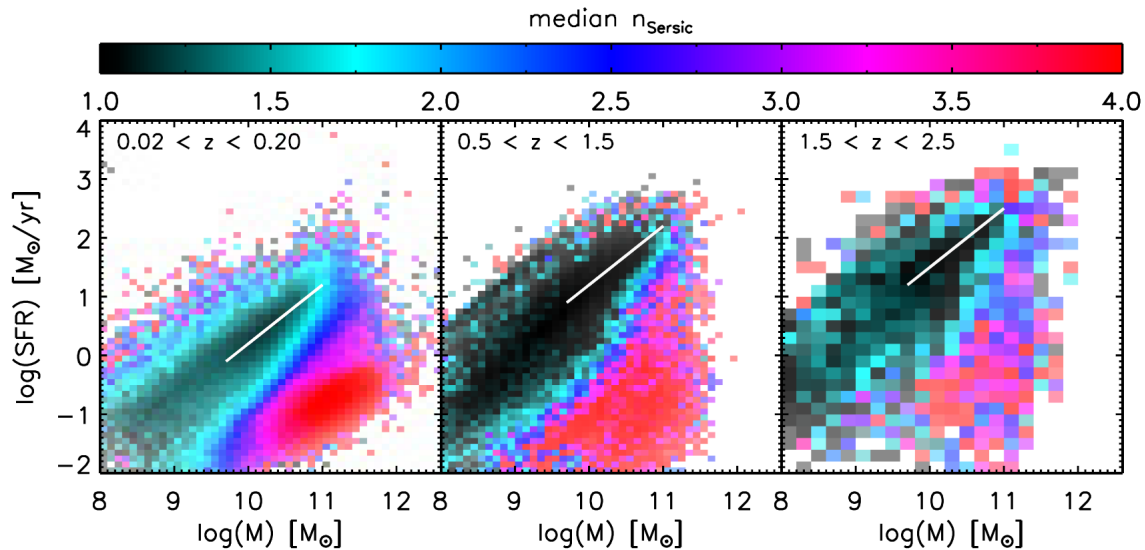


Figure 4.2: The logarithms of star-formation rate and stellar mass show a near-linear relationship for star-forming galaxies called main sequence, as shown in this figure from Wuyts et al. (2011a). The color coding in the plot denotes the Sérsic index n_{Sersic} of the objects, which is a measure for their profile shape of surface brightness. The main sequence mostly shows indices close to $n_{Sersic} = 1$ corresponding to exponential-disk profiles. The white line shows the constant slope of one at all redshifts with increasing zero point. Galaxies below the main sequence are quiescent galaxies, which rather show profiles close to the de Vaucouleurs profile with $n_{Sersic} = 4$.

4.1.1 Probing the Molecular Gas

As known from studies in the Milky Way and nearby galaxies, star formation takes place in the Interstellar Medium (ISM) within Giant Molecular Clouds (GMCs). Because these objects can be resolved in the local Universe, their properties are well-known and can be used for analyzing unresolved molecular gas complexes at higher redshifts. GMCs show sizes of ~ 50 pc, temperatures above 10 K, average volume densities higher than 100 cm^{-3} , masses of order $\sim 10^5 M_{\odot}$ and a constant mean surface density of $\sim 100 M_{\odot}/\text{pc}^2$ (Solomon et al., 1987; Bolatto et al., 2013; Carilli & Walter, 2013; Scoville, 2013; Krumholz, 2017). These complexes can be probed by emission lines.

Emission from Molecular Clouds

The molecular gas in galaxies mainly contains dense molecular hydrogen, H_2 , which is the dominant element in the Universe. The molecule forms on the surface of dust grains within dense, cold clumps. But H_2 is hardly observable.

Emission from Molecular Hydrogen The dense gas clouds are a cold medium with temperatures down to 10 K such that mainly rotational transitions are excited under these

conditions instead of vibrational or electronic ones. For a diatomic molecule, two rotational modes exist such that in good approximation the average energy attributed to rotation after the equipartition theorem

$$E_{rot} = \frac{f}{2}kT \quad (4.1)$$

results in $E_{rot} = kT$ due two rotational degrees of freedom f , with the Boltzmann constant k and temperature T . This relation links the temperature of a medium to energy states of the particles. As described by quantum mechanics, the latter have discrete values and for the rotational energy the discrete levels are characterized by the rotational quantum number J as

$$E_{rot,J} = \frac{J(J+1)}{2I} \left(\frac{h}{2\pi} \right)^2 \quad (4.2)$$

given in good approximation by the model of a linear rigid body with a fixed bond length between two atoms as assumption. I is the moment of inertia for the given molecule and only transitions between two energy states J_1 and J_2 are allowed which fulfill $\Delta J = |J_2 - J_1| = 1$. The rotational transition between the state described by the rotational quantum number J and the lower state with $J-1$ corresponds to the energy $\Delta E_{rot} = E_{rot,J} - E_{rot,J-1}$, by (4.2) resulting in

$$\Delta E_{rot} = \frac{J}{I} \left(\frac{h}{2\pi} \right)^2 \quad (4.3)$$

The emission line triggered by such a transition has the line frequency ν also linked to the energy via

$$\Delta E_{rot} = h\nu \quad (4.4)$$

Equations (4.1), (4.3) and (4.4) can be set equal in order to link a rotational emission line from the state J to the line frequency ν and a temperature T .

For molecular hydrogen, the first rotational excited state with rotational level $J = 1$ has an excitation temperature of 175 K and its transition $J \rightarrow J - 1$ to the ground state, $J - 1 = 0$, is a forbidden one because of its homonuclear nature, which lacks a permanent dipole in contrast to other molecules. Therefore, the lowest transition is the quadrupole $2 \rightarrow 0$, which has an excitation temperature of 510 K leading to a very weak emission in the dense gas due to the low gas temperature and the “forbidden” $\Delta J \neq 1$ of the diatomic rigid-body model, which also lowers the emission rate. The rotational levels of molecular hydrogen have such large spacing due to its low mass as the level spacing varies like $\mu^{-1/2}$ with the reduced mass $\mu = m/2$ of the two hydrogen atoms with mass m .

Emission from Carbon Monoxide The second most abundant molecule in the ISM is ^{12}CO , carbon monoxide. CO is distributed within the ISM similarly to molecular hydrogen and delivers the brightest emission lines. With a permanent dipole moment and heavier atoms than H_2 the first rotational line emission of CO happens at a wavelength of 2.6 mm and corresponds to a temperature of 5.5 K. The level spacing of the lowest CO transitions are shown in Figure 4.3.

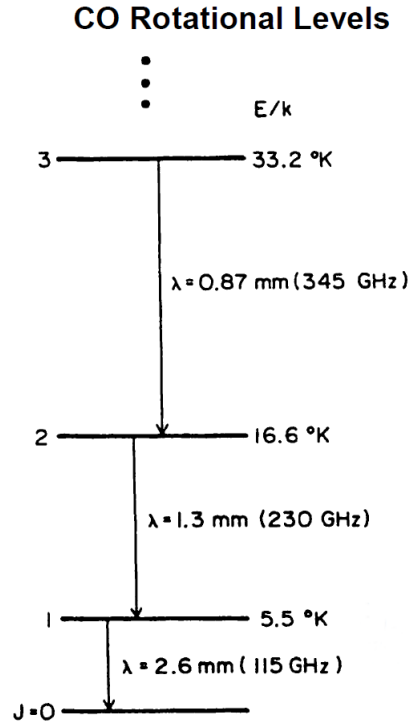


Figure 4.3: Rotational lines of CO for the first three excited states $J = 1, 2, 3$ with temperatures as given by the energy levels E and the Boltzmann constant k via E/k as well as the line wavelengths λ and frequencies ν in brackets, from Scoville (2013).

These low-energy CO emission lines can be excited spontaneously or by collisions with the molecular hydrogen at high densities. When the collisions occur at high frequency with respect to the spontaneous decay rate, thermal equilibrium is reached and the actual gas kinetic temperature will be close to the excitation temperature, which leads to the J and $J - 1$ level being populated according to the Maxwell-Boltzmann distribution. For optically thin gas, which is mostly transparent for the CO radiation, this thermalized state is reached at densities of $\sim 2000 \text{ cm}^{-3}$ for the transition $1 \rightarrow 0$, for which the notation (1-0) will be used from here on.

However, most of the CO emission observed is optically thick emission based on isotope measurements with optical depths of $\tau \gtrsim 10$ as typical for GMCs. In this condition, photons from spontaneous decay become trapped by absorption before leaving the cloud and the critical density drops by a factor $\sim 1/\tau$ to $\sim 200 \text{ cm}^{-3}$, for which thermal equilibrium is reached. This coupling between molecular hydrogen and carbon monoxide allows to probe the molecular gas clouds mainly consisting of H_2 via CO emission. In particular, the brightness temperature of the CO lines as introduced in Chapter 2 corresponds to the excitation and kinetic temperature under the presented conditions of density, temperature and line frequency in the Rayleigh-Jeans approximation of the Planck spectrum demonstrated in Figure 4.4.

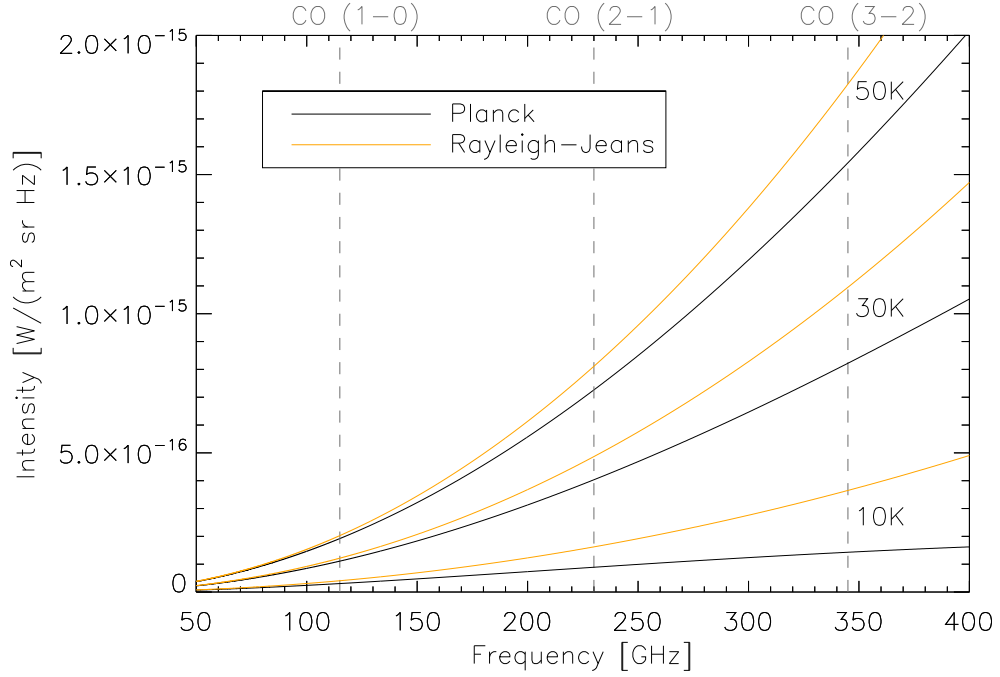


Figure 4.4: Rayleigh-Jeans and Planck's law for the lowest rotational lines of CO for three temperatures typical for molecular clouds. The Rayleigh-Jeans law, in which the intensity is proportional to the temperature, delivers a good description of Planck's law for the lowest CO lines (Carilli & Walter, 2013) in the molecular gas component. Only for CO (2-1) and CO (3-2) at 10 K the laws slowly start to deviate from each other, by factor 1.8 and 2.6 respectively.

Total Molecular Gas Mass from CO Emission

Despite the optical thickness of the molecular clouds, by which the CO brightness temperature as in Equation (2.32) only relates to the cloud surface of $\tau = 1$, the CO line luminosity L'_{CO} can be used as a tracer of total molecular gas mass. This approach is based on both the luminosity and the mass being linked to the velocity dispersion in the medium. For the line luminosity, the dispersion enters as line width as L'_{CO} can be derived from the Rayleigh-Jeans surface brightness $T_B(v)$, as a function of Doppler velocity v as converted from the frequency, integrated over the velocity and the emitting area A :

$$L'_{CO} = \iint T_B(v) dv dA \quad . \quad (4.5)$$

For a line of Gaussian shape with the peak T_B and standard deviation σ , integrating over the velocity leads to the expression $\sqrt{2\pi} \sigma T_B$, while the area introduces the cloud radius squared R^2 such that

$$L'_{CO} \propto \sigma R^2 \quad . \quad (4.6)$$

The line luminosity thus is expressed in the units $\text{K km s}^{-1} \text{ pc}^2$.

Scaling between Cloud Luminosity and Mass via the Radius The self-gravitating molecular clouds are not compressed by external ISM pressure but in or near virial equilibrium between internal pressure and gravity (Dickman et al., 1986; Solomon et al., 1987). The virial theorem therefore sets their relation between potential and kinetic energy E_{pot} and E_{kin} of

$$2E_{kin} = E_{pot} \quad . \quad (4.7)$$

Under these conditions the velocity dispersion is

$$\sigma = \sqrt{GM/R} \quad , \quad (4.8)$$

scaling with the cloud radius R and mass M . Furthermore the relation

$$\sigma \propto R^{0.5} \quad (4.9)$$

enters, which is well-studied empirically (Larson, 1981), such that combining (4.8) and (4.9) results in

$$M \propto \sigma^4 \quad (4.10)$$

and

$$L'_{CO} \propto \sigma^5 \quad . \quad (4.11)$$

As a consequence, the mass and light of a GMC scales nearly linearly according to (4.11) and (4.10). This relation supported by observation fits the so called “mist” model of a cloud consisting of many small optically thick regions, which is effectively optically thin. This condition is achieved for a filling factor of < 1 , where the average density of the cloud is smaller than the density of the sub-structure. For this reason, the overall ensemble is observed as a spectral line with Gaussian distribution being the average of many individual line profiles. The velocity dispersion in molecular clouds typically is much higher than what is induced by the basic level of thermal gas pressure indicating a turbulent medium with supersonic motions.

A linear relation between line luminosity and molecular mass is derived for looking at entire galaxies, which consist of an ensemble of molecular clouds. As in the approach of a single cloud, the involved assumptions, supported by observations, rely on non-overlapping clouds of similar density profile and mass which are self-gravitating and spread in velocity by the galaxy rotation. Under these conditions, measuring L'_{CO} corresponds to a cloud-counting technique (Dickman et al., 1986; Kennicutt & Evans, 2012; Bolatto et al., 2013).

The CO-to-H₂ Conversion Factor Estimating the total gas mass from lower CO emission lines, such as $(1 - 0)$, $(2 - 1)$ and $(3 - 2)$, is an well-established method (Genzel et al., 2012; Bolatto et al., 2013; Genzel et al., 2015). The idea behind is to measure the line luminosity, L'_{CO} , of a lower CO rotational transition and to use an empirically established conversion factor α_{CO1} for the $(1-0)$ transition to get to the total mass of molecular gas

dominated by H_2 . In extragalactic studies and in interferometry, as performed in this work, often flux densities S are measured instead of brightness temperatures. Accordingly, the calculation of the total molecular gas mass M_{molgas} of the observed region writes as (Solomon et al., 1997):

$$\begin{aligned} \frac{M_{molgas}}{M_{\odot}} &= \alpha_{CO1} \times L'_{CO1} & (4.12) \\ &= 1.75 \times 10^9 \left(\frac{\alpha_{CO1} R_{1J}}{\alpha_{MW}} \right) \left(\frac{S_{COJ}}{\text{Jy km/s}} \right) (1+z)^{-3} \left(\frac{\lambda_{obsJ}}{\text{mm}} \right)^2 \left(\frac{D_L}{\text{Gpc}} \right)^2. & (4.13) \end{aligned}$$

This mass-to-light ratio includes a correction for the Helium mass, namely 36% based on cosmological abundances. The ratio $R_{1J} = L'_{CO1}/L'_{COJ}$ corrects for the fact that the conversion factor is determined for the CO (1-0) line in case a higher line is probed. The correction accounts for the frequency leaving the Rayleigh-Jeans tail of the Planck spectrum and a subthermal population of the upper states (Tacconi et al., 2013). The ratios are empirically determined in studies of the so called rotational transition ladder of CO. The flux density S_{COJ} in the equation is velocity integrated over the line width. Furthermore, the redshift z , the observed line wavelength λ_{obsJ} and the luminosity distance D_L enter.

Converting the CO brightness to a mass usually is achieved by $\alpha_{CO1} = \alpha_{MW} = (4.36 \pm 0.90) M_{\odot}/(\text{K km s}^{-1} \text{ pc}^2)$, the Milky Way (MW) value. This conversion factor can be determined from virial masses via measurements of sizes and kinematics, from optically thin tracers of the density or from γ -ray emission. The different methods overall produce agreeing results. However, the conversion strongly depends on metallicity. Larger factors apply for lower metallicities because the surface layers of the molecular clouds which are dark in CO due to its photo-dissociation have greater depth (Wolfire et al., 2010; Genzel et al., 2012; Bolatto et al., 2013).

Observations of CO Emission As different CO rotational lines fall into the transparent window of our atmosphere depending on the observed redshift, one can study the contents of molecular gas in galaxies across cosmic time by millimeter and submillimeter observations of those lines (Bolatto et al., 2013). Indeed, CO was one of the first ISM molecules detected in these wavelengths. The molecular-gas distribution peaks in the inner galaxy regions, where H_2 even dominates over HI, the neutral hydrogen, in mass, while the latter component shows a different distribution in galaxies. More resembling to the location of molecular-gas regions are the ones of HII clumps, ionized hydrogen formed by star-formation feedback and the ionizing radiation from massive stars. These regions therefore are an indicator for young stars. This relation further underlines the strong connection between molecular gas and star formation in the build-up of galaxies.

Especially interferometers help to understand the spatially-resolved distribution of CO in local and high-redshift objects. The latter are analyzed with respect to their molecular gas in higher rotational transitions of CO, which require an understanding of the excitation physics in addition to the abundance ratios of the different molecules in the ISM. Recently,

the PHIBSS surveys have been building a first large census of molecular gas for redshifts around the cosmic peak of star formation. The majority of those observations covers galaxy-integrated measurements in order to provide a large sample. For a few objects spatially-resolved data were acquired serving as basis for this thesis work. Before presenting the latter, a short introduction to the PHIBSS observations is given.

4.1.2 The PHIBSS and PHIBSS2 Surveys

The Plateau de Bure HIgh-z Blue Sequence Survey (PHIBSS) consists of two large programs pursued by an international collaboration. The goal of these studies has been probing molecular gas within a large sample of normal SFGs at the massive end of the MS at high redshift. In this manner PHIBSS1 and 2 provide statistical samples of molecular-gas reservoirs in star-forming galaxies around the cosmic peak of star formation. Such measurements further fill the picture of early galaxy evolution with molecular gas being a main component of star formation. While there are large observational spectroscopic studies such as the SINS and KMOS^{3D} surveys with ~ 700 targets, which analyze the ionized gas in SFGs in great detail at this epoch (Förster Schreiber et al., 2009; Wisnioski et al., 2015), most of the observations by the PHIBSS surveys are unresolved and spatially-resolved molecular studies are still rare.

Census of Molecular Gas at High Redshift

In more detail, the PHIBSS programs measured the ^{12}CO emission of massive, main-sequence SFGs at redshifts $0.5 \leq z \leq 3$ covering three epochs of the cosmic star formation namely its building up, the peak epoch and its winding down from higher to lower redshifts. As such, this large program is a census of molecular gas content around the peak of cosmic star formation with 67 CO (3-2) detections in its first part PHIBSS (Tacconi et al., 2013) and with 88 detections in CO (2-1) or CO (3-2) in its follow-up PHIBSS2, which is still ongoing at the time of writing (Freundlich et al., 2018).

The PHIBSS sample was drawn without morphological selection from large lookback surveys in the sky fields COSMOS, AEGIS and GOODS-N, mostly with HST coverage. Since those surveys were mostly done in the UV, optical and IR, a slight bias against dusty and extreme objects is possibly present. The advantage of these parent samples however is that they have measured stellar masses, SFRs and morphologies. The galaxies relevant for the work presented here were selected from the All-Wavelength Extended Groth Strip International Survey (AEGIS) in the field of the so called Extended Groth Strip (EGS) (Davis et al., 2007; Noeske et al., 2007). From the DEEP2 survey spectroscopic redshifts are available for these sources (Newman et al., 2013). The redshift information determines which CO lines can be detected in which band.

Observations The PHIBSS program was started with the IRAM PdBI in 2008 and has just been completed with PHIBSS2 at the time of writing. Originally, the interferometer consisted of six antennas with 15 m-dishes and later, during PHIBSS2, was upgraded to

the current NOEMA operating nine antennas. In order to analyze molecular gas in galaxies near the peak of cosmic star formation the ^{12}CO (3-2) rotational line was chosen for the first part of PHIBSS, which shifts from its rest-frequency of 346 GHz into the 2 mm band for $z \sim 1.2$. The targeted objects were first observed in the compact configurations of the interferometer array, called C and D, with resulting FWHM beam sizes of $\sim 2''$. For a few targets high-resolution data were then acquired in the extended A and B configurations, delivering beam sizes of $\sim 0.6''$ for the five selected targets discussed in this work. The corresponding FWHM beam sizes and integration times are listed in Table 4.1 for all configurations combined.

For the object EGS13004291 the data set is particularly rich as will be explained later also because additionally the CO (5-4) line with rest-frequency 576 GHz was observed by PdBI as well as the CO (4-3) line with rest-frequency 461 GHz by both PdBI and NOEMA.

Source	Line	Configs	<i>RA</i>	<i>dec</i>	<i>z</i>	<i>t_{int}</i> [h]	Beam FWHM
EGS13003805	(3-2)	AC	$14^h 19^m 40.1^s$	$52^d 49' 38.5''$	1.23	9.5	$0.8'' \times 0.6''$
EGS13004291	(3-2)	AD	$14^h 19^m 15.0^s$	$52^d 49' 30.0''$	1.20	9.7	$0.7'' \times 0.6''$
	(4-3)	AB	$14^h 19^m 15.0^s$	$52^d 49' 30.1''$	1.20	28.2	$0.5'' \times 0.4''$
	(5-4)	A	$14^h 19^m 15.0^s$	$52^d 49' 30.1''$	1.20	5.0	$0.4'' \times 0.3''$
EGS13011155	(3-2)	ABD	$14^h 19^m 41.6^s$	$52^d 52' 55.7''$	1.01	30.2	$0.6'' \times 0.5''$
EGS13011166	(3-2)	ABC	$14^h 19^m 45.2^s$	$52^d 52' 27.3''$	1.53	31.4	$0.8'' \times 0.7''$
EGS13019128	(3-2)	ABC	$14^h 19^m 38.1^s$	$52^d 55' 40.5''$	1.35	12.3	$1.1'' \times 0.8''$

Table 4.1: CO observations, from left to right: source identifier in PHIBSS, CO line, array configurations of the IRAM interferometer, equatorial coordinates of the CO emission peaks in right ascension and declination, CO line redshift, total integration time and FWHM beam size of the combined data from all configurations.

In PHIBSS2 a similar approach has been followed detecting different CO lines. On average, seven hours of equivalent six-antenna integration time were invested per source for similar SNRs resulting in beam sizes of $1''$ to $5''$ and about 30 hours for the high resolution follow-ups. In this manner PHIBSS2 spent a total of 1068 hours on source between 2013 and 2017 targeting 120 sources on and around the MS, while in comparison PHIBSS was more focused on MS-targets.

Related to varying weather conditions the data were weighted according to the system temperature corrected for the atmosphere with a range between 100 K to 200 K. Source observations were interleaved with calibrator measurements of bright quasars within 15° of the science object every 20 minutes for measuring instrumental as well as atmospheric phase and amplitude fluctuations. The quasar MWC349 was used to calibrate the absolute

flux scale and in addition also LKH α 101 for PHIBSS2. The spectral correlators covered 1 GHz per polarization and after winter 2010 also 4 GHz having access to the wide-band correlator WideX.

For each galaxy the data from the different configurations are combined for maximum sensitivity and (u,v)-coverage as well as to prevent any large-scale flux of being washed out for the high resolutions. The beam sizes of the combined configurations with natural weighting on average range from 0.6'' to 1.0'', which represents 5 kpc to 8 kpc scales for the redshift range of the sample $1 \leq z \leq 1.5$.

The data calibration was performed with the CLIC package and the mapping and analysis with MAPPING as described in Chapter 2, both included in the IRAM GILDAS software system (IRAM, 2017). The cleaning of the data with the CLARK version of CLEAN produced the final cubes containing spatial and spectral information. The astrometry of these products is accurate to $\pm 0.2''$ (Tacconi et al., 2013; Genzel et al., 2013). The spectral resolution amounts to roughly 20 km/s for all the sample objects. This resolution corresponds to the channel width of the final cubes, after smoothing four to six original channels.

The velocity-integrated flux density of the CO emission is measured by the taking the average from the results of the two methods explained in Chapter 2 about interferometry. On the one hand, a gaussian (u,v)-fit can be applied to the visibilities and on the other the image cube can be used to integrate over the spectral channels of the source emission for an integrated line map.

Results The results range from measurements of the molecular gas masses and related properties to the comparison of these features to complementary findings for other galaxy components such as the ionized gas, stellar light and star formation. The overall picture emerges that the gas fractions

$$f_{gas} = \frac{M_{gas}}{M_{bar}} \quad (4.14)$$

of gas over baryonic mass, increase with lookback time from $\sim 10\%$ in local giant spirals as found in the COLD GASS survey of CO (1-0) with the IRAM 30 m-telescope (Saintonge et al., 2011a,b, 2017), up to $\sim 50\%$ for redshifts $z \sim 2$ (Tacconi et al., 2010; Genzel et al., 2015; Tacconi et al., 2018).

For $z > 0.4$, the HI contribution is not the dominant mass component in the ISM, as measured in absorption lines (Obreschkow & Rawlings, 2009; Lagos et al., 2011; Fu et al., 2012). Therefore, the gas mass is dominated by the molecular component M_{molgas} in the PHIBSS galaxies, such that the baryonic mass can be estimated by the sum of molecular gas mass and stellar mass M_* :

$$M_{bar} = M_* + M_{molgas} \quad . \quad (4.15)$$

At the same time a trend of diminishing gas fraction with larger stellar mass at the massive end of the MS shows that gas is either removed or transformed to stars in this regime.

Both these findings indicate that the decreasing gas fraction is a key player in the cosmic evolution of star formation.

Furthermore, the central role of molecular gas also strongly shows in the Kennicutt-Schmidt relation between the surface densities of SFR and molecular component

$$\Sigma_{SFR} \sim \Sigma_{gas}^N \quad , \quad (4.16)$$

which is found to be nearly-linear with the parameter $N \gtrsim 1$. The inversion of this relation expresses the depletion time of the gas without replenishment

$$t_{depl} = \frac{M_{molgas}}{SFR} \quad , \quad (4.17)$$

which slightly changes being lower at higher redshifts (Genzel et al., 2015; Tacconi et al., 2018).

High-Resolution Sample

In the PHIBSS samples, 12 objects were imaged in high resolution by using extended configurations A and B of the PdBI resulting in sub-arcsecond CO (3-2) maps. Seven of those sources were also targeted by the Cosmic Assembly Near-Infrared Deep Extragalactic Legacy Survey (CANDELS) (Grogin et al., 2011; Koekemoer et al., 2011) with the HST providing photometry of the stellar continuum in multiple bands.

Such high-resolution imagery can give complementary information next to the molecular gas properties traced by the CO, namely by an insight into the distributions of star formation, stellar mass and visual extinction by dust absorption. These quantities can be derived via Spectral Energy Distribution (SED) fitting for the objects at redshifts $z \geq 1$, for which the CANDELS photometry provides rest-frame far UV information in order to estimate the light extinction by dust.

This narrows the high-resolution sample down to four sources of the first part of the PHIBSS program. In follow-up observations at the PdBI, another PHIBSS object with CANDELS data was observed in extended configurations. In Figure 4.5 the five integrated CO line maps are shown together with HST H band contours and stellar mass peaks.

This selected sample of five targets is located in the EGS field at redshifts $1 \leq z \leq 1.5$ and predominantly covers the massive end of the PHIBSS parent sample as demonstrated in the $M_* - SFR$ plane of Figure 4.6. Detailed sample properties can be found in Table 4.2 on basis of Tacconi et al. (2013). For the lower-mass object EGS13019128 I exclude the data recorded in D configuration for consistent sub-arcsecond average beam sizes for the entire sample and optimum analysis of kinematics, which are not as prominent when D is included. The presented results are based on the CO (3-2) line if not stated differently and they agree with the work of Tacconi et al. (2013) if not outlined otherwise.

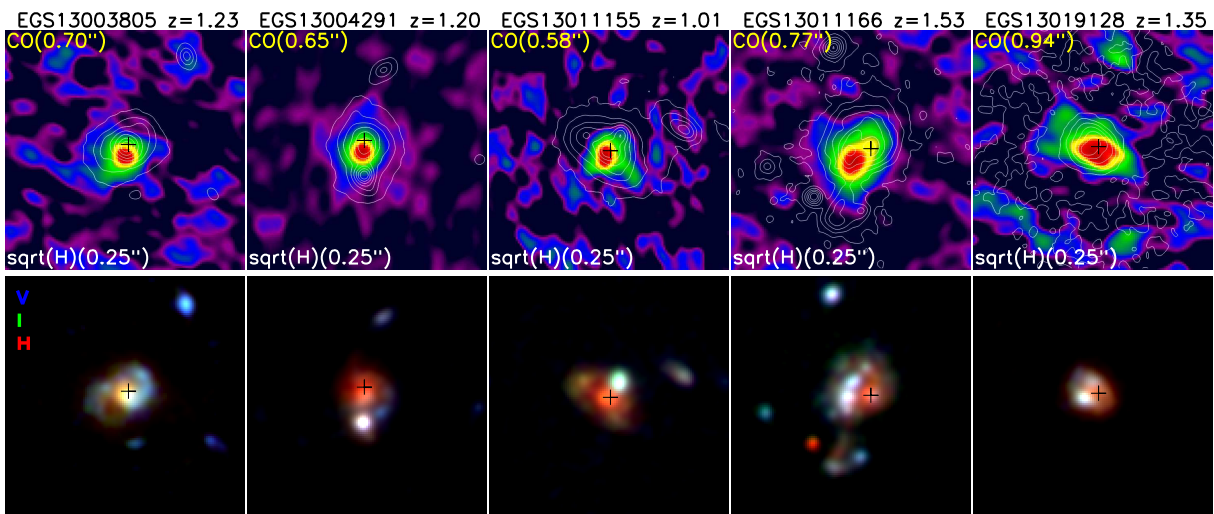


Figure 4.5: High-resolution maps of the presented sample: integrated CO (3-2) maps are shown in color together with the HST H band light distribution in contours in square-root scale (sqrt). The second row displays the composite images of V, I and H band maps in blue, green and red also in $0.25''$ -resolution and sqrt-scale. Stellar mass peaks are denoted as black crosses. The CO profiles show asymmetric distributions probably as a result of a clumpy morphology, which is also seen in the HST data. The CO emission peaks coincide with the stellar mass maxima within the astrometric uncertainties.

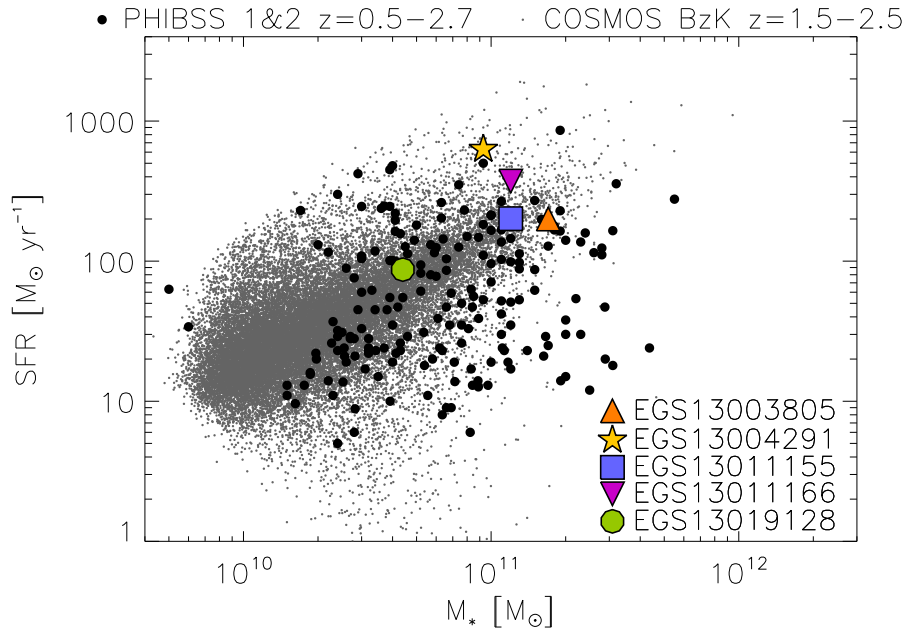


Figure 4.6: Location of the selected sample in the $M_{*} - SFR$ plane: the main sequence of star formation for redshifts $1.5 \leq z \leq 2.5$ is visualized by the corresponding BzK-selected sample in the COSMOS field with gray dots (McCracken et al., 2010). The black filled circles show the complete PHIBSS sample including parts of PHIBSS2, which was ongoing at the time of writing. The five PHIBSS sources imaged with high resolution and crossmatched with the CANDELS survey are denoted by the colored symbols and serve as selected sample for the work presented here. As a side note, the color selection based on B, z and K band selects gas-rich galaxies not biased against passive galaxies and SFGs that are highly reddened (Daddi et al., 2004, 2008).

Source	S_{CO} [Jy km/s]	σ_S [Jy km/s]	S_{CO}/σ_S	SFR [$\frac{M_\odot}{yr}$]	SFR_{SED} [$\frac{M_\odot}{yr}$]	M_* [M_\odot]	M_{molgas} [M_\odot]	M_{bar} [M_\odot]	f_{gas}	t_{depl} [Gyr]
EGS13003805	2.3	0.07	34	200	37	1.7×10^{11}	2.0×10^{11}	3.7×10^{11}	0.54	1.0
EGS13004291	5.4	0.08	63	630	195	1.3×10^{11}	4.4×10^{11}	5.7×10^{11}	0.77	0.70
EGS13011155	2.0	0.09	23	201	22	1.5×10^{11}	1.2×10^{11}	2.7×10^{11}	0.44	0.60
EGS13011166	2.0	0.04	46	373	56	7.9×10^{10}	2.6×10^{11}	3.4×10^{11}	0.77	0.70
EGS13019128	0.6	0.04	16	87	13	6.0×10^{10}	6.6×10^{10}	1.3×10^{11}	0.52	0.76

Table 4.2: Sample properties as derived in this work: the integrated flux densities of the CO (3-2) transition are given with errors and the resulting SNR as S/σ_S . The SFRs derived from the sum of UV and IR luminosities with a systematic uncertainty of $\pm 35\%$ are taken from Tacconi et al. (2013), while the values based on SED fitting were derived in this work with an uncertainty of $\pm 60\%$ on average. The stellar mass M_* comes with a maximum uncertainty of $\pm 30\%$ and for the molecular gas mass M_{molgas} a systematic uncertainty of $\pm 50\%$ is assumed as in Tacconi et al. (2013). On this basis the error on the baryonic mass $M_{bar} = M_* + M_{molgas}$ is $\pm 30\%$, for the gas fraction $f_{gas} = M_{molgas}/M_{bar} \pm 60\%$ and for the depletion time $t_{depl} = M_{molgas}/SFR$ also $\pm 60\%$. The derived quantities agree with the results in Tacconi et al. (2013) within the uncertainties, except for the SFRs due to different methodologies applied, which are explained in the section about SED fitting.

Four of these galaxies were classified as disks with an extended HST morphology and a significant, spatially-resolved CO velocity gradient. The other source, EGS13004291, shows features of a merger in the CANDELS data among others. This object also shows the highest SFR at fixed stellar mass and the largest reservoir of molecular gas within the PHIBSS sample, so it might be undergoing a starburst phase perhaps induced by the merger.

The following sections present a detailed analysis of the sample data and a closer look on EGS13004291. The standard cosmological parameters for a flat Λ -CDM Universe are applied for all the analysis described here, with the Hubble constant $H_0 \approx 70 \text{ km s}^{-1} \text{ Mpc}^{-1}$, the matter density parameter $\Omega_m \approx 0.3$ and the dark energy parameter $\Omega_\Lambda \approx 0.7$, consistent with the results from the Wilkinson Microwave Anisotropy Probe (WMAP) (Komatsu et al., 2011) and the Planck mission (Planck Collaboration et al., 2014). For the redshift range of the sample, $1 \leq z \leq 1.5$, the scale on sky of $1''$ corresponds to 8 kpc.

4.2 Spatially-Resolved Molecular Gas and Star Formation at $z \sim 1$

While the CO data from PHIBSS can be used as molecular-gas tracer as explained previously, stellar properties of the observed galaxies can be derived from rest-frame UV and optical photometry as seen by the HST. These continuum maps are used for a morphological analysis as well as basis for SED fitting in order to derive extinction-corrected maps of stellar mass and SFR surface density distributions. The latter technique requires imagery in four to seven different bands (Wuyts et al., 2013).

The CANDELS survey provides deep imaging in four bands for the presented sample, namely V (filter F606W) and I (F814W) taken by the Advanced Camera for Surveys (ACS) as well as J (F125W) and H (F160W) from Wide Field Camera 3 (WFC3), including respective noise maps. For the redshifts of the sample this corresponds to rest-frame UV and optical wavelengths respectively (Grogin et al., 2011; Koekemoer et al., 2011). As a basis for the following data analysis, the images of the sample galaxies were cut from the CANDELS mosaics in the EGS field to a $7'' \times 7''$ size and have a pixel scale of $0.06''$. On this basis I extracted the CO data such that they fit this size and pixel scale.

Since the HST bands have different resolutions, one needs to match those for further combined analysis. Therefore the higher-resolution V, I and J band images were smoothed in order to obtain the broader H band PSF of $0.18''$ in FWHM for consistency. This task was performed with the PSFMATCH algorithm of IRAF written at the National Optical Astronomy Observatory (Tody, 1993). As another step towards consistent photometry, sky subtraction was performed for the PSF-matched maps. For comparison with the CO data, these HST maps are then rotated such that North is oriented upwards. The products can be found in Figure 4.7.

For a better comparison to the CO data I use further smoothing by convolution of the maps with a Gaussian kernel for a resolution of $\sim 0.3''$ of the continuum maps or the

products derived from them. This level corresponds to roughly half the CO resolution and does not fully disregard the high resolution of the HST observations. Furthermore, the continuum maps, or the products derived from them, are frequently displayed in square-root scale in this work for a better visualization of small values in the outskirts of the galaxies. The astrometric error on the CANDELS data amounts to $\pm 0.5''$.

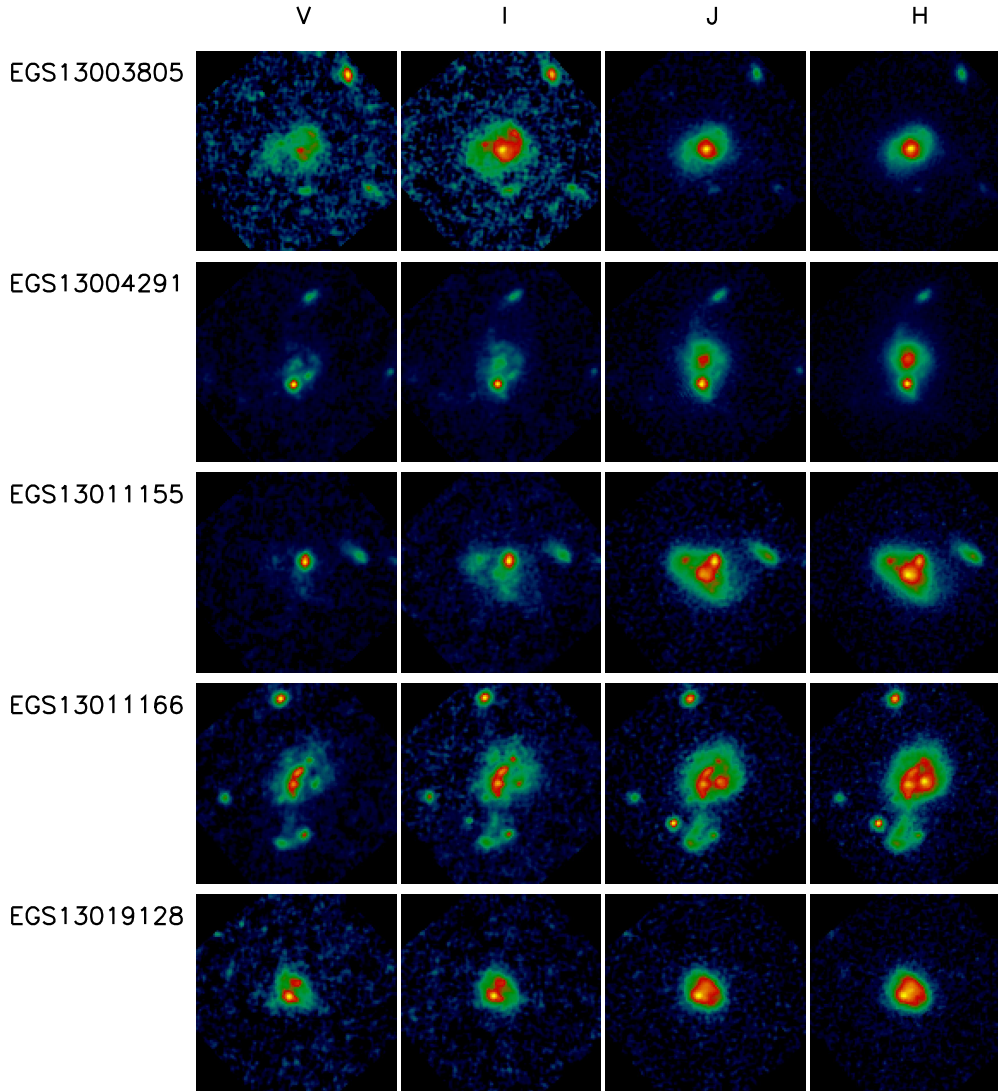


Figure 4.7: Imaging from the Hubble Space Telescope: each row shows the V, I, J and H band light distributions for one particular object as observed in the CANDELS survey (Grogin et al., 2011; Koekemoer et al., 2011). The images are shown in square-root scale and have sizes of $7'' \times 7''$, a pixel scale of $0.06''$ and a matched resolution of $0.18''$ FWHM as defined by the H band PSF. For the redshifts $z \sim 1$ of the sample, $7''$ correspond to roughly 60 kpc.

While the rest-frame UV emission is predominantly produced by young, hot, short-lived O- and B-type stars and therefore associated with star-forming regions, rest-frame optical light covers the majority of all stellar populations, young and old. However, the HST photometry does not resemble the intrinsic stellar light distribution because the latter is influenced by dust extinction and reddening as well as spatial variations in the star formation history. As a consequence, an apparent red stellar population can be intrinsically red because it is old or it consists of younger stars reddened by extinction (Wuyts et al., 2013). A reasonable interpretation of galaxy properties from HST imaging can therefore be attempted best by SED modeling over a wide wavelength range, which provides estimates of stellar mass and SFR corrected by the derived extinction as described in the next section together with other methodology aspects.

4.2.1 Analysis of Properties from Stellar Continuum and Molecular Emission

In this section I outline the methodology used for the data analysis. First, the method of SED fitting is introduced, which provides galaxy properties such as stellar mass and SFR on basis of broadband photometry. Then I continue with the extraction of kinematics from the CO data cubes, before I conclude with morphology fitting and dynamical modeling for further analysis of the kinematics.

SED fitting

For deriving stellar properties from the HST imagery, I perform SED fitting following the procedure described in Wuyts et al. (2012, 2013). The basic approach starts with sky-subtracted HST imagery with matched PSF, on which I then apply pixel binning and afterwards the Stellar Population Synthesis (SPS) models using the code called Fitting And Assessment of Synthetic Templates (FAST) (Kriek et al., 2009).

As a first step, segmentation maps are produced by SExtractor (Bertin & Arnouts, 1996) for all sources in order to define the image pixels which belong to the corresponding galaxy. I use H band data for this step as it covers the longer, redder wavelengths and by that samples the bulk of the stars being more representative for the global morphology of the galaxies than the other bands.

The pixels within these segmentation maps are then binned using the Voronoi scheme from Cappellari & Copin (2003) to account for the variable SNRs across the maps. The applied criterion for the binning is an SNR of 10 per spatial bin in the H band such that faint, outer regions typically show bins covering more pixels than the bright inner regions of a galaxy. The resulting bins also serve as the basis for the other bands in order to probe the same physical regions in all the photometry.

Redshift Information Next to the HST imagery as required input, the redshifts can be optionally fixed for the SED fitting either by spectroscopic measurements for instance as available from the CO data or by photometric ones determined by the algorithm Easy

and Accurate redshifts from Yale (EAZY) (Brammer et al., 2008) on the basis of the HST multi-wavelength photometry. I crosscheck the photometric redshifts as derived by this code with the spectroscopic ones from the CO measurements as well as with the redshifts determined from grism spectroscopy of the 3D-HST survey performed in four of five CANDELS fields (Momcheva et al., 2016) and values from optical spectroscopy in the DEEP2 Galaxy Redshift Survey (Newman et al., 2013). The comparison can be viewed in Figure 4.8.

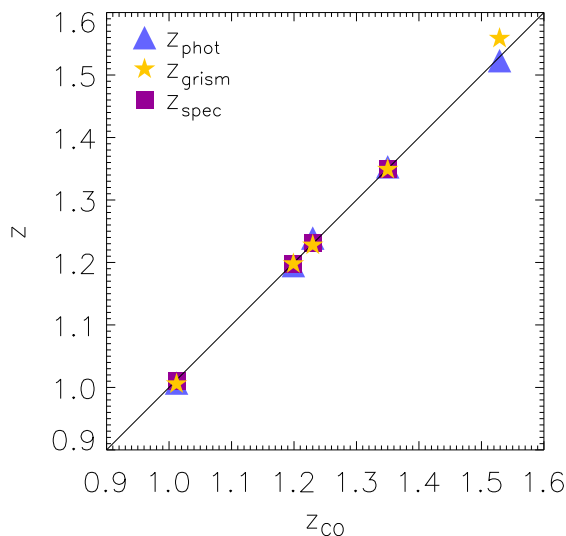


Figure 4.8: Comparison of different redshift measurements: the CO redshifts z_{CO} agree with the photometric values z_{phot} derived with the algorithm EAZY (Brammer et al., 2008). In addition, the grism spectroscopy redshifts z_{grism} of the 3D-HST survey (Momcheva et al., 2016) are shown as well as the available measurements from optical spectroscopy in the DEEP2 Galaxy Redshift Survey z_{spec} (Newman et al., 2013). The deviating grism value of EGS13011166 is attributed to a particularly noisy spectrum at the edge of the spectral band.

Essentially, the photometric redshifts from EAZY are in agreement with all the spectroscopic measurements. For the source EGS13011166, the grism redshift deviates from the other measures, because it is determined from a particularly noisy spectrum at the edge of the spectral band. Due to this consistency of measured redshifts, the CO redshifts as given in Table 4.2 are included in the SED modeling.

Stellar Population Synthesis With the fixed redshifts, the number of free parameters in the SED fitting decreases by one. After these preparatory steps, the photometry of each spatial bin is fitted individually with SPS models from Bruzual & Charlot (2003) in FAST. I assume a Chabrier Initial Mass Function (IMF) (Chabrier, 2003), ages since the

onset of star formation between 50 Myr and the age of the universe, V band extinction in the range $0 \text{ mag} \leq A_V \leq 4 \text{ mag}$ with the Calzetti reddening law (Calzetti et al., 1994; Calzetti, 1997; Calzetti et al., 2000; Wuyts et al., 2011b), fixed solar metallicity of the stellar population across the galaxy and an exponentially declining Star Formation History (SFH) $SFR \propto e^{-t/\tau}$ with e-folding times τ from 10 Gyr down to 300 Myr. FAST performs a χ^2 -fitting of every point within the six-dimensional cube of model fluxes for all filters and the full stellar population grid given by the input parameters. The redshifts are fixed to the closest value in the grid according to the input values.

The Calzetti reddening law links the observed flux density of the stellar continuum $F_o(\lambda)$ to the intrinsic one $F_i(\lambda)$ via the observed color excess of the stellar continuum $E_{s,B-V}$ and a reddening curve as total-to-selective extinction $k(\lambda) = A(\lambda)/E_{s,B-V}$:

$$F_i(\lambda) = F_o(\lambda) 10^{0.4E_{s,B-V}k(\lambda)} \quad . \quad (4.18)$$

The color excess describes the difference between observed and intrinsic color ($B-V$) given by the bands B and V and can also be written in terms of the total B and V extinctions $E_{B-V} = A_B - A_V$ as selective extinction. The reddening curve is determined in empirical studies. The visual extinction by dust A_V scales linearly to the reddening when it acts as a foreground screen removing photons from the Line Of Sight (LOS) by absorption and scattering by dust grains. This assumption might not hold for large areas with patchy dust distribution. By assuming a uniform foreground screen of dust, the SFR derived by SED fitting can miss large fractions of SFR in the dusty SFGs at high redshift, compared to methods that include IR luminosities next to the UV measures. As such, the SFR from SED fitting can be considered a lower limit (Wuyts et al., 2011b).

An exponentially declining SFH is also a rather simplistic first approximation for the actual evolution of galaxies, but the resulting SED-derived stellar mass distribution, the product mainly used in this work, is most robust against variation and uncertainties regarding the assumed model of SFHs. A delayed exponentially declining SFH following $SFR \propto t e^{-t/\tau}$ usually produces similar results in the SED fitting.

The code also calibrates confidence levels, in this case by 100 Monte Carlo simulations. In the simulations, the observed photometric fluxes are randomly perturbed within their errors and also fitted with SPS models. In addition, a rest-frame template error function for the fluxes is included as derived by EAZY in order to take into account the varying uncertainties of the SPS models across the fitted wavelength range. The 1σ -confidence interval is defined by the χ^2 -level of the fit in the grid of the original parameters which confines 68% of the simulations. For a given parameter, the interval is then given by the minimum and maximum value in this defined range.

The final output from FAST therefore consists of maps of the best-fit stellar population properties and maps corresponding to the lower and upper limit of the confidence interval. The derived quantities are V band screen extinction A_V , SFR, stellar mass M_* , star formation timescale τ and age. These products then are also rotated such that North is oriented up and the results for one source are demonstrated in Figure 4.9 for the properties needed for the further analysis, namely visual extinction, SFR and stellar mass.

The products derived in SED fitting can be compared to the CO data, tracing not only the spatial distribution of the molecular gas but also kinematic information, which is extracted as explained in the following.

Extraction of Kinematics

Since the CO cubes produced from interferometric observations contain both spatial and spectral information, kinematic properties can be derived such as velocity and velocity dispersion maps. I perform this task in QFitsView, a Flexible Image Transport System (FITS) file viewer, with its interactive language DPUSER (Ott, 2018). A gaussian profile is fitted to the CO line throughout the data cube by putting in initial estimates of the center wavelength of roughly 2 mm and FWHM of the line as well as a lower flux threshold for which a fit is attempted. The output cube provides maps of the best-fit background, continuum, line center and FWHM, their errors and the χ^2 -map of the fit.

The map of the line center encodes the radial velocity v , with which the observed material is moving along the LOS for every pixel and therefore resembles a velocity map. The velocity dispersion map can be extracted from the line FWHM. The velocity dispersion is usually treated as standard deviation σ of the Gaussian profile, which relates to its FWHM via $v_{FWHM} \approx 2.35\sigma$. Dividing the FWHM map by 2.35 results in the desired map of the radial velocity dispersion along the LOS. Similarly, the errors on the velocity dispersion are derived from the FWHM errors.

From these two-dimensional maps of velocity and velocity dispersion, rotation curves can be deduced by plotting the map values along the line of the largest velocity gradient. For systems dominated by rotation, the largest gradient corresponds to the major axis of the galaxy. The orientation of this axis on the sky as viewed by the observer is denoted Position Angle (PA). For the cases in the sample where two velocity minima or maxima are found, arguments of the total symmetry in velocity and velocity dispersion suggest to draw the largest gradient through the middle of these peaks. The rotation curves are the kinematic profiles along this axis expressed as a function of offset δ from the zero point at the kinematic center.

Deviations from Intrinsic Properties The kinematic information as derived from the observations deviates from the intrinsic properties. On the one hand, the velocity gradient decreases, with the peak velocity shifting to smaller values and larger radii, and on the other hand, the velocity dispersion inflates from a flat curve to a Gaussian-shaped one with higher ground level. The following effects contribute to these deviations.

First of all, the velocity gradient $v(\delta)$ within the galaxy is affected by its orientation towards the observer, in particular by its inclination i such that the observed velocity $v_{obs}(\delta)$ as a function of offset δ becomes:

$$v_{obs}(\delta) = v(\delta) \times \sin(i) \quad . \quad (4.19)$$

While face-on systems with inclinations close to 0° show a very small velocity gradient, if

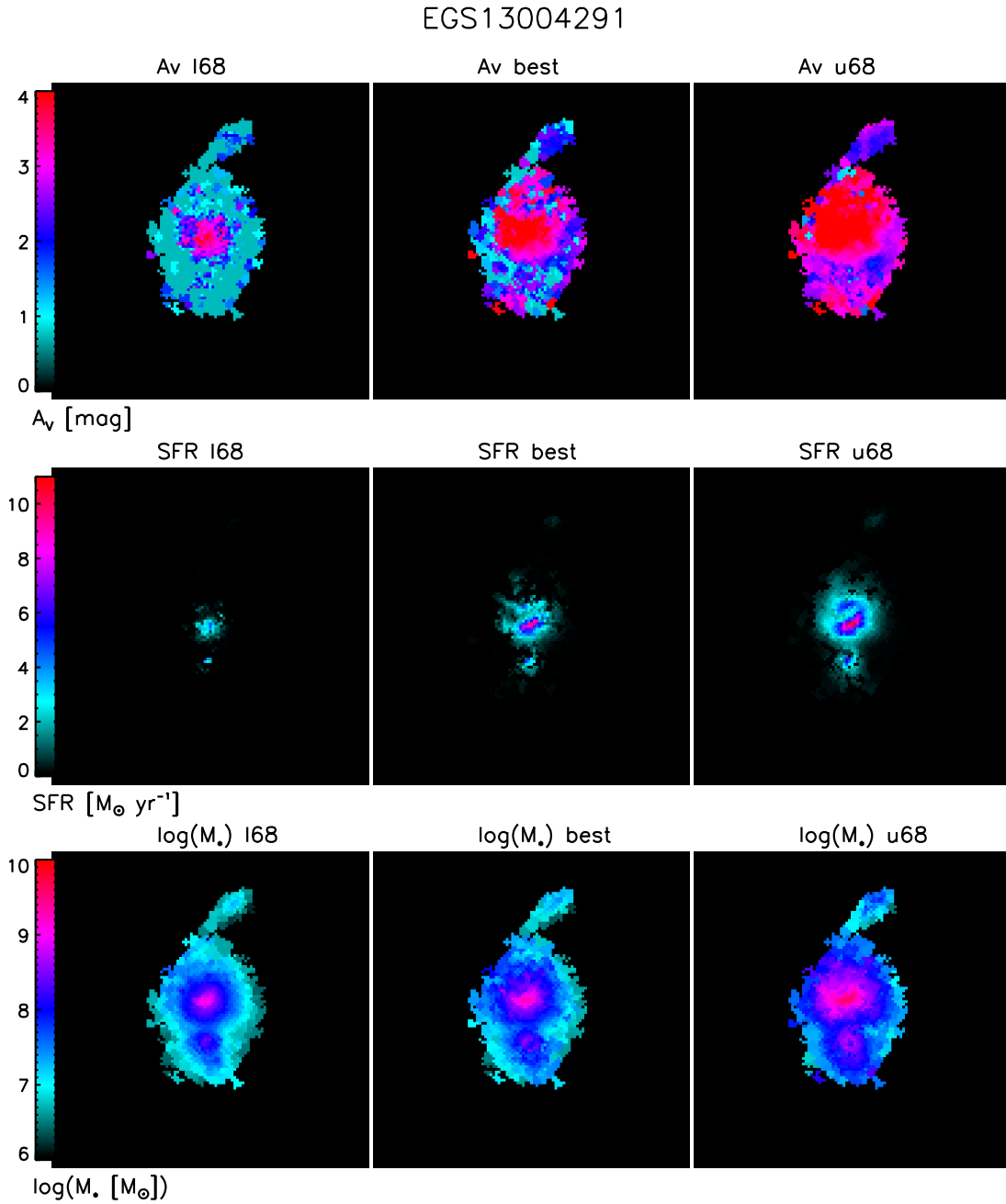


Figure 4.9: Stellar-population properties of EGS13004291 as derived from the resolved SED modeling with FAST (Kriek et al., 2009). In particular, the maps of the lower (l68) and upper limit (u68) fits of the 68% confidence interval are displayed as well as of the best fits. The individual rows show these results for the three parameters visual extinction A_V , SFR and stellar mass M_* . For the different objects, the uncertainties of these properties summed over the given area span ranges from 10% to 70%, 10% to 200% and 0% to 30% of the best-fit value respectively.

at all, more edge-on disks ($\lesssim 90^\circ$) can reveal a more realistic picture of the actual velocity gradient present in the system.

On top of the orientation come beam-smearing effects caused by the spatial and spectral resolution of the observations. The spatial beam smearing comes from the instrumental PSF, in this case the interferometric beam, which enters in convolution with every spatial plane of the flux density cube that has two spatial dimensions and a velocity dimension. The limited spatial resolution causes different LOS velocities being combined into a single spatial pixel, which leads to the deviation in observed kinematics mentioned above.

Another effect is the instrumental broadening of the spectral line attributed to the spectral resolution, which increases the isotropic velocity dispersion σ_0 . Due to these factors the measured LOS dispersion curve as function of radius $\sigma_{obs}(\delta)$ is

$$\sigma_{obs}(\delta) = \sqrt{\sigma_0^2 + \sigma_{spectral}^2 + \sigma_{beam}^2(\delta)} \quad (4.20)$$

with terms of beam smearing $\sigma_{beam}(\delta)$ and the spectral broadening $\sigma_{spectral}$. The latter effect is negligible in millimeter and sub-millimeter observations.

As mentioned before, the overall consequences of the outlined factors are an increase and broadening in observed velocity dispersion and a decrease of the velocity gradient. The discrepancies to the intrinsic properties are most prominent in the galaxy centers and become marginally small in the outer parts except for the instrumental broadening, which adds an isotropic floor to the velocity dispersion.

Given that the observed kinematics mostly trace the inner parts of the sources I perform dynamical modeling to reproduce the observations from intrinsic properties including orientation, spatial beam smearing and instrumental broadening effects. This approach requires input parameters such as the inclination, effective radius and Sérsic index of the galaxy. These morphological properties can be deduced from two-dimensional fitting of the HST imagery as explained in the following.

Morphology Fitting

The morphological information of the stellar continuum in the HST imagery can be used for good estimates of input parameters for the dynamical modeling of the CO kinematics. Especially a valid estimate for the inclination is needed in this respect. For this reason, I fit Sérsic models to the two-dimensional light distributions with GALFIT (Peng et al., 2002, 2010).

This algorithm performs nonlinear least-squares fitting using the Levenberg-Marquardt technique. Many different parametric functions can be used as models such as Gaussian, Moffat, Nuker and also Sérsic profiles. Another strength of this code is the ability to fit multiple components with individual profiles simultaneously. Models for clumpy morphologies as present in the sample can profit from such an approach.

Sérsic Model For the modeling, the following parameters are fitted: center position, integrated magnitude, effective radius R_e , Sérsic index n_{Sersic} , axis ratio b/a and PA. The

observed axis ratio of the galaxy is translated into its inclination i by the simple approximation $\cos(i) = b/a$. As mentioned before, the fits are performed on basis of the Sérsic profile of the surface brightness Σ as a function of radius r :

$$\Sigma(r) = \Sigma_e e^{-\kappa((r/R_e)^{1/n}-1)} \quad , \quad (4.21)$$

where Σ_e is the surface brightness at R_e and κ depends on n_{Sersic} such that half of the total flux is contained within the R_e also known as half-light radius. The Sérsic model is a general description for different types of galaxies or their components (Sersic, 1968).

Star-forming galaxies typically are built of disks with Sérsic indices of order $n_{Sersic} \sim 1$ corresponding to an exponential decrease of surface brightness with radius. Additional central light concentrations in the form of spherical bulges have higher indices close to the de Vaucouleurs profile with $n_{Sersic} = 4$ (de Vaucouleurs, 1948). Such profiles are known from elliptical galaxies, which show nearly no star formation in comparison.

As input I use the two-dimensional light distributions as well as the corresponding noise maps as input such that relative weights can be attributed to the pixels during fitting. Further inputs are the H band PSF to account for image smearing and a constraint file which sets boundaries for the estimated Sérsic index from 0.2 to 8.

Light Distribution As a first step I perform single-component fits applying a Sérsic function for the galaxy and a flat background sky profile for the V, I, J and H band light distributions from HST. In order to estimate the quality of the fit I do a visual inspection and compare the derived PA to the estimates from the CO kinematics. Both checks reveal that the rest-frame UV-light distributions as seen in the V and I band only represent individual clumps of star-forming regions with low extinction rather than the global structure of the galaxy as such.

For the objects EGS13004291 and EGS13011155 this effect is particularly strong, where none of the bright rest-frame UV clumps is located in the galaxy centers as can be seen in Figure 4.7. The visual extinction levels in those areas, as derived in SED fitting, are the highest among the sample and smoothly cover the galaxy centers, while the other extinction maps show an asymmetric, patchy distribution not peaking in the mass centers.

Thus, interpreting light distributions in order to derive global morphological properties should be handled with caution. Therefore, I focus on the results from the other bands containing the rest-frame optical information and giving a more realistic perspective of the overall galaxy morphologies.

Overall the J and H band results seem to agree with the kinematic orientation of CO except for the object EGS13004291, where the derived PAs deviate by more than 40° . Therefore, I add more Sérsic components to the fits for this object, which seems to consist of at least two spherical parts in the rest-frame optical, but the discrepancy in the PA remains as shown in Figure 4.10.

As a consequence, I also fit the stellar-mass distribution for EGS13004291, which indeed provides a better description, also demonstrated in the figure. Therefore, this approach is followed for all objects, as one can expect a more global picture of the galaxies from the

stellar-mass distribution, extracted from the stellar light but corrected for extinction in SED fitting.

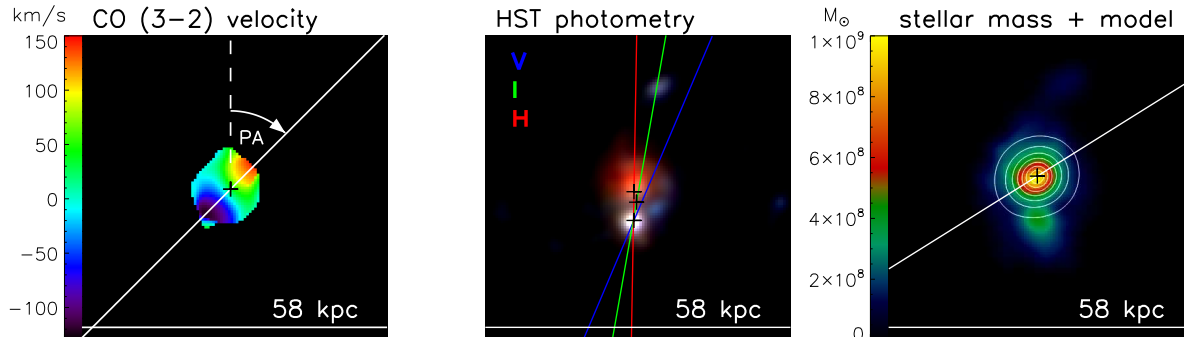


Figure 4.10: Position angles in EGS13004291 derived from different tracers, from left to right: CO (3-2) map with colors that show blue to red-shifted velocities, HST V, I, H photometry in square-root scale (blue, green, red) and the distribution of stellar mass in colors with the GALFIT model in white contours. The colored lines correspond to the derived position angles of the underlying colored quantities and the black crosses mark the respective model peaks.

Stellar-Mass Distribution Before applying GALFIT to the stellar-mass maps I smooth these to a $0.35''$ -resolution by convolving with a Gaussian while keeping the total mass constant in order to remove the discrete structures from the spatial bins of the SED fitting result. A corresponding smoothing width of five pixels is chosen, also for the respective PSF input. Matching noise maps of stellar mass can be derived using the mass-to-light ratio on basis of the H band light distribution and its noise map.

As previously, I add one or more components to the fit whenever the found PA deviates more than a few degrees. This mostly corresponds to a bulge-disk decomposition, with additional clumps in some cases. The best measure of orientation, reflected in the quantities PA and inclination i , is then regarded to come from the disk component. However, for the other morphological parameters such as half-light radius R_e and Sérsic index n_{Sersic} the fitting of one component is considered to be more meaningful, as the dynamical modeling of the CO kinematics in this work is performed with a single component. Therefore, the orientation of the disk component is inserted and fixed in the single-component fitting to derive the final morphological parameters.

Inferred Corrections Multiple components are needed to find the correct orientation of EGS13011166. This source shows a southern extension, which displays signatures of being decoupled from the main component to a certain degree, also visible in the CO kinematics. The resulting PA from the GALFIT model on the stellar mass distribution of EGS13011166 is consistent with the CO value when fitting three Sérsic functions including one for the southern extension.

Source	R_e [kpc]	n_{Sersic}	i [°]
EGS13003805	1.6	3.4	52
EGS13004291	3.0	1.4	27
EGS13011155	3.2	1.9	61
EGS13011166	3.9	1.5	40
EGS13019128	3.1	0.7	34

Table 4.3: GALFIT results on the stellar-mass surface density, from left to right: source identifier in PHIBSS, effective radius, Sérsic index and inclination as calculated from the fitted axis ratio via $\cos(i) = b/a$. The average effective radius and Sérsic index for this sample lie at (2.9 ± 0.8) kpc and 1.8 ± 1.0 .

I also add an additional component to the fit of the J band for EGS13003805, where the single-component fit is misled by the prominent spherical bulge of the source. For consistency, also the H band and the stellar mass distribution are fitted with an additional component with only minor changes to the resulting PAs of $\leq 5^\circ$. Because both the fit in H band and stellar mass produce a Sérsic index of $n_{Sersic} = 3$, I fix this value for the J band fit. If this correction is not applied, the fit produces an inconsistently large effective radius although J and H usually show very similar morphologies in the sample.

In order to correct for the wrong orientation in the light fits of EGS13004291, I fix the inclination to the value determined on the stellar mass distribution, $i = 27^\circ$, and the PA corresponding to the largest gradient found in the CO kinematics. This step ensures that the resulting parameters can be compared to the ones from the other tracers. Probably, the orientation, being close to face-on, challenges finding the correct disk model only on the basis of light distributions, which suffer from extinction and clumpy morphology.

Fitting the rest-frame optical light distributions of EGS13011155 shows a significant discrepancy in inclination compared to the result from the fit onto the stellar-mass distribution. Adding two additional Sérsic components to the fit of the light distributions brings the values into agreement. This three-component model accounts for a bulge and disk component as well as for the external clump seen in EGS13011155.

With the orientations checked by multiple-component fits, the final single-component GALFIT models for the stellar mass distributions are visualized in Figure 4.11 together with the residuals. The resulting structural parameters are summarized in Table 4.3. The average values for effective radius and Sérsic index of the sample lie at (2.9 ± 0.8) kpc and 1.8 ± 1.0 .

Comparison to the Distribution of the CO Emission For an additional cross-check of the resulting orientation parameters I also apply GALFIT single-component models to the CO maps. For all objects except EGS13004291, the derived inclination deviates from

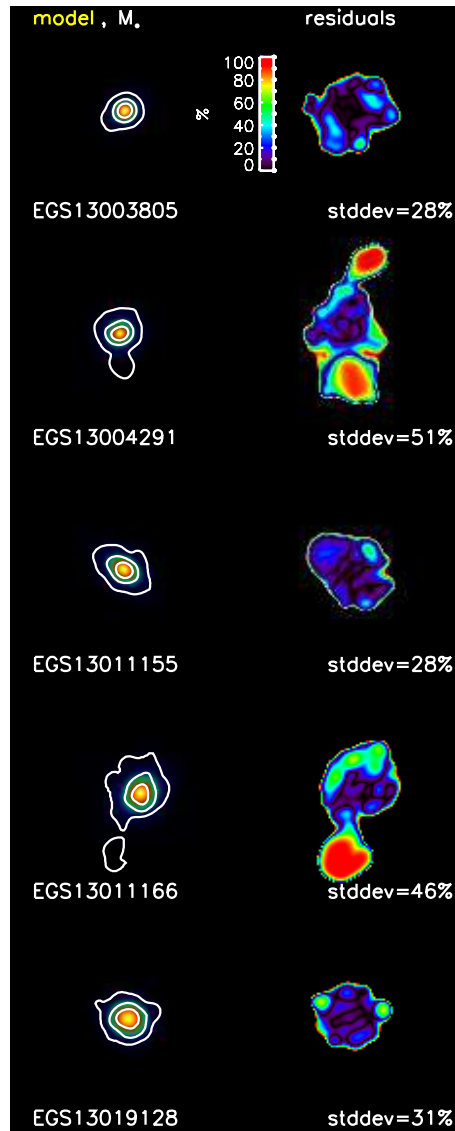


Figure 4.11: GALFIT models and residuals on the basis of the stellar-mass distributions as derived from SED fitting. The latter are presented in white contours and the corresponding models in color, both in square-root scale. On the right the residuals between data and model are displayed in a color scale indicating the percentage of the residuals with respect to the data. The standard-deviation values of the residuals (stddev) amount to roughly 30% for all objects except for EGS13004291 and EGS13011166 due to southern extensions from the main body. Nevertheless, a single-component fit was used to determine the global morphological properties without decomposition, but using the disk orientation from multiple-component fits, whenever bulges or clumps had a distorting influence on the single-component orientation. Therefore, the high residuals in the side regions that were not fitted here can be ignored.

the value of the stellar mass fit by more than 15° . Due to the higher underlying resolution, the inclination value from the stellar-mass profile, consistent with the fit result of the stellar light, is regarded as more reliable than the results from the less resolved, asymmetric CO distributions. Therefore, I fix the inclination to the value from the stellar-mass fit. This adaption always results in PAs consistent with the other tracers within the error bars.

EGS13003805 also needs a fix of Sérsic index $n_{Sersic} = 1$ for the other fit parameters to converge to realistic values. Adding more components to the fitting is of less use here in contrast to the previous modeling, since the CO emission is always concentrated in a single region.

Position Angles from Different Tracers Figure 4.12 demonstrates the comparison between the final PAs found by the different tracers. After these modifications not only inclination but also PA and Sérsic index agree between the different tracers within the uncertainties of $\pm 10^\circ$, $\pm 20^\circ$ and ± 0.6 . The only exception is the Sérsic index of EGS13003805, which shows values close to $n_{Sersic} = 3$ other than the necessary fix of $n_{Sersic} = 1$ in the CO fit.

The effective radii vary more between the different tracers, mainly because the stellar mass is more concentrated than what the light distribution not corrected by extinction reveals. The standard deviation of R_e among the galaxies for the individual tracers is ~ 1 kpc, which is considered as measure of uncertainty for this quantity.

Quality of Morphology Estimates from Different Tracers In summary, the best agreement with the PA from the CO kinematics is achieved for the stellar-mass models. Using the CO GALFIT models is also successful when the inclination parameter as derived from the stellar mass is applied. Otherwise, the fitted orientation in the CO maps is not reliably determined due to the asymmetric distribution of the emission.

Fitting the light distributions can be problematic, in particular for the rest-frame UV part, which strongly deviates from the CO PA value because it rather traces individual clumps than the global morphology of the galaxies. The rest-frame optical bands J and H are more suitable in this respect, however they nevertheless fail when fitted for the object EGS13004291 even if multiple component fits are applied.

I thus conclude that rest-frame UV light distributions should not be used as morphology tracers. Rest-frame optical can be trusted in most cases, but should nevertheless be used with some caution. Among the rest-frame optical, the H band fits are the most robust. Whenever available, a stellar mass fit is the most preferable, where morphological parameters need to be derived.

For this sample only the model for EGS13011166 shows a larger offset of 20° from the CO PA based on a single-component fit of the stellar mass, which is within the estimated PA uncertainty of $\pm 20^\circ$. Thus, even for irregular morphologies as in this sample, a single-component fit can serve as a first approximation. This approach also has the advantage of determining morphological parameters for the overall distribution of a galaxy instead relying only on sub-components.

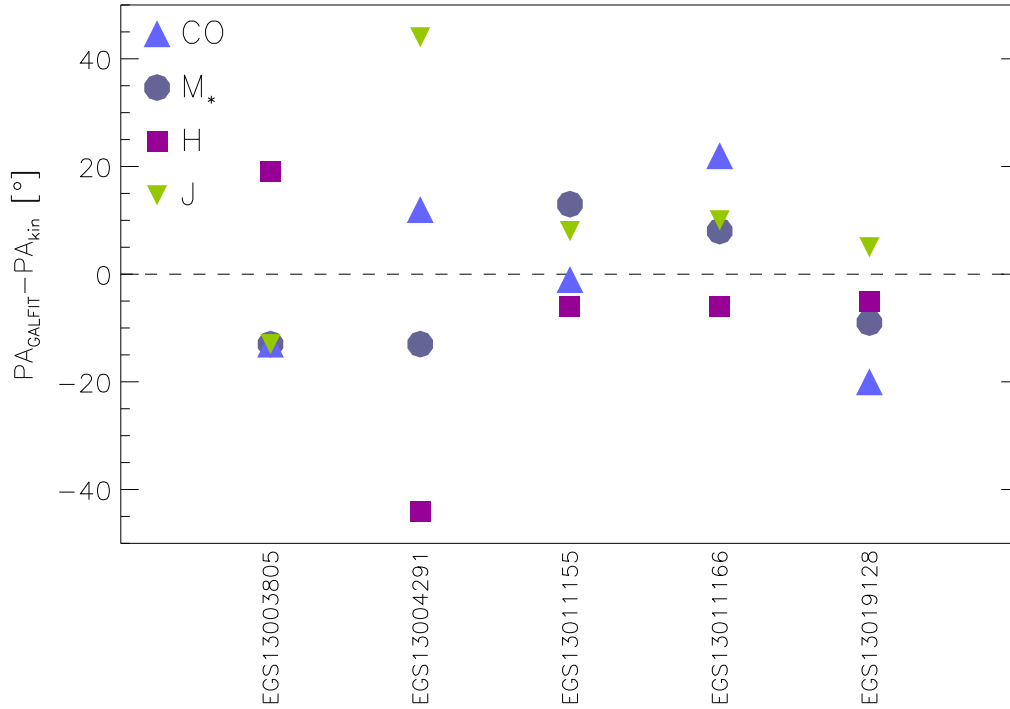


Figure 4.12: Comparison of position angles from different tracers: the PAs as determined by fitting of CO, stellar mass, H and J band maps with GALFIT are plotted against the PA measured in the CO kinematics. The error on the measurements is estimated to be $\pm 20^\circ$. The stellar mass and the CO models show the best agreement in this respect with standard deviations of 12° and 17° . For this result, the inclination of the CO models had to be fixed to the best-fit value of the stellar-mass model for all objects except for EGS13004291. The rest-frame optical bands J and H achieve the best matches among the light distributions with standard deviations of 21° and 23° . They trace more global properties than the rest-frame UV bands, however, for the source EGS13004291 all fits of light distributions miss its true orientation, which is much better traced by the fit to the stellar-mass profile.

As a side remark, this method can also be applied in opposite direction for cases where the CO PA is unclear or completely unknown. Under such circumstances the rest-frame optical light or optimally the stellar surface-density distribution can be fitted to obtain an estimate of the PA. This might be particularly interesting whenever planned observation require such an estimation for example for positioning the slit for spectroscopic measurements. For this application, the choice between the use of single- or multi-component fits has to be made without direct comparison to available kinematics.

The parameters determined by the Sérsic-disk fitting can be used as input for the dynamical modeling of the CO kinematics, which is outlined in the following.

Dynamical Modeling

For the dynamical modeling of the observed CO kinematics, the DYnamical Simulation and Modelling ALgorithm (DYSMAL) as described in Cresci et al. (2009) and Davies et al. (2011) is applied. Via this approach, the intrinsic kinematic properties of the observed sample can be deduced by including the galaxy properties and beam smearing effects as discussed previously in 4.2.1.

Mass Model with Circular Orbits The input parameters are used by DYSMAL to model the flux of a face-on disk galaxy with a radial mass profile of choice, in this case defined by a Sérsic function. This model cube with three spatial dimensions is then rotated regarding the set inclination and position angle to the actual projection on sky. In a next step the LOS velocity $v(r)$ for each pixel is determined describing the large scale motion in the system by the following procedure.

The velocity can be calculated for a given mass on a circular orbit in the disk, as first approximation, enclosing the mass $M(r)$, where the centripetal force equals the gravitational one such that

$$v_{circ}^2(r) = \frac{GM(r)}{r} \quad , \quad (4.22)$$

with r denoting the radius from the galaxy center and the gravitational constant G . On this basis, a Gaussian emission line profile can be modeled for each pixel with coordinates (x, y, z) scaled by the corresponding flux and with a center determined by the LOS velocity. The width of the profile is defined by the specified isotropic velocity dispersion σ_0 .

The Gaussian profiles of all z coordinates at a fixed position (x, y) are then summed up resulting in a cube with two spatial axes and one velocity axis. In the end this modeled cube is convolved with the beam size in each spatial plane in order to cover the effect of spatial beam smearing seen in the observations. From this cube, an integrated flux map and kinematic maps can be derived as introduced previously in Chapter 2 about interferometry.

In Figure 4.13 a DYSMAL model is demonstrated in terms of a flux, velocity and velocity dispersion map of a rotating exponential disk, which has the Sérsic index $n_{Sersic} = 1$.

Model Parameters The galaxy properties as derived by GALFIT models entering DYSMAL are inclination, PA, effective radius and Sérsic index. Additional input parameters are systemic velocity, centroid coordinates, rotationally supported or dynamical mass, isotropic velocity dispersion and geometrical thickness of the disk. The isotropic velocity dispersion is a free fit parameter with an initial value estimated by the minimum value in the velocity dispersion curve. Similarly, the rotationally supported mass is fitted with the starting value determined by the baryonic mass as the sum of stellar and molecular gas mass as introduced by (4.15).

The thickness is chosen here to resemble a thick disk with $h_z/R_{disk} = 0.25$ as it is known from massive SFGs at this epoch, where h_z is the scale height of the disk and

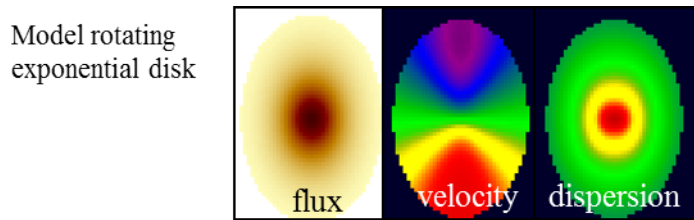


Figure 4.13: DYSMAL flux model of a rotating exponential disk with the resulting velocity and velocity dispersion map. For the velocity map, the zero velocities are visualized in green, while the positive velocities of red-shifted emission peak in the red and the negative velocities corresponding to the blue-shifted parts are at maximum in the purple area. Accordingly, the velocity dispersion peaks in the center denoted by the red color.

$R_{disk} = R_e/1.68$ its radial scale length for an exponential disk (Förster Schreiber et al., 2009; Genzel et al., 2011; van der Wel et al., 2014; Wuyts et al., 2016).

The systemic velocity of the rotation curves I adjust by considering the symmetry given in the velocity profile and/or dispersion peak. For the systems where this handling is not enough I determine the systemic velocity by placing the centroid coordinates to the position, where the CO and stellar mass profiles peak along the largest gradient. This is the case for the rather disturbed kinematics of EGS13011155 and EGS13019128, for which both peaks coincide and therefore are considered a robust center position. The systemic velocity of EGS13011155 is further adjusted by symmetry arguments to -100 km/s instead of -148 km/s.

In the modeling itself I fix the inclination to the value from the stellar-mass fit of the previous section 4.2.1. The Sérsic index is fixed to $n_{Sersic} = 1$ for a exponential disk profile consistent with the GALFIT results on the CO maps. Furthermore, the effective radius is fixed to the H band fit result as this optical size measure traces the galaxy to its outskirts other than the derived CO and stellar mass properties, which are more concentrated. This approach involves all parts of the galaxy, which in total are responsible for the galaxy dynamics also reflected by the CO emission. Using the smaller sizes would lead to underestimating the dynamical mass of each system, which is one of the relevant outputs of the modeling done here.

I also consider the pressure support from the significant random motions seen in the high observed outer dispersion values induced by turbulence, since the high-redshift objects typically are more turbulent than nearby systems. The induced pressure has an effect on the gravitational potential of the modeled mass and the corresponding correction known as asymmetric drift lowers the circular velocity $v_{circ}(r)$ in the outer disk significantly to $v_{rot}(r)$ (Burkert et al., 2010):

$$v_{rot}^2(r) = v_{circ}^2(r) - 2\sigma_0^2 \frac{r}{R_{disk}} \quad . \quad (4.23)$$

Beam Smearing As mentioned before, also instrumental characteristics need to be considered for a proper simulation of the observed kinematics in particular the effect of beam smearing. In this respect, I notice that applying the average of the FWHM from the two dimensions of the asymmetric beam for all objects leads to systematically broader velocity dispersion curves than observed. For two reasons the computed beam might not properly reflect the kinematic data.

As described in Tacconi et al. (2013), the line centers as used in the Gaussian fitting for the kinematics can be determined to higher accuracy than what is given by the beam size for high SNRs. In addition, the derived dynamics are based on data combining different array configurations producing different resolutions such that the computed beam width might not describe reality best. Usually, the compact configuration data hardly resolve velocity profiles of galaxies at these redshifts. This would mean that the measured resolved kinematics should rather be related to the contribution from the extended configurations.

I therefore insert the minimum value of the beam size as derived from a uniform weighting in the cleaning-process of the interferometric data. This method puts more weight on the extended configurations. By that, the adapted input beam size can be considered a lower limit, such that any remaining deviations in the widths of the dispersion curves cannot be explained by instrumental characteristic, but can rather be attributed to galaxy properties. Indeed, the approach improves the fitting, such that the resulting models better catch the widths of the dispersion curves, but deviations still remain.

The obtained dynamical models are shown in Figure 4.14 and can be used to derive intrinsic properties of the galaxies. One has to keep in mind that the derived DYSMAL models are not unique solutions, but rather a combination of many input parameters chosen, such that the model fits the data. For this reason, the models are based on the output of the morphological fitting in order to constrain the parameter space.

The general outcome of the previously outlined methods are presented in the next section.

4.2.2 Results on the Morphologies and Dynamics

In this section I summarize the results obtained with the presented methodology.

Looking only at the stellar-light continuum without the use of SED fitting, there seems to be no connection between the bright star forming-regions and molecular gas in contrast to their strong relation found at all probed epochs. This observation is demonstrated in Figure 4.15, for which CO maps are displayed, created only by the use of extended array configurations. The resulting maps show the small-scale structure of the brightest CO regions.

The bulk of CO emission is usually found in the galaxy centers best traced by the rest-frame optical light, while the UV-bright regions as tracers of star formation with low extinction rather surround the central CO concentrations. SED fitting can help to overcome this bias, which is mainly introduced by the obscuration of UV light in the galaxy centers by dust.

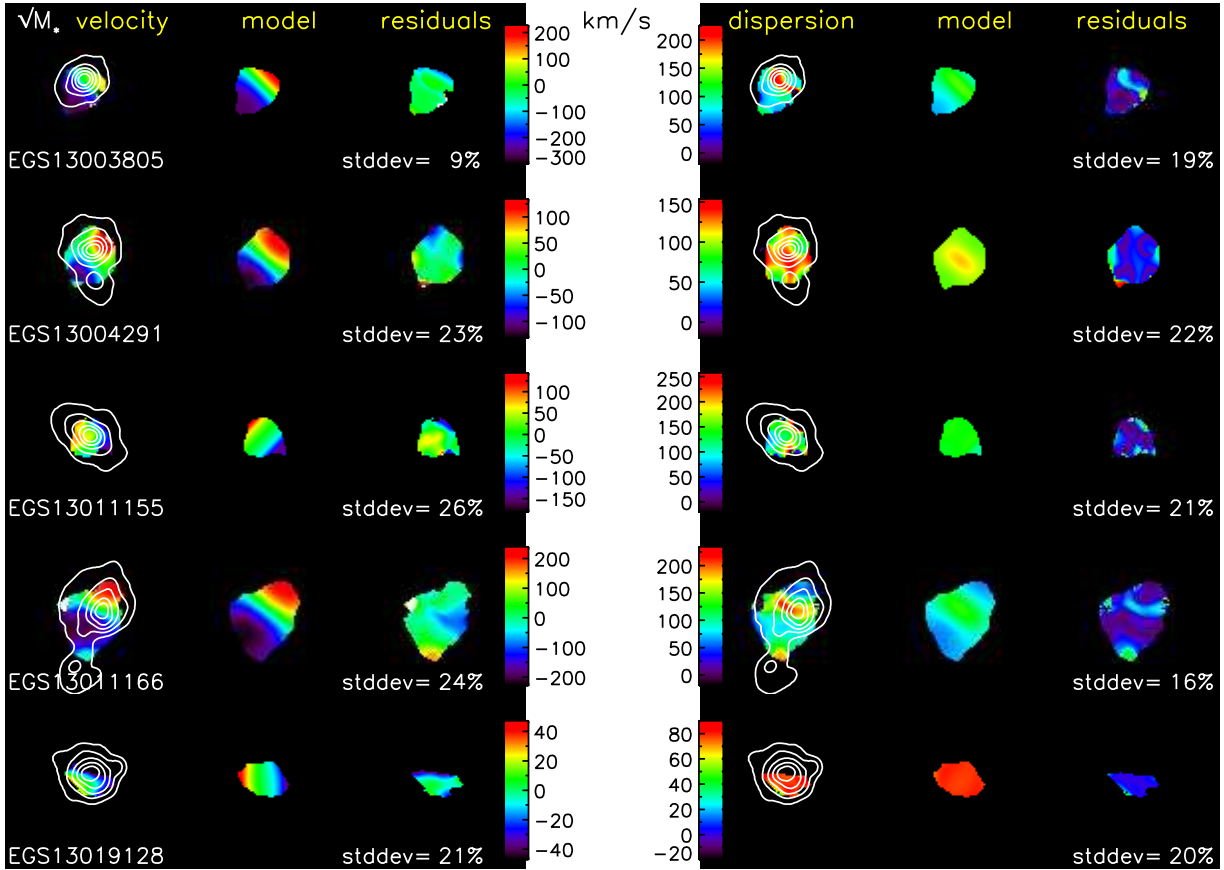


Figure 4.14: Dynamical modeling of the CO kinematics for the sample, from left to right the following quantities are displayed: CO velocity map in color with stellar-mass contours overlaid in square-root scale (smoothed to a $0.35''$ -resolution), velocity model, data-minus-model residuals and their standard deviation (stddev) with respect to the peak value of the velocity scale. The same panels are shown for the velocity dispersion on the right.

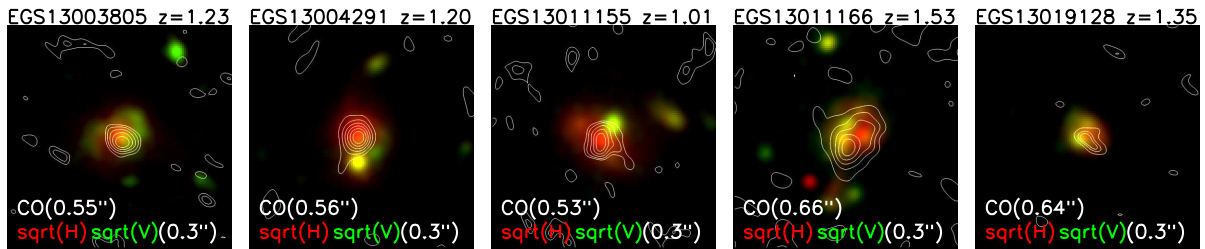


Figure 4.15: CO maps from extended array configurations in white contours together with rest-frame UV/optical stellar continuum in V/H band (green/red) in square-root scale (sqrt).

Distributions of Molecular Gas, Star Formation Rate and Stellar Mass

From the SED fitting I indeed find highly extinguished galaxy centers, in which the bulk stellar mass resides. Also the star formation peaks in those centers, but due to the dust

extinction, the star-forming regions in the outer parts appear brighter in the intrinsic light distribution, in the form of UV-bright clumps with low extinction. For this reason, the rest-frame UV light is not centrally concentrated because of the dust gradient within the galaxies other than the optical component, which also traces the central galaxy regions where the stellar and molecular masses peak. These findings are consistent with work as done for instance by Wuyts et al. (2011a, 2012) and Lang et al. (2014), but provides the additional link to the characteristics of molecular gas.

Figure 4.16 demonstrates the distribution of derived stellar-mass and SFR maps on top of the CO emission. The latter shows asymmetric profiles probably due to underlying kiloparsec-sized clumps as visible in the UV/optical light distributions, but smoothed out due to the lower resolution of the PHIBSS data compared to the HST maps. Freundlich et al. (2013) find such molecular-gas clumps using position-velocity diagrams for a few PHIBSS targets, also for EGS13003805, EGS13004291 and EGS13019128 presented here.

The SED products in Figure 4.16, SFR and stellar mass, roughly show similar distributions of similar sizes like a “main sequence” on sub-galactic level (Wuyts et al., 2013), but with distinct peaks and a few other interesting differences. In general, the SFR distribution resembles the CO emission more closely than in the case of the stellar mass.

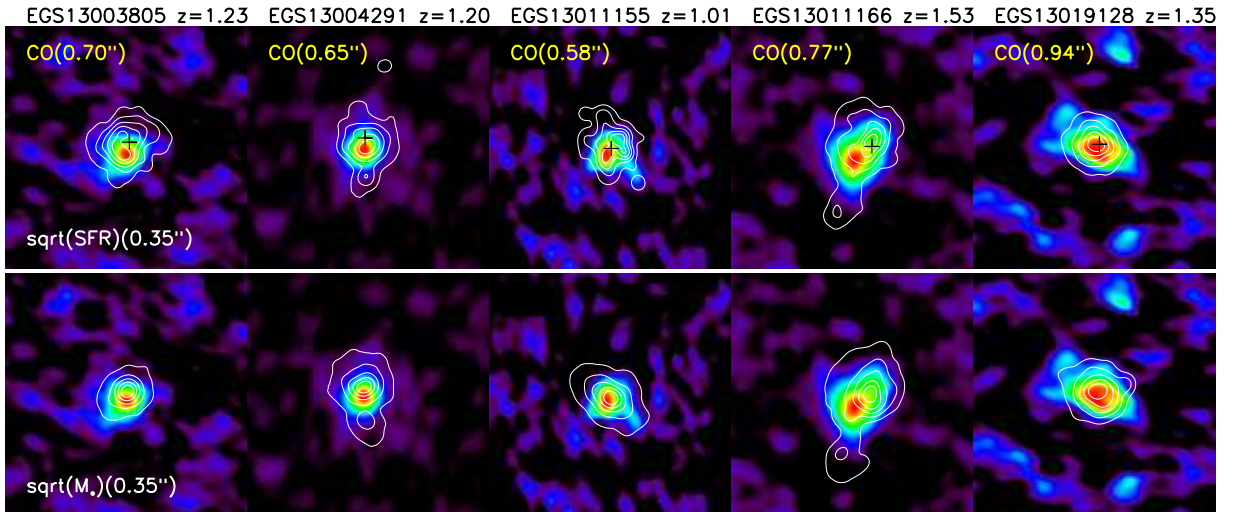


Figure 4.16: Stellar-mass and SFR maps derived from SED fitting in white contours, in square-root scale (sqrt), in comparison to the CO (3-2) emission in color with individual scales. The SED products were smoothed to a $0.35''$ -resolution in order to smear out the binning structure and to get closer to the CO resolution. The black crosses denote the peaks of the stellar-mass distributions.

Particularly, the sources EGS13004291 and EGS13011155 show interesting features of related surface densities of molecular gas and star formation. Both objects have southern tails of CO emission, which are well traced by the derived SFR within the astrometric errors and have similar orientations, which is not found for the stellar-mass distributions.

Especially for EGS13004291, the southern stellar-mass extension is distinct from the

CO and SFR ones, which might hint toward a depletion of gas and quenched star formation in this region. In the case that this southern part is the minor system from a merger, this gas-depleted region might correspond to the former galaxy core. Another explanation for the different orientation of the CO distribution could be outflowing gas, which will be discussed in a separate section about the galaxy EGS13004291.

EGS13011155 seems to be a very clumpy system looking at the asymmetric CO emission and the even more complex double-peaked SFR structure, which is better resolved than the radiation from CO. Irregularities in the CO dynamics also point towards a less smooth distribution than for the other galaxies of the sample, which will be discussed separately later on together with the other kinematics. The extinction map from SED fitting shows a similarly elongated core as the CO emission, revealing a compact but elongated distribution of dust and molecular gas in this object. The central extinction leads to the SFR peak in the galaxy center being faint in the rest-frame UV light while the outer SFR peak is bright in this respect.

In EGS13011166 there is a similar occurrence in the core, where the SFR has a more elongated center as the CO while the stellar mass has a more concentrated center distinct from the CO peak. This difference seems to be real as the mass peak is embedded in a CO concentration connected with the main peak. While the other sources rather show a single compact CO peak agreeing with the stellar mass peak within the astrometric uncertainties, the shifted peaks in EGS13011166 probably result from an interaction or merger event that is likely to take place in this clumpy, extended system. Comparing these aspects to the smoother and more compact distributions in EGS13004291, the interaction in EGS13011166 seems to be a minor merger and in an earlier stage than for EGS13004291.

The CO emission from EGS13009128 is probably marginally resolved and shows a rather broad peak within this compact, lower-mass system.

The most prominent size difference between stellar mass and SFR profile is found for EGS13003805 which will be discussed in the following sections about sizes. In this respect, the Sérsic models of the different tracers give further insights. The average effective radii and Sérsic indices of the sample are summarized in Table 4.4. In order to understand the differences between the parameters from the multiple tracers, the direct comparison of the effective radii as size measurements can be made for each object individually as done in the following.

Parameter	CO	SFR	M_*	H band	J band
R_e [kpc]	3 ± 1	3 ± 1	3 ± 1	5 ± 1	6 ± 2
n_{Sersic}	0.8 ± 0.5	1 ± 1	2 ± 1	1 ± 1	1 ± 1

Table 4.4: Average structural parameters of the sample in terms of effective radius R_e and Sérsic index n_{Sersic} .

Comparison of Sizes

The variety of multi-wavelength data for the presented sample allows also for different size estimates as shown in Figure 4.17. This comparison becomes especially meaningful regarding the agreement of orientation and Sérsic index between the models of the different tracers for each object.

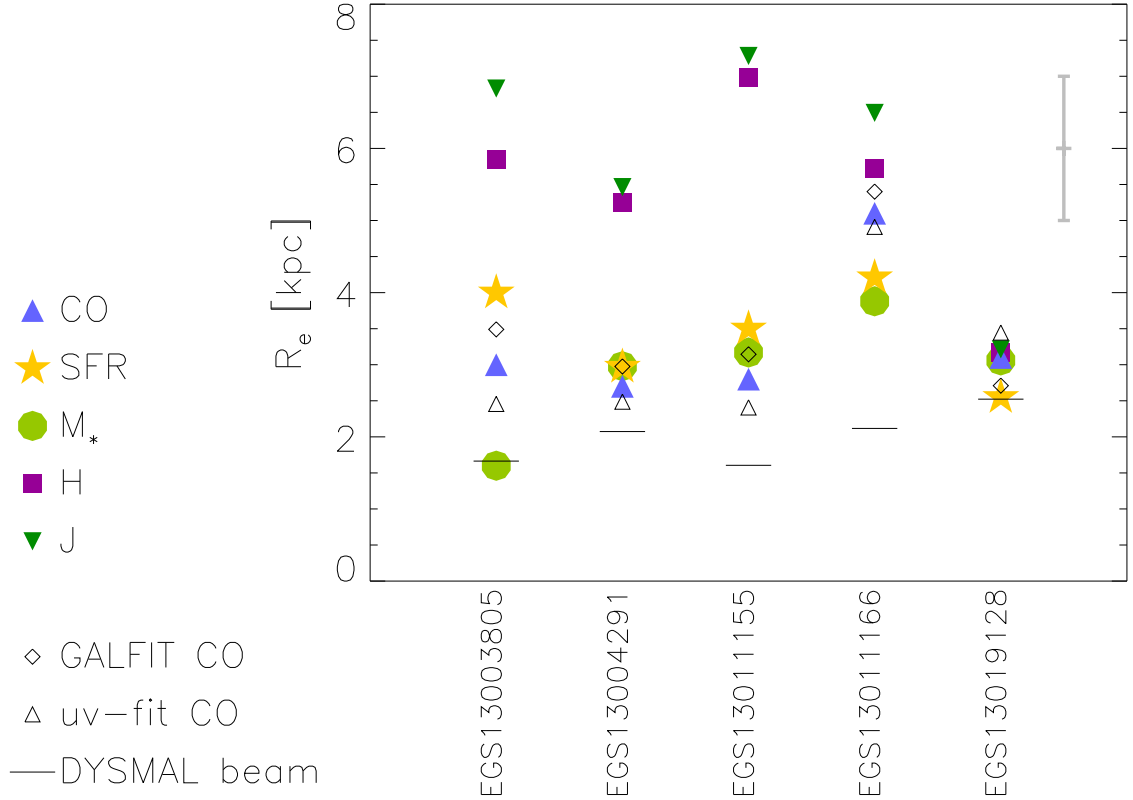


Figure 4.17: Comparison of sizes from different tracers with an uncertainty of the measurements estimated to ± 1 kpc. The CO radius is determined as average from the results determined by a Sérsic model on the CO map in GALFIT and a Gaussian fit in (u,v)-plane.

As a general remark, the I band sizes are not regarded to be reliable, since they often do not represent the real distribution of matter in the galaxies at redshift $z \sim 1$, but only individual star-forming clumps with low extinction. Since literature nevertheless quotes I band values as size measurements, it should be briefly mentioned that in this case the I band values for this sample roughly fall in the regime of the optical sizes, however with wrong fit values of orientation. Therefore, I focus on the rest-frame optical here, which overall shows fit parameter results consistent among the different tracers.

In general, the sizes of the analyzed galaxies range from 2 kpc to 7 kpc in diameter regarding the stellar mass, SFR, CO, H and J band distributions as robust tracers. In

angles on sky, this corresponds to $0.24''$ to $0.75''$. The largest radii are measured in the rest-frame optical, namely in J and H band. The J band estimates exceed the H band values, but given the uncertainties of ± 1 kpc not significantly.

CO Sizes The CO sizes were determined by a Sérsic model in GALFIT on the corresponding image and also by a Gaussian fit in the (u,v)-plane of the interferometric data. The average of both results was adapted here as CO size since they show strong agreement within the uncertainties. The GALFIT measurements seem to lie systematically above the (u,v)-fit sizes. The average effective radius of the CO emission is at (3 ± 1) kpc, similar to the average size of the stellar mass and SFR distribution, while the optical sizes average to (5 ± 1) kpc and (6 ± 2) kpc for H and J band.

Since the CO sizes are derived based on data resolutions three times larger than what is measured by HST, comparisons should be done with caution. It is uncertain whether fainter CO regions in the outer disks are missed or on the contrary whether the CO is even more compact than what is measured. In order to check the resolution quality of the CO measurements I also plot the corresponding beam sizes as used in DYSMAL in Figure 4.17. As explained previously, these are the minimum beam sizes from the reduction with uniform weighting to put more weight on the extended configurations, which are necessary to obtain spatially resolved CO maps and kinematics. As such, these beam sizes represent lower limits, since the analyzed data were created by natural weighting, which does not emphasize the extended-configuration data.

Compact Disk Galaxy EGS13019128 The CO radii mostly are larger than the CO beam translated to a corresponding effective radius. However, this is not the case for the compact lower-mass object EGS13019128, which interestingly shows a size of 3.0 kpc or $0.3''$ in all tracers. Within the uncertainties, EGS13019128 is at the edge of being resolved in CO in its measured effective radius.

While one could argue that the CO is not properly resolved showing a beam size of $0.55'' \times 0.40''$ in natural weighting, this does not explain why also the stellar mass size is similar to the radius of the stellar light. Clearly, this lower-mass object of this sample shows an overall compact morphology. EGS13009128 is also the only source in this sample that does not show any external clumps or companions in the HST data. Therefore, its compact morphology might be also linked to the environment.

EGS13019218 is the only source of the sample for which all morphology tracers used are best-fitted by Sérsic indices $n_{Sersic} < 1$ in favor of a compact disk galaxy. In addition, the disk model for stellar mass of EGS13019128 is the only one among the sample which shows a Sérsic index $n_{Sersic} < 1$, while the other targets result in $n_{Sersic} > 1$. This finding could point towards a build-up of bulge-like components in the sample, whereas for EGS13019128 only a compact disk is resolved, which is of similar size as the CO distribution of the other objects. In the current picture of galaxy evolution, EGS13019128 will probably further grow inside-out by gas accretion, while the currently observed disk might transform into a central bulge component.

To conclude on the quality of the CO measurements, EGS13019128 probably is only marginally resolved in the CO observations. Also the finding that only for this source the GALFIT size of the CO is smaller than the result from the (u,v)-fit could be related to that. The poorly resolved kinematics of EGS13019128 also point towards a low CO resolution compared to its size. Nevertheless some velocity gradient is seen for this galaxy. In interferometric data, a velocity gradient can be detected for seemingly unresolved targets, as the relative centroids of CO emission at different velocities can be measured with much higher accuracy than what is given by the beam size for a sufficiently high SNR (Tacconi et al., 2013). EGS13019128 indeed is observed with a sufficiently high SNR of 16.

Molecular Gas in the Interacting Systems EGS13011166 and EGS13004291

In general, all CO sizes of the sample are of similar order except for EGS13011166, where the CO radius is the largest one and close to the H band value. This might be due to the interaction ongoing between the main body of the galaxy and the southern extension, which leads to an extended CO distribution.

Furthermore, the peaks of the CO and stellar mass distribution differ by more than what is seen for the other targets in Figure 4.5. Since the CO distribution shows an elongation in the direction of the stellar mass peak, this difference probably is not an astrometric error but real and might be caused by the interaction. In total, the observations show a large CO reservoir with an extended disk and probably a bulge-like component as well as interaction or merger features.

EGS13004291 also shows interacting material in the light distribution, with an additional stream as known from mergers. But other than for EGS13011166, a rather compact CO and stellar mass distribution is observed, compared to its optical morphology. This result might relate to the merger being at a late stage already, as seen in the well-ordered rotation dynamics.

Interpretation of Gas and Stellar Distributions The sizes of the stellar and SFR surface densities are of order of the CO radii. Compared to the optical light not corrected for extinction they are a factor of two smaller with the exception of EGS13019128 as mentioned before.

In this respect, the SFR as derived from SED fitting is a lower limit as explained in the methodology, especially in the galaxy center. As a consequence, the real SFR distribution could be more compact with a higher Sérsic index. Similarly, this could apply to the stellar mass, where underestimated extinction in the galaxy centers could be misinterpreted as older and therefore lower-mass stellar populations. Indeed, the used upper-limit fit value for visual extinction $A_V \leq 4$ mag is reached in the centers of all galaxies in the sample especially in EGS13004291 such that higher values of extinction, which might be present in the cores, are not captured.

Similarly, the CO distributions seem to correspond to lower limits due to several reasons. An overestimation of CO sizes could be introduced by beam sizes of similar or larger size indicating that the measurements are unresolved, which is not the case for the sample. For

the scenario where fainter CO is not properly resolved in the outer galaxy regions, the size estimates would increase. A similar trend of correction would be induced if one assumes that CO (3-2) also might not capture the full extent of molecular gas as it is not the lowest rotational transition. In addition, galaxies also host molecular gas which is dark in CO due to photo-dissociation (Hollenbach & Tielens, 1999). Furthermore, outer disks tend to be metal-poor, such that CO does not trace the cold gas as in the inner regions. In all those scenarios however a correction of the current size measures would mean increasing them. The derived effective radius of the CO (3-2) emission can therefore be considered as lower limit of the molecular gas size.

In total, probably the sizes of the distributions from CO, M_* and SFR can be considered lower limits under these conditions. This assumption also can be made due to the fact that if bulge-like components are present in the systems the actual disk sizes as measure of galaxy extent are not fully captured by the analysis here.

In this respect, the biggest difference between the CO and stellar mass radius is found for EGS13003805 and EGS13011166 or order > 1 kpc. Interestingly, these are the two objects with the most prominent signatures of a central mass concentration in the velocity dispersion curves.

Extended Sizes in EGS13011166 The size measurements of EGS13011166 from different tracers span a smaller range than for the other objects excluding the compact EGS13019128. Probably the interaction in this system leads to a general large extent in all tracers, such that also the central concentration of stellar mass and SFR is the largest among the sample. The SFR seems to be more concentrated than the CO (3-2) emission, also in the comparison of Sérsic indices $n_{Sersic} = 2$ and $n_{Sersic} = 0.8$. If this result is not driven by the uncertainties in this analysis, it could be induced by an ongoing interaction. In such a scenario gas is being accreted from large extent, while a more compact starburst is triggered, which is supported by EGS13011166 lying above the MS in the SFR-stellar mass diagram. The SED-derived SFR is a lower limit, which might miss large fractions of star formation in dust-obscured galaxy centers. As such, the found SFR concentration would even increase by a corresponding correction, further supporting a compact starburst. The SFR distribution from the SED modeling furthermore agrees with the one traced by the emission line H α as shown in Genzel et al. (2013). This optical emission from ionized gas is considered a more reliable SFR tracer, as it is less affected by dust extinction than the rest-frame UV emission entering the SED fitting.

Bulge-Disk Morphology in EGS13003805 EGS13003805 shows an obvious bulge in the rest-frame UV and optical as well as outer features, which strongly resemble spiral arms as known from disk galaxies observed at lower redshifts. The object has the smallest effective radius of the stellar-mass distribution among the sample as well as the largest spread of measured sizes by different tracers from stellar continuum light to stellar mass. While for all other objects the sizes of stellar mass and SFR are similar, EGS13003805 shows a significant discrepancy between both. Molecular gas and consistently also star formation

seem to be distributed in a more extended, less centrally-concentrated component than the stellar mass. The SFR distribution shows a larger size than the CO profile either induced by the uncertainties in the analysis or because the more extended molecular gas is not resolved in the CO observations here.

In summary, EGS13003805 seems to consist of a bulge and disk component, which is also supported by the fact that this source is fitted best in GALFIT by a Sérsic index of $n_{Sersic} = 3$ for the J, H band and stellar mass distribution, while all other objects show $n_{Sersic} < 2$, mostly close to $n_{Sersic} = 1$. It is not clear if the external clumps in the HST morphology interact with EGS13003805.

Compact, Dusty Star Formation in EGS13011155 and EGS13004291 The largest size difference in the distribution of CO, stellar mass and SFR with respect to the stellar continuum light is found in EGS13011155. This galaxy shows the largest optical size in the sample, but the sizes of the stellar-mass and CO distribution correspond to the sample average. The most probable explanation is a dust-obscured central mass concentration, which dominates those profiles, while the stellar light shows a more extended profile due to a strong extinction gradient. All Sérsic indices are $n_{Sersic} > 1.4$ except for the J band light with $n_{Sersic} = 1.1$. These elevated values deviating from an exponential profile hint towards a bulge-like component.

Similar results are found for EGS13004291, but with a smaller stellar-light distribution. The stellar-mass profile shows a Sérsic index of $n_{Sersic} = 1.4$, while for the CO and SFR profiles the values are $n_{Sersic} \leq 0.8$. This distribution of molecular gas and star formation hints towards a compact disk-like starburst as known for objects above the MS. In agreement with this scenario, the highest gas fraction among the sample within the smallest CO size speaks for particularly high gas surface densities in EGS13004291 probably induced by a merger event. This source indeed shows the highest gas as well as SFR surface density within the total PHIBSS survey.

As mentioned previously, EGS13011155 and EGS13004291 both also show a high and compact central concentration of dust as seen in the derived extinction maps. In conclusion, those objects host compact, dusty star formation in their centers building up bulges as traced by Sérsic indices of the stellar-mass profiles $n_{Sersic} > 1$.

General Conclusions In summary, the stellar masses on average tend to be most compact followed by the SFR and CO sizes being of similar order or slightly larger with the optical stellar light being most extended. The overall findings presented here strongly suggest that central stellar-mass concentrations are already present in these massive systems, which passed the peak of cosmic star formation as found in Tacchella et al. (2015); Nelson et al. (2016); Barro et al. (2017). Star formation continues to take place in these centers, indicating further bulge growth but also growth beyond, which is visible in the UV-bright clumps only visible in the outer galaxy parts due to low dust extinction.

The next part sets a focus on the kinematic analysis of the CO data, which is also based on the CO sizes that were determined here.

Kinematics of the Molecular Gas

From the interferometric CO data kinematic properties can be derived such as velocity and velocity dispersion maps. These can be modeled in order to extract physical properties of the galaxies such as intrinsic rotation velocities and velocity dispersions. For a more realistic picture I feed the dynamical models with morphological parameters as determined in section 4.2.1.

The resulting model velocity and velocity dispersion maps were shown above in Figure 4.14 in comparison to the observational results. The data-minus-model residuals give a further insight into the physical processes present in those galaxies. Furthermore, from both the models and the observed data rotation curves can be extracted and compared.

Rotation curves The rotation curves show the velocity and velocity dispersion profile versus the offset from the center along the kinematic axis as presented in Figure 4.18 without the correction of the dispersion floor for spectral broadening. Overall the rotation curves confirm the picture of rotationally supported turbulent disks, but also certain deviations can be found as discussed in the following summary of the main results.

Bulge-Like Central Concentrations The observed velocity dispersions overall show the typical signs of disk rotation convolved with beam smearing. The corresponding maps show a central peak in form of a ridge along the minor axis perpendicular to the velocity gradient caused by beam smearing in most cases. For the majority of the sources, which show rotating-disk profiles, the dispersion models underestimate the central dispersion peak, which can also be seen clearly in the rotation curves. In order to exclude instrumental beam smearing effects being the reason for this finding, I inserted lower-limit beam sizes in the modeling.

Therefore, under the assumption that light, here traced by the CO emission, follows mass, these observations hint towards deviations from a purely exponential-mass profile with an additional central mass concentration most likely reflecting a bulge-like component with increased dispersion floor. This finding is also supported by tests with DYSMAL models without fixing the Sérsic index n_{Sersic} to 1, where typically n_{Sersic} results in values above unity close to de Vaucouleurs profiles. As a consequence, the inner rotation curves are modeled better, while the fit quality of the outer parts is reduced.

Probably, modeling a single component does not reflect the actual distribution of matter in those galaxies, which rather consist of disks and bulge-like central concentrations (Lang et al., 2014) both traced by the CO data. In this respect, Genzel et al. (2013) concluded for EGS13011166, that twice the stellar mass is found in the central 1.5 kpc from SED fitting compared to what an exponential profile would suggest.

Regular Rotation in EGS13004291 and EGS13011166 The clearest rotation-velocity profile is found for the galaxy EGS13004291, well-modeled by an exponential disk and with small error bars, although it was only observed shortly in the A and D

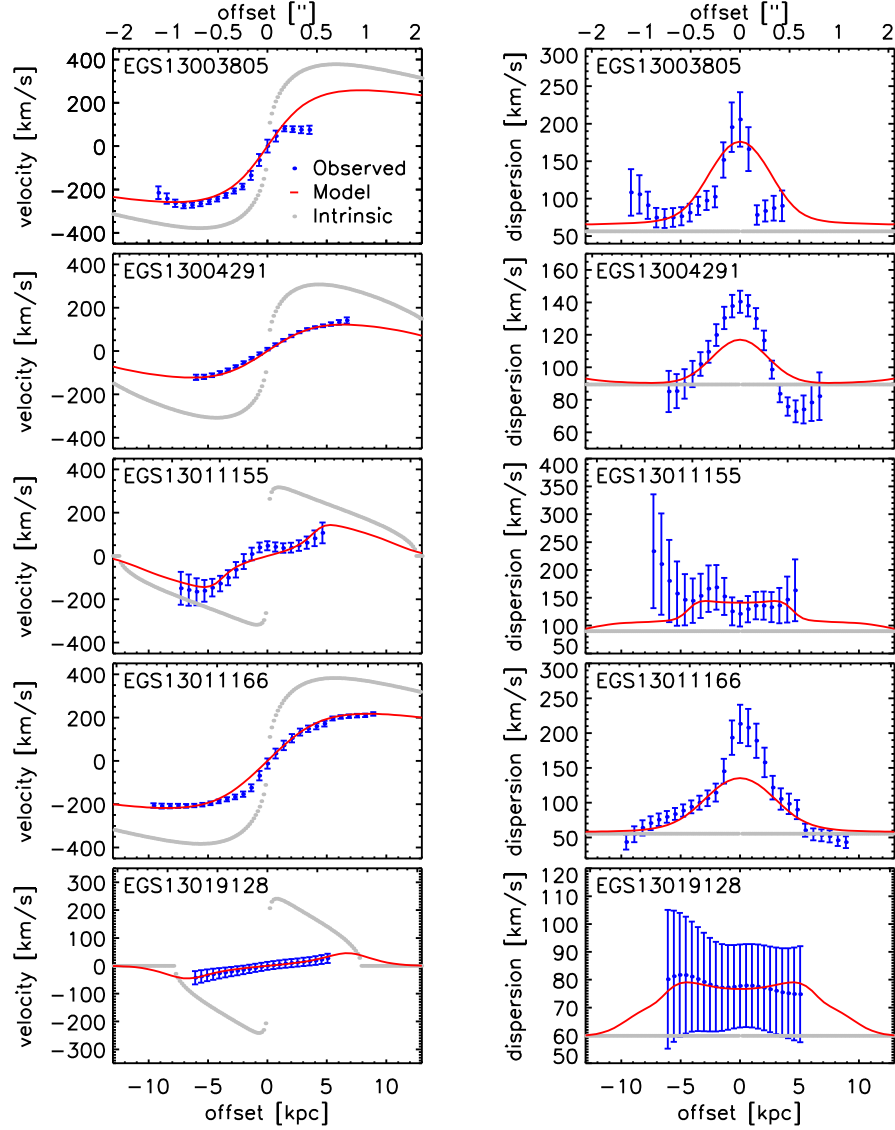


Figure 4.18: Rotation curves as derived from the interferometric CO data of the sample: the blue data points with error bars are the observed velocity and velocity dispersion profiles versus the offset from the center as derived along the kinematic axis in 4.2.1. The modeled red curves were produced with the dynamical modeling capabilities of DYSMAL, which also provides the intrinsic rotation curves as displayed in gray. The intrinsic properties are free from inclination and spatial beam-smearing effects. Compared to the models, the observed velocity dispersions often show higher and narrower peaks. The dispersion floor is not yet corrected for spectral broadening here.

configuration. Indeed, this source is the brightest in CO with the highest SNR and has the largest gas fraction of 0.77 among all PHIBSS galaxies (Tacconi et al., 2013).

But in addition, signs of interaction are visible in the optical morphology of this source as stated above and in combination with its position in the $M_* - SFR$ plane all of this hints towards a starburst-scenario. Under this aspect, it is remarkable how smooth the rotation profile is. The underlying interaction or merger event might therefore be at a late stage already, where a compact, dynamically settled gas core has formed. Nevertheless, in the red-shifted part of the galaxy, deviations of the kinematic model might be caused by the interaction with the stream visible close by in the optical morphology. Furthermore, the central dispersion peak is not fully reached by the model, maybe due to an additional bulge component not present in the disk model.

Similarly, the galaxy EGS13011166 shows very regular kinematics regarding its interaction visible in its southern extension. However, the deviations of velocity and dispersion model from the data in the center of this object might be signs of this interaction and a bulge component in the galaxy as found in Genzel et al. (2013).

Bulge Component in EGS13003805 The kinematic profile of EGS13003805 is more asymmetric but still close to regular rotation in this system on first glance. The deviations in the red-shifted part might be linked to the companion on this side of the system as seen in the UV emission. The observed velocity dispersion curve shows a narrower peak than what can be caught by the model, although the beam size inserted to the model is already a lower limit. Similarly, as for EGS13004291 and EGS13011166 this finding could be interpreted as a central mass concentration next to the rotating disk showing in a velocity dispersion curves consisting of a narrow and broad component.

However, only in the case of EGS13003805 the dispersion curve shows a very abrupt transition from narrow to broad component. This result also supports an established bulge component in the center of the galaxy, as already indicated in the morphological analysis. The latter showed a stellar mass and light distribution with a Sérsic index of $n_{Sersic} = 3$ for EGS13003805, while the rest of the sample is largely dominated by distributions closer to an exponential disk than a de Vaucouleurs profile. Also the optical morphology shows a bulge-disk decomposition and the effective radius of the stellar-mass distribution is particularly compact compared to the one of the optical-light distribution and of the other objects.

Meaning of the de Vaucouleurs Profiles in EGS13011155 and EGS13019128 For both those galaxies, EGS13011155 and EGS13019128, lower gas fractions of ~ 0.48 on average were measured than for the other three objects, which on average show values of 0.69. The rotation curves of the sample mostly trace red- and blue-shifted parts of the galaxies both out to approximately 5 kpc or more, however EGS13011155 and EGS13019128 show more asymmetric curves in this respect. The red-shifted regions of the latter source are detected further out than for the blue-shifted ones, while EGS13011155 completely lacks information about the blue-shifted part in the extracted curves. The kinematic maps of these objects in general show less regular rotation patterns than the others.

Under these circumstances, the determination of the largest gradient and the PA was more challenging for both objects than for the rest of the sample. For EGS13019128 these findings might be explained by its compactness and orientation in combination with lower mass and the largest beam size in the CO observations among the sample, which also leads to a higher level of beam smearing.

For EGS13011155, the situation looks different. It does not show the typical rotation features of a disk galaxy, but is fit best by a Sérsic index of $n_{\text{Sérsic}} = 5$. It is unclear whether this circumstance has a real physical meaning of a rotating bulge-like mass. The GALFIT model of the CO emission gives a Sérsic index of $n_{\text{Sérsic}} = 1.5$, while all other sources in the sample show indices $n_{\text{Sérsic}} < 1$ in CO. Furthermore, the CO emission is very compact in EGS13011155, as only source in the sample with a slight tendency to being more compact than both the stellar-mass and SFR distribution. In addition, EGS13011155 is the only source in the sample to show Sérsic indices of $n_{\text{Sérsic}} > 1$ in all morphological tracers analyzed here.

In principle the deviation of the modeled dynamics could be produced by perturbations in the galaxy dynamics for instance by an interaction with the companion visible in the UV emission. Alternatively, the data resolution could not be good enough to resolve the disk kinematics in this system regarding the large error bars on the dispersion measurements. But even the error bars suggest dispersion values > 100 km/s for all measured radii, in contrast to the other sources in the sample, which show smaller values at larger radii. The measured dispersion profile also shows a central dip between two peaks, characteristic for profiles close to a de Vaucouleurs distribution as modeled here with $n_{\text{Sérsic}} = 5$.

In addition, this source has the CO (3-2) data with the highest resolution in the sample and high SNR. In addition, the integration time spent in the extended configuration is five times higher than for the bright EGS13004291 source and of similar amount as for EGS13011166, for which the kinematics are mapped out to two effective radii. Therefore, the measured rotation curve of EGS13011155 is likely not the result of poorly-resolved kinematics, but rather based on high-quality data of the galaxy with the lowest gas fraction among the sample. The Sérsic index of $n_{\text{Sérsic}} = 5$ in the dynamical modeling could be the result of actual molecular-gas morphology. Recent studies find compact SFGs with similar Sérsic profiles at high redshifts, such as in Barro et al. (2013) and Barro et al. (2014).

The corresponding situation is different for EGS13019128. This object indeed is fit with a dynamical model of $n_{\text{Sérsic}} = 4$, although the GALFIT models of all tracers result in indices $n_{\text{Sérsic}} < 1$. But in the underlying CO observations the worst spatial resolution is achieved among the sample. EGS13009128 is of lower mass and very compact in all size tracers as described in the section 4.3.1 above. As such, this source is only marginally resolved in the CO data, due to its compactness and the relatively low resolution of the CO observations. Furthermore, the inclinations found in the morphological fitting of different tracers range from 16° to 34° , close to a face-on orientation.

The compact size and orientation of EGS13019128 explain the low velocity gradient measured. The low resolution in the CO observations probably lead to the large error bars on the measured velocity-dispersion profile. Other than for EGS13011155, the error bars on the measured dispersion profile of EGS13019128 would allow for interpreting it as a

profile of an exponential disk.

In conclusion, the CO kinematics of EGS13011155 either can be attributed to a bulge profile or a disturbed exponential profile. The overall evidence and data quality summarized above indeed are consistent with the molecular gas rotating within a compact bulge. For EGS13019128, the measured CO dynamics can be explained by both a rotating-disk or bulge profile, while interpretation of a compact exponential disk seems more likely as it is supported by all morphology tracers used here.

After this general interpretation of the derived dynamical models for the CO kinematics, I interpret the residuals in the data-minus-model dynamics in the following.

Residuals Anomalies in the kinematic maps can give a further insight into the processes present in galaxies. I therefore discuss the most prominent residual features of data minus model presented in Figure 4.14. The residuals between data and model show rather small standard deviations of 9% to 25% of the maximum observed velocity.

Interactions in EGS13011166 The most prominent deviations between data and models in terms of velocity are found in the source EGS13011166. On the one hand, the southern extension of this galaxy breaks the rotational symmetry of the main body. Alternatively, this part could be interpreted as companion which is dynamically decoupled from the galaxy. This region shows a separate dispersion peak, which is also found in the kinematic analysis by Genzel et al. (2013) of CO and H α emission, tracing molecular and ionized gas. On the other hand, there is also a residual feature in the west part of the galaxy, which might result from the many clumps in the galaxy center seen in the light distribution. Both findings are probably caused by the interaction ongoing in the system and also support the assumption of the latter. The quite extended CO profile discussed above could be a result from an interaction and in this respect the great amount of clumps found in the UV/optical morphology of EGS13011166 also supports this scenario. Another remarkable feature in the multi-wavelength data of this source is how both the stellar-mass distribution and CO kinematics show the identical northern cusp in the profiles in Figure 4.14. Concluding on these findings and in comparison to the general sample properties, EGS13011166 very likely interacts with another system, maybe even in the form of a merging event.

Bulges in EGS13003805 and EGS13011155 EGS13003805 shows a regular rotation pattern, also in its dispersion, with the smallest residuals. The latter are dominated by the model dispersion peak being too low and too broad compared to the observations as mentioned above. The comparison of velocity versus model demonstrates that the blue-shifted parts are traced to greater extent than the red-shifted ones, which is consistent with the same asymmetry seen in the optical morphology. Regarding the residuals there is a certain ring feature around the center. This observation might be a signature of multiple components of the galaxy as bulge and disk as traced by the optical light.

Also the source EGS13011155 shows residuals with a likely link to the structures visible in the optical morphology. The northern bright clump could be responsible for the residual located there, which is also visible in the elevated velocity dispersion in this region. But the kinematics also show this behavior in the southern part, where no optical clump is seen. Another deviation is found in the center maybe caused by a bulge. Overall the kinematics are very difficult to interpret. They seem rather irregular especially in dispersion, where no central peak can be found, but two offset peaks at two sides of the stellar-mass center. This irregularity triggers the question whether the external clump in the optical morphology has any connection to the found residuals.

Velocity Dispersion Maps As already mentioned, the observed velocity dispersions overall show the typical signs of disk rotation convolved with beam smearing. For the majority of the sources, the dispersion models underestimate the central dispersion peak. In addition, the dispersion curves are also narrower than what the models predict. The residuals relative to the maximum observed dispersion are on average of order 16% to 21%. In order to exclude instrumental beam smearing effects being the reason for this finding, I inserted a lower limit beam size in the modeling. Therefore, under the assumption that light, here traced by the CO emission, follows mass, these observations hint towards deviations from a purely exponential-mass profile with an additional central mass concentration most likely reflecting a star-forming bulge component.

From the velocity dispersion maps, the intrinsic level of random motion in the galaxies can be estimated. This information and other intrinsic galaxy properties extracted in the dynamical modeling are discussed next.

Intrinsic Properties I derive the following estimates of intrinsic properties of the galaxies from the dynamical modeling: rotationally supported dynamical mass, the rotation velocity defined as the inclination and beam-smearing corrected maximum velocity as well as the intrinsic velocity dispersion. The corresponding quantities are summarized in Table 4.5 and the intrinsic rotation curves are displayed in gray color in Figure 4.18.

For the intrinsic velocity dispersion σ_0 the model values of intrinsic velocity dispersion $\sigma_{0,model}$ are corrected for spectral broadening by quadratically subtracting the spectral resolution $\sigma_{spectral}$ according to

$$\sigma_0 = \sqrt{\sigma_{0,model}^2 - \sigma_{spectral}^2} \quad , \quad (4.24)$$

where the model value already includes the correction for beam smearing $\sigma_{0,model}^2 = \sigma_{obs}(\delta)^2 - \sigma_{beam}(\delta)^2$ introduced in (4.20). I use the spectral-channel width as estimate for the spectral resolution of the interferometric data, which is roughly 20 km/s for the sample. Since the spectral binning of the data cubes mostly is determined by the user, typically it is larger than the actual resolution and therefore can be considered as an upper limit. The uncertainty of the rotational velocity is estimated to ± 50 km/s and ± 30 km/s for σ_0 . For these error estimates I take into account the variations between different DYSMAL models

Source	M_{dyn} [M_{\odot}]	v_{rot} [km/s]	σ_0 [km/s]	v_{rot}/σ_0	M_{bar}/M_{dyn}
EGS13003805	4.0×10^{11}	378	53	7	0.9
EGS13004291	2.8×10^{11}	312	88	4	2.0
EGS13011155	2.2×10^{11}	317	88	4	1.2
EGS13011166	4.1×10^{11}	383	51	7	0.8
EGS13019128	7.2×10^{10}	241	57	4	1.8

Table 4.5: DYSMAL results for the sample, from left to right: source identifier in PHIBSS, dynamical mass M_{dyn} within a radius of half the image size, $3.5''$ or 30 kpc, rotation velocity v_{rot} , intrinsic velocity dispersion σ_0 , the ratio of the latter two as a disk-stability diagnostic and the ratio of baryonic to dynamical mass M_{bar}/M_{dyn} . The uncertainties amount to $\pm 50\%$, ± 50 km/s, ± 30 km/s, ± 2 and $\pm 60\%$. The results agree with the overall PHIBSS results presented in Tacconi et al. (2013) within the uncertainties.

when varying the input parameters within the uncertainties as well as the results from Tacconi et al. (2013) and Genzel et al. (2013). The minimum dispersion values on the kinematic axes, corrected for observational effects, lie within the derived uncertainty of σ_0 , also including their error bars. Looking at the rotation curves, the modeled intrinsic velocity dispersion seem to be upper limits because the fitting tries to capture the higher dispersion peaks by increasing the intrinsic values.

Baryon-Dominated Dynamical Masses The determined dynamical masses can be compared to the mass estimates for this sample. In principle, the dynamical mass is expected to resemble the baryonic galaxy mass, consisting of a gas component and a stellar one, potentially with an additional contribution from dark matter. The gas component can be estimated by the dominant molecular-gas mass deduced from the CO emission. The determination of molecular-gas masses depends linearly on the CO-to- H_2 conversion factor applied. For normal, rotating star-forming galaxies, the standard value of the Milky Way can be applied $\alpha = 4.36 \pm 0.9 M_{\odot}/(K \text{ km s}^{-1} \text{ pc}^2)$. The uncertainty of this factor directly transfers into the uncertainty of the calculated molecular gas mass together with other systematic uncertainties in the conversion to molecular mass (Bolatto et al., 2013).

According to this, the PHIBSS gas masses have an estimated uncertainty of $\pm 50\%$ (Tacconi et al., 2013). The molecular-gas masses as determined by this analysis from the CO data typically have errors of order $\pm 50\%$. The PHIBSS values in Tacconi et al. (2013), using the same methodology and errors, deviate only by 0% to 35% with respect to the measurements here, which shows their general agreement.

Stellar masses are measured by the SED fitting of the HST imagery. The stellar masses as derived here agree with the values published with PHIBSS within the uncertainties of $\pm 30\%$. The 30% correspond to the maximum deviation of the 1σ -confidence intervals of

the derived stellar-mass maps from the actual best fit. The resulting baryonic masses in total carry an uncertainty of $\pm 30\%$.

For this sample, the ratio of baryonic-to-dynamical mass ratio ranges from 0.8 to 2.0 for the five galaxies with the individual values displayed in Table 4.5. This result matches the expectations regarding the large uncertainties that are present for the different mass estimates entering the baryonic masses.

Also the dynamical masses can have large errors especially for systems that show inclinations below 45° . This is the case for EGS13011166, EGS13019128 and particularly for EGS13004291, which will be discussed in a separate section. Applying the uncertainty for the inclination of 10° dynamical mass variations of order 50% are possible in this regime, which is adapted as error estimate here. A baryonic-to-dynamical mass ratio of two therefore has no significant meaning regarding the error budget, which can explain differences up to a factor three between both masses. Despite the large uncertainties of the mass measurements, these findings are consistent with the analyzed objects being baryon-dominated in the probed regions. Probably no major contribution from dark matter affects the dynamics of those centrally concentrated molecular-gas reservoirs consistent with recent findings (Förster Schreiber et al., 2009; van Dokkum et al., 2015; Price et al., 2016; Stott et al., 2016; Alcorn et al., 2016; Wuyts et al., 2016; Genzel et al., 2017; Lang et al., 2017; Übler et al., 2018).

It should be mentioned here that the dynamical masses move towards unphysical values smaller than the baryonic masses when using the stellar mass radii instead of the H-band numbers and for models without pressure support. The highly turbulent molecular gas apparently induces a relevant pressure term in the measured kinematics. Furthermore, this result shows that the stellar-mass size is not representative of the total baryonic size responsible for the galaxy kinematics, because it traces mostly the galaxy centers while the H band not corrected for extinction also catches the disk component to its outskirts.

Thick and Turbulent Rotation-Dominated Systems From the modeled rotation curves, the rotation velocities, defined as the maximum intrinsic velocities, of the galaxies were derived. The rotational velocities v_{rot} range from 300 km/s to 400 km/s except for the lower-mass object EGS13019128, which shows 241 km/s. The intrinsic velocity dispersions σ_0 after subtraction of observational effects are high for all the galaxies with values between 50 km/s and 90 km/s. These dispersions can be attributed to significant random motions in the observed objects next to the ordered rotation. The ratios of rotation velocities to intrinsic dispersions thus range from $v_{rot}/\sigma_0 = 4$ to $v_{rot}/\sigma_0 = 7$. This disk-stability diagnostic of $1 < v_{rot}/\sigma_0 < 10$ indicates that the sources are dominated by rotation not by dispersion. But these rotating disks are rather thick compared to the nearby thin-disk systems with $v_{rot}/\sigma_0 > 10$. The thickness in those high-redshift objects can relate to the stability diagnostic via

$$\frac{h_z}{R_d} = \frac{\sigma_0}{v_{rot}} \quad . \quad (4.25)$$

The thickness of $h_z/R_d = 0.25$ assumed for the modeling therefore is appropriate for the sample corresponding to $v_{rot}/\sigma_0 = 4$. EGS13003805 and 13011166 seem to be less thick with $h_z/R_d = 0.14$ due to less turbulent motions and higher rotation velocities leading to $v_{rot}/\sigma_0 = 7$. These are also the two sources in the sample which show rather prominent bulge-disk decompositions in their rotation curves sampling the largest extent up to radii of 10 kpc.

Clearly, this sample of five massive galaxies on average shows features of rotationally-supported thick and turbulent disks. Three of those objects can be described by exponential disks with bulge-like central mass concentrations. For the two others de Vaucouleurs profiles fit better. In the case of EGS13011155, this could be caused by a compact bulge-like profile, where in the dynamical modeling a Sérsic index of $n_{Sersic} = 5$ is needed to fit the data, where it is not clear if really the rotation of such a bulge-like system is underlying or distorted kinematics. The latter case might be linked to the companion found in the UV emission. However, the bulge profile fits the observed rotation curves remarkably well. Together with the very compact gas distribution also in comparison to the stellar mass as shown in Figure 4.14 and the lowest gas fraction in the sample, a likely explanation is that indeed only the gas component in the rotating bulge is detected.

EGS13019128 is even more compact and of lower mass and therefore probably not properly resolved such that an interpretation of its kinematics is difficult. Especially the error bars on the dispersion curve do not allow to distinguish between an exponential disk or a de Vaucouleurs profile. In the attempted best-fit model, the result is a de Vaucouleurs profile with a ratio of rotation velocity to intrinsic dispersion $v_{rot}/\sigma_0 = 4$ indicating rotation-dominated kinematics. However, it is not clear if this object is properly resolved in its CO emission and the corresponding kinematics.

Sample Dynamics in the Context of Galaxy Evolution In order to place the derived intrinsic properties in global context of galaxy evolution I overplot results from work being done within the KMOS^{3D} survey for rather massive star-forming MS systems around the peak of cosmic star formation by Wisnioski et al. (2015) and Wuyts et al. (2016) in Figure 4.19.

In more detail, the plots show the evolution of the intrinsic velocity dispersion σ_0 and ratio of the rotation velocity to the latter v_{rot}/σ_0 versus redshift based on several large studies analyzing gas properties and a comparison of dynamical mass to baryonic one. The corresponding results from the sample of the five galaxies presented here are put on top with error estimates and in this form align well within the average trends.

The origin of these trends is not fully understood. Probably the larger gas fractions at higher redshifts come with higher levels of turbulence in the giant star-forming clumps formed by gravitational instabilities and fragmentation of the gas-rich disks. Models and simulations show how bulges are formed from these massive clumps in young galaxies (Noguchi, 1999; Immeli et al., 2004a,b; Bournaud et al., 2007; Elmegreen et al., 2008; Genzel et al., 2008; Dekel et al., 2009; Bournaud et al., 2010; Genzel et al., 2011). Several mechanisms could explain the induced turbulence such as random motions by gas accretion or

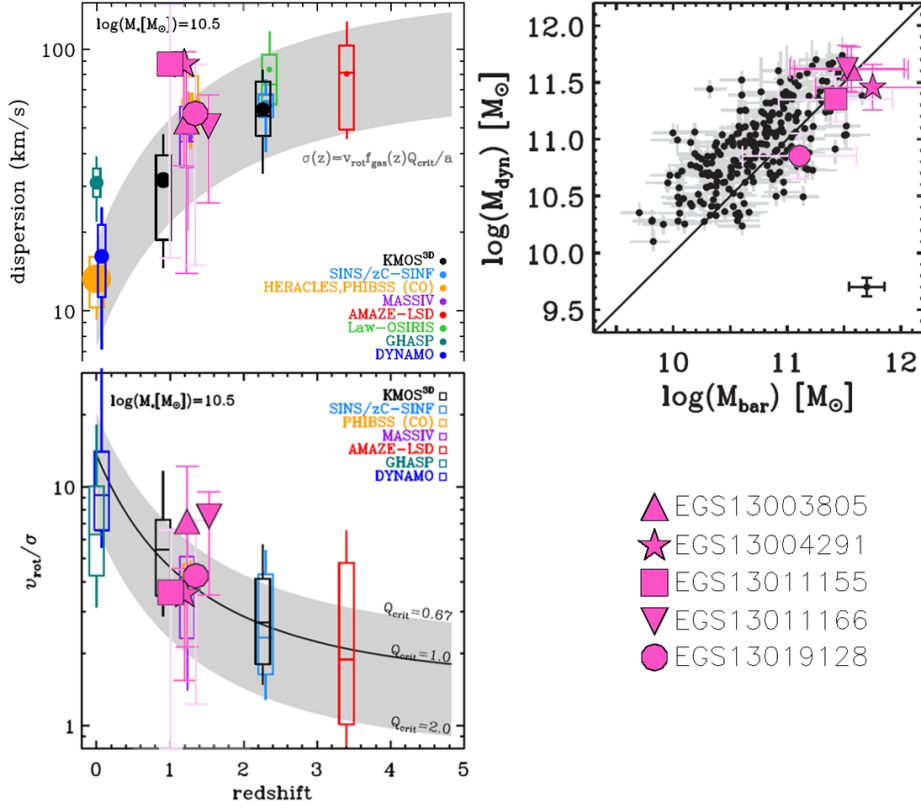


Figure 4.19: Sample dynamics in pink symbols in the context of galaxy evolution on the basis of figures from Wisnioski et al. (2015) on the left and Wuyts et al. (2016) on the right side. The left column shows the observed redshift evolution of the intrinsic velocity dispersion and the ratio of the rotation velocity to the latter v_{rot}/σ based on the listed studies of ionized or molecular gas properties. Regarding the plot symbols, horizontal lines show medians, boxes denote the 50% distributions and vertical lines the case of 90%. The circles stand for means and are sized to the average effective radius, which was adjusted to an average stellar mass of $M_{*} = 10^{10.5} M_{\odot}$. The upper gray band corresponds to the description of the printed equation with Toomre Q-parameter $Q_{crit} = 1$ (ratio of pressure to gravity) and the parameter $a = \sqrt{2}$ for a disk of constant rotational velocity with $M_{*} = 10^{10.5} M_{\odot}$ (Toomre, 1964). The upper boundaries represent an observed velocity difference between maximum and minimum velocity in the velocity axis profile $v_{obs} = \frac{1}{2}(v_{max} - v_{min})$ of 250 km/s and the lower boundaries 100 km/s. The lower gray band boundaries have a $Q_{crit} = 0.67$ and 2.0 of thick gas disk and a composite stellar-plus-gas disk. The average between those typical for $z \sim 1$ is $Q_{crit} = 1$ of a quasi-stable thin gas disk. The right plot shows the derived dynamical versus the measured baryonic mass of the KMOS^{3D} survey, with a median error bar as in the lower right corner. Most galaxies are baryon-dominated within their visible extent with a median $M_{bar}/M_{dyn} = 0.56$.

gravitational torques and collisions. Theoretical studies suggest that stellar feedback could probably not be strong enough to invoke the observed constant dispersion floor throughout the galaxies (Krumholz & Burkert, 2010). High-resolution observations of molecular gas in high-redshift systems as presented here are needed to probe these processes empirically.

For a particularly careful comparison of these results to found redshift trends mostly based on ionized-gas studies, I use more conservative error estimates for σ_0 than presented above, as this quantity is not directly measured, but extracted from the data by several corrections.

Error Discussion for the Derived Intrinsic Velocity Dispersions On the one hand there are the observational constraints such as beam smearing and spectral broadening. The dynamical results are corrected for both effects. But the modeling is based on the observed dispersion profiles, which mostly trace inner regions of the galaxies, such that the intrinsic dispersion floor is only marginally resolved. Typically, the velocity dispersion of molecular gas clouds are dominated by turbulent motions with a minor contribution from thermal pressure. But, also merger-induced components might be present, especially in the probed young, massive systems of high gas fractions. As the sample consists of rotation-dominated galaxies, probably random motions induced by interactions or mergers are not dominating the dispersion floor.

Nevertheless since many factors affect the estimation of the intrinsic velocity dispersion in the analyzed galaxies, conservative error bars are used in the following. Instead of the assuming the uncertainty of ± 30 km/s, which already includes the minimum dispersion values with errors on the kinematic axes, I use the minimum robust dispersion values with their errors in the underlying maps as lower limits. These numbers might not be representative for the average dispersion floor in the galaxies, when the probed region is not typical for the object. But this approach excludes that uncertainties in the extraction of the kinematic axes lead to an overestimation of the intrinsic dispersions. As most uncertainties in the dispersion measurements lead to such an overestimation, the upper error is chosen as the upper limit of the lowest dispersion value in the rotation curve which lies on or above the modeled intrinsic dispersion floor. The entire analysis also corrects for the spectral broadening present in the rotation curves and maps.

Two objects, EGS13011155 and EGS13019128, are best modeled by distributions close to a de Vaucouleurs profile in contrast to the typical exponential-disk rotation. While the case of EGS13011155 potentially really might resemble the rotation of a bulge, the data of EGS13019128 are rather resolution-limited not allowing for any firm conclusions. For these reasons, the interpretation of the intrinsic dispersions modeled for these targets should be done with great caution. Therefore in order to distinguish these results from the rest of the sample, the error bars of EGS13011155 and EGS13019128 are drawn in a lighter color in the plots of Figure 4.19 discussed in the following.

Comparison to Other Studies The redshift trend of velocity dispersions can be described by decreasing gas fractions $f_{gas}(z)$ within a scale-length radius of R_{disk} as predic-

ted by marginally-stable disk theory. The sample agrees with the findings at the respective redshift, but aligns within the higher dispersion values than the average at redshift $z \sim 1$ of $\sigma_{0,av} = 30$ km/s for stellar masses of $M_* = 10^{10.5} M_\odot$. A possible explanation would be that the sample resembles more massive galaxies, which have large molecular-gas reservoirs by gas accretion or interactions.

In particular two of the galaxies are at the upper limits, namely EGS13004291 and EGS13011155, which are the most compact in the CO observations among the sample. However, their particularly high intrinsic dispersions are not linked by the largest observed velocity gradients in contrast to what the upper limit of the gray band suggests. On the one hand, both objects show a tendency to higher Toomre parameters in the plot below than the $Q_{crit} = 1$ assumed for the gray band. For EGS13004291, this result is also rather consistent with its high gas fraction $f_{gas} = 0.77$.

EGS13011155 however has the lowest gas fraction in the sample with $f_{gas} = 0.44$, but in general shows features of a bulge-like system with respect to its kinematics, clumpy SFR distribution as well as its asymmetric and compact CO emission. A high dispersion value matches the overall picture. This comparison indicates that EGS13011155 deviates from the model of a quasi-stable thin gas disk with constant rotation velocity, as is also captured in its other data. The other sources of the sample seem to be described better by this model. The exception is EGS13019128, which is difficult to interpret due to the marginally resolved CO data in this compact object.

Looking at the disk-stability diagnostic v_{rot}/σ_0 versus redshift also agreement is found between the general trend and the sample points with a more average location with respect to the main trend. The upper limit is populated by EGS13003805 and EGS13011166 here as typical for marginally-stable thick disks. These are also the two sources in the sample which show rather prominent bulge-disk decompositions in their rotation curves sampling the largest extent up to radii of 10 kpc.

For EGS13011166, the situation is a little more complex since it shows strong signs of an interaction. Since the derived CO kinematics trace the major component of the galaxy excluding the external interaction features, this finding might underline that the interaction happens in the form of a minor merger or even less invasive. Other than a major-merger event the bulk mass keeps regular kinematics and in that sense dominates over an additional minor turbulence term introduced by mass accretion from the interaction.

The other sources of the sample lie closer to $Q_{crit} = 1$ of quasi-stable thin gas disks. EGS13019128 has a tendency in the direction of a thick disk. But due to the limited resolution of the underlying CO data, no further interpretation is attempted here. For the sources EGS13004291 and EGS13011155 the trend is found towards composite stellar-plus-gas disks. Although for EGS13011155 the kinematics do not correspond to a rotating exponential disk, together with EGS13004291 it shows a compact distribution of stellar and molecular gas mass with similar sizes other than the for the rest of the sample. A composite disk therefore seems like an adequate description.

In the last comparison of dynamical to baryonic mass, the sample again matches the overall trend with a tendency of baryonic masses being larger than the dynamical ones. As discussed previously, an interpretation of these numbers is difficult due to the large

uncertainties, since the detected and resolved CO distributions rather cover the inner galaxy parts, while the baryonic mass as calculated here includes the stellar mass on the basis of the stellar continuum, which is better resolved to larger extent. Therefore, the dynamical mass measured here might not resemble the full picture, which could emerge from an analysis of outer rotation curves. In addition, EGS13019128, also showing this trend, is hardly resolved such that the dynamical mass is very uncertain.

In summary, the comparison of kinematic data and models show many interesting details on top of the general finding that the molecular gas in star-forming galaxies around the cosmic star-formation peak is resembling rotationally-supported, turbulent disks as it is known from ionized-gas studies. Clearly, EGS13004291 has very special properties and its IRAM data show remarkable quality and several CO lines such that a more detailed study could be performed on this source as outlined in the following.

4.3 Molecular Outflows in EGS13004291

EGS13004291 not only shows signs of an interaction in its UV/optical morphology, a high gas fraction and SFR together with remarkably ordered rotation, but also molecular outflows in the CO data. At fixed stellar mass, this source shows the highest SFR as well as surface density of SFR and molecular gas among the sample. All of these indications point towards a possible starburst in this object. In addition, several CO lines were observed for this source, which allow for comparing their individual distributions within the galaxy.

Molecular outflows and bright CO emission with high excitation are frequently seen at various redshifts in extreme systems, such as in Ultra Luminous Infrared Galaxies (ULIRGs) in the local Universe (Sanders & Mirabel, 1996). In ionized gas, some outflows are connected to AGN activity (Genzel et al., 2011; Förster Schreiber et al., 2014), others are driven by stellar feedback. These processes often are accompanied by strong central bursts of star formation due to large gas reservoirs assembled either by accretion or even more by an interaction or merger event with another galaxy. Due to enhanced star formation, these systems tend to lie above the MS such as EGS13004291 does. The presence of an AGN was ruled out in literature in SED fitting as well as analyzing X-ray radiation, which seems rather to originate from a starburst (Gowardhan et al., 2017).

The observations of this galaxy performed with the IRAM interferometer include multiple lines namely CO (3-2), CO (4-3) as well as CO (5-4). General CO measurements are based on the CO (3-2) line if not stated differently as this line traces the major part of the molecular gas component. In Figure 4.20 the integrated line-flux maps of the three different CO transitions detected are shown including a continuum measurement from the CO (4-3) cube, together with the HST H band contours and the stellar mass peak. The CO (3-2) line is detected at a SNR of > 60 , the SNR of CO (4-3) at almost 100, while the CO (5-4) has a very low SNR below 10. The observed quantities are quoted in Table 4.6. Continuum emission from dust is only visible in the CO (4-3) data due to the long integration time and the wide-band correlator providing a broader band (rest-frame (650 ± 10) μm) of 4 GHz instead of the 1 GHz used for the other lines. The resulting SNR of the continuum is > 20 .

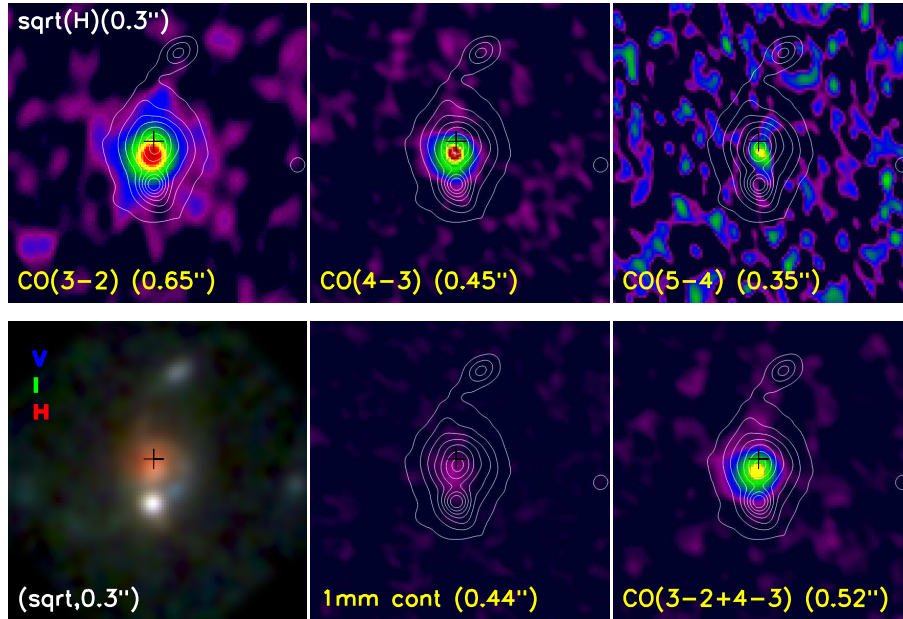


Figure 4.20: First row: integrated CO line maps are shown in color together with the HST H band light distribution in contours. The CO profiles show asymmetric distributions probably as a result of a clumpy morphology, which is also seen in the HST VIH data below. The second row shows this HST imagery in three colors (blue and green for rest-frame UV, red for rest-frame optical), the (650 ± 10) μm continuum and a merge of two CO lines. All images have sizes of $7'' \times 7''$ corresponding to roughly 60 kpc and a pixel scale of $0.06''$. The CO maps all are shown with the same color scale given by the maximum flux density measured in the CO (3-2) map. The stellar mass peak as derived from SED fitting is denoted as black cross. The CO emission peaks coincide with the stellar mass maximum within the astrometric uncertainties.

EGS13004291	S [Jy km/s]	σ_S [Jy km/s]	S/σ_S
CO (3-2)	5.4	0.08	63
CO (4-3)	5.9	0.05	98
CO (5-4)	1.9	0.21	8
CO (3-2+4-3)	5.2	0.05	96
dust continuum	4.2	0.17	24

Table 4.6: Integrated flux densities of different CO transitions and the dust continuum with errors and the resulting SNR as S/σ_S .

With a methodology similar to what was described in Section 4.2 about the analyzed

galaxy sample, the data of EGS13004291 was analyzed. In addition, spectral fitting in several CO lines was performed, in order to get further insight on the molecular outflows detected.

4.3.1 Resolved Mapping of Stellar Continuum and Molecular Emission

In this part, I present the results of analyzing the data of EGS13004291 tracing properties of the stellar component as well as molecular gas in the form of mapping their distributions. Comparing the derived disk models in H band, stellar mass and CO (3-2), the average Sérsic index is $n_{Sersic} = 1.1 \pm 0.6$ while the inclination value is $i = (30 \pm 4)^\circ$ excluding the H band value, which had to be fixed to the stellar-mass parameter $i = 27^\circ$. The parameters determined by the Sérsic disk modeling later on are used as input for the dynamical modeling of the CO kinematics.

Discussion of the Properties Derived from Stellar Continuum

The stellar light of EGS13004291 as detected by HST in principle shows three distinct components as can be seen the V-I-H composite image of Figure 4.7 and Figure 4.20.

Merger Tail in UV/Optical Photometry The rest-frame optical light traces all parts including the bulk mass of the galaxy. A northern tail and a southern clump are bright in all bands including the rest-frame UV.

The tail strongly hints towards a merger event in this galaxy. Such tails or also called tidal streamers are produced by major mergers of two disk galaxies of similar mass in contrast to minor mergers which involve two systems of very different masses (Binney & Tremaine, 2008). In this picture, the gas component loses large fractions of its angular momentum by collisions in a short time frame of less than an orbital period. As a result a central compact, dense gas disk of sub-kiloparsec size forms triggering a fast starburst and bulge formation together with the growth of the central black hole to a SMBH (Noguchi, 1988; Mihos & Hernquist, 1996). The characteristic tails are present in a time span < 0.5 Gyr (Toomre, 1977).

The southern component is a bright star-forming region not obscured by dust other than the main body of EGS13004291. There is a link between this clump and the bulk galaxy mass in the form of a bright, blue tail as detected in the northern part, but located closer to the main body. The latter difference in position potentially could be a projection effect, especially regarding the small inclination of $i = 27^\circ$. Therefore, it is not excluded that this galaxy shows several tidal streams as consequence of a merger event as shown for instance in Mihos & Hernquist (1996). At both sides of EGS13004291 further UV-bright extensions are visible but with lower SNR.

Starburst in the Dust-Obscured Galaxy Center There is a strong color gradient between the inner and outer parts of this galaxy. The center is red, which could be due to

an older stellar component or extinction by dust. According to the SED modeling, indeed, the center is highly extinguished. A large dust component is furthermore likely considering the high gas fraction of this system.

Out of the five sample objects at similar redshift spatially-resolved in CO, EGS13004291 is found to have the highest total average extinction of $A_V > 2.2$ mag as derived from SED fitting while the other galaxies averages of $A_V < 1.4$ mag. The outer parts are blue showing bright star-formation regions of low extinction traced by the light of young blue and bright stars. Because this UV-radiation is strongly extinguished in the center of the galaxy by dust, its distribution is not centrally concentrated as opposed to the rest-frame optical emission.

As mentioned previously, the effects of extinction can be derived in SED fitting of the photometric bands. The derived maps of stellar mass and SFR corrected by the extinction give a deeper insight to the galaxy than the dust-affected light. All three quantities peak in the red, central part of the galaxy. The visual extinction A_V reaches its maximum value of four magnitudes in those regions as set by the fitting range while the outskirts are less affected by one to three magnitudes in the best fit. When considering these dust effects, the SFR reveals to be not the highest in the outskirts, as suggested by the uncorrected UV-emission, but also peaks in the center of the galaxy. Similarly, the bulk stellar mass is not reflected by the brightest parts of the object.

The derived total stellar mass amounts to $1.3 \times 10^{11} M_\odot$, which is consistent with the value presented in Tacconi et al. (2013) within the uncertainties. This is not the case for the total SFR, which here is found as $195 M_\odot/\text{yr}$. Also, when considering the uncertainties, this value is at least a factor two lower than what is found when factoring in the IR luminosities, as done for the value cited in Tacconi et al. (2013). This is a common finding, which not only holds for this source. SED fitting provides a lower-limit SFR, as it is strongly affected by extinction.

The comparison between those quantities derived from SED fitting is not based on measurements independent of each other. Comparing them to independently derived CO maps helps to put the measurements into a broader context. I discuss this comparison with the CO maps in the next section.

Comparison of Sizes

The different CO transitions can also be compared in size to each other as well to the other tracers used in this study as shown in Figure 4.21. The effective radii of the CO measurements with errors, including the continuum size, were calculated on the basis of a Gaussian fit in the (u,v)-plane of the interferometric data, while other size estimates were found by GALFIT models with a typical error of ± 1 kpc. In the previous analysis of a handful of galaxies the estimated sizes from (u,v)-fitting are comparable to GALFIT results on the CO distribution in the image plane. I therefore consider the size estimates from both methods to be comparable.

Lower Limits Typically higher line transitions trace denser regions. On first glance this trend can also be seen in this data set. But the comparison needs to be treated with

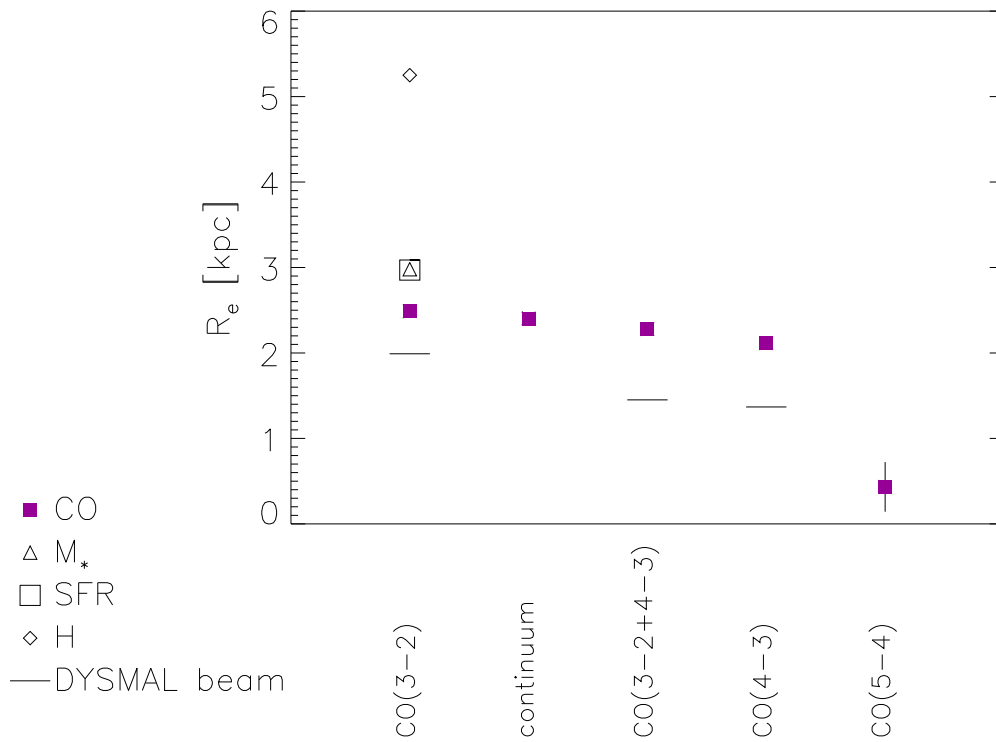


Figure 4.21: Comparison of effective radii as traced in the different CO data: the numbers were derived by fitting in the (u,v) -plane of the interferometric data with size errors below ± 0.1 kpc if not shown differently. Also the H band, SFR and stellar-mass sizes are shown as derived by GALFIT image fitting with an uncertainty estimated to ± 1 kpc.

caution. On the one hand, the different CO lines were measured at various configurations and resolutions. However, the size estimates were made on the basis of (u,v)-fitting, which in principle can measure sizes smaller than the beam in contrast to the measurements in the image plane as done for the other tracers. In addition, for the lines with high SNR as indicated in Table 4.6 the small errors on the effective radius are hidden by the display of the plot symbols.

Only the (5-4) transition has a low SNR and therefore a larger fitting error. Due to the low SNR, the (u,v)-fitting required more constraints for a reliable size fit, because otherwise the fitted flux converged to values different than what was measured by integrating over the spectral cube. Therefore, the size measurement for the (5-4) case can be considered a lower limit, since it was observed only shortly and in the most extended interferometer configuration resolving small-scale structure. As such, it is very likely that this transition was only marginally resolved.

The lower transitions deliver robust results in this respect, but also here the results probably are lower limits due to several reasons. In principle, it is possible the outer, fainter structure was not detected or in the other extreme resolved out due to the dominant use of extended configurations. If used as a tracer of molecular gas, furthermore the measured lines also might not capture the full extent of the latter not being the lowest energy states. In addition, galaxies also host molecular gas which is dark in CO due to photo-dissociation. In all those scenarios however a correction of the current size measures would mean increasing them. The derived effective radius of the CO (3-2) emission can therefore be considered as lower limit of the molecular gas size.

Size of Dust Continuum For the continuum, a relatively large effective radius is derived from Gaussian (u,v)-fitting of (2.40 ± 0.03) kpc, which is of similar order as found for the CO (3-2) emission. In a study of two starburst galaxies at $z = 2.5$, the dust continuum shows smaller extent than the molecular gas with effective radii of ~ 1 kpc (Tadaki et al., 2017). While here the continuum was only observed with extended configurations of the IRAM interferometer, the measurements of the CO (3-2) line also included compact arrays. One therefore would expect the fairly large continuum size is probed by actual small-scale measurements and is not the result of smearing out the latter by the use of compact configuration.

The relatively large continuum size is consistent with the red and smooth appearance in the optical/UV morphology of this target, where the main body of the galaxy does not show any bright clumps of star formation due to extinction by several orders of magnitude as found in SED fitting. Such a dusty, compact burst of star formation likely leads to the rapid build-up of a central bulge (Wuyts et al., 2011a).

Clumpy Distribution of Molecular Gas The resolved nature of the underlying measurements also shows itself in the asymmetric profiles deviating from pure spherical, emitting regions. In this respect, especially the Gaussian fit to the CO (3-2) emission leaves residuals of streams, which are also visible in the CO (3-2) map in Figure 4.20. The bulk

of molecular and dust emission thus seems to originate from a region with a radius smaller than 2.5 kpc. The CO (3-2) emission shows that the molecular gas probably extends further out to the disk traced by the stellar light than what is captured by the Gaussian fit.

Comparison of Gas and Stellar Component Comparing this result to the one of the stellar mass and SFR distribution under this aspect, one can state that the molecular gas size is found to be similar or very likely even larger than for those stellar tracers. The latter do not differ in size with a measurement uncertainty of ± 1 kpc. Since the CO sizes are derived based on data resolutions three times larger than what is measured by the HST, it is not possible to interpret the determined sizes as support for an inside-out growth in those galaxies with high confidence. But the results do not contradict this scenario.

EGS13004291 is a massive system close to the Schechter mass with a large gas fraction and it shows signs of being a late merger in a starburst phase as well as producing outflows as will be demonstrated later. With the effective radius of the molecular gas being probably larger with respect to the sizes of stellar mass and SFR distribution, EGS13004291 fits this picture of inside-out growth, which likely results in bulge formation and inner quenching of star formation.

Obscured Mass Center and Bright Stellar Disk From the available mapping, the largest sizes for the galaxy are found in the rest-frame optical, here traced by the H band. Not corrected for extinction, this measure emphasizes the disk of the galaxy in contrast to the stellar mass distribution, which shows a more concentrated component. The size of the stellar surface density is of order of the CO radii. Compared to the optical light not corrected for extinction, the stellar surface density and the CO radius are of order factor two smaller. This finding also hints towards the statement above that the extent of the molecular gas disk is not resolved in the observations, but rather only its core in the galaxy center.

Sérsic Indices Concerning the size distributions of different components in the galaxy, the Sérsic indices can add even more pieces of information to the global picture. The distributions of stellar mass, SFR and CO show values of 1.38, 0.83 and 0.4 in this respect with an error of ± 0.3 . As such, all three tracers show typical exponential-disk distributions. The slightly elevated Sérsic index of the stellar surface density might be indicative of a bulge build-up. This observation is not traced by the CO value, which is smaller than one. Although the CO size seems to be similarly compact as the stellar mass radius, it is less centrally concentrated. Since the CO radius serves as lower-limit proxy for the molecular gas size, this statement also holds for correcting the size to higher values. Further indications for the build-up of a central bulge component can be found in the CO kinematics discussed next.

4.3.2 Spectral Analysis of Molecular Emission

Next to the mapping of the CO distributions and stellar properties, the spectral information gained by the use of radio interferometry can be analyzed for additional characteristics such as kinematics and line profiles. Such an analysis allows for extracting maps of velocity and velocity dispersion, rotation curves and intrinsic properties derived from the latter by dynamical modeling, namely rotation velocity, intrinsic velocity dispersion and dynamical mass. Typical characteristics that can be found in spectral lines as analyzed here are double peaks for thin rotating disks and underlying broad floor if outflows are present. The first part of the analysis here sets a focus on the kinematic features in the CO data, including dynamical modeling based on the CO sizes that were determined previously.

CO Kinematics

The kinematics derived from the CO line cubes provide velocity and velocity dispersion maps. Within the sample analyzed in this work the observed kinematics of EGS13004291 have the smallest errors. Dynamical modeling of the maps allow to estimate intrinsic properties of the galaxy such as rotational velocity, intrinsic velocity dispersion and dynamical mass. The resulting maps of the data, models and data-minus-model residuals are displayed in Figure 4.22.

The residuals not only show the quality of the models but also give a further insight into the physical processes present in those galaxies. With an inclination of $i = 27^\circ$, the orientation of EGS13004291 is close to a face-on and therefore the dynamical mass as derived here comes with a substantial error. The assumed inclination value however is the minimum among the different morphology tracers and therefore can be treated as lower limit resulting in an upper limit of dynamical mass.

The obtained dynamical models shown in Figure 4.22 can be used to derive intrinsic properties of the galaxies. One has to keep in mind that the derived DYSMAL models are not unique solutions, but rather a combination of many input parameters chosen, such that the model fits the data. For this reason, I based the models on the output of the morphological fitting in order to constrain the parameter space.

In general the observed kinematics show rotating-disk profiles for both the CO (3-2) and CO (4-3) data, while the data of the former show a larger extent especially in the northern part of the galaxy. The kinematic axes derived from the two data sets agree in position and orientation within the uncertainties. The compactness of the CO (4-3) data aligns with this transition being excited by slightly higher densities than CO (3-2) and the observations performed only with extended configurations. The residuals of the dynamical models and the shape of the dispersion peak in CO (3-2) probably are linked to merger morphology of EGS13004291 as discussed next.

Merger Context The kinematics of EGS13004291 show very regular disk rotation compared to the analyzed sample of galaxies and regarding the likely merger background of the system. Probably, this galaxy is in a late merger stage after the gas has lost its angular

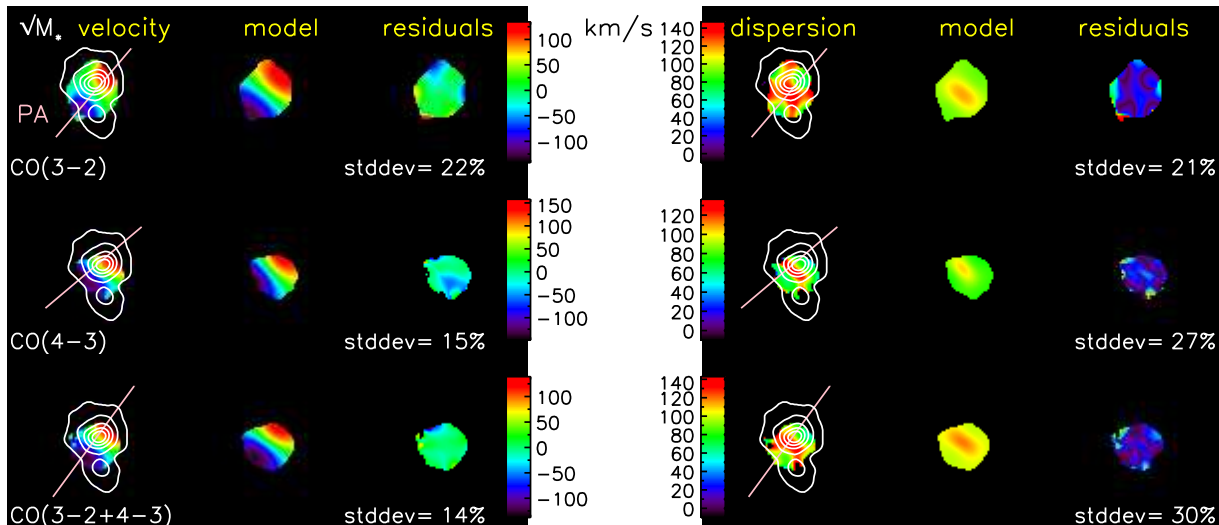


Figure 4.22: Dynamical modeling of the CO kinematics for EGS13004291, from left to right the following quantities are displayed: CO velocity map in color with the position angle (PA) of its largest gradient in pink and the stellar-mass contours overlaid in square-root scale (smoothed to FWHM $0.35''$), followed by the velocity model, data-minus-model residuals and their standard deviation with respect to the peak value of the velocity scale (stddev). The same panels are shown for the velocity dispersion.

momentum during the collision of two massive systems, such that it has settled dynamically in the center of EGS13004291. This scenario is supported by the morphology found in the stellar continuum of a single main body next to one or more tidal streams. The compactness of the large molecular-gas reservoir in the previous comparison of sizes for the different galaxy components also matches this explanation of a late merger.

The kinematic maps and in particular the residual maps from the dynamical modeling can be analyzed with respect to merger signatures. This comparison is done in Figure 4.23 using the V-band image where the tidal streams appear most prominently. Indeed, for the CO (3-2) data the velocity residuals show two minima and maxima where the streams connect to the main body. Similarly, these locations are traced by the x-shaped dispersion peak.

This x-shape is only found in the CO (3-2) dispersion profile, not in CO (4-3), and only for EGS13004291 in the analyzed sample of galaxies. The typical shape of the dispersion peak of a rotating disk beam-smearred in the observation would be a central ridge. The additional dispersion peaks at the arms of the measured x-shape therefore likely are not produced by beam smearing alone, but could be intrinsically linked to the tidal streams and inflowing material from these directions. The locations of these deviations are also visible in the dispersion residuals for CO (3-2). In comparison, the CO (4-3) kinematics only marginally show such features in the residuals and the beam-smearred dispersion. This might be linked to the emission being more compact and mainly distributed in the southern part of the galaxy. As discussed previously, this size difference could be induced by the lack

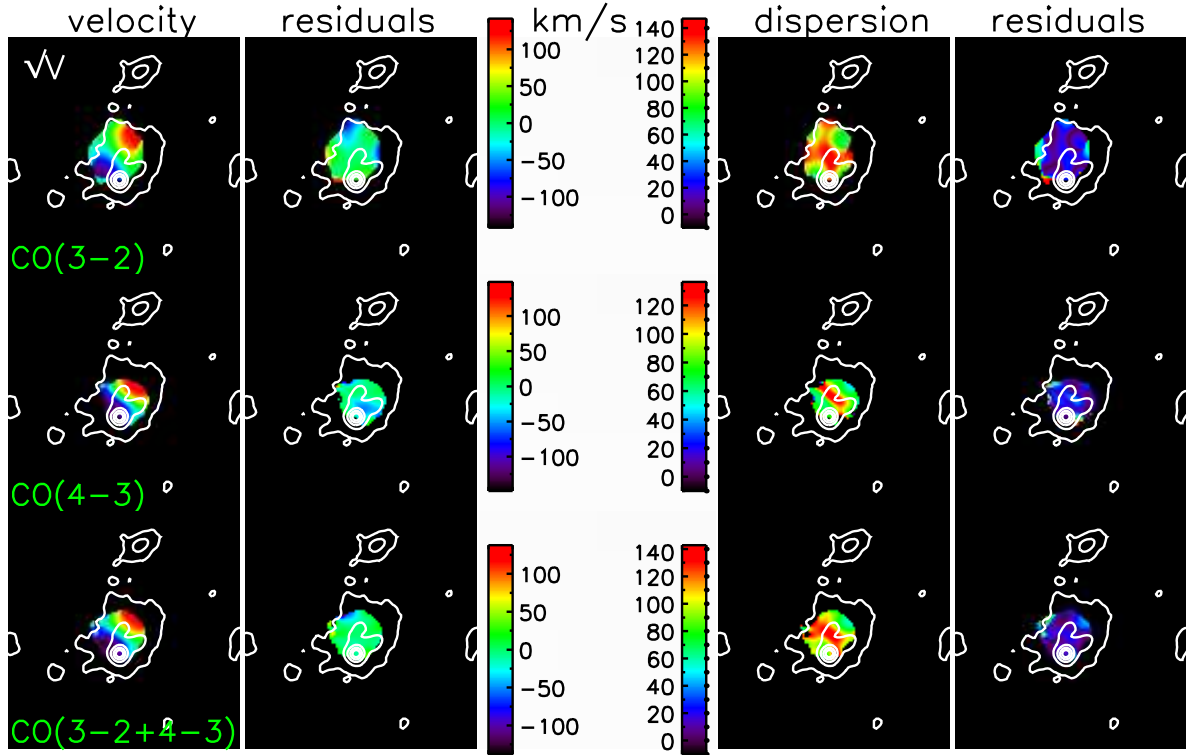


Figure 4.23: Comparison of the CO kinematics to potential tidal streams for CO (3-2), CO (4-3) and the combined data, from left to right the following quantities are displayed in color together with the V-band contours overlaid in square-root scale (smoothed to FWHM 0.25''): CO velocity map, the corresponding data-minus-model residuals, CO velocity dispersion, also followed by the data-minus-model residuals. Potential tidal streams are visible in the V-band contours, namely the right side of the main body as well as on both sides of the latter and in the North.

of compact-configuration data for CO (4-3). But the slightly lower spatial resolution and SNR of the CO (3-2) line is probably not responsible for the x-shaped dispersion peak. The spatial resolution is included by the beam smearing in the dynamical modeling and both lines show high SNRs, also in the derived kinematics.

The CO (4-3) dispersion also shows a lower intrinsic floor than CO (3-2), as will be shown in the following discussion of the corresponding rotation curves.

Rotation Curves I plot rotation curves along the kinematic axis of the derived dynamics in Figure 4.24. The correction of the dispersion floor for spectral broadening is performed afterwards.

The curves indeed show rotation in the velocity profiles as well as non-circular motion in the elevated intrinsic velocity dispersions. Although this galaxy shows signs of an interaction or merger, the rotation features overall are remarkably regular with only minor

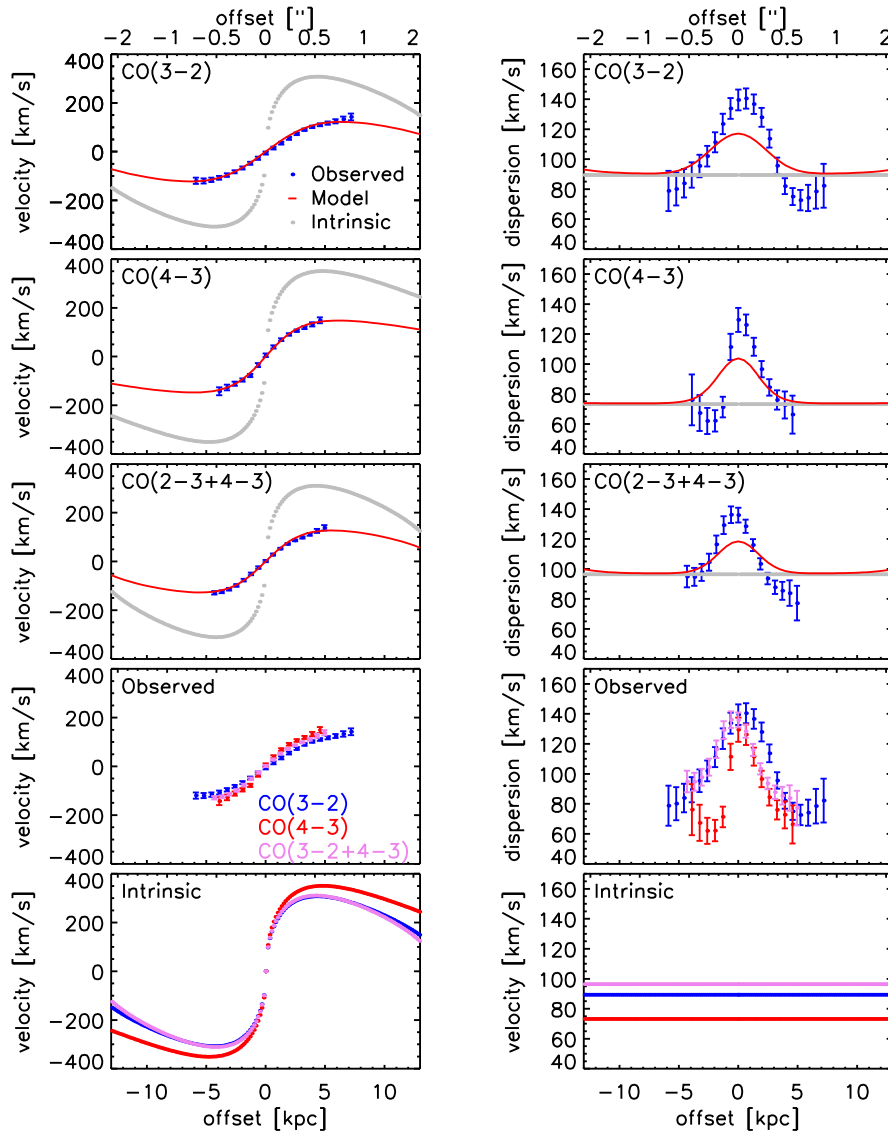


Figure 4.24: Rotation curves as derived from the interferometric CO data of EGS13004291: the blue data points with error bars are the observed velocity and velocity dispersion profiles (left and right), derived as explained in 4.2.1. The modeled red curves were produced with the dynamical modeling capabilities of DYSMAL, which also provides the intrinsic rotation curves as displayed in gray. The intrinsic properties are free from orientation and spatial beam-smearing effects. Compared to the models, the observed velocity dispersions often show higher and narrower peaks. The dispersion floor is not yet corrected for spectral broadening here. From top to bottom the results for CO (3-2), (4-3) and the merge of both data sets are shown followed by direct comparisons of the observed curves and the modeled intrinsic ones.

irregularities and small error bars due to the high SNR of the data resulting from the CO brightness. A late stage of merging would be a possible explanation for this finding, consistent with the late-merger classification of this source in PHIBSS (Tacconi et al., 2013).

Deviations from the models occur mostly around the dispersion peaks, due to beam smearing. Although a minimum estimate of the beam size is used, the models produce broader and lower peaks than what is actually measured. This could be a hint that the galaxy might have a central mass concentration with an elevated intrinsic-dispersion floor below the beam smearing. This dispersion floor might be distinct from the one of the more extended exponential-disk component used for the modeling. Also strong stellar feedback of the central starburst could elevate the intrinsic dispersion. The asymmetries of the measured kinematics, also seen in the residuals of dynamical modeling, might be linked to the northern stream visible in the optical morphology in the redshifted part of the CO emission and in the blueshifted component to the bright star-forming clump in the south of the galaxy.

As mentioned previously, the intrinsic dispersion in CO (4-3) seems to be slightly lower than for the CO (3-2) transition. This and other intrinsic properties as derived from the dynamical modeling are summarized in the following section.

Intrinsic Properties Intrinsic properties of the galaxy can be determined from the dynamical models namely estimates for the rotationally-supported dynamical mass, the rotation velocity defined as the inclination and beam-smearing corrected maximum velocity as well as the intrinsic velocity dispersion after the correction for rotation and spectral broadening. The resulting quantities are listed in in Table 4.7.

Source	M_{dyn} [M_{\odot}]	v_{rot} [km/s]	σ_0 [km/s]	v_{rot}/σ_0	M_{bar}/M_{dyn}
CO (3-2)	2.8×10^{11}	312	88	4	2.0
CO (4-3)	3.3×10^{11}	350	72	5	1.7
CO (3-2 + 4-3)	2.9×10^{11}	313	95	3	2.0

Table 4.7: DYSMAL results for EGS13004291, from left to right: source identifier in PHIBSS, dynamical mass M_{dyn} within a radius of the image size $3.5''$ or 30 kpc, rotation velocity v_{rot} , intrinsic velocity dispersion σ_0 , the ratio of the two latter as a disk-stability diagnostic and the ratio of baryonic to dynamical mass M_{bar}/M_{dyn} . The uncertainties amount to $\pm 50\%$, ± 50 km/s, ± 30 km/s, ± 2 and $\pm 60\%$.

Error Discussion For the intrinsic velocity dispersion σ_0 , the model values of the intrinsic velocity dispersion $\sigma_{0,model}$ are corrected for spectral broadening by quadratically subtracting the spectral resolution $\sigma_{spectral}$ as described by Equation (4.24). The spectral channel width can be used as estimate for the spectral resolution of the interferometric

data, which is roughly 10 km/s in this case. Since the spectral binning of the data cubes mostly is determined by the user, typically it is larger than the actual resolution and therefore can be considered as an upper limit. The uncertainty of the rotational velocity is estimated to ± 50 km/s and ± 30 km/s for σ_0 .

The error on baryonic masses of such studies is rather large due to uncertainties in SED fitting and the CO-to-H₂ conversion factor. According to this, the molecular gas mass has an estimated uncertainty of $\pm 50\%$. The stellar mass is measured by the SED fitting of the HST imagery with an error of $\pm 30\%$ corresponding to the maximum deviation of the 1σ -confidence intervals of the derived stellar-mass map from the actual best fit. The resulting baryonic mass in total carries an uncertainty of $\pm 30\%$.

The error on the dynamical mass can be high due to elevated uncertainties for inclinations below 45° of systems being close to a face-on orientation. Here, this case applies with a value of $i = 27^\circ$. Uncertainties of 10° at this inclination can cause dynamical-mass variations of order 50%. Since differences up to 10° are found in the disk models of the different tracers used here, I estimate an error of $\pm 50\%$ for the dynamical mass.

Mass Measurements The found discrepancy of factor two between the baryonic and dynamical masses can have different origins. But given the uncertainties, there is no significant difference between them. If so, there is no substantial additional contribution of dark matter to the dynamical mass on these inner scales of the galaxy traced by the CO, similar to what was recently found in the analysis of outer rotation curves in ionized gas at similar epochs (Wuyts et al., 2016; Lang et al., 2017; Genzel et al., 2017).

But, as discussed in Wuyts et al. (2016), both stellar and molecular-gas masses usually are rather underestimates as provided by the methods used here. As a consequence, the real baryonic-to-dynamical mass ratio would even further increase to more “unphysical” values above 1. Wuyts et al. (2016) find that 70% of the galaxies with gas surface densities $\Sigma_{gas} \geq 10^9 M_\odot/\text{kpc}^2$ show such mass ratios of > 1 , which indeed is found for all the sample, but especially for EGS13004291 with $\Sigma_{gas} \approx 10^{10} M_\odot/\text{kpc}^2$ calculated via the formula

$$\Sigma_{gas} = 0.5 \frac{M_{molgas}}{\pi R_{e,CO}} \quad . \quad (4.26)$$

For this work, two explanations arise which could solve the paradox of the baryonic mass being larger than the dynamical one.

On the one hand, the regular conversion factor might not apply to EGS13004291, which is not a standard system due to its properties discussed in this work. In the context of a starburst galaxy the validity of the standard conversion factor was questioned in some studies. For ULIRGs, literature finds smaller conversion factors, which would lower the baryonic-mass estimate by up to a factor of five (Downes & Solomon, 1998; Hodge et al., 2012). However, recent results show that in galaxies above the MS as EGS13004291, the conversion factor does not deviate from the standard value by that much, but rather within the expected measurement errors (Bournaud et al., 2015; Scoville et al., 2016; Carleton et al., 2017; Tacconi et al., 2018).

As discussed previously, this error and the other uncertainties do not imply that the baryonic mass measured for EGS13004291 is larger than the derived dynamical mass. However, due to the special properties of EGS13004291, compared to the sample analyzed previously including the largest baryonic-to-dynamical mass ratio, the question arises in which direction the actual conversion factor in this source could deviate from the standard value within its uncertainties. Indeed, a lower conversion factor within the uncertainties could apply for this compact dust and gas-rich starburst galaxy for instance due to a higher dust temperature and molecular excitation than for other SFGs. This adaption would reduce the calculated molecular-gas mass by a factor of 0.8.

In addition, the overall similar compact sizes of dust and the two CO transitions with high SNR in EGS13004291 support that the calculated molecular-gas mass does not miss significant fractions of molecular gas which are dark in CO emission. Together with an actual conversion factor lower than the standard value, the molecular-gas mass could be slightly overestimated here.

Another reason for the found tendency of the dynamical mass being smaller than the baryonic one might be that a bulge component needs to be added to the modeling, as proposed by the general results on morphologies and dynamics in the sample work presented here. This approach could increase the dynamical mass by accounting for this fraction that might be missed in the modeling by an exponential disk alone. In addition, more robust constraints on dynamical masses can be given when outer rotation curves are measured at larger radii than what was observed here. The dynamical mass found here could be a lower limit.

In summary, the baryonic mass potentially could be slightly overestimated by the average conversion factor, while the derived dynamical mass might miss a bulge component or fractions in the outer regions of the galaxy not traced here. However, considering the overall uncertainties on the measurements, no significant difference between baryonic and dynamical mass can be found.

Another interesting feature observed in EGS13004291 by the spectroscopic capabilities of the IRAM interferometer next to the kinematics of the molecular gas is a molecular outflow detected. The analysis of this molecular outflow is the focus of the final section of this chapter.

Molecular Outflow

Next to the narrow lines, other emission components appear in both the high-resolution spectra of the CO (3-2) and CO (4-3) transition, as well as in the merged data denoted as CO (3-2 + 4-3).

All the results discussed here were extracted from continuum-subtracted spectra if not stated differently. Nearly flat continuum emission from dust can be detected in the probed bands. This potential continuum was fitted within a range of 300 km/s at both edges of the spectrum. This range is narrow for a continuum fit, but it was found to provide average line widths within the useful ranges between 100 km/s and 500 km/s. As a consequence, the velocity range around the line is excluded by ± 700 km/s from the velocity zero point. The

comparison between the line fitting of the spectra without and with continuum subtraction shows that this approach is the best trade-off properly accounting for both continuum emission and broad-line components.

CO (3-2) The CO (3-2) emission can be fitted by two narrow Gaussian line profiles and a broad one as shown in Figure 4.25. The continuum fitting shows that the CO (3-2) measurement is not significantly affected by continuum emission, as supported by two findings. On the one hand, the fit implies negative continuum flux densities, while any measured emission should be positive. On the other hand, the line fitting provides similar results without and with continuum subtraction. Therefore, the results without continuum subtraction are summarized in the following.

The two narrow components show FWHM values of (142 ± 4) km/s and (207 ± 2) km/s. The error on the measured line widths is based on the average difference between the results from the regular and smoothed version of the spectrum. Such double-peaked line profiles are known from disk galaxies which show ordered rotation, where the line emission from the part moving away from the observer is red-shifted and the other one shifted to blue wavelengths.

The fitted broad component has a FWHM of (630 ± 2) km/s, however the underlying wings on both sides of the narrow line emission do not exceed the noise level in the spectrum without smoothing. The smoothed version shows more prominent wings. But due to the limited bandwidth, it is not clear whether they lie above the noise. Looking at the edges of the band shows a noise peak larger than the wings of the fitted broad component. But these regions usually always tend to have higher noise levels. Therefore, the smoothed version of the spectrum hints towards a bipolar outflow, which shows up on both sides of the rotationally red- and blue-shifted narrow components of the galaxy. Mapping of the broad component and the analysis of the CO (4-3) spectrum, also combined with the CO (3-2) data, can provide further insight as tested next.

The mapping of this broad feature does not provide any significant detection. However, the line flux density derived by integration directly in the cube is by 20% larger than the flux density measured on the integrated map. In the other resolved PHIBSS sources, the deviation usually amounts to less than 10%. The integrated map usually is build from the velocity channels which show emission. This means that there might be channels which do not show emission, but still in total would contribute to the integrated line flux density if included. I therefore re-do the integrated map with the broad component channels known from the spectral fit. This procedure does not result in any significant increase of flux. Acquiring more data beyond the existing ten hours of integration would probably be needed for further investigation in this respect.

As the CO (4-3) line was observed with an integration time of 22 hours and with a wide-band correlator of 4 GHz instead of only 1 GHz, this data set gives an additional perspective on the spectral analysis as discussed in the following.

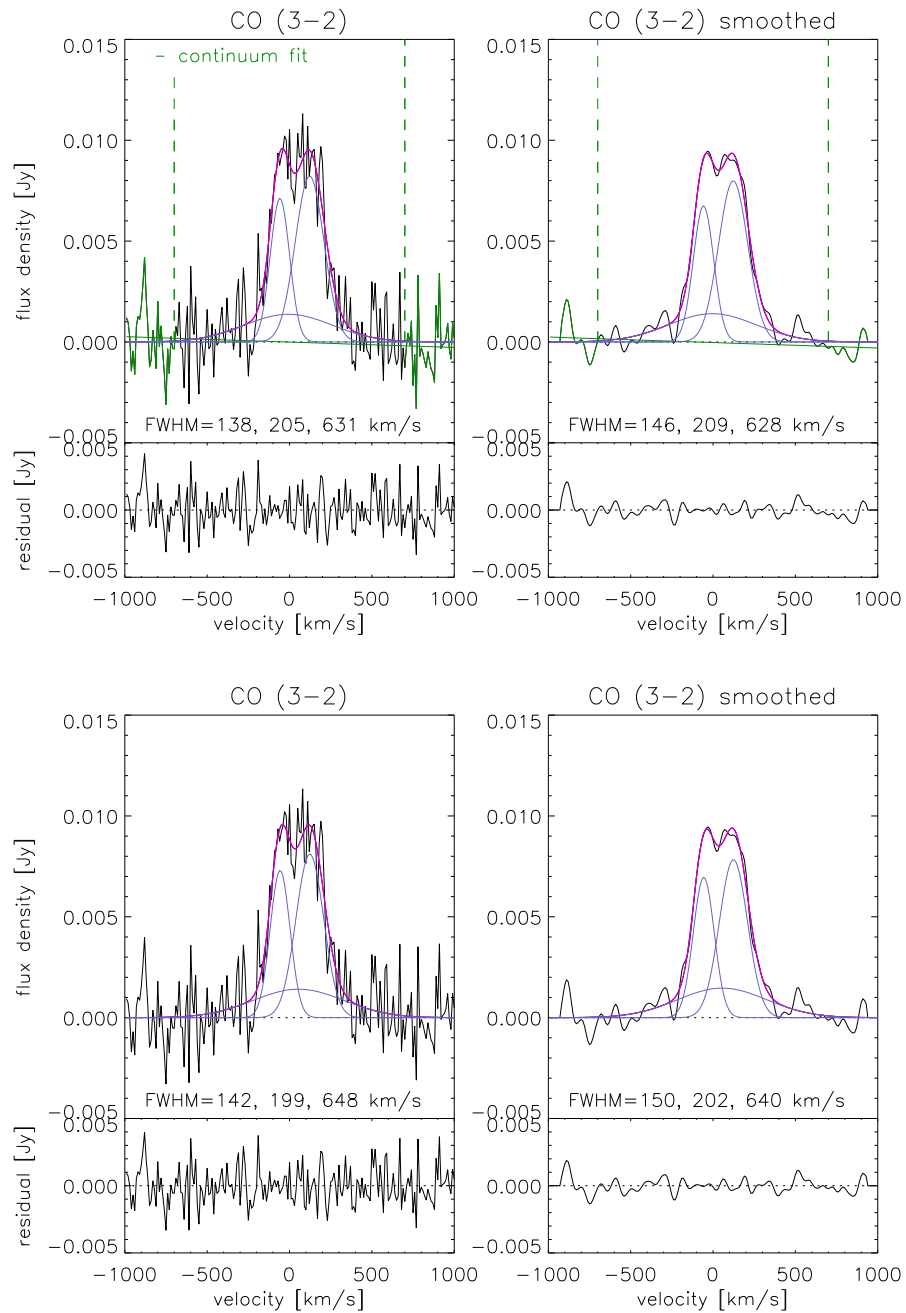


Figure 4.25: Spectral fitting (purple line) of the CO (3-2) line by three Gaussian components in blue together with a version on the right which is smoothed by a Gaussian kernel with a standard deviation of 20 km/s for better visualization. In addition, the FWHM values are shown as well as the fit residuals on the bottom. The parts of the spectrum marked green are used for the continuum fit performed in the upper panels and subtracted in the lower ones.

CO (4-3) The CO (4-3) spectrum is fitted by two narrow components without an underlying broad Gaussian. However, there is continuum emission next to the two-peak line profile visible in spectrum shown in Figure 4.26. The origin of continuum emission at these wavelengths can be attributed to thermal radiation from dust. 30 hours of integration for the CO (4-3) covering the band (650 ± 10) μm were able to detect the dust emission.

The continuum in the CO (4-3) spectrum can be mapped, which is done in Figure 4.27 excluding all spectral channels that are attributed to the fitted line. The flux density of 1.1 mJy measured in the (u,v)-fit for the continuum is a factor of 10 lower than from the (3-2) or (4-3) emission. This number also corresponds to the average flux density of the continuum in the spectrum. In comparison, for the CO (3-2) data this average flux density is found to be < 0.3 mJy.

Interestingly, the dust emission is well-embedded in the overlaid contours of the SFR distribution from SED fitting. In addition, the regions of star formation without or with lower dust emission correspond to the UV-bright emission found in the HST imagery of Figure 4.20 in contrast to the optical in red. Although it is known that SFRs derived from optical/UV emission alone misses a large fraction of star formation only traced by IR measurements, the SED fitting clearly still results in a SFR distribution matching the global picture, as given by the UV/optical morphology measured by HST and the dust distribution observed by the IRAM interferometer.

For Figure 4.28 I performed the line fitting on a continuum-subtracted version of the spectrum as previously for CO (3-2) together with a smoothed version to make the detected emission more evident among the noise. In these spectra, the narrow components are characterized by FWHM values of (177 ± 4) km/s and (141 ± 4) km/s.

Thus, the CO (4-3) data show the double peak of ordered disk rotation as the lower transition CO (3-2). But no typical broad Gaussian component of outflow structure is visible in the spectrum. Either there is no outflow in the CO (4-3) emission or the outflow is not detected here. A non-detection could be explained by several factors. On the one hand, the long integration on the CO (4-3) line lead to the detection of the continuum emission from the dust component in EGS13004291. Not only could the potential outflow be confused with this emission, the dust continuum is expected to be a factor of two stronger around the CO (4-3) line than for (3-2) as displayed in Figure 4.29.

Another difference between the CO (3-2) and (4-3) data is that the latter was only observed in extended array configurations while (3-2) also includes observations in the compact D configuration. Independent of the spatial extent of the potential outflow, usually data sets combining both extended and compact configurations show a better data quality also due to the better (u,v)-coverage. Therefore, the CO (3-2) and (4-3) data can be merged in order to better probe the spectral profile of the molecular gas with a maximum of integration time and combined array configurations. The corresponding analysis is presented in the next section.

Merged CO (3-2) and (4-3) The combined CO (3-2) and (4-3) spectrum include observations in extended and compact array configurations as well as an integration time of

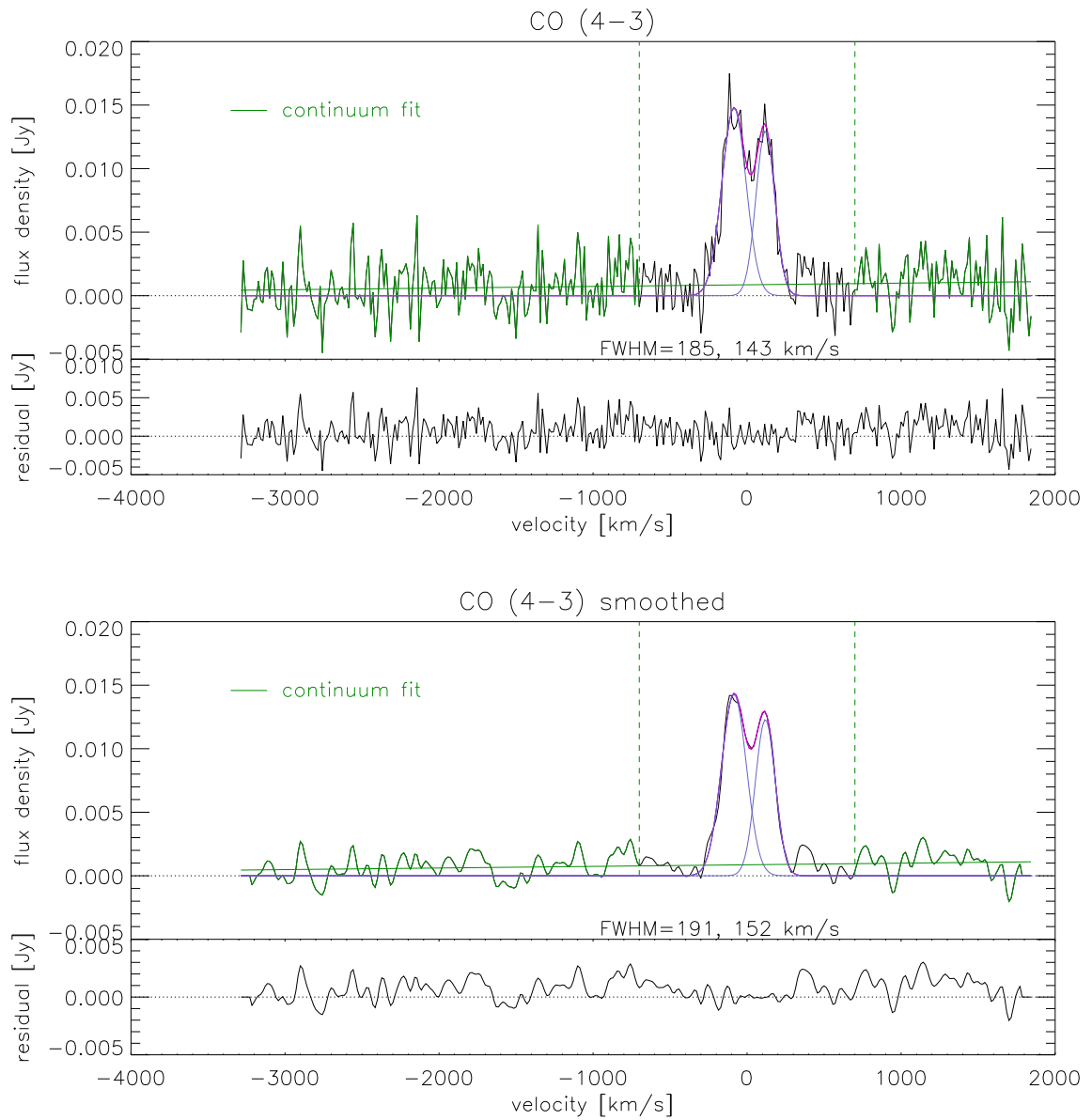


Figure 4.26: Spectral fitting (purple line) of the CO (4-3) line prior to continuum subtraction, by two Gaussian components in blue together in a version of the spectrum on the bottom, smoothed by a Gaussian kernel with a standard deviation of 20 km/s for better visualization. In addition, the FWHM values are shown as well as the fit residuals below, which show remaining continuum emission also visible in the spectrum. The parts of the spectrum marked green are used for the continuum fit.

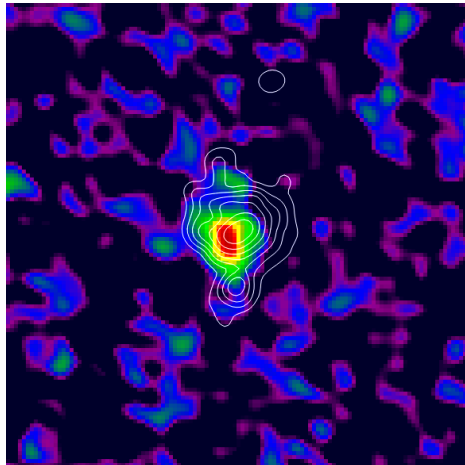


Figure 4.27: Map of the continuum emission from dust detected in the CO (4-3) data in color ($0.4''$) as well as the SED-derived SFR in contours, smoothed to a $0.3''$ resolution.

32 hours. The merged spectra are limited to the shorter 1 GHz-band due to the contribution from the CO (3-2) measurements. This spectral range is indeed narrow for continuum fitting, but as found previously, the included CO (4-3) data provide a robust detection of this dust emission, due to its higher intensity around the (4-3) frequency by a factor of two and the long integration time of 22 hours.

Consistently with the previous findings, the merge of the two high-SNR CO lines shows both signatures found in their individual spectra, namely a broad component in the line emission and the continuum radiation from dust. Figure 4.30 shows the spectrum in regular and smoothed version in the original measurement and the continuum-subtracted one. With an average flux density of < 0.4 mJy, the fitted continuum level is stronger than in the CO (3-2) spectrum and weaker than in the (4-3) data, compared to < 0.3 mJy and 1.1 mJy respectively. Subtracting the continuum for the line fitting is particularly important in this case since otherwise continuum and broad emission are confused as can be seen when comparing the FWHM values of the latter for both fits.

When the continuum is not subtracted the broad component is fitted by a Gaussian with FWHM of (881 ± 126) km/s, which is larger than what the CO (3-2) spectrum alone reveals and also comes with a much higher error corresponding to the difference between the results from the regular and smoothed spectrum. If the continuum is subtracted though, the line widths are (178 ± 15) km/s, (153 ± 15) km/s and (521 ± 15) km/s.

These results are closer to the CO (3-2) results and reveal a much more prominent outflow component than in the latter, especially looking at the continuum-subtracted, smoothed version of the spectrum and the corresponding fit residuals. In this merged spectrum the broad component is mostly visible on the red side of the narrow line emission, attributed to positive velocities. In contrast, to the case of the CO (3-2) spectrum, the fitted broad Gaussian distribution exceeds the noise level in its peaks and the fit residuals are smaller, comparing peak-to-peak values of 8 mJy and 3 mJy to 5 mJy and 2 mJy, in the

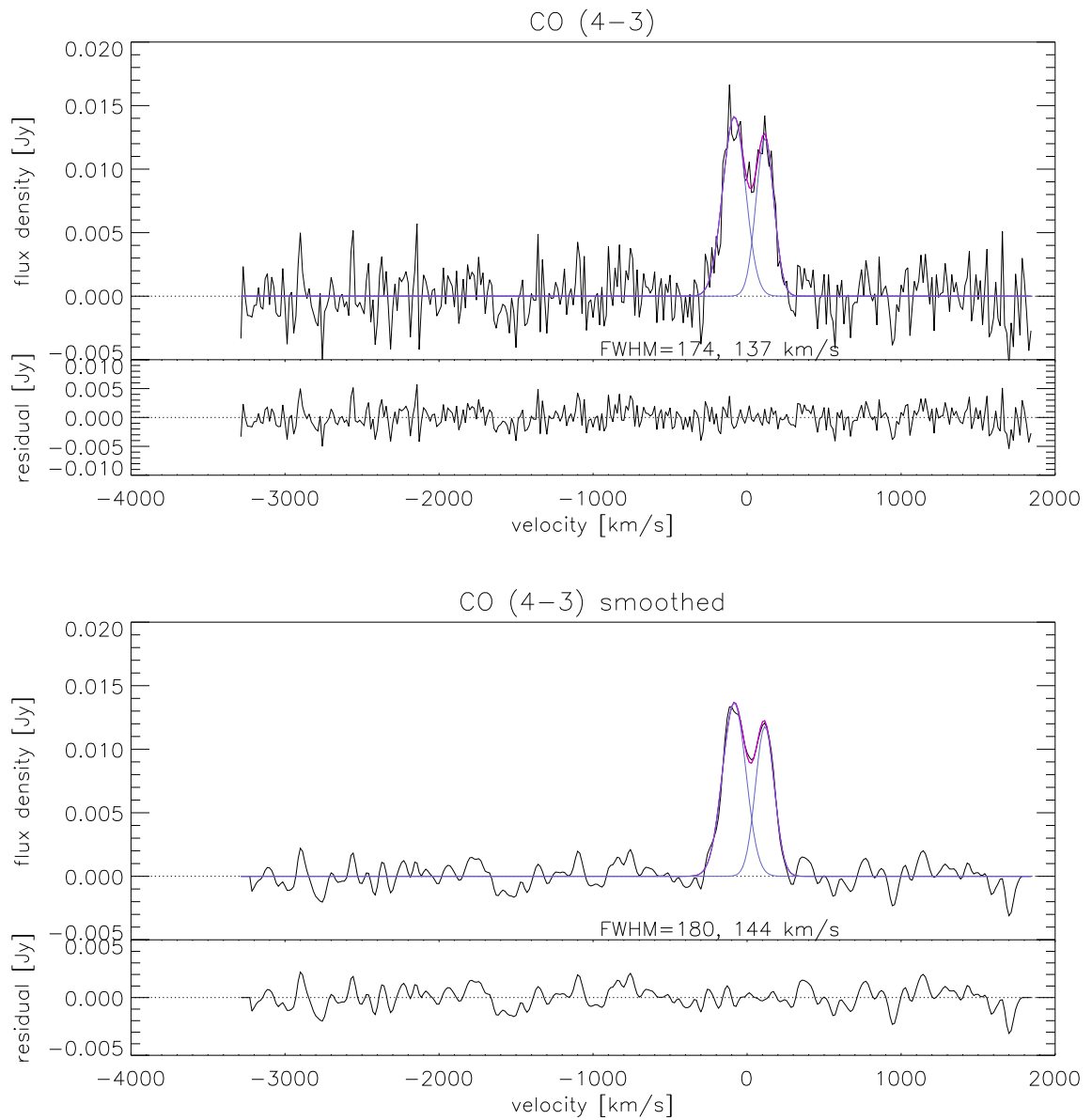


Figure 4.28: Spectral fitting (purple line) of the continuum-subtracted CO (4-3) line by two Gaussian components in blue. Below a version of the spectrum is shown which is smoothed by a Gaussian kernel with a standard deviation of 20 km/s for better visualization. In addition, the FWHM values are shown as well as the fit residuals.

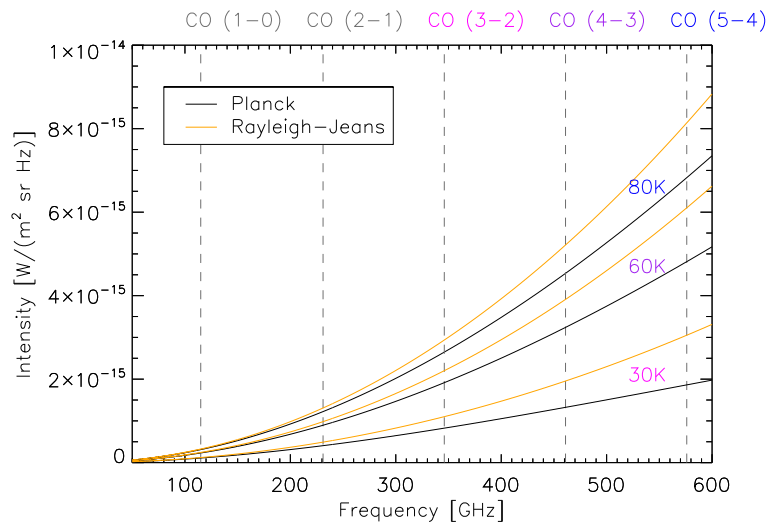


Figure 4.29: Model spectrum of the dust continuum around the five lowest CO rotational transitions, estimated by a blackbody spectrum according to Planck’s law and the Rayleigh-Jeans approximation. The selected temperatures are typical for the observed molecular gas and correspond to the excitation temperatures of the three CO lines observed for EGS13004291. In this picture, the continuum emission from dust is a factor of two higher around the CO (4-3) line compared to (3-2).

original and smoothed version. In addition, the residuals are more evenly distributed around the zero point, while in the CO (3-2) spectrum, the positive residuals seem to dominate slightly over the negative ones. These findings speak for a more robust subtraction of the continuum emission in the merged data than for the CO (3-2) line alone.

In comparison, the residuals of the (4-3) fitting shows larger peak-to-peak values of 11 mJy and 5 mJy. Therefore, the outflow component in CO (4-3), if present, could be hidden in the elevated noise level relative to the other measured spectra.

Based on the color filling in Figure 4.30, I map the red and blue wing of the outflow in Figure 4.31. I also include the continuum on the blue side of the CO emission to test whether the narrow blue wing can be confused with the latter. The mapping of the blue wing includes a fraction of the narrow-line emission, while the red component is dominated by the broad feature as indicated by the line fitting.

The red and blue wing of the broad component are aligned along the kinematic axis close to the center of the CO emission. The blue dust continuum is located in this center distinct from the mapped blue wing, which excludes the possible confusion between these components.

In summary, the merged data of CO (3-2) and (4-3) provide the best basis for the analysis of the outflow signature in the following interpretation of the derived results.

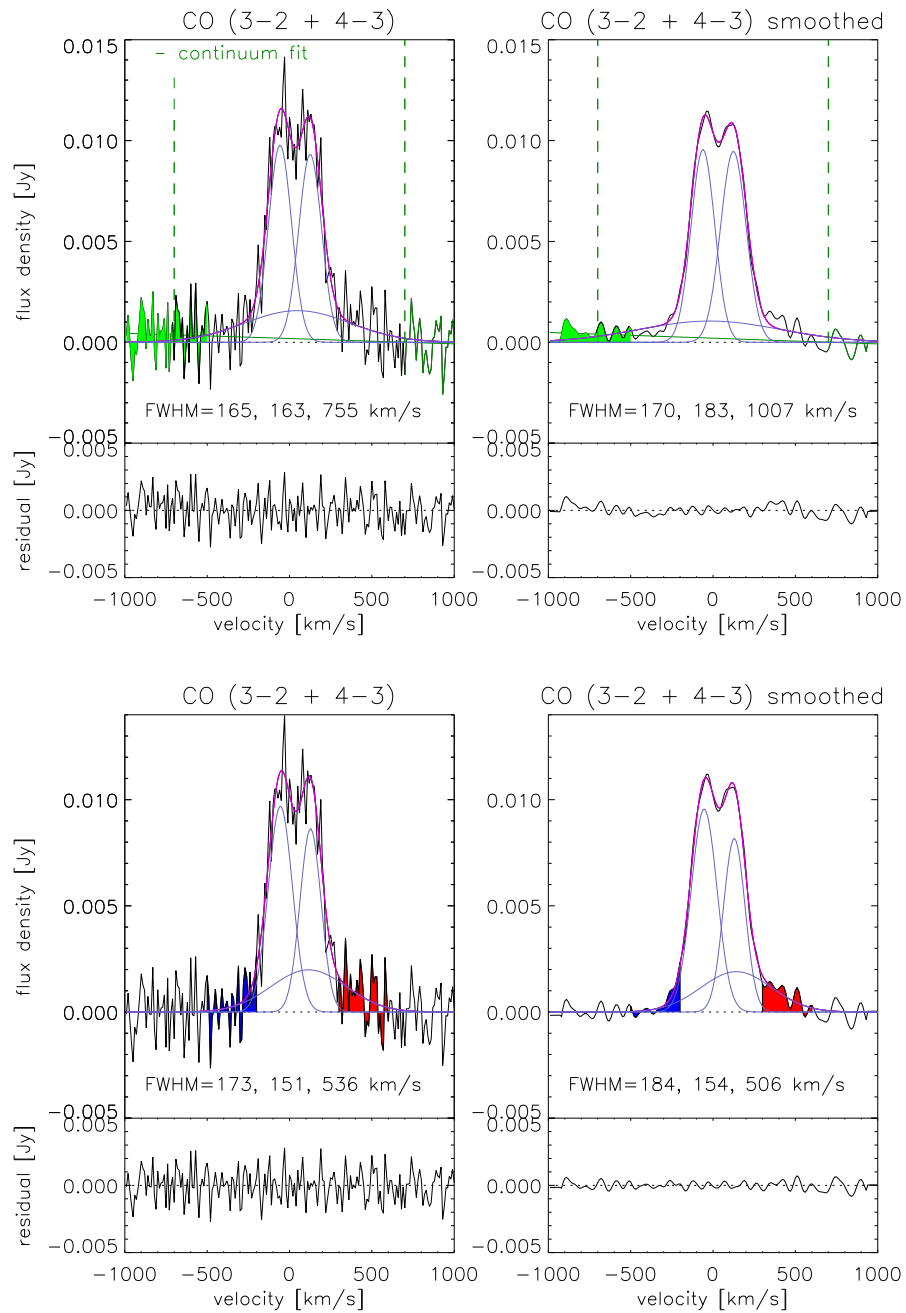


Figure 4.30: Spectral fitting of the merged CO (3-2 + 4-3) lines by three Gaussian components together with a version on the right which is smoothed by a Gaussian kernel with a standard deviation of 20 km/s for better visualization. In addition, the FWHM values are shown as well as the fit residuals below. The green lines mark the continuum fit performed in the upper panels and subtracted in the lower ones. The color filling is used for mapping in Figure 4.31.

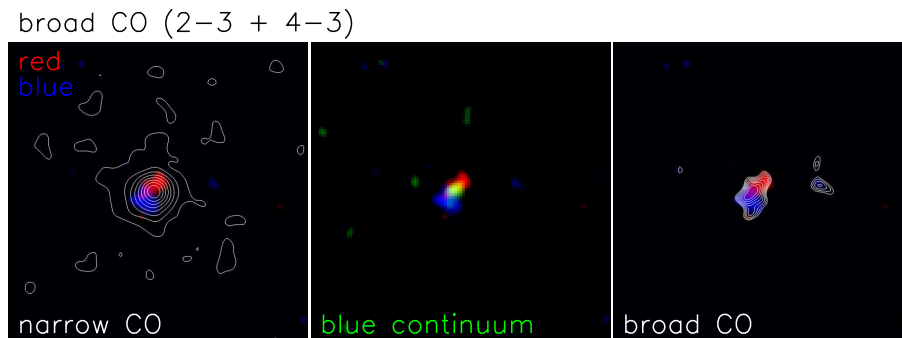


Figure 4.31: Mapped outflow of the CO (3-2 + 4-3) data as red and blue wing of the broad component shown with other properties, from left to right: contours of the narrow CO emission, continuum on the blue side of the CO emission in green, average of red and blue wing in contours. All displayed data show signals above 3σ .

Interpretation The merged data set includes the long integration time from the CO (4-3) observations and the compact D configuration from (3-2). By the combination of both spectra, the emission in the broad component can be distinguished from the underlying continuum emission and the general noise.

The found FWHM of the broad component in the fit of the merged spectrum based on the CO (3-2) and (4-3) line amounts to (521 ± 15) km/s, taking the average between the original and the smoothed version. The peak of this broad feature is slightly redshifted, on average by ≈ 75 km/s with respect to the rotation center in between the two narrow components.

On the basis of this velocity FWHM a maximum velocity of the material emitting the broad line can be estimated. A standard approach as developed in Rupke & Veilleux (2013) is to subtract twice the broad dispersion $\sigma_{broad} = v_{FWHM}/2.35$ from the velocity shift of the broad peak v_{shift} as

$$v_{max} = v_{shift} + 2\sigma_{broad} \quad . \quad (4.27)$$

This equation defines the maximum velocity such that 98% of the gas emitting the broad spectral featured is less redshifted than v_{max} . The maximum velocity attributed to the broad component detected here therefore is ≈ 518 km/s. This observed value can differ from the intrinsic one due to beam smearing and orientation. Considering the effect from instrumental beam smearing, the derived maximum velocity would be an upper limit. The opposite trend of a lower limit is given by the correction from inclination i when dividing the maximum velocity by $\sin(i)$.

The orientation of the outflow cannot be constrained by the observations. But as first approximation, an orientation along the path of the least resistance perpendicular to the galaxy disk can be assumed, as is frequently found for disk systems. This assumption matches the redshifted disk and outflow emission observed in the northern direction and the blueshift in the South as demonstrated in Figure 4.32. The outflow inclination would then amount to $i = 27^\circ + 90^\circ$ leading to a corrected maximum velocity of $v_{max,corr} = 559$ km/s.

Regarding potential contributions from beam smearing of unresolved orbital motion, this maximum velocity should be regarded an upper limit under the assumption that the outflow is directed perpendicular to the disk. Furthermore, also stellar feedback from the central starburst and the central bulge-like mass concentration can contribute to the elevated velocity dispersion found in the broad line emission.

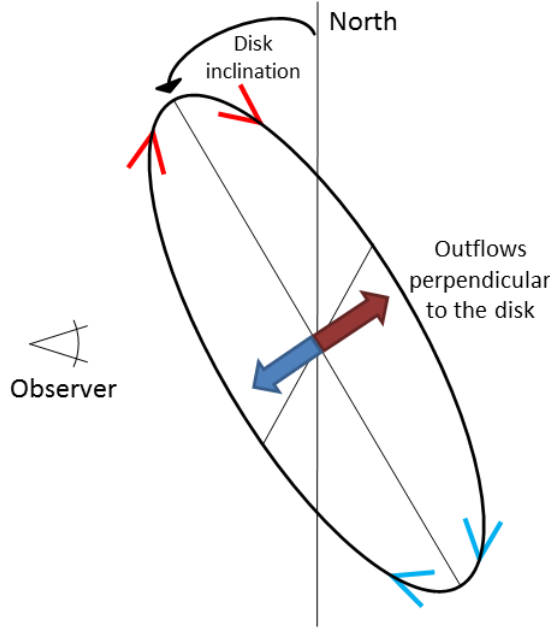


Figure 4.32: Model of the outflow orientation, where the redshifted disk and outflow emission are observed in the northern half of the image plane and the blueshift in the South respectively.

The estimated outflow velocity of order ~ 500 km/s supports the previous findings of strong star-formation feedback in EGS13004291 without indication of AGN activity, which can result in higher outflow velocities, sometimes above 1000 km/s. The underlying assumption of the orientation is reasonable as outflows tend towards the direction of the least resistance and the less likely case of an inclination close to the disk orientation $i = 27^\circ$ would result in $v_{max,corr} > 1000$ km/s. Such high velocities are usually attributed to AGN activity, which is not observed in EGS13004291.

Outflows from nuclear starbursts are known to be momentum-driven in contrast to energy-driven thermal pressure, which additionally appears in AGN. This means that momentum is conserved and the triggering processes for this are radiation pressure, winds and supernovae remnants (González-Alfonso et al., 2017). Together, the starburst and the outflows typically lead to an inside-out quenching of star formation. On this basis, the outflows rather appear on small radii not extending far out. This scenario matches the observations here, for which the CO emission is compact and no evidence is found that the broad component detected extends further out.

Looking at the measured CO excitation in different lines, EGS13004291 is a starbursting

SFG above the MS, with a large compact gas reservoir after an interaction or merger event. The measured depletion time is 0.7 Gyr, similar to the other galaxies in the sample, in contrast to 10 Myr found for ULIRG objects (Carilli & Walter, 2013).

The origin of molecular gas in outflows is still debated. Numerical simulations such as by Richings & Faucher-Giguère (2018) show that in their framework the molecular component cannot be accelerated to such velocities without the molecules being destroyed. In this scenario, the molecule emission observed here would form within the outflows. This condensation of a hot ionized-gas phase is currently favored by the results of performed studies in simulations and empirically (Walter et al., 2017).

Another question in this respect is which fraction of outflowing gas will be re-accreted by the system. In a similar system analyzed by Walter et al. (2017) re-accretion predominantly is expected and the dense molecular gas which is ejected seems to display similar properties as the initial molecular component. In this respect, the molecular emission in the central outflow is optically thick, while outflows in more extreme objects such as AGN often are widely spread and include optically thin molecular gas.

Since the outflows detected here are related to CO emission coming from the galaxy center and show moderate velocities, the outflowing material probably will not escape from the gravitational potential of the galaxy. But the outflows strip gas from the inner regions, potentially fueling star formation in the outer parts. This picture is consistent with an inside-out growth of galaxies. Outer regions are fueled if the ejected gas, which mostly conserves angular momentum, gains significant momentum at large radii for long times as shown in theoretical work about these so called galactic fountains (Shapiro & Field, 1976; Oppenheimer & Davé, 2008; Oppenheimer et al., 2010; Brook et al., 2012; Übler et al., 2014).

The overall conclusions on EGS13004291 and the sample of galaxies is presented in the following last chapter, which summarizes the results from the application of interferometry in two different fields of astronomy.

Chapter 5

Conclusions

Interferometry is used in many fields of research including astronomy. This technique helps increasing the spatial resolution of observations as it overcomes the limit of aperture diameter. Instead, the separation between the telescopes, the so called baseline, is the relevant quantity. Moreover, interference measurements include observables which cannot be traced by single-aperture imaging such as the phase information. GRAVITY uses this quantity to perform phase-referenced imaging and narrow-angle astrometry in the optical realization of interferometry, by means of a metrology system based on phase-shifting interferometry itself.

The IRAM interferometer on the other hand is based on the radio principles of interferometry. The latter allow gaining spectral information in addition to the spatial brightness distribution without a dedicated spectroscopic instrument. I used this capability to probe galaxy evolution for a small sample of galaxies at high redshifts close to the peak of cosmic star formation. In particular, I could spatially resolve the molecular gas in these systems, which has frequently been done for nearby systems, but is still rather rare for higher-redshift sources. The conclusions on this work are summarized next.

5.1 Galaxy Evolution with the IRAM Interferometer

Molecular gas in massive star-forming galaxies on the main-sequence could be spatially resolved around redshift $z \sim 1$ based on the PHIBSS surveys at the IRAM Interferometer. Previous studies have already provided similar results for the ionized-gas component in such systems, but in larger, statistical samples. This thesis focused only on a few objects as the radiation from the cooler molecular gas requires longer integration times to acquire such data. Since molecular gas mainly consists of hydrogen, which has excitation temperatures higher than typically found in the dense and cold molecular medium, the second most abundant molecule, CO, is used as tracer for the cold gas.

Five galaxies around redshift $z \sim 1$ were spatially resolved by PHIBSS with sub-arcsecond resolution, in addition to existing imagery by HST in the rest-frame UV and optical light. The latter traces the stellar continuum. Via SED-fitting, properties, such

as stellar mass, SFR and visual extinction by dust, can be derived from the photometry in multiple bands. Therefore, the presented analysis links different components of star formation, which drives galaxy evolution. The star formation peak is of particular interest in this respect as the conditions for the underlying processes are different than in the nearby Universe and linked to particularly large gas fractions triggering high SFRs.

The sample galaxies, consisting of the five objects EGS13003805, EGS13004291, EGS13011155, EGS13011166 and EGS13019128, are massive representatives of this population of star-forming galaxies. Their masses lie close to the Schechter mass, at which the high SFRs quench, often with a preceding starburst by large gas reservoirs from accretion, galaxy interactions or even mergers, minor or major. The main findings of this analysis on the sample, as well as in more detail on the outflow-object EGS13004291, are collected in the following.

5.1.1 Spatially-Resolved Molecular Gas and Star Formation at $z \sim 1$

Clumpy Distributions of the Stellar Continuum

Clumpy morphologies are found due to patchy dust obscuration, tidal interactions or mergers:

- The galaxies appear very clumpy in their stellar continuum due to extinction effects and exhibit highly dust-obscured, red centers. In contrast, the derived distributions of stellar mass and star formation rate are rather smooth and peak in the centers.
- Clumps and streams outside the main bodies of the galaxies are observed in the stellar continuum, which potentially originate from interactions or mergers.
- The rest-frame UV emission mainly consists of clumps of star formation with low extinction. It does not trace the bulk of star formation or stellar mass, but rather the outer regions in the galaxies. As such, this emission is not an appropriate tracer of the overall galaxy morphology.

Central Stellar-Mass Concentrations and Exponential Disks in the Stellar Continuum

The smooth distribution of stellar mass is a reliable tracer of the position angle and inclination. However, the morphology of the stellar mass is dominated by bulge growth. Therefore, the structural parameters for the dynamical modeling are extracted from the rest-frame optical, which also covers the extended disk regions:

- From comparison to the kinematic axes as found in the CO data, the best morphological tracer is the distribution of stellar mass, and to some level the rest-frame optical images. The latter however are not a reliable tracer in the case of EGS13004291,

which has a particularly large extinction in the center and is close to face-on with an inclination of $i = (27 \pm 20)^\circ$.

- The rest-frame optical light distributions show exponential-disk profiles with Sersic indices $n_{Sersic} = 1 \pm 1$ and effective radii of $R_e = (5 \pm 1)$ kpc.
- While the orientation parameters from the stellar-mass distributions deliver robust estimates, their compact effective radii of (3 ± 1) kpc and average Sersic indices $n_{Sersic} = 2 \pm 1$ are probably not representative for the disks of the galaxies, as they are dominated by the forming central bulges. The exception is lower-mass object, EGS13019128, which in all tracers shows the features of a compact star-forming disk without external clumps. EGS13003805 shows the most prominent bulge-disk composition both in the stellar continuum and mass.

Similar Distributions of Star Formation and Molecular Gas

The distribution of star formation and molecular gas show similar features:

- The distributions of SFR and molecular gas on average are similarly compact as the stellar mass, but with exponential-disk Sersic indices of $n_{Sersic} = 1 \pm 1$ and $n_{Sersic} = 0.8 \pm 0.5$. Bulge growth in the centers might be responsible for this slight trend towards depletion of molecular gas in the central regions.
- As for the SFR, the molecular distributions peak in the dust-obscured galaxy centers and also show clumpy distributions, but less prominent than for the stellar continuum, due to limited resolution and faint signals from the cold medium.
- The morphology of the SFR seems to be more closely related to the one of the molecular gas, than the stellar-mass distribution does. This finding matches the picture of star formation taking place in the molecular-gas reservoirs, while stellar mass includes regions of past star formation with lower gas content.

The overall findings on the morphology traced by different tracers are compatible with the paradigm of inside-out growth in galaxies: star formation depletes the inner molecular-gas reservoirs forming bulges and by that moves to the outer regions, as the galaxy grows through accretion, interactions or mergers.

Molecular-Gas Kinematics

- The molecular gas shows rotating, turbulent disks with indications towards growing bulges in the galaxy centers. The rotation velocities and intrinsic velocity dispersions are high compared to local systems, with values of > 300 km/s and > 50 km/s.
- The resulting disk-stability diagnostic shows rotation-dominated systems with $v_{rot}/\sigma_0 > 4$.

- The dynamics for radii < 10 kpc are dominated by the baryonic masses of the galaxies.

The overall results on the kinematics of the molecular gas align well with the findings from previous ionized-gas studies, showing that both gas components have similar dynamics despite different underlying conditions.

5.1.2 Molecular Outflows in EGS13004291

Compact Starburst in Late Merger

- In the stellar continuum, this object shows signs of a merger by at least one tidal stream. Remarkably regular rotation of the molecular gas points to a late merger with relaxed dynamics. The residuals from dynamical modeling indicate tidal streams connecting to the main galaxy body.
- EGS13004291 has the highest gas fraction, visual extinction and SFR among the sample.
- Several rotational transitions were detected in this source. The derived effective radii slightly decrease with excitation tracing denser regions. The CO (5-4) effective radius does not follow this trend, however it is regarded as lower limit due to poor SNR.
- The detected dust continuum is found to be marginally smaller in effective radius with $R_e = (2.40 \pm 0.03)$ kpc than the lowest CO transition probed, CO (3-2). The continuum shows very remarkable resemblance with the derived SFR distribution.

Outflows

- An outflow is found in the merged CO (3-2 + 4-3) spectrum, indicated by a broad component with a FWHM of (521 ± 15) km/s. The mapping of the respective spectral channels shows that this high-velocity component is located in the galaxy center. Under likely assumptions about the outflow orientation with respect to the galaxy disk, a maximum velocity of ≤ 560 km/s is estimated for the outflowing component.
- The outflow is only marginally visible in the CO (3-2) spectrum alone. It shows a broad component with FWHM of (644 ± 4) km/s, but cannot be mapped due to a low SNR.
- No outflow is detected in the CO (4-3) spectrum. The observed line shows a higher SNR than for CO (3-2), but was only observed in extended configurations. Furthermore, dust continuum is detected in the CO (4-3) spectrum, which shows a spatial distribution very similar to the SED-derived SFR map. If an outflow is present in the CO (4-3) emission, it is very likely hidden in the continuum.

The overall compact distribution of molecular gas and dust, together with the high SFR, gas fraction and visual extinction, strongly point towards a central starburst probably triggered by a merger event, leading to the observed molecular outflow. Such starbursting galaxies at the upper MS rapidly build up central mass concentrations forming bulges (Wuyts et al., 2011a).

Overall, the analysis of the sample properties, with a special view on the starburst object EGS13004291, could deliver spatially resolved information on several components of star formation in high-redshift galaxies including molecular gas. The latter could not only be analyzed in its spatial distribution but also spectroscopically. This gave a first insight into the molecular-gas dynamics at high redshift in a small sample, as well as on outflows triggered in the starburst galaxy EGS13004291.

Similar results are found as for ionized-gas studies, with the difference that the molecular component is more centrally concentrated. But in this comparison, the underlying molecular-gas data are still limited by small samples and resolution. Further extensive studies with the world's largest radio to sub-millimeter interferometers including IRAM will be necessary to increase the resolution in molecular-gas observations.

5.2 The GRAVITY Metrology System

The metrology system of GRAVITY traces internal differential optical path differences between the two observed objects in order to subtract those from the total dOPD measured. This allows measuring the actual separation on sky between the targets. The primary science case for the instrument and the metrology system is the Galactic Center, to probe physics close to the event horizon of the SMBH. Flare models will be tested and ultimately general relativity will be probed in this unique laboratory of the strong-field limit close to black holes.

GRAVITY has already demonstrated its remarkable capabilities for various science cases, revealing previously unprobed phenomena. Due to the combined use of AO, fringe tracking and metrology, observations in the K-band are pushed to new limits in interferometry. As a result, the IR radiation of the SMBH in the Galactic Center can be constantly monitored for the first time, also in its non-flaring state.

Originally, the metrology was based on a dual-beam design interfering the metrology laser beams from the science and fringe-tracker channels. The sampling is performed with four receivers per telescope and by phase-shifting the interference pattern. The phase-shifter calibration is the first part of this work. The second part is the analysis and mitigation of the backscattering of the metrology light onto the science detectors. This unexpected phenomenon required a design change to a three-beam scheme. The main results of this work are summarized in the following.

5.2.1 Phase-Step Insensitive Calibration of the Phase Shifter

A previously established calibration method for the phase shifter by a linear scan lead to an accuracy of 2 nm for the calibrated phase shifts. However, the limitations of this method by various non-linear effects left doubts about the underlying assumptions and the results. The phase-step insensitive method developed as part of this thesis work omits some of those effects in a quite elegant way:

- The phase shifts are applied subsequently in a quasi-static environment in contrast to a scan through the complete phase range during environmental fluctuations.
- The phase steps are extracted directly instead by assuming a detailed model function between applied voltage and effective phase shifts.
- The key component to this scheme is a delay line, which scans the fringe with respect to the phase shift to be calibrated.
- Robust ellipse fitting by χ^2 -minimization was established leading to a calibration accuracy of 1 nm in the laboratory.
- This accuracy is thus improved by a factor of two compared to the previous, biased method. The bias of the old method was found to be > 5 nm.
- The remaining limitations are laser power fluctuations, the transmission function of the phase shifter and its contrast modulation from birefringence.
- Calibrating and including these factors in the modeling did not produce a higher accuracy for the phase-shift calibration. Probably they induce errors well below the general level of the systematics in this calibration routine.

The results of the improved phase-shifter calibration are consistent with the specified astrometric error budget for narrow-angle astrometry of 10 μas , corresponding to the scale of the event horizon of the SMBH in the Galactic Center. The previously established method was biased and did not deliver such an accuracy.

5.2.2 Raman Scattering and Fluorescence in Optical Fibers

The metrology laser causes Raman scattering and fluorescence from rare-earth elements in the fluoride-glass fibers of GRAVITY. This backscattering on the instrument detectors prevented the science operation by several orders of magnitude.

Raman Scattering

- The metrology laser light with a wavelength of 1908 nm triggers Raman scattering with a Stokes peak in the scientific K-band of the instrument detectors at 2150 nm.

- The Raman scattering results from the coupling of light to vibrational modes of the medium, producing constant frequency shifts independent of the incident beam frequency.
- Laboratory tests showed that the Raman peak is polarized.
- The Raman radiation is not the dominant contribution in the backscattering.

Fluorescence from Holmium

- Fluorescence from the REE Holmium dominates the detected backscattering spectrum at wavelengths shorter than the Raman peak.
- The underlying process is the absorption of light within a certain band, depending of the energy states within the element. The re-emission also happens in a characteristic band, by de-excitation typically similar to the incident energy or slightly below.
- The fluoride-glass fibers are contaminated by this element and not doped on purpose.
- The fibers in the instrument show a factor six stronger fluorescence than the prototype fibers used for the laboratory measurements, due to higher contamination by the rare-earth elements.
- Other than Raman scattering, fluorescence does not produce a defined polarization state.
- No method was found to suppress the fluorescence without interventions to the GRAVITY instrument.

The overall backscattering was found to be proportional to fiber length and laser power. These results were used as a basis for different mitigation scenarios.

Mitigation Strategies

Different concepts were evaluated in order to reduce the backscattering of the metrology light onto the instrument detectors by a factor 10^4 to 10^5 . The evaluated concepts are summarized in the following.

(a) Modifications of the Fluoride-Glass Fibers

- Replacing the fiber components from fluoride-glass by bulk optics was investigated and found to be feasible. However, a throughput loss of several 10% would be introduced, and it would not be possible to completely avoid fluoride-glass fibers, which are necessary to feed the IOs.
- Installing newly produced fluoride-glass fibers with smaller contamination was found to have a long lead time and an unpredictable outcome of contamination.

(b) Changing the Laser Wavelength

- The metrology wavelength cannot be easily shifted towards values above the K-band, because there are no commercial fiber components in this range. In addition, the overall instrument properties are less compatible with this approach than with shorter wavelengths than the K-band.
- Thulium contamination in the fluoride-glass fibers produces fluorescence for laser wavelengths between 1550 nm and 1950 nm, but up to a factor 10^3 weaker than the Holmium fluorescence, depending on the incident wavelength. A laser wavelength of 1650 nm together with a more sensitive detection can lead to the required reduction of backscattering.
- An analysis of the fiber modes showed that at 1650 nm the metrology light is not propagated in a single mode anymore, potentially corrupting the metrology phase measurements.
- The wavelength of 1750 nm was found to be an acceptable compromise between a lower backscattering level and almost single-mode operation.

(c) Reduced Laser Power

- Different injection schemes were investigated to enable the operation of the metrology at lower laser power. The optical paths in the fluoride-glass fibers can be tracked by low-power beams. The high power needed for the signal detection at the telescopes can be injected behind the fibers. In this scenario, the original dual-beam scheme is transformed to a three-beam scheme.
- More sensitive detectors were evaluated, with the easiest modification being the exchange of photodiodes to components with a smaller photosensitive area, which have lower noise levels. The increase in SNR is roughly a factor of two. Implementing other detectors requires major changes to the original design.

From all these evaluated concepts such a three-beam scheme and increasing the sensitivity of the metrology detectors were the best solution. The implementation does not require long development phases or exchanging optical elements, as altering the laser wavelength would induce. The system impact of the transition to the three-beam scheme was overall moderate.

Three-Beam Scheme

- The original metrology laser is used to produce three beams: a high-power component and two faint beams. While the two faint beams trace the optical paths within GRAVITY, the third beam is superimposed at a later stage in the fiber couplers, not passing the fluoride-glass fibers.

- At the telescopes, the three-beam interference is analyzed in a homodyne detection scheme, where lock-in amplifiers are coupled to the individual frequencies at which the faint beams are phase-modulated.
- AC coupling of the receivers is introduced to prevent saturation in the signal chain.
- The phase difference between the faint beams can be extracted by the difference of their respective phases and the high-power phase.
- The limitations of this scheme are laser fluctuations and receiver sensitivity. The latter point was addressed by implementing smaller photodiodes as well as larger focusing lenses at the UT receivers.

The reduction of the backscattering levels by $\sim 10^4$ in the three-beam scheme is compliant with the specified values. On the science detector, the backscattering exceeds the thermal background only by a factor of < 5 and only in a few pixels of the short wavelengths. The fringe tracker detector is effectively not affected by the backscattering due to a high frame rate.

At the time of writing, the pericenter passage of S2 is observed during several months. These observations will probe effects of general relativity for the first time in the vicinity of a SMBH.

Bibliography

- Agger, C., Petersen, C., Dupont, S., et al. 2012, *J. Opt. Soc. Am. B*, 29, 635
- Alcorn, L. Y., Tran, K.-V. H., Kacprzak, G. G., et al. 2016, *ApJL*, 825, L2
- Amorim, A., Lima, J., Anugu, N., et al. 2012, in *Proc. SPIE*, Vol. 8445, *Optical and Infrared Interferometry III*, 844534
- Arsenault, R., Alonso, J., Bonnet, H., et al. 2003, in *Proc. SPIE*, Vol. 4839, *Adaptive Optical System Technologies II*, ed. P. L. Wizinowich & D. Bonaccini, 174–185
- Baganoff, F. K., Bautz, M. W., Brandt, W. N., et al. 2001, *Nature*, 413, 45
- Barro, G., Faber, S. M., Pérez-González, P. G., et al. 2013, *ApJ*, 765, 104
- . 2014, *ApJ*, 791, 52
- Barro, G., Faber, S. M., Koo, D. C., et al. 2017, *ApJ*, 840, 47
- Bertin, E., & Arnouts, S. 1996, *A&AS*, 117, 393
- Binney, J., & Tremaine, S. 2008, *Galactic Dynamics: Second Edition* (Princeton University Press)
- Blind, N., Eisenhauer, F., Haug, M., et al. 2014a, in *Proc. SPIE*, Vol. 9146, *Optical and Infrared Interferometry IV*, 91461U
- Blind, N., Huber, H., Eisenhauer, F., et al. 2014b, in *Proc. SPIE*, Vol. 9146, *Optical and Infrared Interferometry IV*, 914624
- Boffin, H. M. J., Hussain, G., Berger, J.-P., & Schmidtobreick, L., eds. 2016, *Astrophysics and Space Science Library*, Vol. 439, *Astronomy at High Angular Resolution*
- Bolatto, A. D., Wolfire, M., & Leroy, A. K. 2013, *ARA&A*, 51, 207
- Born, M., & Wolf, E. 1999, *Principles of Optics*, 986
- Bouché, N., Dekel, A., Genzel, R., et al. 2010, *ApJ*, 718, 1001
- Bournaud, F., Daddi, E., Weiß, A., et al. 2015, *A&A*, 575, A56

- Bournaud, F., Elmegreen, B. G., & Elmegreen, D. M. 2007, *ApJ*, 670, 237
- Bournaud, F., Elmegreen, B. G., Teyssier, R., Block, D. L., & Puerari, I. 2010, *MNRAS*, 409, 1088
- Boyd, R. W. 2008, in *Nonlinear Optics (Third Edition)*, third edition edn., ed. R. W. Boyd (Burlington: Academic Press), 473 – 509
- Brammer, G. B., van Dokkum, P. G., & Coppi, P. 2008, *ApJ*, 686, 1503
- Brook, C. B., Stinson, G., Gibson, B. K., et al. 2012, *MNRAS*, 419, 771
- Bruzual, G., & Charlot, S. 2003, *MNRAS*, 344, 1000
- Burke, B. F., & Graham-Smith, F. 2014, *An Introduction to Radio Astronomy*
- Burkert, A., Genzel, R., Bouché, N., et al. 2010, *ApJ*, 725, 2324
- Burtscher, L., Wieprecht, E., Ott, T., et al. 2014, in *Proc. SPIE, Vol. 9146, Optical and Infrared Interferometry IV*, 91462B
- Calzetti, D. 1997, *AJ*, 113, 162
- Calzetti, D., Armus, L., Bohlin, R. C., et al. 2000, *ApJ*, 533, 682
- Calzetti, D., Kinney, A. L., & Storchi-Bergmann, T. 1994, *ApJ*, 429, 582
- Cappellari, M., & Copin, Y. 2003, *MNRAS*, 342, 345
- Carilli, C. L., & Walter, F. 2013, *ARA&A*, 51, 105
- Carleton, T., Cooper, M. C., Bolatto, A. D., et al. 2017, *MNRAS*, 467, 4886
- Chabrier, G. 2003, *PASP*, 115, 763
- Chelli, A., Utrera, O. H., & Duvert, G. 2009, *A&A*, 502, 705
- Choquet, É., Menu, J., Perrin, G., et al. 2014, *A&A*, 569, A2
- Clark, B. G. 1980, *A&A*, 89, 377
- Conroy, C., & Wechsler, R. H. 2009, *ApJ*, 696, 620
- Coudé du Foresto, V., Perrin, G., Ruilier, C., et al. 1998, in *Proc. SPIE, Vol. 3350, Astronomical Interferometry*, ed. R. D. Reasenberg, 856–863
- Cresci, G., Hicks, E. K. S., Genzel, R., et al. 2009, *ApJ*, 697, 115
- Daddi, E., Cimatti, A., Renzini, A., et al. 2004, *ApJ*, 617, 746

- Daddi, E., Dannerbauer, H., Elbaz, D., et al. 2008, *ApJL*, 673, L21
- Davé, R., Finlator, K., & Oppenheimer, B. D. 2011, *MNRAS*, 416, 1354
- . 2012, *MNRAS*, 421, 98
- Davies, R., Förster Schreiber, N. M., Cresci, G., et al. 2011, *ApJ*, 741, 69
- Davis, M., Guhathakurta, P., Konidaris, N. P., et al. 2007, *ApJL*, 660, L1
- de Vaucouleurs, G. 1948, *Annales d’Astrophysique*, 11, 247
- Dekel, A., Sari, R., & Ceverino, D. 2009, *ApJ*, 703, 785
- Delplancke, F., Nijenhuis, J., de Man, H., et al. 2004, in *Proc. SPIE*, Vol. 5491, *New Frontiers in Stellar Interferometry*, ed. W. A. Traub, 1528
- Derie, F. 2000, in *Proc. SPIE*, Vol. 4006, *Interferometry in Optical Astronomy*, ed. P. Léna & A. Quirrenbach, 25–30
- Dickman, R. L., Snell, R. L., & Schloerb, F. P. 1986, *ApJ*, 309, 326
- Dodds-Eden, K., Porquet, D., Trap, G., et al. 2009, *ApJ*, 698, 676
- Downes, D., & Solomon, P. M. 1998, *ApJ*, 507, 615
- Durteste, Y., Monerie, M., & Lamouler, P. 1985, *Electronics Letters*, 21, 723
- Eckart, A., Baganoff, F. K., Morris, M., et al. 2004, *A&A*, 427, 1
- Eisenhauer, F., Genzel, R., Alexander, T., et al. 2005, *ApJ*, 628, 246
- Eisenhauer, F., Perrin, G., Brandner, W., et al. 2011, *The Messenger*, 143, 16
- Elmegreen, B. G., Bournaud, F., & Elmegreen, D. M. 2008, *ApJ*, 688, 67
- ESO. 2017, <https://www.eso.org/sci/facilities/paranal/telescopes/>
- Farrell, C. T., & Player, M. A. 1994, *Measurement Science and Technology*, 5, 648
- Finger, G., Dorn, R. J., Eschbaumer, S., et al. 2008, in *Proc. SPIE*, Vol. 7021, *High Energy, Optical, and Infrared Detectors for Astronomy III*, 70210P
- Finger, G., Baker, I., Alvarez, D., et al. 2016, in *Proc. SPIE*, Vol. 9909, *Adaptive Optics Systems V*, 990912
- Fitzgibbon, A. W., Pilu, M., & Fisher, R. B. 1996, in *Proceedings of 13th International Conference on Pattern Recognition*, Vol. 1, 253–257 vol.1

- Folkenberg, J. R., Nielsen, M. D., Mortensen, N. A., Jakobsen, C., & Simonsen, H. R. 2004, *Optics Express*, 12, 956
- Förster Schreiber, N. M., Genzel, R., Bouché, N., et al. 2009, *ApJ*, 706, 1364
- Förster Schreiber, N. M., Genzel, R., Newman, S. F., et al. 2014, *ApJ*, 787, 38
- Fortin, V., Bernier, M., Carrier, J., & Vallée, R. 2011, *Opt. Lett.*, 36, 4152
- Freundlich, J., Combes, F., Tacconi, L. J., et al. 2018, to be published in *A&A*
- . 2013, *A&A*, 553, A130
- Fried, D. L. 1965, *Journal of the Optical Society of America (1917-1983)*, 55, 1427
- Fu, J., Kauffmann, G., Li, C., & Guo, Q. 2012, *MNRAS*, 424, 2701
- Fujikura. 2017, www.fujikura.co.jp/eng/resource/pdf/16pnb04.pdf
- Gai, M., Menardi, S., Cesare, S., et al. 2004, in *Proc. SPIE*, Vol. 5491, *New Frontiers in Stellar Interferometry*, ed. W. A. Traub, 528
- Genzel, R., Eisenhauer, F., & Gillessen, S. 2010, *Reviews of Modern Physics*, 82, 3121
- Genzel, R., Schödel, R., Ott, T., et al. 2003, *Nature*, 425, 934
- Genzel, R., Burkert, A., Bouché, N., et al. 2008, *ApJ*, 687, 59
- Genzel, R., Newman, S., Jones, T., et al. 2011, *ApJ*, 733, 101
- Genzel, R., Tacconi, L. J., Combes, F., et al. 2012, *ApJ*, 746, 69
- Genzel, R., Tacconi, L. J., Kurk, J., et al. 2013, *ApJ*, 773, 68
- Genzel, R., Tacconi, L. J., Lutz, D., et al. 2015, *ApJ*, 800, 20
- Genzel, R., Schreiber, N. M. F., Übler, H., et al. 2017, *Nature*, 543, 397
- Ghez, A. M., Salim, S., Weinberg, N. N., et al. 2008, *ApJ*, 689, 1044
- Gillessen, S., Lippa, M., Eisenhauer, F., et al. 2012, in *Proc. SPIE*, Vol. 8445, *Optical and Infrared Interferometry III*, 84451O
- Gillessen, S., Plewa, P. M., Eisenhauer, F., et al. 2017, *ApJ*, 837, 30
- Glindemann, A. 2011, *Principles of Stellar Interferometry*, doi:10.1007/978-3-642-15028-9
- Gonté, F. Y. J., Alonso, J., Aller-Carpentier, E., et al. 2016, in *Proc. SPIE*, Vol. 9907, *Optical and Infrared Interferometry and Imaging V*, 990720

- González-Alfonso, E., Fischer, J., Spoon, H. W. W., et al. 2017, *ApJ*, 836, 11
- Gowardhan, A., Riechers, D. A., Daddi, E., et al. 2017, *ApJ*, 838, 136
- Gravity Collaboration. 2017, *The Messenger*, 170, 10
- Gravity Collaboration, Sanchez-Bermudez, J., Weigelt, G., et al. 2018, submitted to *A&A*
- Gravity Collaboration, Petrucci, P.-O., Waisberg, I., et al. 2017a, *A&A*, 602, L11
- Gravity Collaboration, Abuter, R., Accardo, M., et al. 2017b, *A&A*, 602, A94
- GRAVITY Collaboration, Waisberg, I., Dexter, J., et al. 2017, ArXiv e-prints, arXiv:1705.02351
- Grogin, N. A., Kocevski, D. D., Faber, S. M., et al. 2011, *ApJS*, 197, 35
- Grould, M., Vincent, F. H., Paumard, T., & Perrin, G. 2017, ArXiv e-prints, arXiv:1709.04492
- Guilloteau, S. 1997, in *NATO Advanced Science Institutes (ASI) Series C*, Vol. 501, NATO Advanced Science Institutes (ASI) Series C, ed. A.-M. Lagrange, D. Mourard, & P. Lena, 145
- Guilloteau, S., Delannoy, J., Downes, D., et al. 1992, *A&A*, 262, 624
- Haguenauer, P., Abuter, R., Andolfato, L., et al. 2012, in *Proc. SPIE*, Vol. 8445, *Optical and Infrared Interferometry III*, 84450D
- Halir, R., & Flusser, J. 1998, in , 125–132
- Haug, M., Haussmann, F., Kellner, S., et al. 2014, in *Proc. SPIE*, Vol. 9151, *Advances in Optical and Mechanical Technologies for Telescopes and Instrumentation*, 91513C
- Hodge, J. A., Carilli, C. L., Walter, F., et al. 2012, *ApJ*, 760, 11
- Högbom, J. A. 1974, *A&AS*, 15, 417
- Hollenbach, D. J., & Tielens, A. G. G. M. 1999, *Reviews of Modern Physics*, 71, 173
- Immeli, A., Samland, M., Gerhard, O., & Westera, P. 2004a, *A&A*, 413, 547
- Immeli, A., Samland, M., Westera, P., & Gerhard, O. 2004b, *ApJ*, 611, 20
- IRAM. 2017, <http://www.iram-institute.org/>
- Jackson, N. 2008, in *Lecture Notes in Physics*, Berlin Springer Verlag, Vol. 742, *Jets from Young Stars II*, ed. F. Bacciotti, L. Testi, & E. Whelan, 193

- Jocou, L., Perraut, K., Moulin, T., et al. 2014, in Proc. SPIE, Vol. 9146, Optical and Infrared Interferometry IV, 91461J
- Kaminskii, A. 1996, *Crystalline Lasers: Physical Processes and Operating Schemes*, Laser & Optical Science & Technology (Taylor & Francis)
- Kauffmann, G., White, S. D. M., & Guiderdoni, B. 1993, MNRAS, 264, 201
- Kawasaki, B. S., & Hill, K. O. 1977, Appl. Opt., 16, 1794
- Kennicutt, R. C., & Evans, N. J. 2012, ARA&A, 50, 531
- Kervella, P., Coudé du Foresto, V., Glindemann, A., & Hofmann, R. 2000, in Proc. SPIE, Vol. 4006, Interferometry in Optical Astronomy, ed. P. Léna & A. Quirrenbach, 31–42
- Kervella, P., Mérand, A., Ledoux, C., Demory, B.-O., & Le Bouquin, J.-B. 2016, A&A, 593, A127
- Kishimoto, M., Hönig, S. F., Antonucci, R., et al. 2011, A&A, 527, A121
- Kister, C. F. 2011, diploma thesis, Ludwig-Maximilians-Universität, München
- Koekemoer, A. M., Faber, S. M., Ferguson, H. C., et al. 2011, ApJS, 197, 36
- Kok, Y., Gillessen, S., Lacour, S., et al. 2014, in Proc. SPIE, Vol. 9146, Optical and Infrared Interferometry IV, 914625
- Kolmogorov, A. 1941, Akademiia Nauk SSSR Doklady, 30, 301
- Kolmogorov, A. N. 1991, Proceedings of the Royal Society of London Series A, 434, 9
- Komatsu, E., Smith, K. M., Dunkley, J., et al. 2011, ApJS, 192, 18
- Kriek, M., van Dokkum, P. G., Labbé, I., et al. 2009, ApJ, 700, 221
- Krumholz, M. 2017, Star Formation
- Krumholz, M., & Burkert, A. 2010, ApJ, 724, 895
- Labeyrie, A., Lipson, S. G., & Nisenson, P. 2006, An Introduction to Optical Stellar Interferometry, 360, doi:10.2277/0521828724
- Lacour, S., Eisenhauer, F., Gillessen, S., et al. 2014, A&A, 567, A75
- Lagos, C. D. P., Baugh, C. M., Lacey, C. G., et al. 2011, MNRAS, 418, 1649
- Landsberg, G., & Mandelstam, L. 1928, Naturwissenschaften, 16, 557
- Lang, P., Wuyts, S., Somerville, R. S., et al. 2014, ApJ, 788, 11

- Lang, P., Förster Schreiber, N. M., Genzel, R., et al. 2017, *ApJ*, 840, 92
- Lapeyrere, V., Kervella, P., Lacour, S., et al. 2014, in *Proc. SPIE*, Vol. 9146, *Optical and Infrared Interferometry IV*, 91462D
- Larson, R. B. 1981, *MNRAS*, 194, 809
- Lawson, P. R., ed. 2000, *Principles of Long Baseline Stellar Interferometry*
- Le Bouquin, J.-B., Berger, J.-P., Lazareff, B., et al. 2011, *A&A*, 535, A67
- Leinert, C., Graser, U., Przygodda, F., et al. 2003, *Ap&SS*, 286, 73
- Lippa, M. 2012, master thesis, Ludwig-Maximilians-Universität, München
- Lippa, M., Gillessen, S., Blind, N., et al. 2018, in preparation
- Lippa, M., Blind, N., Gillessen, S., et al. 2014, in *Proc. SPIE*, Vol. 9146, *Optical and Infrared Interferometry IV*, 914622
- Lippa, M., Gillessen, S., Blind, N., et al. 2016, in *Proc. SPIE*, Vol. 9907, *Optical and Infrared Interferometry and Imaging V*, 990722
- Madau, P., & Dickinson, M. 2014, *ARA&A*, 52, 415
- Marechal, A. 1947, *Rev. Opt. Theor. Instrum.*, 26, 257
- Matter, A., Lopez, B., Antonelli, P., et al. 2016, in *Proc. SPIE*, Vol. 9907, *Optical and Infrared Interferometry and Imaging V*, 99070A
- McCracken, H. J., Capak, P., Salvato, M., et al. 2010, *ApJ*, 708, 202
- Menu, J., Perrin, G., Choquet, E., & Lacour, S. 2012, *A&A*, 541, A81
- Mihos, J. C., & Hernquist, L. 1996, *ApJ*, 464, 641
- Mo, H. J., Mao, S., & White, S. D. M. 1998, *MNRAS*, 295, 319
- Momcheva, I. G., Brammer, G. B., van Dokkum, P. G., et al. 2016, *ApJS*, 225, 27
- Monnier, J. D. 2003, *Reports on Progress in Physics*, 66, 789
- Monnier, J. D., & Allen, R. J. 2013, *Radio and Optical Interferometry: Basic Observing Techniques and Data Analysis*, ed. T. D. Oswalt & H. E. Bond, 325
- Nakamoto, K. 2008, *Theory of Normal Vibrations* (John Wiley & Sons, Inc.), 1–147
- Nelson, E. J., van Dokkum, P. G., Förster Schreiber, N. M., et al. 2016, *ApJ*, 828, 27
- Newman, J. A., Cooper, M. C., Davis, M., et al. 2013, *ApJS*, 208, 5

- Nobel Media. 2018, http://www.nobelprize.org/nobel_prizes/physics/laureates/1930/
- Noda, J., Okamoto, K., & Sasaki, Y. 1986, *Journal of Lightwave Technology*, 4, 1071
- Noeske, K. G., Weiner, B. J., Faber, S. M., et al. 2007, *ApJL*, 660, L43
- Noguchi, M. 1988, *A&A*, 203, 259
- . 1999, *ApJ*, 514, 77
- Obreschkow, D., & Rawlings, S. 2009, *ApJL*, 696, L129
- Oppenheimer, B. D., & Davé, R. 2008, *MNRAS*, 387, 577
- Oppenheimer, B. D., Davé, R., Kereš, D., et al. 2010, *MNRAS*, 406, 2325
- Ott, T. 2018, <http://www.mpe.mpg.de/~ott/QFitsView/>
- Ott, T., Wieprecht, E., Burtscher, L., et al. 2014, in *Proc. SPIE*, Vol. 9146, *Optical and Infrared Interferometry IV*, 91462A
- Peng, C. Y., Ho, L. C., Impey, C. D., & Rix, H.-W. 2002, *AJ*, 124, 266
- . 2010, *AJ*, 139, 2097
- Penninckx, D., Beck, N., Gleyze, J.-F., & Videau, L. 2006, *J. Lightwave Technol.*, 24, 4197
- Perraut, K., Jocou, L., Berger, J. P., et al. 2018, accepted for publication in *A&A*
- Perrin, G., Ollivier, M., & Coudé du Foresto, V. 2000, in *Proc. SPIE*, Vol. 4006, *Interferometry in Optical Astronomy*, ed. P. Léna & A. Quirrenbach, 1007–1013
- Perrin, G., Ridgway, S. T., Coudé du Foresto, V., et al. 2004, *A&A*, 418, 675
- Petrov, R. G., Malbet, F., Weigelt, G., et al. 2007, *A&A*, 464, 1
- Pfuhl, O., Haug, M., Eisenhauer, F., et al. 2014, in *Proc. SPIE*, Vol. 9146, *Optical and Infrared Interferometry IV*, 914623
- Planck Collaboration, Ade, P. A. R., Aghanim, N., et al. 2014, *A&A*, 571, A16
- Price, S. H., Kriek, M., Shapley, A. E., et al. 2016, *ApJ*, 819, 80
- Quirrenbach, A. 2001, *ARA&A*, 39, 353
- Raman, C. V. 1928, *Nature*, 121, 501
- Raman, C. V., & Krishnan. 1928, *Indian J. Phys.*, 2, 387
- Richings, A. J., & Faucher-Giguère, C.-A. 2018, *MNRAS*, 474, 3673

- Roddier, F. 1999, Adaptive optics in astronomy
- Rupke, D. S. N., & Veilleux, S. 2013, ApJL, 775, L15
- Russell, H. N., & Saunders, F. A. 1925, ApJ, 61, 38
- Sahlmann, J., Ménardi, S., Abuter, R., et al. 2009, A&A, 507, 1739
- Saintonge, A., Kauffmann, G., Kramer, C., et al. 2011a, MNRAS, 415, 32
- Saintonge, A., Kauffmann, G., Wang, J., et al. 2011b, MNRAS, 415, 61
- Saintonge, A., Catinella, B., Tacconi, L. J., et al. 2017, ApJS, 233, 22
- Saissy, A., Botineau, J., Macon, L., & Maze, G. 1985, J. Physique Lett., 46, 289
- Sanders, D. B., & Mirabel, I. F. 1996, ARA&A, 34, 749
- Scheithauer, S., Brandner, W., Deen, C., et al. 2016, in Proc. SPIE, Vol. 9909, Adaptive Optics Systems V, 99092L
- Schödel, R., Ott, T., Genzel, R., et al. 2002, Nature, 419, 694
- Scholle, K., Lamrini, S., Koopmann, P., & Fuhrberg, P. 2010, in Frontiers in Guided Wave Optics and Optoelectronics, ed. B. Pal (Rijeka: InTech)
- Scoville, N., Sheth, K., Aussel, H., et al. 2016, ApJ, 820, 83
- Scoville, N. Z. 2013, Evolution of star formation and gas, ed. J. Falcón-Barroso & J. H. Knapen, 491
- Sersic, J. L. 1968, Atlas de Galaxias Australes
- Shao, M., & Colavita, M. M. 1992, A&A, 262, 353
- Shao, M., & Staelin, D. H. 1980, ApOpt, 19, 1519
- Shapiro, P. R., & Field, G. B. 1976, ApJ, 205, 762
- Simpson, D. A. 2008, PhD thesis, Victoria University
- Singh, S. P., Gangwar, R., & Singh, N. 2007, PIER, 74, 379
- Smekal, A. 1923, Naturwissenschaften, 11, 873
- Solomon, P. M., Downes, D., Radford, S. J. E., & Barrett, J. W. 1997, ApJ, 478, 144
- Solomon, P. M., Rivolo, A. R., Barrett, J., & Yahil, A. 1987, ApJ, 319, 730
- Speagle, J. S., Steinhardt, C. L., Capak, P. L., & Silverman, J. D. 2014, ApJS, 214, 15

- Stark, J. 1914, *Annalen der Physik*, 348, 965
- Stehl, K. 1902, *Zeitschrift für Instrumentenkunde*, 22, 213
- Stott, J. P., Swinbank, A. M., Johnson, H. L., et al. 2016, *MNRAS*, 457, 1888
- Straubmeier, C., Yazici, S., Wiest, M., et al. 2014, in *Proc. SPIE*, Vol. 9146, *Optical and Infrared Interferometry IV*, 914629
- Tacchella, S., Carollo, C. M., Renzini, A., et al. 2015, *Science*, 348, 314
- Tacconi, L. J., Genzel, R., Neri, R., et al. 2010, *Nature*, 463, 781
- Tacconi, L. J., Neri, R., Genzel, R., et al. 2013, *ApJ*, 768, 74
- Tacconi, L. J., Genzel, R., Saintonge, A., et al. 2018, *ApJ*, 853, 179
- Tadaki, K.-i., Kodama, T., Nelson, E. J., et al. 2017, *ApJL*, 841, L25
- Tatulli, E., Millour, F., Chelli, A., et al. 2007, *A&A*, 464, 29
- Thompson, A. R., Moran, J. M., & Swenson, Jr., G. W. 2017, *Interferometry and Synthesis in Radio Astronomy*, 3rd Edition
- Thorlabs. 2017, <https://www.thorlabs.com>
- Tody, D. 1993, in *Astronomical Society of the Pacific Conference Series*, Vol. 52, *Astronomical Data Analysis Software and Systems II*, ed. R. J. Hanisch, R. J. V. Brissenden, & J. Barnes, 173
- Toomre, A. 1964, *ApJ*, 139, 1217
- Toomre, A. 1977, in *Evolution of Galaxies and Stellar Populations*, ed. B. M. Tinsley & R. B. G. Larson, D. Campbell, 401
- Übler, H., Naab, T., Oser, L., et al. 2014, *MNRAS*, 443, 2092
- Übler, H., Genzel, R., Tacconi, L. J., et al. 2018, *ApJL*, 854, L24
- van der Wel, A., Chang, Y.-Y., Bell, E. F., et al. 2014, *ApJL*, 792, L6
- van Dokkum, P. G., Nelson, E. J., Franx, M., et al. 2015, *ApJ*, 813, 23
- Vincent, F. H., Paumard, T., Perrin, G., et al. 2014, *MNRAS*, 441, 3477
- Waisberg, I., Dexter, J., Gillessen, S., et al. 2018, *MNRAS*, arXiv:1802.08198
- Walter, F., Bolatto, A. D., Leroy, A. K., et al. 2017, *ApJ*, 835, 265
- Weber, J. 2014, master thesis, Technische Universität München, München

- Weigelt, G., Hofmann, K.-H., Kishimoto, M., et al. 2012, *A&A*, 541, L9
- Whitaker, K. E., Franx, M., Leja, J., et al. 2014, *ApJ*, 795, 104
- White, S. D. M., & Rees, M. J. 1978, *MNRAS*, 183, 341
- Wisnioski, E., Förster Schreiber, N. M., Wuyts, S., et al. 2015, *ApJ*, 799, 209
- Wuillez, J., & Lacour, S. 2013, *ApJ*, 764, 109
- Wuillez, J., Wizinowich, P., Akeson, R., et al. 2014, *ApJ*, 783, 104
- Wolfire, M. G., Hollenbach, D., & McKee, C. F. 2010, *ApJ*, 716, 1191
- Wooten, E. L., Kissa, K. M., Yi-Yan, A., et al. 2000, *IEEE Journal of Selected Topics in Quantum Electronics*, 6, 69
- Wuyts, S., Förster Schreiber, N. M., van der Wel, A., et al. 2011a, *ApJ*, 742, 96
- Wuyts, S., Förster Schreiber, N. M., Lutz, D., et al. 2011b, *ApJ*, 738, 106
- Wuyts, S., Förster Schreiber, N. M., Genzel, R., et al. 2012, *ApJ*, 753, 114
- Wuyts, S., Förster Schreiber, N. M., Nelson, E. J., et al. 2013, *ApJ*, 779, 135
- Wuyts, S., Förster Schreiber, N. M., Wisnioski, E., et al. 2016, *ApJ*, 831, 149
- Wyant, J. C. 1975, *ApOpt*, 14, 2622
- Yan, X., Kito, C., Miyoshi, S., et al. 2012, *J. Opt. Soc. Am. B*, 29, 238
- Zhang, W. J., Zhang, Q. Y., Chen, Q. J., et al. 2009, *Opt. Express*, 17, 20952

List of Acronyms and Abbreviations

ACS	Advanced Camera for Surveys
AEGIS	All-Wavelength Extended Groth Strip International Survey
AGN	Active Galactic Nuclei
AO	Adaptive Optics
AT	Auxiliary Telescope
BC	Beam Combiner
BCI	Beam Combiner Instrument
BH	Black Hole
CANDELS	Cosmic Assembly Near-Infrared Deep Extragalactic Legacy Survey
CDM	Cold Dark Matter
CO	Carbon Monoxide
CU	Calibration Unit
DDL	Differential Delay Line
dec	declination
DL	Delay Line
DM	Deformable Mirror
dOPD	differential Optical Path Difference
DYSMAL	DYnamical Simulation and Modelling ALgorithm
EAZY	Easy and Accurate redshifts from Yale
EGS	Extended Groth Strip

ER	Extinction Ratio
ESO	European Southern Observatory
FAST	Fitting And Assessment of Synthetic Templates
FBT	Fused Biconical Taper
FC	Fiber Coupler
FCU	Fiber Control Unit
FDDL	Fiber Differential Delay Line
FFT	Fast Fourier Transform
FITS	Flexible Image Transport System
FOV	Field of View
FPR	Fiber Polarization Rotator
FT	Fringe Tracker
FWHM	Full Width at Half Maximum
GC	Galactic Center
GMC	Giant Molecular Cloud
HST	Hubble Space Telescope
IMF	Initial Mass Function
IO	Integrated Optics
IR	Infrared
IRAF	Image Reduction and Analysis Facility
IRAM	Institut de Radioastronomie Millimétrique
ISM	Interstellar Medium
LO	Local Oscillator
LOS	Line Of Sight
LVF	Le Verre Fluoré
MIR	Mid-Infrared

MM	Multi-Mode
MPE	Max Planck Institute for Extraterrestrial Physics
MS	Main Sequence
NIR	Near-Infrared
NOEMA	NOthern Extended Millimeter Array
OPD	Optical Path Difference
PA	Position Angle
PdBI	Plateau de Bure Interferometer
PHIBSS	Plateau de Bure HIgh-z Blue Sequence Survey
PM	Polarization-Maintaining
PS	Phase Shifter
PSF	Point Spread Function
P2VM	Pixel-to-Visibility Matrix
RA	Right Ascension
REE	Rare-Earth Element
rms	root mean square
SC	Science
SED	Spectral Energy Distribution
SFG	Star-Forming Galaxy
SFH	Star Formation History
SFR	Star Formation Rate
SH	Shack-Hartmann
SI	Système International d'unités
SM	Single-Mode
SMBH	SuperMassive Black Hole
SMG	Sub-Millimeter Galaxy

SNR	Signal-to-Noise Ratio
SPS	Stellar Population Synthesis
SR	Strehl Ratio
STS	Star Separator System
ULIRG	Ultra Luminous Infrared Galaxy
UT	Unit Telescope
UV	Ultraviolet
VLT	Very Large Telescope
VLTI	Very Large Telescope Interferometer
WFC3	Wide Field Camera 3
WFS	Wavefront Sensor
WLF	Wight-Light Fringe
WMAP	Wilkinson Microwave Anisotropy Probe

Acknowledgments

I am deeply grateful to many different people, who helped me in thought, word and deed and by that contributed to this thesis.

First of all, I would like to thank Prof. Dr. Reinhard Genzel for supervising this thesis and for giving me the opportunity to work in the infrared/millimeter group, which I have always been highly appreciating. I am also very grateful to Linda Tacconi and Frank Eisenhauer. With your guiding hands you supported me and my work such that I felt safe, despite of the uncertainty of experimental physics that accompanied my daily work. Many thanks also go to Oliver Pfuhl, who always had good advice on how to handle this intense double project of instrumentation and astronomy, since he had been in the same position not too long ago.

Also many other people contributed to an encouraging work atmosphere with their knowledge and support. These include Stefan Gillessen, Nicolas Blind, Yitping Kok, Marcus Haug, Frank Haußmann, Stefan Kellner, Thomas Ott, Ekki Wieprecht, Şenol Yazıcı, Leonard Burtscher, Karine Perraut, Laurent Jocou, Guy Perrin, Stijn Wuyts, Philipp Lang, Hannah Übler, Natascha Förster-Schreiber, Ken-ichi Tadaki, Liz George, Peter Buschkamp and many more at MPE or within the GRAVITY consortium, who are not mentioned by name here.

Special thanks go to my fellow graduate students Annemieke, Ming-Yi, Philipp, Idel, Rebecca, Alejandra, Sebastiano, Martina, Christoph, Raphael and Felix for the daily lunch time spent together pleasantly.

Last but not least I send my warmest thanks to my nearest and dearest for their love and support, in particular ...

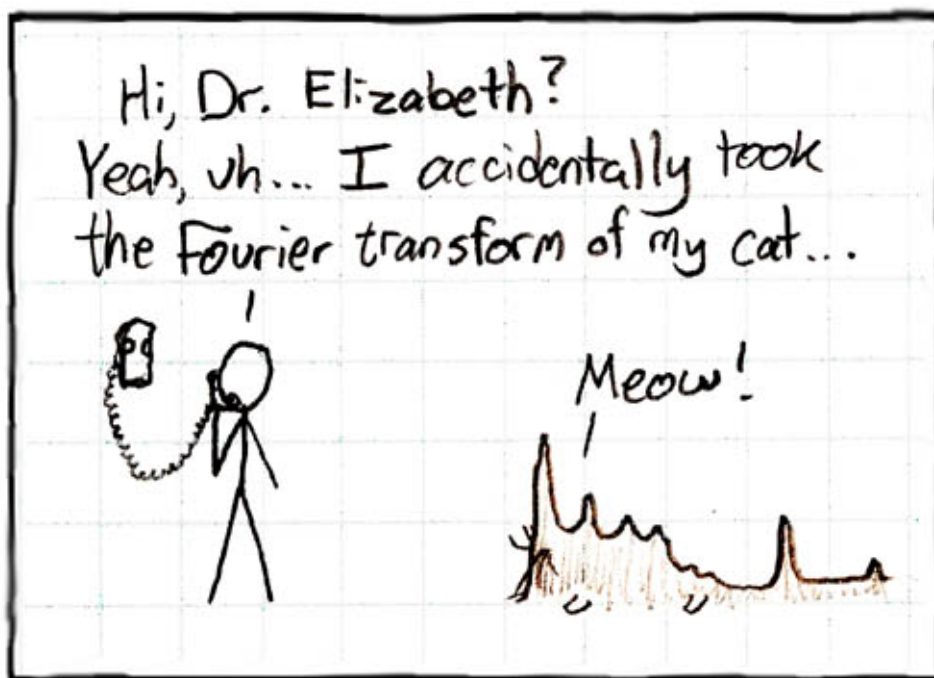
... to Michael, who makes me feel happy no matter what, by his heart, mind, strong shoulders and culinary skills.

... to my brother, Kamill, who is my best friend forever and makes me laugh like no one else.

... to my parents, who explained the world to me and now are proud of me explaining it to them.

... as well as to my big (German/Polish/Silesian/...) family, who has kept asking me about the Big Bang, black holes and other revelations, shining a light on all the details that I did not know as well as I had thought, but at the same time enhancing the feeling that I am doing something exciting and relevant.

Thank you! Danke! Dzieki! Dziynki!



<http://imgs.xkcd.com/comics/fourier.jpg>